Filtration of Macromolecules by Renal Glomerular Capillaries

by

Aurélie Edwards

Submitted to the Department of Chemical Engineering
in partial fulfillment of the requirements for the degree of
Doctor of Philosophy
at the
MASSACHUSETTS INSTITUTE OF TECHNOLOGY

February 1996

© Massachusetts Institute of Technology 1996. All rights reserved.

Author ....
Department of Chemical Engineering
January 22, 1996

Certified by ....
William M. Deen
Professor of Chemical Engineering
Thesis Supervisor

Accepted by ....
Robert E. Cohen
Chairman, Committee for Graduate Students

ARCHIVES
MASSACHUSETTS INSTITUTE
OF TECHNOLOGY

MAR 22 1996

LIBRARIES

Filtration of Macromolecules by Renal Glomerular Capillaries

by

Aurélie Edwards

Submitted to the Department of Chemical Engineering
on January 22, 1996, in partial fulfillment of the
requirements for the degree of
Doctor of Philosophy

Abstract

The overall goal of this thesis was to understand the biophysical basis for glomerular filtration, the impairment of which characterizes most forms of kidney disease. The permselectivity of the glomerular capillary wall in vivo is usually assessed by measuring sieving coefficients (Θ) of tracer solutes, and relating these data to the intrinsic properties of the barrier using a mathematical model. Membrane models based on the concept of equivalent cylindrical pores have traditionally been used for that purpose, but they do not reflect the real ultrastructure of the capillary wall, which consists of three layers: a fenestrated endothelium, a glomerular basement membrane (GBM), and epithelial cells spanned by slit diaphragms. We first showed that pore models could not be used to estimate the mean transmural hydraulic pressure difference ($\overline{\Delta P}$) from macromolecular sieving data, due to the effect of random measurement errors and uncertainties in the models.

A novel "ultrastructural" model was developed to relate the sieving coefficients of neutral macromolecules to the structural characteristics of the individual layers of the glomerular capillary wall. To characterize solute transport across each layer, we first measured diffusion rates of Ficoll across intact and cell-free glomerular capillaries isolated from the rat, using confocal microscopy. The contribution of the GBM to the mass transfer resistance of the barrier varied between 10 and 30 % of the total, depending on molecular size. Diffusional hindrance coefficients for GBM were determined from the data, as well as ultrastructural parameters related to the slit diaphragms. We also measured Ficoll sieving coefficients for isolated rat GBM, and determined diffusional and convective hindrance coefficients as a function of solute size and $\overline{\Delta P}$. The dependence of the Darcy permeability of GBM on $\overline{\Delta P}$ was examined, and the results were interpreted assuming that the GBM consists of a random fibrous network with two populations of fibers of distinct sizes.

The ultrastructural model was then extended to permit simulations of glomerular filtration in vivo, and predictions of sieving coefficients. The simulations indicated that basement membrane thickness and the spacing of the epithelial slits, one or both of which change in certain glomerular diseases, have relatively little effect on glomerular permselectivity. The main determinants were found to be the diffusional and convective hindrance coefficients in the GBM and the parameters which describe the structure of the epithelial slit diaphragm. This new approach has the potential to provide a much better understanding of the physical basis for the functional impairments seen in glomerular disease.

Thesis Supervisor: William M. Deen
Title: Professor of Chemical Engineering

ACKNOWLEDGMENTS

I would like to thank:

- my advisor, Prof. William Deen, for his remarkable wisdom, teachings, and understanding. I will remember above all his wonderful human qualities.

- the member of my thesis committee, Prof. Linda Cima, Prof. Ken Smith and Prof. Roger Kamm, for their continued encouragement.

- Dr. Daniels, who provided invaluable measurements and ideas.

- my dear friends Linda, Berit, Margaret, Colleen and Radha, for always being there.

- the students in the lab, Jim Oliver, Claudia Drumond, Randy Lewis, Erin Johnson, Glen Bolton, Scott Johnston, Manesh Keshive, Jeff White and Patrick Gwynne. I am particularly grateful to Erin and Claudia for their advice and patience.

- Janet Fisher and Elaine Aufiero-Peters for their help in my last year as a non-resident.

- Peter Romanow and Glori Collver-Jacobson, for their continued help and support.

- Joan Chisolm, a big heart on the fifth floor.

- my parents, brothers and sister, for making this adventure possible.

- last but not least, David, my husband, for too many reasons to be listed here.

Table of Contents

1. Introduction 12
1.1 Relevance of Glomerular Function..12
1.2 Thesis Summary 12

2. Structure and Function of the Glomerulus.............................. 14
2.1 Anatomy and Role of the Kidney 14
2.2 Structure of the Glomerular Capillary Wall....................................16
2.2.1 Endothelial Cells...18
2.2.2 Glomerular Basement Membrane...19
2.2.2.1 Chemical Constituents..19
2.2.2.2 Ultrastructure..21
2.2.3 Epithelial Slit Diaphragm 23
2.3 Glomerular Ultrafiltration..24
2.4 Dependence of SNGFR on the Primary Determinants of Glomerular Filtration 28
2.5 Regulation of Glomerular Filtration...29
2.5.1 By Exogenous Substances 29
2.5.2 Autoregulation 31
2.6 Permselectivity of the Glomerular Capillary Wall..............................31
2.6.1 Sieving Coefficients..31
2.6.2 Glomerular Diseases 33
2.7 Pore Models of Glomerular Filtration 34
2.7.1 The Isoporous Model 35
2.7.2 Heteroporous Models...38
2.8 Summary and Conclusions 40

3. Error Propagation in the Estimation of Glomerular Pressure.......... 41
3.1 Introduction..41
3.2 Methods...45
3.2.1 Models for Glomerular Filtration..45
3.2.2 Creation of Synthetic Sets of Data..48
3.2.3 Parameter Estimation Procedures...48
3.2.4 Reliability Measures for Parameter Estimates..............................52
3.2.5 Reliability Measures for Models 53

3.3 Results 55
  3.3.1 Random Errors Only 55
  3.3.2 Systematic Errors Only 58
  3.3.3 Random and Systematic Errors Combined 61
3.4 Discussion 66

4. Previous Work on Ultrastructural Models for Glomerular Ultrafiltration 72
4.1 Introduction 72
4.2 Mathematical Model for Hydraulic Permeability 72
  4.2.1 Idealized Structural Unit 72
  4.2.2 Endothelium 76
  4.2.3 Glomerular Basement Membrane 77
  4.2.4 Epithelium 80
  4.2.5 Comparison with Experimental Data 81
4.3. Transport of Macromolecules Across the Epithelial Slit Diaphragm 82
  4.3.1 Mathematical Model 82
  4.3.2 Distribution of Cylinder Spacings 86
4.4 Conclusions 90

5. Concentration Polarization in Ultrafiltration Studies 92
5.1 Background 92
5.2 Methods 95
5.3 Calculations 96
  5.3.1 Sieving Coefficients 96
  5.3.2 Mass Transfer Coefficient 98
5.4 Results 99
5.5 Discussion 102
5.6 Conclusions 104

6. Hindered Diffusion of Macromolecules across Isolated Glomerular Basement Membrane and Glomerular Capillary Wall 106
6.1 Introduction 106
6.2 Methods 107
6.3 Results 112
6.4 Diffusional Permeability of the Epithelial Slit 120
  6.4.1 Epithelial Slit Diaphragm 122

6.4.2 Epithelial Slit Channel 126
6.5 Discussion 129

7. Filtration of Macromolecules across Isolated Glomerular Basement Membrane 136
7.1 Introduction 136
7.2 Methods 138
7.3 Results 142
7.3.1 Darcy Permeability of the GBM 142
7.3.2 Sieving Curves 143
7.3.3 Hindrance Coefficients 147
7.4 Discussion 152
7.4.1 Comparison with Fiber Matrix Models 154
7.4.2 Models for the Darcy Permeability 161
7.5 Conclusion 167

8. Macromolecular Sieving Coefficients across the Glomerular Capillary Wall 170
8.1 Introduction 170
8.2 Transport of Macromolecules across the Glomerular Basement Membrane 170
8.3 Contribution of the Endothelium to the Permselectivity of the Barrier 173
8.4 Glomerular Capillary Wall Sieving Coefficients 174
8.5 Results 177
8.5.1 Effect of Ultrastructural Parameters on Sieving Curves 177
8.5.2 Predicting In Vivo Ficoll Sieving Data 181
8.5.3 Fitting In Vivo Ficoll Sieving Data 186
8.5.4 Comparison with Pore Models for Glomerular Filtration 191

9. Conclusions and Recommendations 197

Bibliography 200

A: List of Principal Symbols 210

B: Program for Computing Sieving Coefficients 212

List of Figures

2-1 Organisation of the glomerulus.......15
2-2 Schematic representation of the glomerular capillary wall.......17
3-1 Predicted efffects on sieving curves of selective changes in transmembrane pressure ($\overline{\Delta P}$) and pore radius (r_0).......43
3-2 Simulated sieving curves illustrating the meaning of the probability p.......50
3-3 Ratio of the fitted to the exact pressure vs. χ^2 with random errors only.......57
3-4 Ratio of the fitted to the exact pressure vs. the probability p, with modeling errors only.......59
3-5 Effect on the pressure estimate of augmenting the number of pore-size parameters, using "complete" models.......60
3-6 Effect on the pressure estimate of augmenting the number of pore-size parameters, using simpified models.......62
3-7 Ratio of the fitted to the exact pressure vs. the probability p, with both random and systematic errors.......64
3-8 Reliability of the statistic p as a predictor of success in estimating $\overline{\Delta P}$.......65
4-1 Idealized structural unit of the glomerular capillary wall.......74
4-2 Structure of the epithelial slit diaphragm.......75
4-3 Structural unit substituting stripes for the endothelial fenestrae.......79
4-4 Idealized representation of the epithelial slit diaphragm for solute transport.......83
5-1 Concentration polarization in an ultrafiltration cell.......93
5-2 Mass transfer coefficient of albumin at 21°C versus volume flux.......100
6-1 Fluorescence in the capillary lumen and in the bath as a function of time.......111
6-2 Mass transfer coefficient of Ficoll across isolated GBM and glomerular capillary wall.......113
6-3 Relative resistance of the cells and the GBM to macromolecular diffusion across across the capillary wall.......116
6-4 Schematic representation of the slit diaphragm.......123
6-5 Schematic representation of the slit channel.......127
6-6 Measured values and theoretical predictions of the mass transfer coefficient for the cells, assuming that all filtration slit diaphragms are either intact or entirely absent.......130
6-7 Measured values and theoretical predictions of the mass transfer coefficient for the cells, assuming that a small fraction of the filtration slit diaphragms were removed.......135

7-1 Predicted efffects of changes in the flow rate on sieving coefficients across a membrane perforated by uniform pores.......139
7-2 Ficoll sieving coefficients for isolated GBM, for $\Delta P = 35$ and 60 mmHg.......146
7-3 Ficoll sieving coefficients for GBM in vitro and in vivo glomerulus.......148
7-4 Hindrance coefficients in the GBM as a function of macromolecular size.......150
7-5 Dextran and Ficoll sieving coefficients for isolated GBM.......153
7-6 Theoretical dependence of the diffusional hindrance coefficient on the transmembrane pressure.......158
7-7 Theoretical predictions of the membrane hydraulic permeability at $\Delta P = 35$ mmHg using the fiber matrix model of Curry and Michel (1980).......162
7-8 Representation of the GBM as a composite fibrous medium with two populations of fibers.......166
7-9 Theoretical predictions of the Darcy permeability of the matrix as a function of the spacing between the coarse fibers, using a two-component fibrous medium approach.......169
8-1 Theoretical effect of changes in the cylinder radius of the slit diaphragm on the sieving coefficients.......182
8-2 Theoretical effect of changes in the spread s of the cylinder spacing distribution on the sieving coefficients.......183
8-3 Theoretical effect of changes in the GBM thickness and the unit cell width on the sieving coefficients.......184
8-4 Theoretical effect of changes in the GBM hindrance coefficients on the sieving coefficients.......185
8-5 Experimental values and theoretical predictions of in vivo Ficoll sieving coefficients from the study of Oliver et al. (1992).......187
8-6 Experimental values and theoretical predictions of in vivo Ficoll sieving coefficients from the study of Remuzzi et al. (1993).......188
8-7 Experimental values and theoretical predictions of in vivo Ficoll sieving coefficients from the study of Oliver et al. (1994).......189
8-8 Best-fit to in vivo Ficoll sieving data.......195
8-9 Experimental values and theoretical predictions of in vitro mass transfer coefficient for the epithelium.......195

List of Tables

3-1 Summary of model characteristics....47
3-2 Hemodynamic quantities and pore-size parameters used to generate sieving data....49
3-3 Comparison of directly measured pressures in rat with estimates from fits to sieving data....70
5-1 Mass transfer coefficient of albumin at 21°C....101
5-2 Effect of transmembrane pressure on the permeability of GBM filters at 4 g/dl albumin....102
5-3 Effects of albumin concentration on L_p at $\Delta P = 50$ mmHg....105
5-4 Hydraulic resistance of the capillary wall....105
6-1 Ficoll permeabilities for the glomerular capillary wall....114
6-2 Size-dependent hindrances to diffusion in the GBM and the cells layers....118
6-3 Parameters values calculated for the slit diaphragm....134
7-1 Experimental values of flow rates and permeabilities....143
7-2 Ficoll measured sieving coefficients for isolated glomerular basement membrane....144
7-3 Ficoll calculated sieving coefficients for isolated glomerular basement membrane....145
7-4 Measured and predicted values of the diffusional hindrance coefficient in the GBM....157
7-5 Values of the Peclet number in the filtration experiments....160
7-6 Measured and predicted values of the sieving coefficients for isolated GBM....163
8-1 Upper bound on the effect of endothelial fenestrae on solute sieving....175
8-2 Ultrastructural parameters and hemodynamic quantities used to predict sieving data....179
8-3 Ultrastructural parameters for the slit diaphragm....192
8-4 Comparison between the ultrastructural and the pore models....193

Chapter One

Introduction

1.1 Relevance of Glomerular Function

The glomerulus plays an essential role in homeostasis by converting blood into an ultrafiltrate that is virtually devoid of proteins. Impairment of glomerular filtration is observed not only in most diseases affecting primarily the kidney but also in systemic diseases, such as essential hypertension and diabetes. Nearly half the patients who become diabetic in their youth develop renal failure 10 to 30 years after the onset of diabetes, and the most common cause of mortality among that population is kidney disease.

Glomerular diseases can be related to alterations in the structure of the glomerulus, resulting in a loss of overall permselectivity, or to variations in intrarenal hemodynamics, or to both. The main manifestations of glomerular disorder are a marked reduction in the glomerular filtration rate (GFR) accompanied by proteinuria, i.e., the loss of serum protein in the urine. The depression in GFR causes a decrease in the urinary output and the accumulation in the blood of substances at potentially dangerous levels.

To characterize these diseases, the selectivity of the glomerular capillary wall needs to be assessed quantitatively, which constitutes the purpose of mathematical models of glomerular filtration. By relating observable concentrations, flow rates, and pressures to the intrinsic properties of the membrane, these models can yield measures of the hydraulic and macromolecular permeability of the barrier based upon hemodynamic and sieving data, and thereby provide a better understanding of the underlying causes for glomerular disease, and a foundation for developomg new diagnostic and treatment means.

1.2 Thesis Summary

The overall goal of this thesis was to develop a novel theoretical model to relate the size-selective properties of the glomerular capillary wall to the specific ultrastructure of the barrier. Chapter 2 describes the structure and function of the glomerulus and summarizes previous mathematical models for glomerular filtration. The specific issues adressed in the thesis are then as follows:

1. The estimation of glomerular transmembrane hydraulic pressure from hemodynamic and sieving data, using pore models of glomerular filtration (Chapter 3).

2. The development of a novel approach to glomerular filtration, based upon the structure of the three layers forming the barrier (Chapter 4). Mass transfer coefficients in an ultrafiltration cell were measured in order to interpret anwe earlier water permeability data as well as in vitro Ficoll sieving data (Chapter 5).

3. The determination of Ficoll diffusional permeability across isolated glomerular capillary wall and basement membrane. The data were also interpreted so as to characterize the structure of the epithelium (Chapter 6).

4. The measurement of Darcy's permeability and Ficoll sieving coefficients for the glomerular basement membrane (GBM). Macromolecular hindrance coefficients were then inferred, and a new framework for interpreting the water permeability data was proposed (Chapter 7). The experimental work presented in Chapters 6 and 7 was done in collaboration with Dr. Barbara S. Daniels at the University of Minnesota.

5. The assembly of the novel ultrastructural model for glomerular filtration of neutral macromolecules. Theoretical predictions compared favorably with in vivo Ficoll sieving data (Chapter 8).

Chapter Two

Structure and Function of the Glomerulus

2.1 Anatomy and Role of the Kidney

The role of the two kidneys is to maintain a constant extracellular environment by regulating the volume and concentration of the constituents of the extracellular fluid and excreting the waste products of metabolism. The kidneys lie on both sides of the vertebral column, between the twelfth thoracic vertebra and the third lumbar vertebra. Each is fed by a renal artery arising from the abdominal aorta, which then divides itself into smaller segmental, interlobar, and interlobular arteries, which in turn break into afferent arterioles. Two zones can be distinguished in the kidney; the outer one is referred to as the cortex and the inner one as the medulla.

The nephrons are the functional units of the kidney. Each consists of a glomerulus, a series of tubules and a collecting duct. The number of nephrons per kidney is approximately 1.2×10^6 in humans, and 3.2×10^4 in rats (Tisher and Madsen, 1986). Blood is first filtered in the glomerulus, reabsorption and secretion of water and solutes then occur in the tubules, and urine is finally concentrated in the collecting duct.

The glomeruli are responsible for the production of an ultrafiltrate of plasma, the first step in the formation of urine. As illustrated in Figure 2-1, each glomerulus is composed of a capillary network, a capsule known as Bowman's space which surrounds it, and a central region of mesangial cells. The average diameter of the glomerulus is 200 μm in humans, 135 μm in rats (Tisher and Madsen, 1986). As blood passes through the interweaving capillaries of the glomerulus, emanating from a single afferent arteriole and converging towards one efferent arteriole, it is filtered selectively, and the resulting product

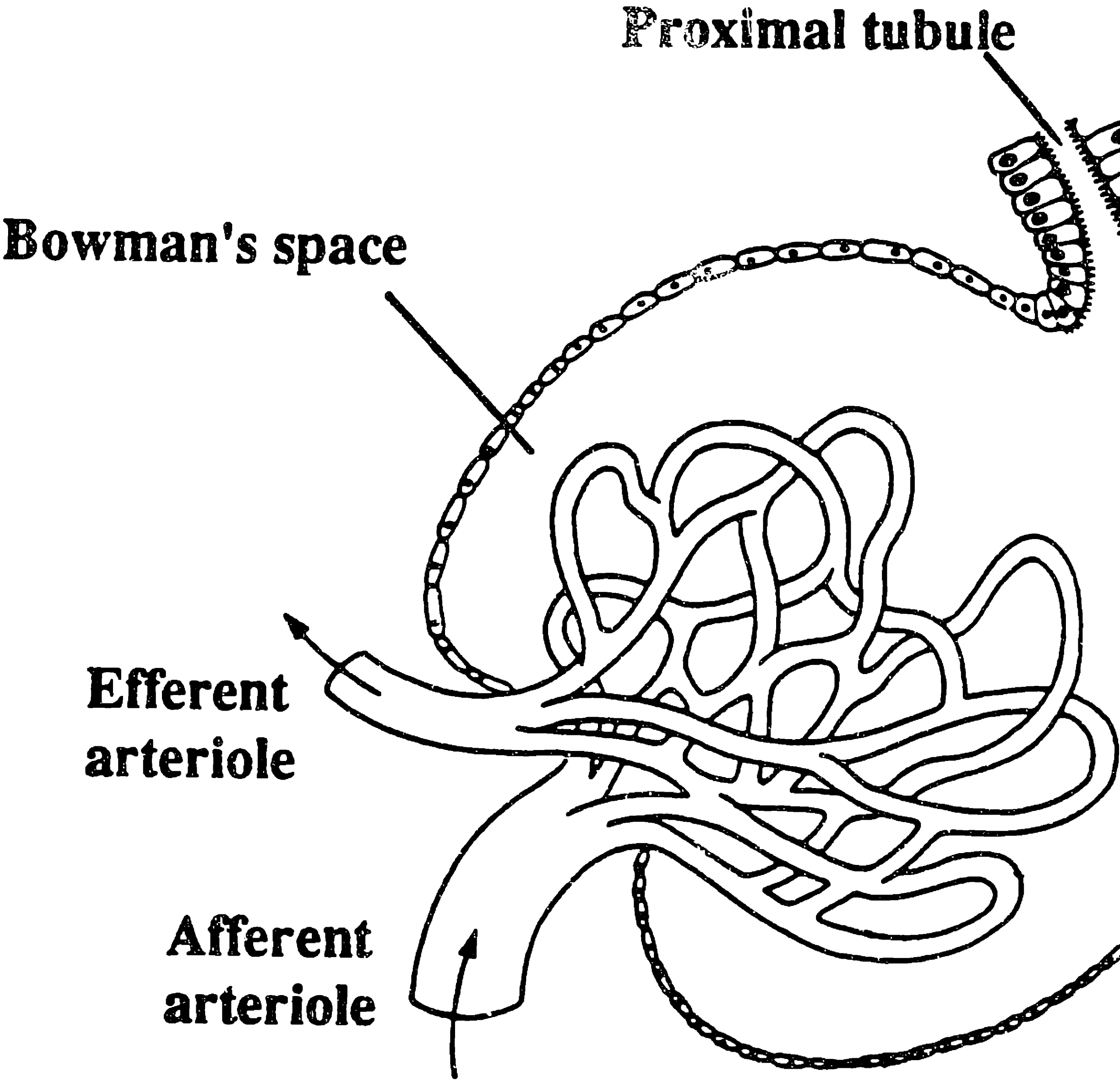
Proximal tubule
Bowman's space
Efferent arteriole
Afferent arteriole

Figure 2-1
Organisation of the glomerulus

is collected in Bowman's capsule. In humans, about 20 % of the cardiac output flows through the nephrons, resulting in a renal plasma flow (RPF) on the order of 550 ml/min. Approximately one fifth of the plasma volume is filtered across the capillary walls of the glomerulus, yielding a glomerular filtration rate (GFR) on the order of 110 ml/min (Deen et al., 1985), or about 170 liters of ultrafiltrate per day, most of which is then reabsorbed by the tubules; a total volume of 1 to 1.5 liters of urine is thus produced daily (Kanwar and Venkatachalam, 1992). In rats, measurements are most often reported on the basis of a single nephron; typical values for the afferent plasma flow rate (Q_A) and the single nephron glomerular rate (SNGFR) are 150 nl/min and 45 nl/min, respectively.

Glomerular mesangial cells are believed to also participate in the ultrafiltration of plasma by taking up colloidal particles through endocytosis and pinocytosis (Kanwar and Venkatachalam, 1992). The extent of their contribution has not been quantified precisely and is usually assumed to be negligible.

The composition of the glomerular ultrafiltrate is that of nearly ideal ultrafiltrate of plasma. The Bowman's space-to-plasma concentration ratios for glucose, amino acids and small solutes are very close to unity, whereas the ultrafiltrate is almost entirely protein free (Maddox et al., 1992). As described further, the glomerular capillary wall is a highly selective filter that discriminates on the basis of size, charge and molecular configuration.

2.2 Structure of the Glomerular Capillary Wall

The glomerular capillary wall consists of three distinct layers, namely, the endothelium, the glomerular basement membrane (GBM) and the epithelium, as illustrated in Figure 2-2. Endothelial cells form the inner lining, in between the lumen and the glomerular basement membrane. Firmly attached to the outer base of the GBM are the "foot processes", or pedicels, which are interdigitating extensions emanating from the large central body of the epithelial cells, also termed podocytes.

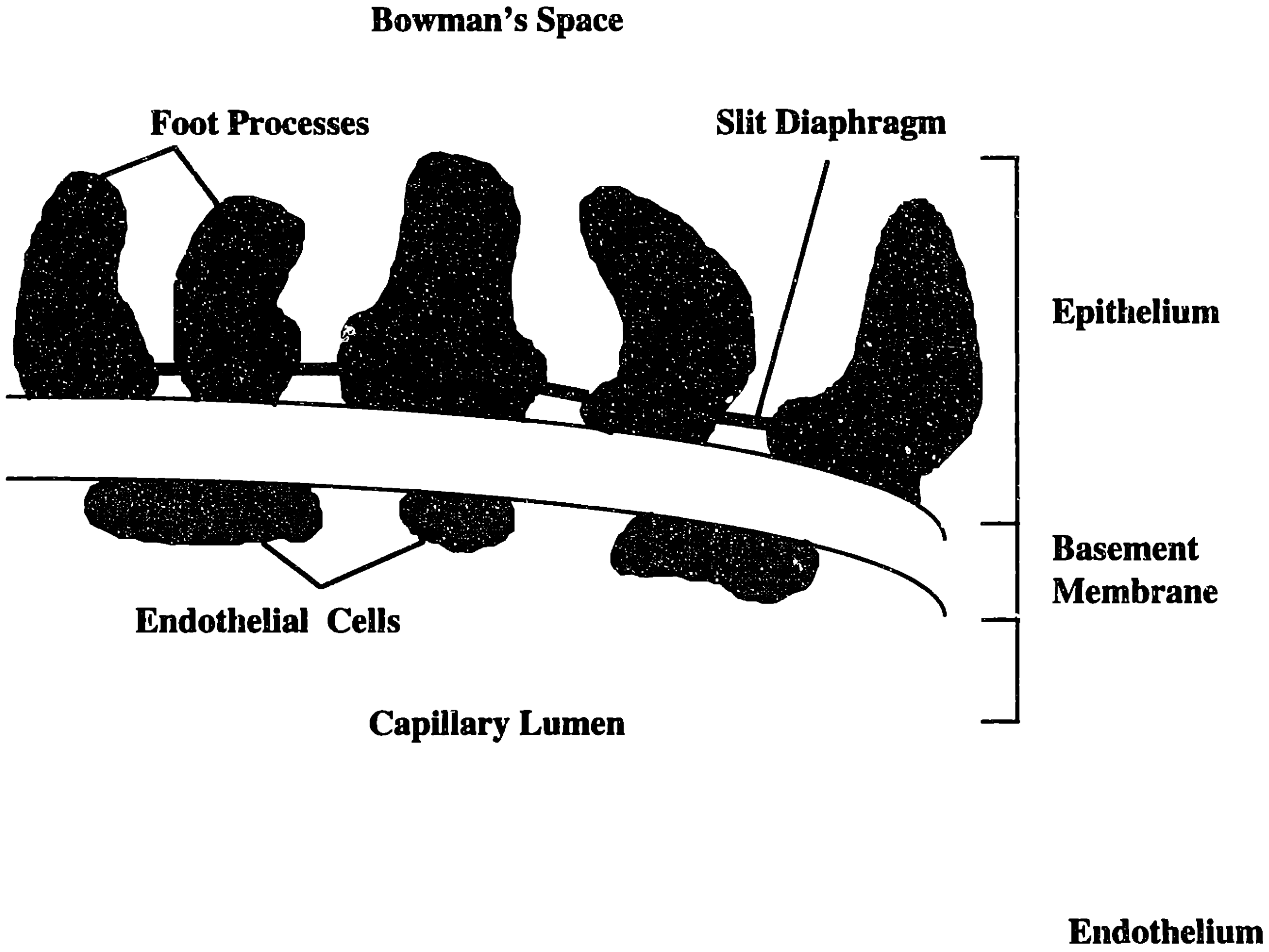
Bowman's Space
Foot Processes
Slit Diaphragm
Epithelium
Basement Membrane
Endothelial Cells
Capillary Lumen
Endothelium

Figure 2-2
Schematic representation of the glomerular capillary wall

2.2.1 Endothelial Cells

The endothelial cells of the glomerular capillaries are perforated by large fenestrae, or pores. Embedding mouse and rat kidney in Epon and staining the sections with lead hydroxide, Rhodin (1962) estimated the average diameter of the fenestrae as 70 nm. The author also found that the fenestrae were invariably closed by a diaphragm with a thickness identical to that of the plasma membrane of the endothelial cells. Clementi and Palade (1969) later suggested that endothelial cell diaphragms are composed of a protein-polysaccharide film that is highly permeable, thus presenting no significant barrier to the passage of even large molecules. Kanwar and Venkatachalam (1992) later concluded that fenestrae were closed by thin diaphragms only at an early stage of differentiation. According to these authors, with further maturation the diaphragms disappear, fenestrae enlarge to a diameter of 100 nm, and the cytoplasm of the endothelium becomes highly attenuated. Most of the recent studies do not report the existence of such diaphragms (Farquhar, 1981; Abrahamson, 1987; Avasthi and Koshy, 1988; Lea et al., 1989; Kondo, 1990; Takami et al, 1991).

Endothelial cells are covered by an anionic fiber matrix, the glycocalyx, and several studies suggest that this cell coat also fills the fenestrae (Abrahamson, 1987; Avasthi and Koshy, 1988). The major anionic component of the glycocalyx is podocalyxin, a sialoglycoprotein, but heparan sulfate proteoglycans and hyaluronic acid have also been identified in the matrix present in the fenestrae (Avasthi and Koshy, 1988).

Kondo (1990) reported that the fenestrae are 80-200 nm in diameter and have an oval shape. Different observations were made by Lea et al (1989), who determined that the fenestrae are channels of circular cross-section with varying radii, the walls of the endothelial cells being curved outwards. The minimal mean diameter of the fenestrae was measured as 61 nm, the mean cross-sectional diameter of the endothelial cells as 62 nm.

The number of fenestrae per square micrometer was estimated as 70, yielding a fractional area of glomerular basement membrane exposed by fenestrae of 20%.

Recent work indicates that the contribution of endothelial cells to the overall selectivity of the glomerular capillary wall is not significant (Farquhar, 1981; Drumond and Deen, 1994), and resistance to transport across the endothelium is assumed to be negligible.

2.2.2 Glomerular Basement Membrane

2.2.2.1 Chemical Constituents

Basement membranes are specialized sheet-like extracellular matrices, which are seen in many locations such as the dermal-epidermal junction of the skin, the base of lumen-lining epithelia, around Schwann cells, skeletal, and cardiac muscle cells, as well as throughout the digestive, respiratory, reproductive and urinary tracts. These thin sheets function both as structural supports, providing interactive surfaces for cell attachment, migration and differentiation, and as semipermeable membranes, passively regulating exchange of solutes and cell migration.

Basement membranes were first visualized by light microscopy following staining with periodic acid-Schiff and silver. Since then, electron microscopy of metal impregnated aldehyde-fixed tissue has shown the existence of two separate layers, the electron-lucent lamina lucida (lamina rara) which is adjacent to the plasma membrane, and the electron-dense lamina densa. In the glomerular basement membrane, the lamina densa lies between the subendothelial lamina rara interna, and the subepithelial lamina rara externa. Yurchenko and O'Rear (1993) report that a third type of lucent layer, the lamina fibroreticularis, has been observed in some tissues. However these authors also suggest that basement membrane layering could be a mere fixation artifact due to a phase separation or a contraction of cells; Goldberg and Escaig-Haye (1986) studied epithelial basement membranes fixed by rapid-freeze substitution, and saw no evidence of layers in what they described as homogeneous matrices.

Basement membranes are composed principally of type IV collagen, laminin, entactin, heparan sulfate proteoglycan and fibronectin. Collagen is the primary structural protein of the body, comprising about one third of the total protein content. Collagen molecules consist of three left-handed, helical polypeptide chains assembled as a right-handed superhelix ($[\alpha 1(IV)_2, \alpha 2(IV)]$ for type IV collagen). Each of the chains contains about 1000 amino acid residues, yielding a total molecular weight of about 300,000 Daltons. The entire molecule is approximately 300 nm long and 1.4 nm in diameter (Grodzinsky, 1983). The molecules tend to aggregate into fibrils of varying diameter, ranging from 2.5 to 7 nm (Yurchenko and O'Rear, 1993).

The very large glycoprotein laminin (10^6Da) is formed from three polypeptide chains (A, B1, B2). Electron microscopy reveals its unique cruciform shape with one long and three short arms. The long arm, which is about 3 nm thick (Kasinath and Kanwar, 1993) possesses a large globule thought to interact with heparin. Entactin, also known as nidogen, is a dumbbell-shaped glycoprotein of 148,000 Da. Aumailley et al. (1989) showed that entactin binds to type IV collagen, and suggested that it may serve an important cross-linking function, acting as a bridge between laminin and collagen IV polymers. Heparan sulfate is a linear polysaccharide chain composed of uronic acid-N-acetylglucosamine repeating subunits with sulfate substitutions. It is believed to play an important role in determining the charge-selectivity of the barrier. Heparan sulfate proteoglycans of varying size and charge have been identified in basement membranes. The major form, perlecan, appears to be present in all tissue basement membrane. It consists of one elongated polypeptide chain (400-450 kDa) containing six globular domains with heparan sulfate groups attached at one end. Laminin has been shown to bind to highly sulfated heparan sulfates (Yurchenko and O'Rear, 1983). Lastly, fibronectin, a sialoglycoprotein abundant in extracellular matrices, has been observed in several types of basement membranes, including the GBM (Courtoy et al., 1980).

Alterations in the content and structure of these components are associated with a variety of glomerular diseases, as reviewed by Kasinath and Kanwar (1993). In moderate diabetic nephropathy, an increase in type IV collagen content accounts for the observed thickening of the GBM. Nephrotoxic nephritis and diabetic nephropathy are both accompanied by changes in the amount and distribution of laminin present in the GBM. A decreased density of anionic sites is seen in proteinuric states, thereby suggesting that a loss of heparan sulfate proteoglycans could be one of the mechanisms causing proteinuria.

In the emerging picture of basement membranes, as summarized by Yurchenko and O'Rear (1993), two independent polymers, type IV collagen and laminin, appear to form the basic framework. The former provides a covalently stabilized scaffolding, the latter a more plastic network array. To this basic mesh are attached a variety of macromolecules which give the matrix its functional properties. Basement membrane attributes such as porosity, charge, and growth factor activity are regulated by these other components. Entactin is believed to function as an additional link between type IV collagen and laminin. The role of proteoglycans is the most well understood. By virtue of their sulfate and carboxyl radicals, proteoglycans determine the charge-selectivity of the GBM. They also contribute to its size-selectivity by steric exclusion effect, and may be responsible for the gel-like consistency of the GBM (Kasinath and Kanwar, 1993).

2.2.2.2 Ultrastructure

The glomerular basement membrane is approximately 300-350 nm thick in humans, 125-200 nm thick in rats (Tisher and Madsen, 1986; Daniels et al., 1992). Based on transmission electron micrographs, Laurie et al. (1984) found three structures in the glomerular basement membrane: a predominant network of 4-nm-thick cords; straight hollow 7-10-nm-thick rods, referred to as "basotubules"; and 3.5 nm paired rods, designated "double-pegs". In addition, the authors performed immunostaining studies showing that type IV collagen, laminin, entactin, heparan sulfate proteoglycans and fibronectin are colocalized in the GBM, and that all these components seem to be present in the cords.

Kubosawa and Kondo (1985) used a deep-etch replica method to examine the ultrastructure of the basement membrane, and observed in the laminae rarae externa and interna a three-dimensional, polygonal network, formed from interconnected 6-8-nm-thick fibrils; the size of the mesh was variable, ranging mostly between 20 and 25 nm in width. The lamina densa, composed of closely packed particles, showed a similar network structure only after removal of its fine particles with trypsin or ultrasonic waves. It was postulated that this fibrillar network consists of regularly arranged units of type IV collagen, perhaps attached by some materials such as laminin. Using high-resolution scanning electron microscopy, Shirato et al. (1991) confirmed some of these findings. In their study as well, the lamina densa appeared as densely packed granular material with scattered fibrils, while both laminae rarae formed a meshwork presenting some structural heterogeneities. In the lamina rara interna, the fibrils were 5-9 nm thick, enclosing round or polygonal pores 11-30 nm in diameter; in the lamina rara externa, the fibrils were 6-11 nm thick, and the pores were larger under the filtration slits (16-32 nm wide) than under the foot processes (10-24 nm wide). The three-dimensional mesh-like structure of the lamina densa was visualized in situ by Takami et al. (1991) with a quick-freeze and deep-etch replica method. The middle layer was shown to be composed of 6 to 10 nm fibrils arranged as a polygonal network. The average long dimension of the space between fibrils was estimated as 16.8 ± 8.7 nm, the short one as 12.0 ± 6.2 nm. Both laminae rarae contained perpendicular fibrils, 6-9 nm in thickness, connecting podocytes on one side and endothelial cells on the opposite side to the meshwork of the lamina densa. Similar observations were made by Kondo (1990), using platinum replication of embedment-free sections of GBM. The membrane appeared to consist of meshworks whose size was not precisely determined, due to dimensional changes caused by the method itself. In the laminae rara externa and interna 4 nm-thick strands, loosely arranged, were seen to cross-link the lamina densa with podocyte pedicels or endothelial cells.

These results seem to indicate that the meshwork structure of the glomerular basement membrane is not a rigid but rather a flexible framework, as suggested by Takami et al. (1991).

2.2.3 Epithelial Slit Diaphragm

The plasma membrane of the epithelial foot processes is covered by a thick polyanionic glycocalyx containing multiple residues of sialic acid (Kanwar and Venkatachalam). This anionic coat, similar to that found on glomerular endothelial cells but much thicker (Ryan, 1986), is believed to play a role in maintaining the charge selectivity of the glomerular capillary wall.

The epithelial slit diaphragm is a continuous two-dimensional band which extends between all adjacent epithelial foot processes. Rodewald and Karnovsy (1974) first described the zipper-like structure of the glomerular slit diaphragm. Using tannic acid-glutaraldehyde-osmium tetroxide as a fixative, the authors observed alternating periodic cross-bridges extending from the podocyte plasma membranes to a central filament running parallel and equidistant from the cell membranes. The cross bridges were approximately 7 nm in diameter and 14 nm in length, the central filament 11 nm in diameter. The average center-to-center spacing of adjacent cross-bridges was estimated as 11 nm. The cross-sectional dimensions of the pores formed by the arrangement of the cross-bridges were found to average 4 by 14 nm.

Confirming these findings, Kubosawa and Kondo (1985) also observed the zipper-like structure of the slit diaphragm. Transverse fibrils, 6-8 nm in thickness, were seen connecting adjacent membranes of epithelial cells, with a longitudinal fibril running in the center of the transverse ones. The width of the interpedicel space was later measured by Kondo (1990) using two different methods: it was estimated as 40-50 nm in epoxy sections, 60-80 nm in embedment-free sections. The author assumed that the change was due to the dehydration procedure in the latter case, which caused the size of empty spaces to increase by roughly 30-40 %.

The zipper-like hypothesis was challenged by Hora et al. (1990), who compared three different fixation procedures based on the quick-freeze and deep-etch replica method. The authors reported that in fresh unfixed glomeruli, only sheet-like substructures were visible. Ladder-like and zipper-like substructures appeared solely when the samples were fixed with glutaraldehyde and osmium tetroxide. It was suggested that the sheet-like structure is the natural form of the slit diaphragm, and that fixation is responsible for the formation of ladder-like and zipper-like structures as podocytes undergo contraction during sample preparation. In a later study of the same group (Furukawa et al., 1991), the width of slit diaphragms was measured using different methods. It was found that conventional fixation methods based on tannic acid, glutaraldehyde and osmium tetroxide, cause the cytoplasm of foot processes to shrink by osmotic effect, thereby broadening the slits and possibly transforming their sheet-like structure into a zipper-like structure. The average width of the slit diaphragms was estimated to be 34 nm. Conclusive evidence regarding the real structure of the diaphragm is still lacking.

2.3 Glomerular Ultrafiltration

The theoretical approach to ultrafiltration in the glomerulus was first developed by Deen et al. (1972). The glomerulus is represented as a number of identical cylindrical capillaries in parallel, without any variation in circumference or permeability properties along their length L. Axial diffusion within a capillary is neglected. Drumond and Deen

(1991) have shown that the effects of pulsatile flow may also be neglected, and all pressures and flows described below are averaged over a cardiac cycle. The local transmural flux J_v (volume flux) at a point y in the capillary can be expressed as the product of a permeability and a driving force:

$$J_v(y) = \frac{K_f}{S} \left(\Delta P(y) - \sigma \Delta \Pi(y) \right) \tag{2.1}$$

where S is the total capillary surface area, K_f is the ultrafiltration coefficient (the product of S and the effective hydraulic permeability of the barrier k), $\Delta P(y) = P_{GC}(y) - P_T$ is the radially-averaged transmural hydraulic pressure difference, $\Delta \Pi(y) = \Pi_{GC}(y) - \Pi_T$ is the radially-averaged transmural oncotic pressure difference, and σ is the reflection coefficient for plasma proteins. (The subscripts GC and T stand for glomerular capillary and Bowman's space, or tubule, respectively.) The axial drop in hydraulic pressure over the entire length of the capillary has been estimated to be small, on the order of 2-3 mmHg (Huss et al., 1975; Lambert et al., 1982). Moreover, the hydraulic pressure in Bowman's space P_T is assumed to be independent of position. Consequently, the local pressure difference $\Delta P(y)$ can be replaced by the length-averaged and time-averaged value, $\overline{\Delta P}$. The fractional loss of protein along a capillary is assumed to be negligible, even in heavy states of proteinuria, so that the reflection coefficient in equation (2.1) is equal to unity. Since the amount of protein present in Bowman's space can be neglected, $\Pi_T \approx 0$, and $\Delta \Pi(y) \approx \Pi_{GC}(y)$. The oncotic pressure in the plasma is given by the following empirical relation, valid for both rats and humans (Deen et al., 1985):

$$\Pi_{GC} = 1.629\, C_p + 0.2935\, C_p^2 \tag{2.2}$$

where C_p is the plasma protein concentration in g/dl and Π_{GC} is in mmHg.

Since proteins remain entirely in the circulation while solvent is being filtered across the membrane, the oncotic pressure increases along the capillary, more so near the afferent arteriole than towards the outlet due to the resulting decrease in the driving force. The state of filtration pressure equilibrium is reached when the oncotic pressure at the efferent end of the capillary equals the hydraulic pressure difference $\overline{\Delta P}$. As reviewed by Maddox et al. (1992), equilibrium conditions are commonly observed in hydropenic rats, where fluid losses due to surgery are not compensated; they are less often encountered in euvolemic rats, in which hematocrit and plasma volume have been restored to normal levels. As a rule, equilibrium is reached in hydropenic and euvolemic rats when the afferent plasma flow rate is less then 130 ml/min. When it is greater than 130 ml/min, filtration pressure equilibrium is very seldom achieved.

Under these conditions, the set of differential steady-state equations expressing material balances for plasma volume, plasma proteins and solute i can be written as:

$$\frac{\partial Q}{\partial y} = - S J_v \tag{2.3}$$

$$\frac{\partial (QC_p)}{\partial y} = 0 \tag{2.4}$$

$$\frac{\partial (QC_i)}{\partial y} = - S J_i \tag{2.5}$$

where y, the position along the capillary, has been normalized by capillary length ($0 \leq y \leq 1$). Q is the local plasma flow rate, J_i and C_i are the flux and luminal concentration of solute i, respectively. The complete volume flux and oncotic pressure profiles can be determined by solving equations (2.3-2.5) knowing the afferent plasma flow rate $Q_A = Q(0)$, the afferent plasma protein concentration $C_{pA} = C_p(0)$, as well as K_f and $\overline{\Delta P}$.

The single nephron glomerular filtration rate (SNGFR) is then given by:

$$\mathrm{SNGFR} = \int_0^1 S\, J_v(y)\, dy \tag{2.6}$$

Deen et al. (1972) derived a closed form expression relating SNGFR to Q_A, C_{pA} , K_f and $\overline{\Delta P}$; K_f can thus be calculated given the value of the four other quantities. This equation is valid if the oncotic pressure difference at the efferent end of the capillary is less than the hydraulic pressure difference $\overline{\Delta P}$. If filtration pressure equilibrium does occur, the value of the ultrafiltration coefficient remains unknown since the exact position where equilibrium is reached cannot be determined.

In the approach described above, radial variations in protein concentration are not taken into consideration, i.e., the model neglects the phenomenon of concentration polarization whereby the concentration of any selectively retained solute increases near the glomerular capillary wall relative to the midline axis. According to a study of Deen et al. (1974), the osmotic pressure Π_{GC} and therefore K_f are underestimated by approximately 10% when using bulk protein concentrations.

Anatomical studies of the rat glomerulus have shown that both capillary length and radius vary significantly within a single glomerulus. Remuzzi and Deen (1986, 1989) investigated the theoretical effects of distributions in capillary radius or length, and calculated that the ultrafiltration coefficient K_f is underestimated by approximately 30% in models which assume that the capillaries are identical. However, filtration of macromolecules was not significantly affected by network heterogeneity, and the authors concluded that models based on uniform capillary networks remain valid. If one assumes that the network consists of n identical capillaries in parallel, equations (2.3-2.5) are applicable to a single capillary, a single glomerulus, or all of the glomeruli in one or both kidneys, provided that the total capillary surface area S and the plasma flow rate Q be defined accordingly.

The afferent and efferent arteriolar resistances R_A and R_E are defined as:

$$R_A = \frac{P_A}{AABF} \qquad (2.7)$$

$$R_E = \frac{P_E}{EABF} \qquad (2.8)$$

where P_A and P_E are the afferent and efferent arteriolar pressures, respectively; AABF and EABF correspond to the afferent and efferent arteriolar blood flow rates, respectively. Whereas changes in K_f are directly related to alterations in capillary permeability and/or filtration surface area, changes in R_A and R_E reflect variations in vascular tone. Hence each of these three parameters will be affected differently by the regulation of glomerular filtration, according to which mechanisms are involved.

2.4 Dependence of SNGFR on the Primary Determinants of Glomerular Filtration

The single nephron filtration fraction SNFF is defined as:

$$SNFF = \frac{SNGFR}{Q_A} \qquad (2.9)$$

Under physiological conditions, the different hemodynamic determinants of ultrafiltration vary simultaneously, making it difficult to isolate the effects of a change in only one of these parameters. However, by pooling the results of a large variety of measurements and comparing data with similar sets of values, theoretical trends predicted by the model can be compared with experimental observations.

Regarding the consequences of isolated changes in Q_A, $\overline{\Delta P}$ or K_f, theory and data are in excellent agreement (Maddox et al., 1992). Under filtration pressure equilibrium conditions, assuming that $\overline{\Delta P}$, Π_A and K_f are not altered, an increase in the afferent plasma flow rate Q_A results in proportional changes in SNGFR, and SNFF remains constant. Eventually, the rise in Q_A provokes disequilibrium, the changes in SNGFR become nonlinear, and SNFF decreases.

For a given set of Q_A, Π_A and K_f values, SNGFR and SNFF remain equal to zero until $\overline{\Delta P}$ reaches the value of the afferent osmotic pressure. Further increases in $\overline{\Delta P}$ are accompanied by increases in SNGFR and SNFF, although not in a linear manner since the rise in the single nephron glomerular rate also causes the intracapillary osmotic pressure to rise.

Increases in K_f, all other parameters being fixed, cause SNGFR and SNFF to rise similarly until filtration pressure equilibrium is achieved, after which they remain constant. The only effect of an additional increase in K_f is to bring the point along the capillary where equilibrium is attained closer to the afferent arteriole.

According to the model, changes in SNGFR and SNFF should be inversely proportional to changes in Π_A, if Q_A, $\overline{\Delta P}$ and K_f remain constant. Experimental evidence however shows that a decrease in Π_A results in an increase in SNGFR smaller than expected (Blantz, 1974; Blantz et al., 1974). The explanation lies in the fact that reductions in Π_A produce concurrent reductions in the ultrafiltration coefficient K_f (Baylis et al., 1977; Tucker and Blantz, 1981), by a mechanism not yet elucidated.

2.5 Regulation of Glomerular Filtration

2.5.1 By Exogenous Substances

Indeed, far from being a constant for a given individual, K_f is constantly regulated by a variety of hormonal and vasoactive substances that are present in the plasma or produced by the kidney. Altering the surface area S available for filtration is one way in which K_f may be controlled, changing the hydraulic permeability k of the barrier another. Glomerular mesangial cells are believed to play a role in the former mechanism, epithelial cells in the latter one, both by means of their contractile properties. Contraction of the mesangial cells could modify the pathways accessible to flow among the network capillaries (Zimmerhackl et al., 1985; Haley et al., 1987), whereas contraction of the foot processes could result in changes in the frequency and structure of the epithelial slit diaphragms (Andrews and Coffey, 1983).

Glomerular mesangial cells are believed to contract in response to angiotensin II, for which specific receptors have been identified on these cells (Shorecki et al, 1983). Receptors for AII have also been found on epithelial and endothelial cells, in fewer number however (Maddox et al., 1992).

The renin-angiotensin system plays an important role in regulating renal hemodynamics. Its main function is to modify vascular resistance and renal salt excretion in response to alterations in extracellular volume (Ballermann et al., 1986). Renin is a proteolytic enzyme which triggers the reactions responsible for the formation of the active octapeptide angiotensin II. A reduction in the circulating blood volume stimulates the secretion of renin, resulting in an increased production of AII. AII causes the vascular smooth muscles to contract (Gunther et al., 1982), thereby increasing peripheral vascular resistance and maintaining arterial pressure constant. Both RPF and GFR decrease due to the augmented renal vascular resistance, the reduction in GFR being one of the mechanisms by which renal salt excretion is diminished (Ballermann et al., 1986).

The action of angiotensin II on the glomerulus is both indirect and direct. A number of studies show that AII specifically constricts efferent glomerular arterioles (Edwards, 1983; Myers et al., 1975), the rise in R_E leading to an increase in $\overline{\Delta P}$. The more direct effect of angiotensin II is that described earlier, whereby mesangial cells contract in response to AII, causing a reduction in K_f (Blantz et al., 1976; Brenner et al., 1982; Dworkin et al., 1983).

The effects of angiotensin II on filtration have been extensively studied, however AII is only one among many other hormones and vasoactive substances regulating glomerular hydrodynamics. A more detailed review is provided by Ballermann et al.(1986) and Maddox et al. (1992).

2.5.2 Autoregulation

In the absence of any neural or hormonal control, the kidney also has the ability to maintain relative constancy of renal plasma flow and glomerular filtration rate over a wide range of mean arterial pressure, from approximately 80 to 200 mmHg (Forster and Maes, 1947; Robertson et al., 1972; Edwards, 1983). The autoregulation of the GFR is mediated by changes in the afferent arteriolar resistance R_A, R_E remaining constant. A rise in systemic pressure provokes an increase in the afferent arteriolar tone which prevents the pressure rise from being transmitted to the glomerulus. Conversely, a decline in systemic pressure results in a dilatation of the afferent arteriole so that the renal plasma flow and the glomerular filtration rate are not affected. Below 80 mmHg, both RPF and GFR vary directly with arterial pressure, possibly because the afferent arteriole cannot be dilated any further (Rose, 1977).

2.6 Permselectivity of the Glomerular Capillary Wall

2.6.1 Sieving Coefficients

Fractional clearance techniques have been used extensively in experimental animals and humans to characterize the selectivity of the glomerular barrier to macromolecules. Tracers of varying size, charge, and molecular configuration are added to the plasma, and the amount filtered through the membrane provides a quantitative measure of its selectivity. The urinary clearance of solute i is defined as:

$$CL_i = \frac{C_{iU}\, Q_U}{C_{iA}} \tag{2.10}$$

where Q_U is the urinary flow rate, C_{iU} and C_{iA} are the concentration of solute i in the urine and in the afferent arteriole, respectively. The clearance of i corresponds to the rate at which the plasma is cleared of solute i by renal excretion. If the solute is freely filtered through the glomerular capillary wall and is neither secreted nor reabsorbed in the tubules, then its clearance is equal to the glomerular filtration rate GFR. Such is the case with the fructose polymer inulin, which is therefore commonly used as a marker for water. The fractional clearance FRC_i of solute i is defined as the clearance of i divided by the GFR, or equivalently by the clearance of inulin.

The sieving coefficient Θ_i of solute i is defined as the ratio of the average concentration of i in Bowman's space, $< C_{iB} >$, to that in the afferent arteriole, C_{iA}:

$$\Theta_i = \frac{< C_{iB} >}{C_{iA}} \tag{2.11}$$

If solute i is neither secreted nor reabsorbed downstream, it can be shown that $FRC_i = \Theta_i$.

The polymers dextran and Ficoll, the latter being a copolymer of sucrose and epichlorohydrin, are such examples. Interpreting sieving data for these test macromolecules has been a common means of assessing the selectivity of the glomerular capillary wall for more than two decades. Indeed, these test solutes are available as polydisperse samples of different charge content, and comparisons between fractional clearances of macromolecules of varying size, charge and molecular configuration have led to a better understanding of the barrier properties. The main findings can be summarized as follows. For a set of uncharged solutes of similar structure, sieving coefficients decrease progressively as molecular size increases, a phenomenon referred to as the size-selectivity of the glomerular capillary wall. In addition, the filtration of anions is diminished compared to that of uncharged solutes of same size and configuration, and that of cations augmented. For instance, the sieving coefficient of serum albumin is ≤ 0.1%, i.e., two to three orders of magnitude less than values of Θ for neutral macromolecules of similar dimensions. All pertinent studies have confirmed that the so-called charge selectivity of the barrier results from the presence of negatively charged components in the capillary wall (Maddox et al., 1992). Finally, transport of uncharged macromolecules of similar size will be restricted to different degrees according to molecular configuration. Dextran is filtered more readily than Ficoll, possibly owing to its random coil nature. Ficoll on the other hand has been shown to behave as an almost ideal sphere (Oliver et al., 1992), and because its behavior is thus easier to characterize, it is now preferred to dextran as a test macromolecule for sieving measurements. The effects of molecular configuration on macromolecule filtration are all the more difficult to understand as differences can not be quantified using a single parameter.

2.6.2 Glomerular Diseases

Glomerular diseases are characterized by marked alterations in the permselectivity properties of the capillary wall. The manifestations of glomerular injury are proteinuria (i.e., greater than trace amounts of protein in the urine), hematuria (corresponding to an increased excretion of erythrocytes), reduced GFR and alterations in sodium excretion leading to hypertension, edema and circulatory congestion. The clinical syndromes of glomerular injury are usually classified into three categories (Glassock et al., 1986):

- glomerulonephritis, which can be acute, rapidly progressive or chronic, depending on the rapidity of the onset. This syndrome is characterized by variable degrees of proteinuria and hematuria, a loss of renal function, hypertension, and sometimes oliguria (i.e., a urine volume of less than 500 ml per day).

- nephrotic syndrome, which is marked by heavy proteinuria (defined as a urine content of protein greater than 3.5 gm per day) accompanied by a significant decrease in plasma albumin, frequently resulting in hypertension and edema.
- persistent asymptomatic urine abnormalities. Patients in that group suffer from mild proteinuria, sometimes hematuria, but other symptoms such as reduced renal function, hypertension or edema are seldom seen.

Whereas the glomerular capillary wall in healthy individuals acts as a highly effective filter preventing plasma proteins from being filtered, a defect in the size-selective barrier which affects only a small percentage of the total filtering area is sufficient to induce massive proteinuria (Glassock et al., 1986). By allowing changes in the properties of the barrier to be quantified, theoretical models of ultrafiltration have led to a better understanding of the causes of glomerular diseases.

2.7 Pore Models of Glomerular Filtration

Mathematical models of glomerular filtration are designed to relate the functional properties of the glomerular capillary wall to variables that can be measured experimentally, such as hemodynamic quantities and sieving coefficients.

The pore model, today commonly employed to describe transport across capillary walls, was first developed by Pappenheimer (1953) and Renkin (1954). A series of refinements and modifications were made in the early 1970s: the effects of concentration and flux variations along the length of the capillary were included (Deen et al., 1972; Chang et al., 1975), and new developments in the hydrodynamic theory of restricted transport of solid spheres in cylindrical pores were added (Bungay and Brenner, 1973; Anderson and Quinn, 1974; Brenner and Gaydos, 1977).

The pore model is based on the assumption that the glomerular capillary wall is a uniform membrane perforated by pores. The main hypotheses were summarized by Chang et al. (1975) and are presented below. In the so-called "isoporous" model, the filtration barrier is idealized as a membrane containing a homogeneous population of pores of identical size. Later improvements have consisted of postulating different pore-size distributions, and the predictions of heteroporous models are in excellent agreement with sieving data.

Models based on slits instead of cylindrical pores have been shown to yield similar results (Hall, 1977; Lambert et al., 1972; Renkin and Gilmore, 1973) and have therefore not received much further attention. Other approaches to glomerular filtration have been proposed, none of which has been considered so far as a viable alternative to the pore model. The fiber matrix model developed by Curry and Michel (1980) is based on the early work of Ogston et al. (1958, 1973) on partitioning and diffusion in a random network of fibers. However, in the absence of a suitable theory for solute convection in random fiber arrays, and given that the analysis of Ogston does not take into account hydrodynamic interactions, this model remains incomplete, as discussed in Chapter 6. Wolgast and Öjteg (1988) attempted to treat the basement membrane as a charged, deformable gel, but oversimplifying assumptions render their predictions unrealistic.

2.7.1 The Isoporous Model

The isoporous model assumes that the glomerular capillary wall is perforated by right cylindrical pores of uniform radius r_0. All test macromolecules are added in minimal amounts, and the concentration of the tracer solutes is assumed to be sufficiently small so that it does not contribute to osmotic pressure. It is also assumed that the concentration of solute i in the Bowman's space at any position along a capillary is given by the local ratio of solute-to-volume flux (J_i/J_v), the so-called ultrafiltration boundary condition. In addition, all solute molecules are assumed to behave as rigid spheres, with a radius equivalent to that of the Stokes-Einstein radius r_i:

$$r_i = \frac{K_B T}{6 \pi \mu D_i} \tag{2.12}$$

where K_B is Boltzmann's constant, T is the absolute temperature, μ is the solvent viscosity and D_i the diffusivity of the solute in bulk solution. Based on the hydrodynamic theory of hindered transport through uniform cylindrical pores, the solute flux J_i of a neutral macromolecule is then given by (Deen et al., 1985):

$$J_i = \frac{J_v C_i W_i}{1 - (1 - W_i) \exp(-Pe)} \tag{2.13}$$

$$Pe = \frac{W_i J_v L}{H_i D_i f} \tag{2.14}$$

where L here is the thickness of the membrane (the pore length), f is the fraction of the capillary surface occupied by pores, and H_i and W_i are solute pore hindrance factors for diffusion and convection, respectively. The Peclet number Pe is a dimensionless function indicating the relative importance of the convective to diffusive forces driving the solute through the membrane pores. The quantities f, S and L need not be explicitly determined; needed in equation (2.14) is fS/L, the ratio of total pore area to pore length, which can be related to K_f and r_0 using the Poiseuille equation for flow through uniform, parallel, cylindrical pores:

$$\frac{f S}{l} = \frac{8 \mu K_f}{r_0^2} \tag{2.15}$$

where μ is the viscosity of the glomerular filtrate, taken to be that of water.

The hindrance factors H_i and W_i express the steric and hydrodynamic hindrances to transport of solute i. They depend only on the ratio of solute-to-pore radius, $\lambda = r_i/r_0$. They are equal to unity for small, freely-filtered molecules, to zero for solutes that are completely excluded from the pores. In an extensive review of hindered transport, Deen (1987) showed that both hindrance coefficients can be written as the product of a steric term, the partition coefficient Φ, and a hydrodynamic term (K_d or K_c). Φ accounts for the difference between the solute concentration in the capillary lumen and that in the pore. In cylindrical pores, the partition coefficient is given by $\Phi = (1-\lambda)^2$. The hydrodynamic factors K_d and K_c account for the effects of finite pore size, the presence of pore walls resulting in an increase in the frictional force acting on a solute moving through the pore. K_d is related to the inverse enhanced drag coefficient, K^{-1}, and K_c to the lag coefficient G. The most accurate values for H_i and W_i over the entire range $0 \leq \lambda \leq 1$ were obtained by Bungay and Brenner (1973), who combined centerline asymptotic results for small and close fitting spheres. H_i and W_i can be calculated using the following expressions:

$$W_i = \frac{K_s \Phi (2-\Phi)}{2 K_t} \tag{2.16}$$

$$H_i = \frac{6 \pi \Phi}{K_t} \tag{2.17}$$

$$K_t(\lambda) = \frac{9}{4} \pi^2 \sqrt{2} (1-\lambda)^{-5/2} \left[1 - \frac{73}{60}(1-\lambda) + \frac{77,293}{50,400} (1-\lambda)^2\right] - 22.5083 - 5.6117 \lambda - 0.3363 \lambda^2 - 1.216 \lambda^3 + 1.647 \lambda^4 \tag{2.18}$$

$$K_s(\lambda) = \frac{9}{4} \pi^2 \sqrt{2} (1-\lambda)^{-5/2} \left[1 + \frac{7}{60}(1-\lambda) - \frac{2,227}{50,400} (1-\lambda)^2\right] + 4.0180 - 3.9788 \lambda - 1.9215 \lambda^2 + 4.392 \lambda^3 + 5.006 \lambda^4 \tag{2.19}$$

The sieving coefficient Θ_i of solute i, the ratio of the average concentration of i in Bowman's space to that in the afferent plasma, is then given by:

$$\Theta = \frac{\int_0^1 J_i(y)\,dy}{C_{iA}\int_0^1 J_v(y)\,dy} \tag{2.20}$$

The local solute and volume fluxes J_i and J_v can be determined by integrating the mass balance equations (2.3-2.5) which yield $C_p(y)$ and $C_i(y)$, the concentrations of protein and solute i at position y along the capillary, respectively. These equations can be integrated numerically to any desired level of accuracy, but an analytical solution based on a simple approximation is sometimes preferred. This approach was outlined by Deen et al. (1985), and is based upon the assumption that J_v decreases exponentially. This approximation is mostly useful in heteroporous models, where equation (2.20) has to be integrated many times for a wide range of pore radii, as described in the next section. Deen et al. (1985) compared the results of both the exact and the approximate methods, and concluded that the later was sufficiently accurate for its intended use in estimating membrane parameters from sieving curves.

2.7.2 Heteroporous Models

The isoporous model predicts a sharp cut-off of sieving coefficients at $r_i = r_0$, a feature that is not exhibited by experimental data. Typical values for r_0 are 45-50 Å in the rat, yet larger tracer macromolecules are filtered through the barrier. For this reason, heteroporous models which include varying pore sizes can fit sieving data much more accurately. Deen et al. (1985) outlined the formal approach to account for pore-size distribution. Briefly, if g(r) is the pore-size probability distribution, then the fraction $\Omega(r)dr$ of the filtrate volume passing through pores with radii between r and (r + dr) is given by:

$$\Omega(r) = \frac{r^4\, g(r)}{\int_0^\infty r^4\, g(r)\, dr} \tag{2.21}$$

and the sieving coefficient of solute i can be calculated by performing the following integration:

$$\Theta_i = \int_0^\infty \Omega(r)\, \Theta_i(r)\, dr \tag{2.22}$$

where $\Theta_i(r)$ is the fractional clearance that would be predicted for solute i from the isoporous model using $r_0 = r$.

Of most frequent use in the literature are the isoporous-with-shunt and the lognormal models, both of which are characterized by two membrane parameters. The latter model assumes a lognormal distribution of pore radii with the parameters u and s:

$$g(r) = \frac{1}{\sqrt{2\pi}\, r \ln(s)} \exp\left[-\frac{1}{2}\left(\frac{\ln(r) - \ln(u)}{\ln(s)}\right)^2\right] \tag{2.23}$$

where u is the mean value of r, and ln(s) is the standard deviation of the distribution.

The isoporous-with-shunt model assumes that the membrane has a large number of pores of uniform radius in parallel with a few large, nonselective pores of effectively infinite size. This model is characterized by the radius of the smaller pores (r_0) and the fraction ω_0 of the filtrate volume that would pass through the shunt pores in the hypothetical situation of $\Pi_G = 0$. In another approach, termed the two-pore model, the membrane is assumed to have two homogeneous populations of pores with radii r_1 and r_2; the fractional number of pores of each type is given by x_1 and $x_2 = 1 - x_1$, respectively.

2.8 Summary and Conclusions

The glomerular capillary wall acts as a filter which discriminates on the basis of size, charge, and molecular configuration; its unique permselective properties are imparted by the specific structural features of the barrier: a fenestrated endothelium, a fibrous glomerular basement membrane, and epithelial foot processes bridged by slit diaphragms. The selectivity of the wall is usually assessed by measuring sieving coefficients of test solutes; these measurements are then related to the intrinsic properties of the barrier using models of glomerular filtration. The most common approach until now has been to assume that the barrier is a uniform membrane perforated by pores.

We first examined pore models of glomerular filtration in this work in order to establish whether the hydraulic pressure difference, $\overline{\Delta P}$, can be inferred from macromolecular sieving data. Due to the inherent limitations of these models, the most important of which is their inability to capture specific changes in any of the three layers of the capillary wall, a different approach to glomerular filtration was then developed, which will be presented in the later chapters.

Chapter Three

Error Propagation in the Estimation of Glomerular Pressure

3.1 Introduction

The importance of glomerular capillary hydraulic pressure as a determinant of glomerular filtration rate has created a long-standing interest in methods for measuring that pressure. The quantity most relevant for the filtration process is the mean transmural hydraulic pressure difference ($\overline{\Delta P}$), i.e., the mean pressure in the glomerular capillary lumen minus that in Bowman's space. As reviewed by Maddox et al. (1992), the servo-null micropuncture technique has been used for many years to measure $\overline{\Delta P}$ in experimental animals under a variety of physiological or pathophysiological conditions. The most direct measurements are possible in animals where glomeruli regularly reside on the cortical surface, accessible to micropuncture (as in the Munich-Wistar rat); when surface glomeruli are absent, the stop-flow technique provides a somewhat less direct, but still effective, approach. In normal rats $\overline{\Delta P}$ is typically 35-40 mmHg. The routine use of micropuncture is rats and other animals notwithstanding, the inability to apply these methods to humans has left a need for a noninvasive method for measuring $\overline{\Delta P}$. The interest in measuring $\overline{\Delta P}$ in humans has been greatly heightened by the reported association between glomerular hypertension and glomerular disease (Anderson et al., 1986) and the consequent importance of assessing the effects of therapeutic interventions on $\overline{\Delta P}$.

Fractional clearance techniques have been used extensively in experimental animals and humans to characterize the selectivity of the glomerular barrier to macromolecules (Maddox et al., 1992). The fractional clearance (Θ_i) of solute i is the urinary clearance of i divided by that of inulin (or some other marker for water); for a test macromolecule that is neither secreted nor reabsorbed, Θ_i equals the sieving coefficient of i, the Bowman's space-to-plasma concentration ratio. It has long been recognized on theoretical grounds that for a given macromolecule, the sieving coefficient Θ_i will tend to vary inversely with $\overline{\Delta P}$ and that fractional clearance measurements might therefore provide a noninvasive means to determine $\overline{\Delta P}$. In essence, the dependence of Θ_i on $\overline{\Delta P}$ comes from the fact that only the convective part of the transmural flux of a macromolecule is proportional to the volume (water) flux. Thus, to the extent that diffusion also contributes to transport of a macromolecule, increase in $\overline{\Delta P}$ will augment macromolecule fluxes to a lesser degree than volumes fluxes, thereby decreasing Θ_i. The theoretical effect of $\overline{\Delta P}$ on a sieving curve is illustrated in Figure 3-1. The isoporous model was used here, the capillary wall being represented as a solid barrier perforated by a homogeneous population of pores of radius r_0. Comparing curve B with curve A, the effect of an increase in $\overline{\Delta P}$ from 35 mmHg to 40 mmHg is as just described. The decreases in Θ_i are more pronounced for the smaller molecules, where diffusion contributes more prominently to the solute flux. In contrast to the effect of $\overline{\Delta P}$ on the sieving curve is that of an isolated change in r_0. As shown by a comparison of curves C and A, changes in pore radius tend to yield a more uniform shift in the sieving curve along the abscissa. Thus there is reason to believe one might be able to distinguish the effect of $\overline{\Delta P}$ on sieving curves from those of r_0 (or the parameters describing pore-size distributions in other models), thereby allowing one to simultaneously fit both of these quantities to a given set of data.

The idea of inferring values of from sieving data was first pursued extensively by Lambert and co-workers in the 1970s (Dubois et al., 1975; Gassee et al., 1974, 1976; Lambert et al., 1971, 1972, 1975; Verniory et al., 1973). Values of $\overline{\Delta P}$ were computed by applying a series of increasingly rigorous mathematical models to fractional clearance data for polyvinylpyrrolidone (PVP) in dogs. In a retrospective study, Chang (1978) analyzed dextran sieving data obtained in Munich-Wistar rats (Chang, 1975, 1976). More recently, Myers and co-workers have used dextran sieving data to deduce information about

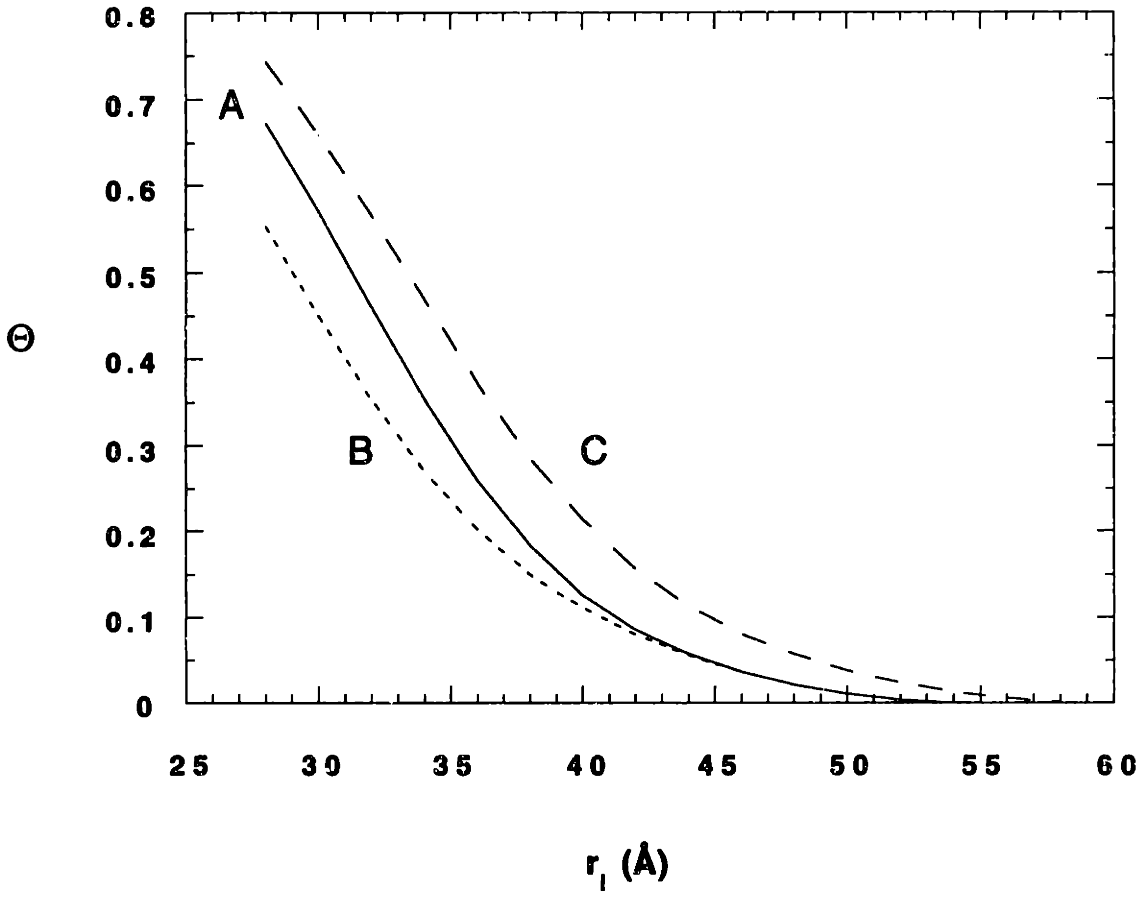

Figure 3-1

Predicted efffects on sieving curves of selective changes in transmembrane pressure ($\overline{\Delta P}$) and pore radius (r_0). The sieving coefficient (Θ_i) is plotted as a function of Stokes-Einstein radius (r_i). *Curve A*: $r_0 = 55$ Å, $\overline{\Delta P} = 35$ mmHg. *Curve B*: $r_0 = 55$ Å, $\overline{\Delta P} = 40$ mmHg. *Curve C*: $r_0 = 60$ Å, $\overline{\Delta P} = 35$ mmHg. The other inputs in each case were glomerular filtration rate = 110 ml/min, renal plasma flow = 550 ml/min, and afferent protein concentration = 6.6 g/dl.

glomerular pressures in humans, with an emphasis on inferring directional changes in $\overline{\Delta P}$ caused by disease or by certain experimental maneuvers.

The various attempts to calculate $\overline{\Delta P}$ from group-mean sieving data have generally yielded physiologically reasonable results. On a more quantitative level, however, there is little evidence that this approach reliably gives accurate values. In the aforementioned PVP studies with dogs, no micropuncture measurements of $\overline{\Delta P}$ were available for direct comparison with the values calculated from the sieving data. The approach was shown to yield accurate results when applied to PVP sieving data obtained using synthetic membranes, but this system posed fewer difficulties than the study of glomerular filtration in vivo. Chang (1978) found that the values of $\overline{\Delta P}$ inferred from sieving curves were 2-9 mmHg lower than those measured by micropuncture in the same groups of rats. Oliver (1992) fitted values of $\overline{\Delta P}$ to dextran or Ficoll sieving data from a number of published studies in rats and found the extent of agreement with micropuncture results to be excellent on occasion but highly variable, with the calculated values ranging from an underestimate of 16.0 mmHg to an overestimate of 15.2 mmHg. Thus, despite the theoretical promise of this approach, detailed comparisons with available data are mostly discouraging. Such erratic results lead one to suspect problems arising from the propagation of errors in the calculations, but there has been no systematic effort to identify the main sources of difficulty and thereby to define the limitations of this method for determining $\overline{\Delta P}$.

The goal of this study was to determine the extent to which experimental errors and imperfections in the theoretical models limit the ability to obtain reliable estimates of $\overline{\Delta P}$ from sieving curves. The approach used was to generate many sets of synthetic "experimental data" from computer simulations of glomerular sieving and to compute values of $\overline{\Delta P}$ from those data in the presence of various types and magnitudes of errors. The use of synthetic data enabled us to systematically vary the size of the simulated errors. Success or failure was judged by comparing the computed values of $\overline{\Delta P}$ with those used to generate the data. The most straightforward type of error consisted of random variations in

Θ_i. To examine the effects of systematic errors, such as those caused by using a physically incomplete mathematical model, we analyzed each set of data using several models, which differed in the type of pore-size distribution assumed and/or in the mass balance equations employed. The results permit certain generalizations to be made concerning the level of experimental and modeling accuracy required to reliably estimate $\overline{\Delta P}$ from sieving data.

3.2 Methods

In this section, we first describe the different models that were employed. We then outline the approach used to create synthetic data sets. The procedures used to estimate the unknown parameters of the models, including $\overline{\Delta P}$, are described. Finally, methods are described for assessing the reliability of the parameter estimates and the reliability of specific models.

3.2.1 Models for Glomerular Filtration

The glomerulus was represented as a number of identical capillaries in parallel, without any variation in circumference or permeability properties along their length. Radial variations in concentration within a capillary were neglected, as was axial diffusion. The effects of pulsatile flow were assumed to be negligible, so that steady-state equations involving only time-averaged variables were used. The resulting set of differential equations expressing material balance for plasma volume, plasma proteins, and test solutes was described in Chapter 2, and is repeated here for convenience:

$$\frac{dQ}{dy} = - S\, J_v \tag{3.1}$$

$$\frac{d(QC_p)}{dy} = 0 \tag{3.2}$$

$$\frac{d(QC_i)}{dy} = - S J_i \tag{3.3}$$

where y is normalized position along a capillary ($0 \leq y \leq 1$); Q is the local plasma flow rate; S is the total capillary surface area; J_v and J_i are the transmural fluxes of volume and solute i, respectively; and C_p and C_i are the luminal concentrations of total protein and solute i, respectively.

As described in Chapter 2, the volume flux out of a capillary was written as:

$$J_v = \frac{K_f}{S} (\overline{\Delta P} - \Pi_G) \tag{3.4}$$

where K_f is the ultrafiltration coefficient (the product of S and the effective hydraulic permeability), and Π_G is the intracapillary osmotic pressure, expressed as a quadratic function of C_p. Each test macromolecule was assumed to be present in tracer amounts, so that its contribution to the osmotic pressure was neglected. The pressure drop has been estimated to be a small fraction of $\overline{\Delta P}$, so that in equation (3.4) the local pressure difference has been replaced by $\overline{\Delta P}$, which is both a time-averaged and a length-averaged value.

Based on hindered transport theory, the solute flux was expressed as a function of C_i, J_v, the Stokes-Einstein radius of the solute (r_i), and parameters that describe the membrane pore-size distribution; the details of these relationships are given in Chapter 2. The sieving coefficient of the solute i was calculated by integrating J_v and J_i over the length of a capillary:

$$\Theta_i = \frac{1}{C_{iA}} \frac{\int_0^1 J_i dy}{\int_0^1 J_v dy} \tag{3.5}$$

where C_{iA} is the afferent arteriolar (or systemic arterial) concentration of the solute.

As already mentioned, systematic errors where investigated by applying several different models to each set of data. Pore models for glomerular filtration were described in Chapter 2. The ones used in this study were the isoporous model, the isoporous-with-shunt model, the two-pore model and the lognormal model. In addition simplified versions of the isoporous and two-pore models were employed, in which the mass balance equations (3.3-3.5) were ignored. That is, the "simplified isoporous" and "simplified two-pore" models constitute lumped descriptions in which all variables are regarded as being independent of position along a capillary. Thus, the simplified models were deliberately made less accurate than the corresponding models that included equations (3.3-3.5). The main features of the glomerular filtration models used are summarized in Table 3-1.

Table 3-1

Summary of model characteristics

Model	Mass Balance Equations	Pore-size Parameters
Isoporous	Yes	r_0
Two pore	Yes	r_1, r_2, x_1
Lognormal	Yes	u, s
Isoporous with shunt	Yes	r_0, ω_0
Simplified isoporous	No	r_0
Simplified two pore	No	r_1, r_2, x_1

3.2.2 Creation of Synthetic Sets of Data

Baseline sieving coefficients were computed first using the input parameters shown in Table 3-2. The three cases were based on hemodynamic values representative of healthy humans, nephrotic humans, and normal euvolemic rats, respectively (Deen et al., 1985; Maddox et al., 1992; Yoshioka et al., 1988). The simulations for humans used whole kidney data, while those for rats employed single-nephron quantities. Values for K_f (whole kidney or single nephron) were computed from the other inputs. Various models were used to generate sieving data for each of the three hemodynamic cases. Each sieving curve included molecular radii in the range $28 \leq r_i \leq 58$ Å, at intervals of 2 Å, yielding a set of 16 Θ_i values. Random measurement errors were then simulated by adding positive or negative "errors" to the baseline sieving coefficients. The errors were assumed to follow a normal distribution with a mean error of zero, and a standard deviation (σ_i) that was a fixed percentage of the baseline value of Θ_i. Random deviates with a normal probability distribution were computed using the program GASDEV (Press et al., 1989).

Figure 3-2 shows examples of a baseline sieving curve and a corresponding sieving curve with random errors added. For clarity, the random errors shown are larger that those normally employed in the simulations.

3.2.3 Parameter Estimation Procedures

When a given model was applied to a specified set of sieving data, the unknown parameters were taken to be the pore-size parameters (1 to 3, depending on the model), and $\overline{\Delta P}$. The two to four unknown parameters were estimated by fitting the model to the data. If the errors in a set of data follow a normal distribution, then the widely used method of weighted least-squares is appropriate. This method consists of finding the parameter values that minimize the quantity χ^2, defined as:

Table 3-2

Hemodynamic quantities and pore-size parameters used to generate sieving data

	Normal Humans	Nephrotic Humans	Normal Euvolemic Rats
GFR, ml/min	110	50	
SNGFR, nl/min			45
RPF, ml/min	550	400	
Q_A, nl/min			150
C_{pA}, g/dl	6.6	4.7	5.7
$\overline{\Delta P}$, mmHg	35	40	35
r_0, Å	57	54	50
ω_0	0.002	0.01	0.0001
u, Å	55	44	43
s	1.1	1.2	1.2

GFR, glomerular filtration rate; SNGFR, single nephron GFR; RPF, renal plasma flow rate; Q_A, afferent plasma flow rate, C_{pA}, afferent protein concentration.

$$\chi^2 = \sum_{i=1}^{n} \left(\frac{\Theta_i^{model} - \Theta_i^{data}}{w_i} \right)^2 \tag{3.6}$$

where n is the number of observations (i.e., the number of molecular radii studied, 16 in our data sets) and w_i is a weighting factor. The optimal choices for the weighting factors

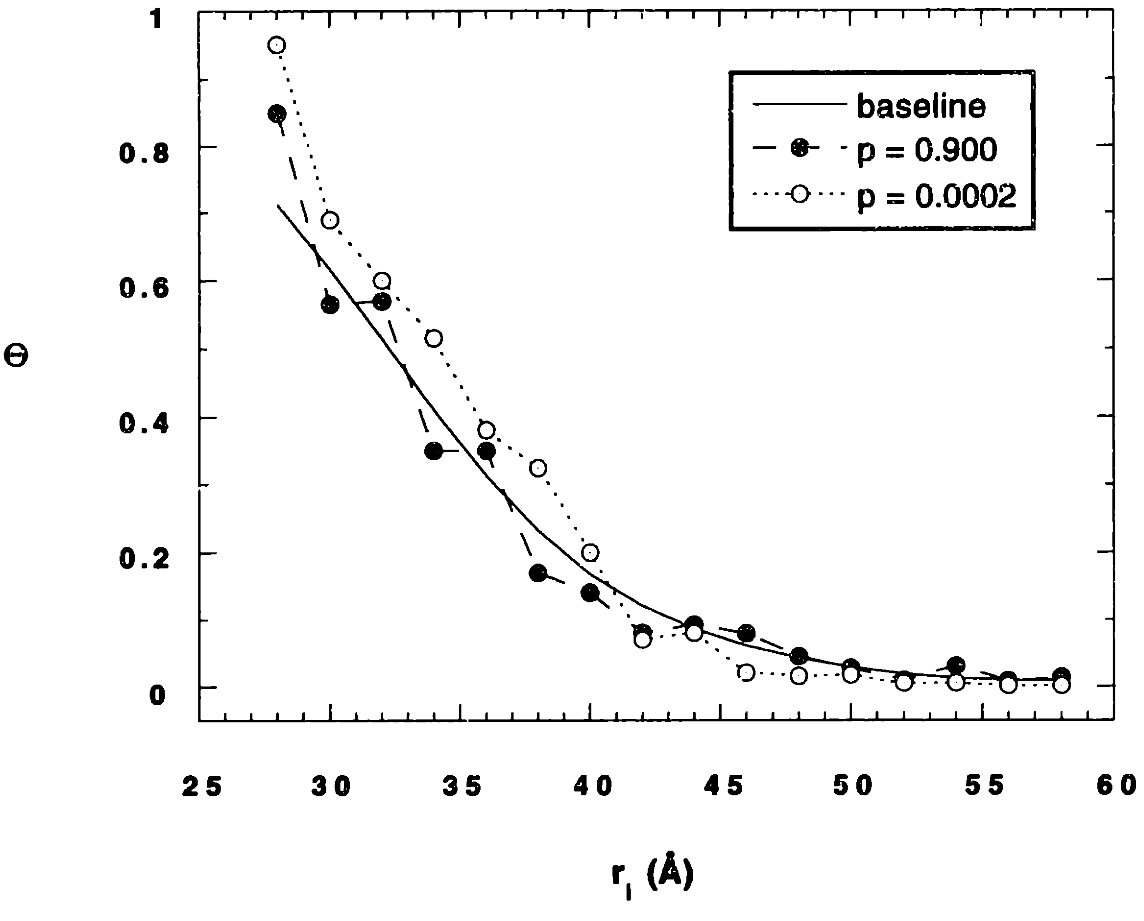

Figure 3-2
Simulated sieving curves illustrating the meaning of the probability p. For the curve labeled "p = 0.90" in comparison to baseline curve, the 8 positive and 8 negative residuals exhibit 11 runs, a highly random distribution of residuals. For the curve labeled "p = 0.0002" the 9 positive and 7 negative residuals exhibit only 2 runs, a nonrandom distribution.

are the elements of the covariance matrix of the measurement errors, in which case this method is equivalent to the more rigorous method of maximum likelihood. If we assume that the measurement errors in the sieving coefficients are independent, then the weights w_i are equal to σ_i, the standard deviation of Θ_i. We used $w_i = \sigma_i$ except were noted.

Because all fitting procedures rely upon assumptions regarding the distribution of measurement errors, we tested the hypothesis that the errors follow a normal distribution. For this purpose we used sieving data for individual rats studied by Bohrer et al.(1979) and Oliver et al. (1992). Two different tests were used, the Kolmogorov-Smirnov statistic K, and the Cramer-Von-Mieses statistic W^2. The procedure is outlined by Krishnaiah (1980). For a given solute radius, let n_r be the number of measured sieving coefficients (written as Θ^j), $\overline{\Theta}$ the average and σ the standard deviation of these n_r measurements. The normalized sieving coefficients can be written as:

$$z_j = \frac{\Theta^j - \overline{\Theta}}{\sigma}, \qquad j = 1,...,n_r. \tag{3.7}$$

K and W^2 are then given by:

$$K = \max \{D^+, D^-\} \tag{3.8}$$

$$\text{where } D^+ = \max \{ j/n_r - z_j \}, \quad D^- = \max \{z - (j-1)/n_r\}, \qquad j = 1,...n_r. \tag{3.9}$$

$$W^2 = \sum_{j=1}^{n_r} [z_j - (2j-1)/2n_r]^2 + \frac{1}{12\, n_r} \tag{3.10}$$

The hypothesis that the distribution is normal was rejected when the significance level was less than 5 %. This hypothesis appeared acceptable for most of the range of molecular radii in each of the five data sets examined. We therefore considered the assumption of normally distributed errors to be valid.

To test the weighted least squares method, we used the simplified isoporous model. Baseline sieving curves were first generated by adding fixed values to $\overline{\Delta P}$ and r_0; those quantities were then estimated as parameters by minimizing χ^2. Because no experimental errors were included, we used $w_i = 1$ in this case. Powell's method (Press et al., 1989) was used to compute the estimates. We found the least-squares method to be very reliable for our purposes; it always yielded the original values of $\overline{\Delta P}$ and r_0, irrespective of the initial guesses used to start Powell's method. In summary, these tests indicated that χ^2 was a reliable objective function for fitting our theoretical models to the data.

3.2.4 Reliability Measures for Parameter Estimates

Assuming that the theoretical model used has the correct functional form and that the only sources of variation in the data are random measurement errors, the standard errors of the model parameters are given by either of two methods, one based on the covariance matrix **V** of the estimates and the other obtained from Monte Carlo simulations. We compared the two methods by using the simplified isoporous model to generate baseline sieving data and then adding normally distributed errors as described above. When the number of Monte Carlo simulations was greater than 10^3, the resulting standard errors of the estimates were identical to those obtained from the covariance matrix. Monte Carlo simulations are performed by constructing a very large number of simulated data sets based on the original "measurement data", estimating the parameters for each of these sets, and finally mapping out the probability distribution of the parameters. Because **V** is easier to compute, it was used in all the subsequent analysis of the precision of parameter estimates.

The covariance matrix V for the parameter vector α is given by:

$$\mathbf{V} = \mathbf{M}^{-1} \tag{3.11}$$

where

$$M_{jk} = \sum_{i=1}^{n} \frac{1}{\sigma_i^2} \frac{\partial \Theta_i}{\partial \alpha_j} \frac{\partial \Theta_i}{\partial \alpha_k} \tag{3.12}$$

The standard error s_i of the estimated parameter α_i is then given by:

$$s_i = \left[V_{ii} \frac{\chi^2}{(n - n_p)} \right]^{1/2} \tag{3.13}$$

where n_p is the number of fitted parameters. These relations assume that α is estimated using the method of weighted least-squares, with $w_i = \sigma_i$.

The accuracy of the parameter estimates was assessed using confidence intervals. An interval with a 90 % confidence level for a parameter α_i is defined as follows (Bard, 1974). If an experiment were repeated 100 times, then each replication would yield a separate estimate α_i^*. For each such estimate, we could form the corresponding confidence interval. The true value of α_i should be in 90 of these intervals. With the assumption of normally distributed errors, confidence intervals for the fitted parameters are easily determined once the matrix **V** is known. The method is outlined by Bates and Watts (1988). Let c be the chosen confidence limit (e.g., c = 0.90 for 90 %). The corresponding interval is given in terms of s_i and the t-distribution by:

$$\alpha_i = \alpha_i^* \pm s_i \, t(n - n_p, \frac{1-c}{2}) \tag{3.14}$$

3.2.5 Reliability Measures for Models

A more difficult question is whether the model itself is sufficiently accurate to predict the data. The answer will be affirmative if the residuals, $\Theta_i^{model} - \Theta_i^{data}$, can be attributed to random errors in the observations. However, whereas a poor fit to the data constitutes strong grounds for rejecting the model, a good fit does not prove that the model is correct; it merely indicates that there is no reason to reject the model on the basis of the data at hand. Several criteria must be met. As discussed by Bates and Watts (1988), the ratio s_i/α_i should be small, and the parameters should not be excessively correlated. In addition, the residuals should be randomly distributed. A nonrandom behavior of the residuals can be judged from plots of the residuals versus the fitted values; it can also be assessed in a quantitative manner, as we shall now describe.

A run is defined as a sequence of residuals of the same algebraic sign. If the number of runs is much lower than expected, the randomness of the residual is suspect. Let m represent a number of runs, with m_{obs} being the number of runs actually observed in fitting a given set of data. Let q and v be the number of positive and negative residuals, respectively; if there are n data points, then $q + v = n$, assuming that none of the data points is fitted exactly. Swed and Eisenhart (1943) computed the probability of having a number of runs that is no larger than m_{obs}, assuming that there are no systematic errors (i.e., the model is complete and correct). This probability, denoted as $p(m \le m_{obs})$, is given by:

$$p(m \le m_{obs}) = \frac{1}{C_{q+v}^{q}} \sum_{m=2}^{m_{obs}} f_m(q,v) \tag{3.15}$$

where

$$C_{q+v}^{q} = \frac{(q+v)!}{q!v!} \tag{3.16}$$

When m is even,

$$f_m(q,v) = 2\, C_{q-1}^{k-1}\, C_{v-1}^{k-1} \tag{3.17}$$

where $k = m/2$. When m is odd,

$$f_m(q,v) = C_{q-1}^{k-1} C_{v-1}^{k-2} + C_{q-1}^{k-2} C_{v-1}^{k-1} \tag{3.18}$$

where $k = (m+1)/2$.

If p is small (i.e., $p < 0.05$), it is likely that the residuals are not randomly distributed. An example is shown by the curve for $p = 0.0002$ in Figure 3-2. A comparison of that curve with the baseline case reveals that there are only 2 runs among the 16 residuals, leading to a value of p near zero. In contrast, comparing the curve with random errors to the baseline case yields 11 runs, and consequently a value of p near unity. (In those comparisons the baseline curve is treated as if it were obtained by fitting a model to either of the other sets of points). It will be shown that p is indeed a useful means for assessing the reliability of the model.

The computations were done using a Cray X-MP EA/464 at the MIT Supercomputer Center.

3.3 Results

3.3.1 Random Errors Only

The effects of random measurement errors were simulated using three of the "complete" models, the isoporous, two-pore and isoporous-with-shunt models. (The lognormal model was excluded here because of the excessive computer time required to fit it to a large number of data sets.) The standard deviation σ_i of the experimental errors was taken to be 1, 2, 5 or 10% of the corresponding sieving coefficients, Θ_i. Each of the 4 levels of error was generated 100 times for each of the 9 combinations of hemodynamic inputs and model, yielding a total of 3,600 comparisons. To isolate the effect of random errors, the models were made "exact" by fitting each model only to data sets generated using that model.

Confidence intervals. When σ_i was ≤ 5 % of Θ_i, the estimated pressure ($\overline{\Delta P}^*$) was almost always within 10% of the true value ($\overline{\Delta P}$) and very often within 5% (in 96.2% and 88.0% of all cases, respectively). When σ_i was 10% of Θ_i, the corresponding percentages fell to 80.6% and 60.1%. Thus, as one would expect, the accuracy of the pressure estimates declined as the random errors in the sieving coefficients were increased. To test the reliability of the confidence intervals for $\overline{\Delta P}$ calculated using equation (3-14), the 98% confidence interval was computed for each case. The percentage of those intervals which actually contained the true value of $\overline{\Delta P}$ was then compared with the predicted value of 98%. When σ_i was 5% of Θ_i, the measured level of confidence was 92.7%. When σ_i was 10% of Θ_i, the measured level of confidence declined to 89.1%. Although the actual levels of success tended to be somewhat lower than those predicted by equation (3.14), there was sufficient agreement to conclude that the predicted confidence intervals are reasonably reliable when only random measurement errors are present.

Values of χ^2 and p. We found that neither the value of χ^2 nor that of the average residual (normalized or absolute) indicated in a reliable manner whether $\overline{\Delta P}^*$ was close to $\overline{\Delta P}$. There seemed to be no correlation between the magnitude of the residuals and the accuracy of the pressure estimates; the residuals could be small and $\overline{\Delta P}^*$ very far from $\overline{\Delta P}$, or vice versa. As Figure 3-3 illustrates, it was impossible to predict from the value of χ^2 whether or not $\overline{\Delta P}^*/\overline{\Delta P}$ was close to unity. Whatever the magnitude of the simulated experimental errors, the calculated probability p that the residuals were randomly distributed was always high ($p > 0.1$ in 98.6% of the 3,600 cases, and $p > 0.2$ in 95.2% of the cases). The relatively large values of p were to be expected, because in these particular comparisons the "experimental" errors were deliberately made random.

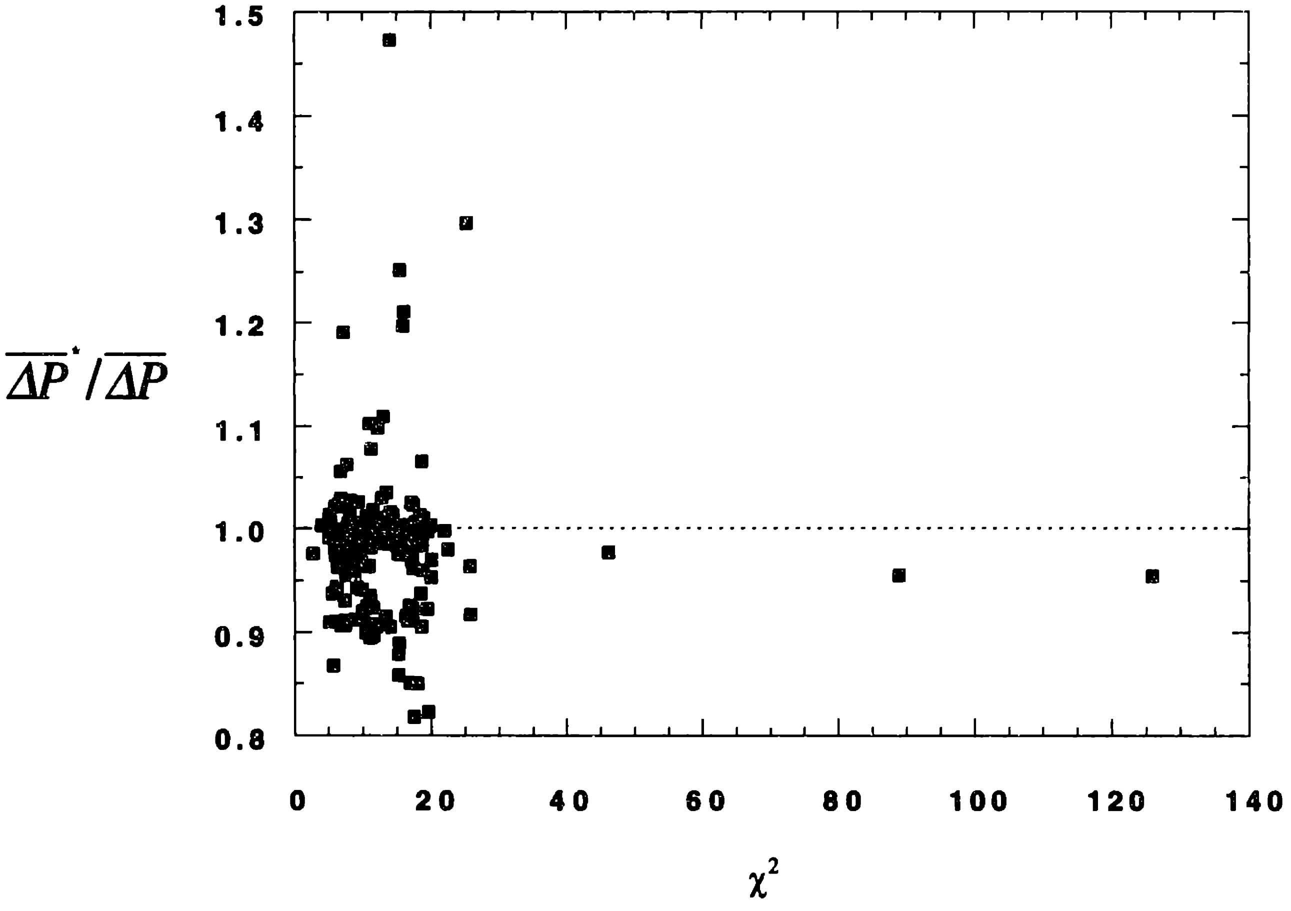

Figure 3-3
Ratio of the fitted to the exact pressure ($\overline{\Delta P}^* / \overline{\Delta P}$, where $\overline{\Delta P}^*$ is the pressure estimate) vs. χ^2, based on 3600 simulations of cases involving only random errors. Dotted line indicates unity.

3.3.2 Systematic Errors Only

We examined the effects of systematic errors, such as those caused by employing an inaccurate mathematical model, by generating data using the four complete models and then using each of the other three complete models to fit the data. Thus, systematic errors were created by attempting to fit the data using an "incorrect" form of pore-size distribution (i.e., not the type used to generate the data). Because random errors were excluded, confidence intervals for the estimated pressure were not calculated.

Values of χ^2 and p. As before, neither the value of χ^2 not that of the average residual was useful for predicting the accuracy of the estimated pressure. However, we found that a large value of p was a remarkably reliable indicator of success when only systematic errors were present. As shown in Figure 3-4, the estimated pressure was within 5% of the true value in all cases when $p > 0.2$.

Increasing the number of pore-size parameters. A simple strategy for increasing the goodness of fit to a sieving curve, and perhaps then also increasing p, is to augment the number of pore-size parameters in the model. To test the effectiveness of this approach, we generated data using the isoporous-with-shunt model and the lognormal model and attempted to fit the data using three models that were physically similar but had differing numbers of parameters. For the fit we used the isoporous model (1 pore parameter, r_0), a constrained two-pore model with x_1 fixed at 0.5 (2 pore parameters, r_1 and r_2), and the usual two-pore model with x_1 free to vary (3 pore parameters, r_1, r_2 and x_1). We found that augmenting the number of degrees of freedom in this manner always decreased the values of χ^2, increased the probability p, and very often yielded a better estimate for $\overline{\Delta P}$. As shown by the results on Figure 3-5, when the estimate of $\overline{\Delta P}$ failed to improve through this strategy, it did not get significantly worse; in those cases the difference between the estimates was less than 1.5% of the true value of $\overline{\Delta P}$.

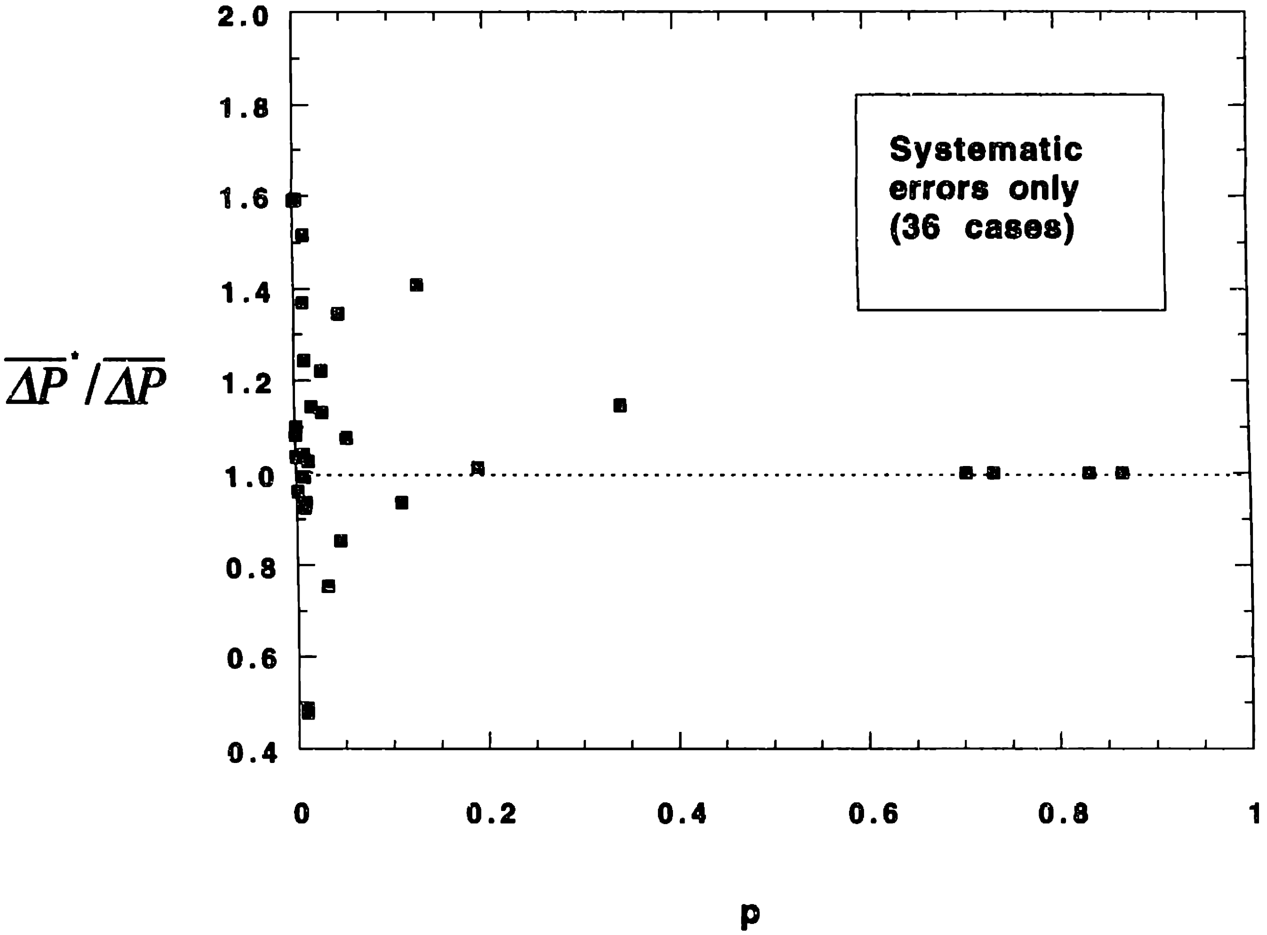

Figure 3-4

Ratio of the fitted to the exact pressure ($\overline{\Delta P}^*/\overline{\Delta P}$, where $\overline{\Delta P}^*$ is the pressure estimate) vs. the probability p, based on 36 simulations of cases involving only modeling errors. Two points have been omiteed for clarity, one with $p = 0.0002$ and $\overline{\Delta P}^*/\overline{\Delta P} = 7.20$ and the other with $p = 0.002$ and $\overline{\Delta P}^*/\overline{\Delta P} = 3.55$.

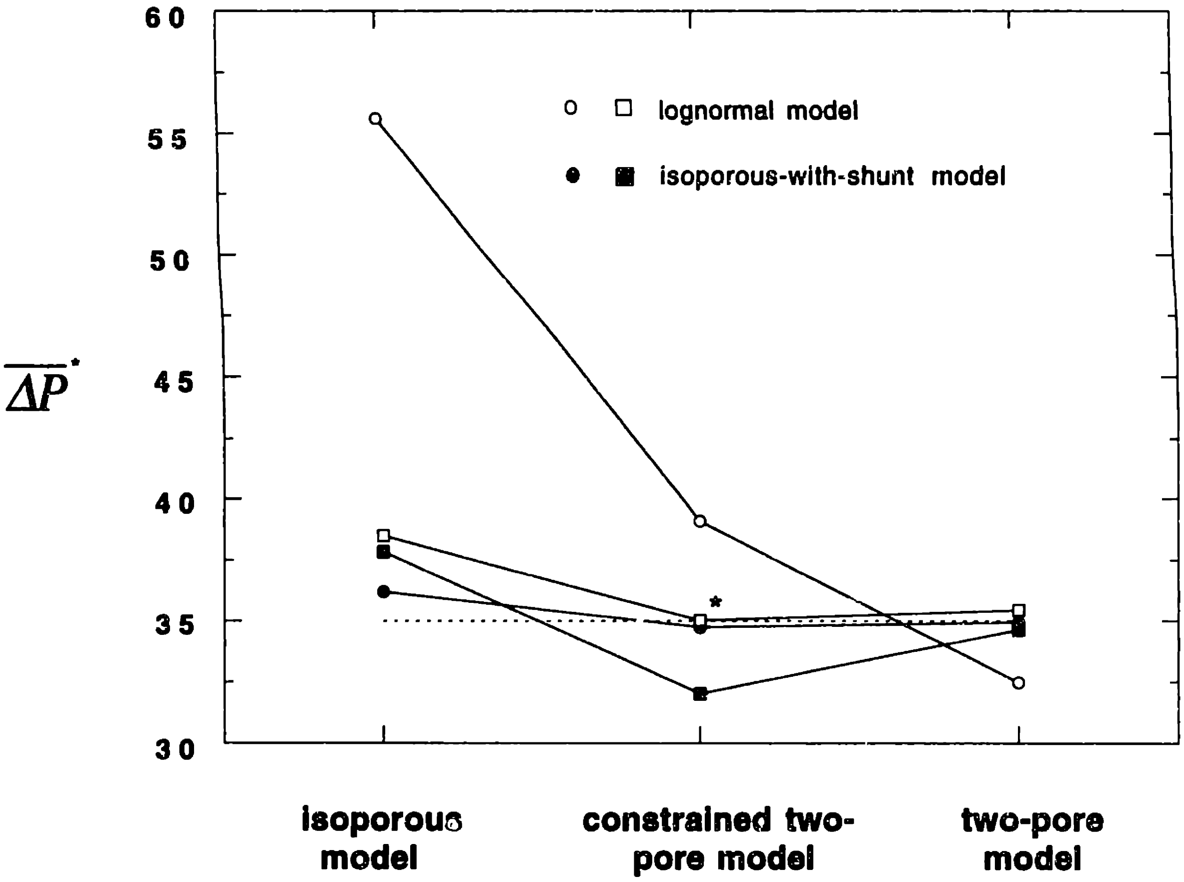

Figure 3-5

Effect on the pressure estimate ($\overline{\Delta P}$ *) of augmenting the number of pore-size parameters, by using 3 "complete" models containing the differential mass balance equations. The exact value of $\overline{\Delta P}$ is indicated by the dashed line. "Data" were generated using either the lognormal model or the isoporous-with-shunt model. As the number of pore-size parameters was increased from 1 (isoporous model) to 3 (two-pore model), the fitted pressure tended toward the correct value. Values of p were always < 0.05, except for the point marked with an asterix, where p = 0.108.

Importance of mass balance equations. In the four "complete" models, which include the differential mass balance equations, changes in $\overline{\Delta P}$ affect the sieving curve in two ways. Both are mediated by the pressure dependence of the volume flux J_v (equation 3-4). The more direct effect is that described earlier, whereby changes in J_v alter the convective part of the solute flux. The additional effect stems from the influence of J_v on the rate at which solute concentrations rise with increasing distance along a glomerular capillary. It is the latter phenomenon that explains the well-known dependence of single-nephron glomerular filtration rate on plasma flow rate (Maddox et al., 1992). In the two simplified models, where equations (3.3-3.5) are not used, all concentrations are assumed to be constant along a capillary, and the second effect is absent. Thus the simplified models may be viewed as containing a gross systematic error.

To examine the effect of such an error, we again generated data using the isoporous-with-shunt model and the lognormal model and fitted these data with the simplified isoporous model (parameter r_0), a constrained, simplified two-pore model with $x_1 = 0.5$, and the simplified two-pore model (parameters r_1, r_2 and x_1). As seen before, the model with the most degrees of freedom always yielded a lower χ^2 and a higher p. As shown by the results in Figure 3-6, it now yielded a much worse estimate for $\overline{\Delta P}$. These findings seem to indicate that, if a model contains a major error or omission, such as the neglect of the mass balance equations, then the results can be very misleading; i.e., increasing the number of pore parameters may improve the fit, the residuals may be smaller and distributed more randomly, yet the estimated pressure may be further from its true value.

3.3.3 Random and Systematic Errors Combined

The combined effects of random and systematic errors were simulated by first generating baseline data using the four complete models and then adding random errors as

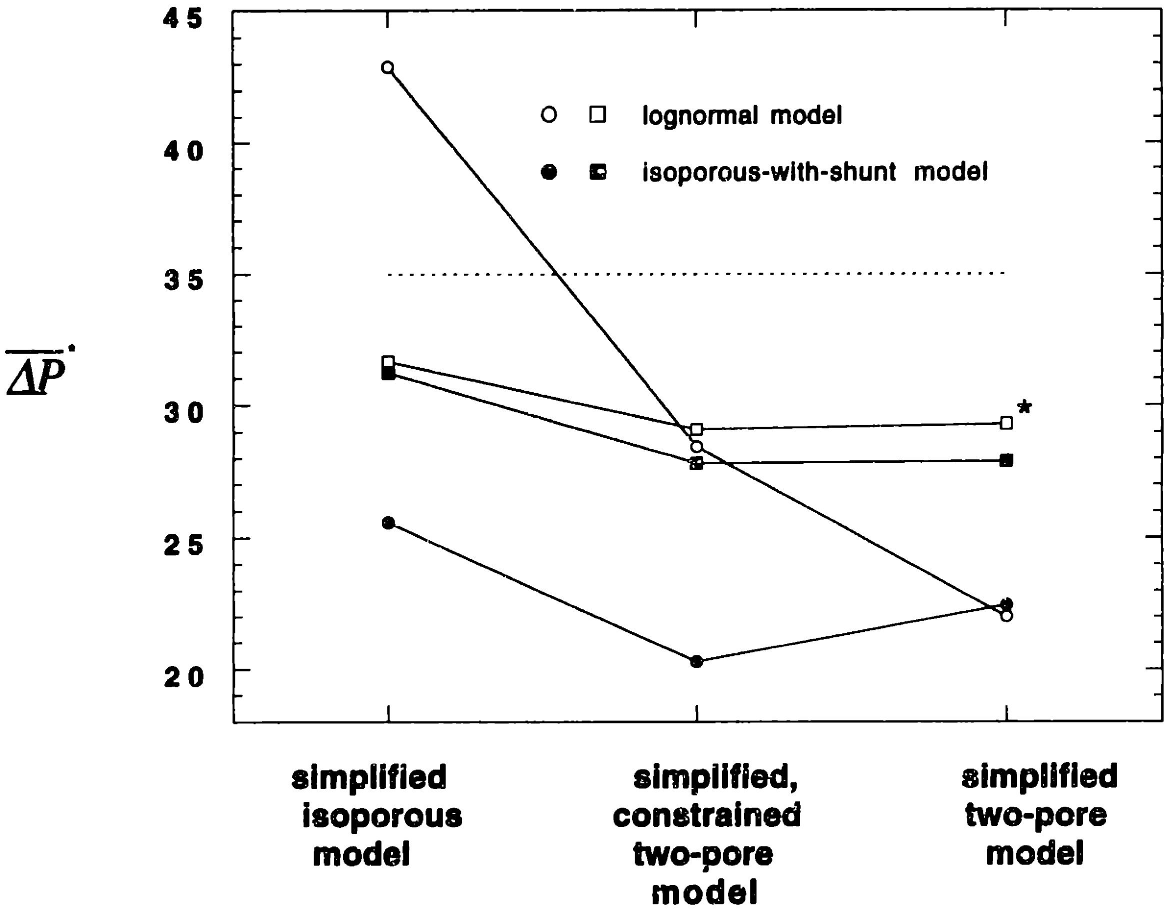

Figure 3-6

Effect on the pressure estimate ($\overline{\Delta P}$ *) of augmenting the number of pore-size parameters, by using 3 "simpified" models without the differential mass balance equations. The exact value of $\overline{\Delta P}$ is indicated by the dashed line. "Data" were generated using either the lognormal model or the isoporous-with-shunt model. As the number of pore-size parameters was increased from 1 (simplified isoporous model) to 3 (simplified two-pore model), the fitted pressure tended to become less accurate. Values of p were always < 0.1, except for the point marked with an asterix, where $p = 0.108$.

described above. With 4 models, 3 sets of hemodynamic inputs, 4 levels of random errors, and 20 examples at each level of error, a total of 960 data sets was generated. Finally, each set was fitted using the three models that were not used to generate it. (Because of excessive computational time, the lognormal model was not used for fitting the many sets of data). Thus in all instances the use of a different model introduced a systematic error.

Confidence intervals. With the combination of random and systematic errors, the predicted confidence intervals for $\overline{\Delta P}^*$ were found to be quite reliable, but also very large. The predicted 98% level of confidence contained the true value of $\overline{\Delta P}$ in 86.4%, 88.1%, 88.5%, and 89.1% of cases corresponding to random errors of 1%, 2%, 5% and 10%, respectively. However, approximately two-thirds to three-fourths of these intervals exceeded 10 mmHg (62.4%, 64.5%, 73.3% and 73.9% respectively). Estimates of $\overline{\Delta P}$ with such large confidence intervals are unlikely to be very useful.

Values of χ^2 and p. Once again, neither χ^2 nor the magnitude of the residuals were useful predictors of success in estimating $\overline{\Delta P}$. The probability p remained a reliable predictor, provided that the random errors in the sieving coefficients were sufficiently small. Shown in Figure 3-7 is a representative subset of results for σ_i equal to 1% of Θ_i ; when $p > 0.2$; we found that $\overline{\Delta P}^*$ was within 10% of $\overline{\Delta P}$ in 96.5% of the cases tested and within 5% in 92.4% of the cases. As the magnitude of the experimental errors was increased, the criterion $p > 0.2$ became progressively less predictive, as illustrated on Figure 3-8. When $p > 0.2$, the fitted pressure was within 10% of the true value in 80.7 % of the cases when σ_i was 5% of Θ_i and in 69.1 % of the cases when σ_i was 10% of Θ_i. It was also found that the higher the value of p, the more reliable were the results at any given level of random error. For example, with σ_i set at 5% of Θ_i, $\overline{\Delta P}^*$ was within 10% of $\overline{\Delta P}$ in 78.2% of cases when $p > 0.1$, 80.7% when $p > 0.2$, and 87.2% when $p > 0.3$.

It should be acknowledged that $p > 0.2$ is a conservative criterion. There were a significant number of cases in which $\overline{\Delta P}^*$ was close to $\overline{\Delta P}$, and yet $p < 0.2$. For example,

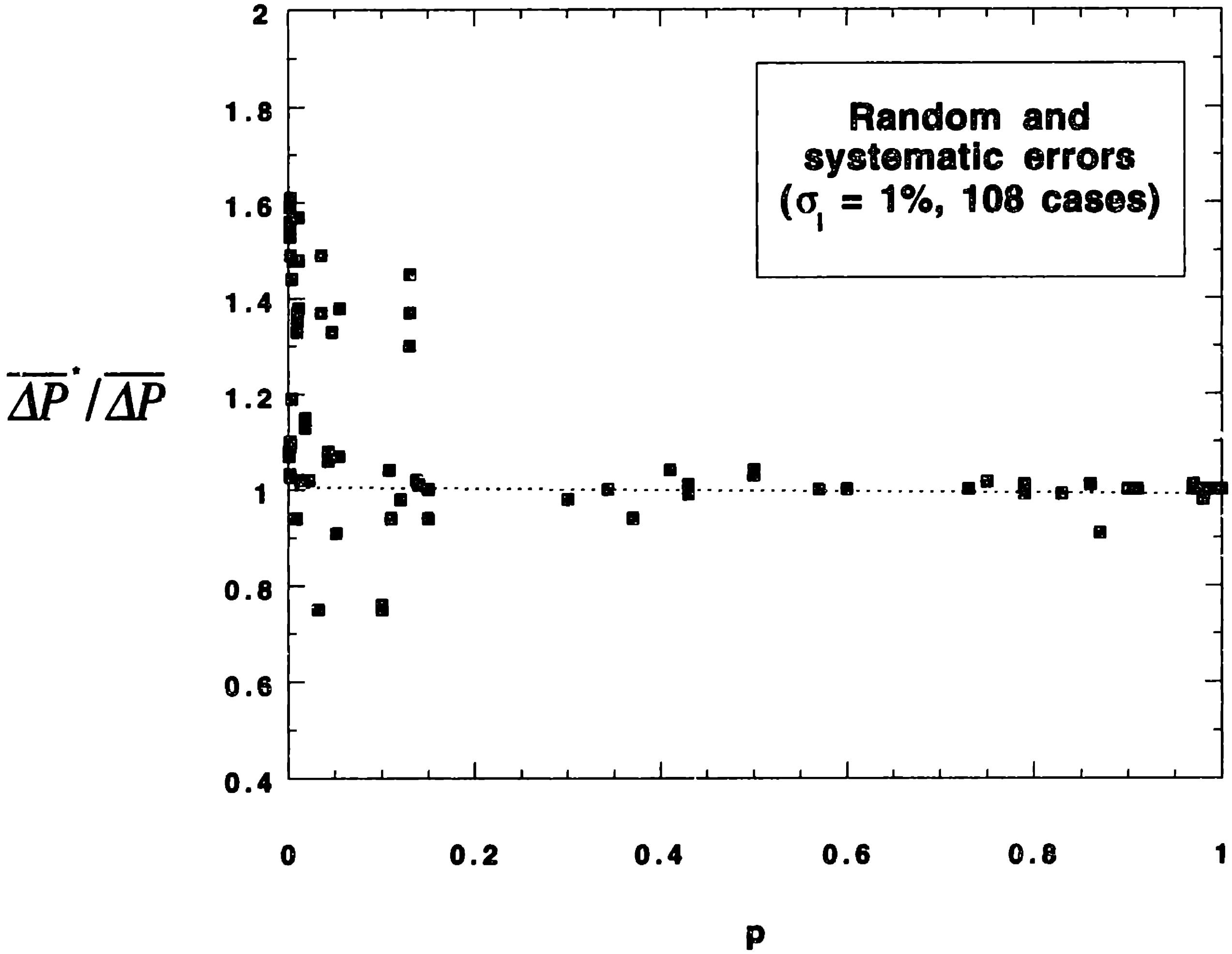

Figure 3-7

Ratio of the fitted to the exact pressure ($\overline{\Delta P}^* / \overline{\Delta P}$, where $\overline{\Delta P}^*$ is the pressure estimate) vs. the probability p, based on 960 simulations of cases involving both random and systematic errors. Results are shown for a representative subset of data.

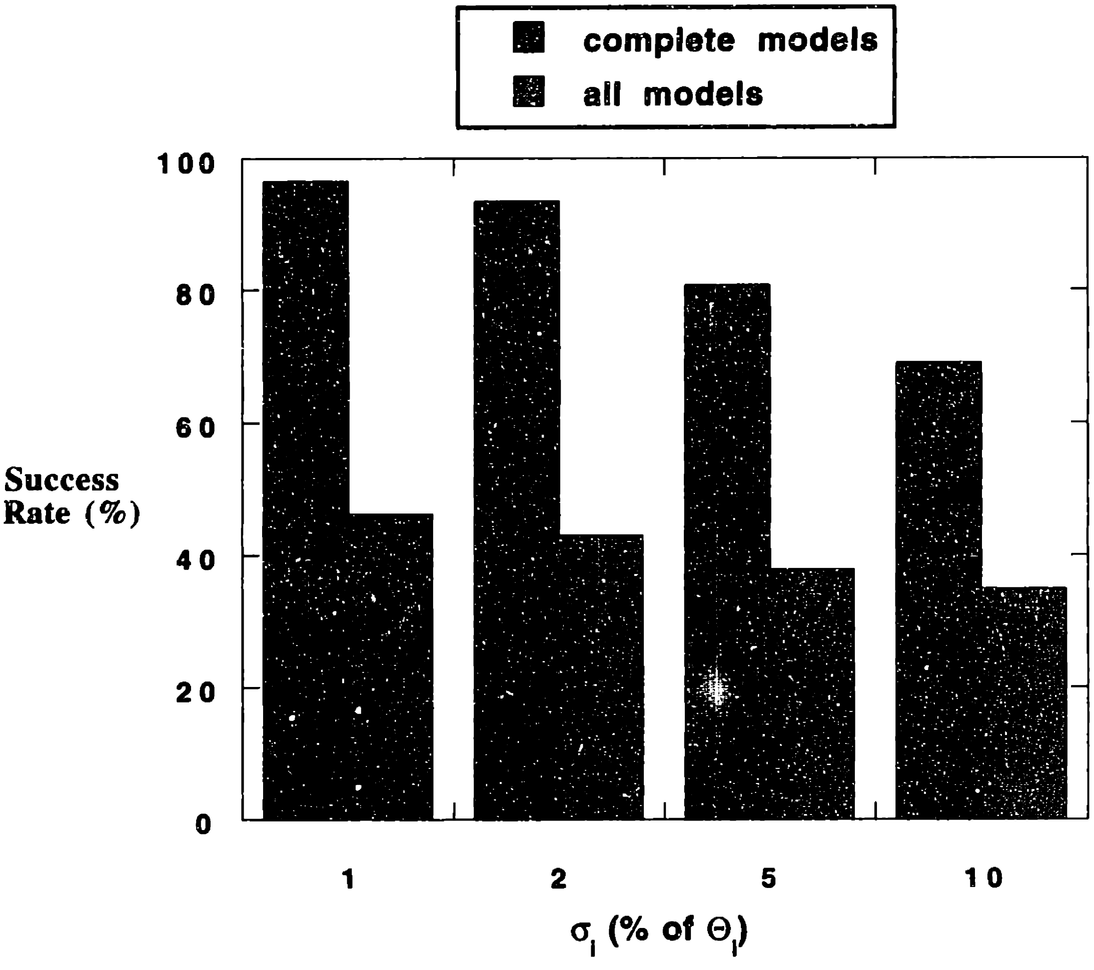

Figure 3-8

Reliability of the statistic p as a predictor of success in estimating $\overline{\Delta P}$. Ordinate, percentage of cases when $\overline{\Delta P}^* = \overline{\Delta P} \pm 10$ % with $p \geq 0.2$. Abcissa, various levels of random error, with the standard deviation (σ_i) expressed as a percentage of the sieving coefficient (Θ_i). Results are based on 2,160 simulations from only the "complete" models with mass balance equations and a total of 6,000 simulations involving all models ("complete" plus "simplified").

when σ_i was 5% of Θ_i, it was found that $p < 0.2$ in 30.3% of all cases in which the fitted pressure was within 10% of the true value.

To further examine the influence of a gross systematic error, we enlarged the number of data sets by also using the simplified models to generate data and added the simplified models to those used to fit the various data sets. As shown in Figure 3-8, with $p > 0.2$ and at any given level of random error, including the simplified models greatly reduced the overall reliability of the estimated pressures.

3.4 Discussion

As reviewed in the introduction, the idea of fitting theoretical models to sieving data as a nonivasive means to measure $\overline{\Delta P}$ has been pursued by various laboratories over many years. The resulting estimates of $\overline{\Delta P}$ have sometimes been in excellent agreement with independent measurements obtained more directly using micropuncture, but more often the agreement has not been very satisfactory. The reasons for the erratic results have remained puzzling. This study represents the first attempt to examine the problem using a propagation of error analysis. By using computer simulations to generate thousands of synthetic sets of data containing various types and levels of error, we sought to estimate the separate influences of random experimental errors and model uncertainties on the ability to estimate $\overline{\Delta P}$, and to identify criteria that would predict success or failure of the method.

When only random experimental errors are present, the level of uncertainty in a parameter estimated by fitting a model to the data can be calculated in a well-established manner. Our results confirmed that the parameter covariance matrix can be used very efficiently and reliably for this purpose (equations 3.3-3.5). In contrast, there is very little guidance from the literature on assessing the effects of modeling uncertainties on parameter estimation. By "modeling uncertainties" or "modeling errors", we mean a situation where the theoretical model used to fit the data may be largely sound but may contain a functional relationship between the data (sieving coefficients) and one or more of the fitted parameters (e.g., $\overline{\Delta P}$) that is only approximately correct. This problem does not arise in most physical or chemical experimentation. In the present context, however, given the complex arrangement of the glomerular capillary network, the intricate and not fully defined ultrastructure of the glomerular capillary wall, and the limitations of available theories for hindered transport in porous media, such situations are unavoidable.

It is important to recognize that modeling errors are merely one kind of systematic error and that other systematic errors may be present in any given sieving study. For example, an inaccurate calibration of the chromatographic columns used to fractionate plasma and urine samples by molecular size would tend to shift the sieving curve to the left or to the right, along the molecular-size axis. Problems with, for instance, an inulin assay might shift the mean values of the measured fractional clearances up or down. Faced with the inability of a model to accurately fit a given set of sieving data, one finds that there is no clear way to distinguish modeling errors from systematic experimental errors. The usual effect of a systematic error is to make it impossible for the model to accurately fit the mean sieving curve, even if the latter is based on a large number of repetitions. Accordingly, the comments made here about the effects of modeling errors on the ability to estimate $\overline{\Delta P}$ are largely applicable to any type of systematic error.

Press et al. (1989) have proposed one way of assessing the appropriateness of a model. If the measurement errors follow a normal distribution and if the parameters are estimated by minimizing χ^2 (see equation 3.6), then one can compute the probability Q that χ^2 would exceed the particular minimum value obtained in the fit, denoted as $\chi^2_{(obs)}$. In principle, the value of Q should give a quantitative measure of the goodness-of-fit of the model; a very small Q indicates that $\chi^2_{(obs)}$ is unexpectedly large, that the residuals are unlikely to be random fluctuations, and therefore, that the model is inaccurate. Although the statistic Q was easy to compute, we did not find it helpful or reliable .The values of Q ranged from 10^{-15} to ~ 1.0 without any clear pattern; no correlation between Q and the ratio

$\overline{\Delta P}^*/\overline{\Delta P}$ was evident. Another approach was proposed by Eno et al. (1985), using the partial derivatives of the model parameters with respect to the experimental observables. The authors derived expressions for the degree of parameter deviation arising from uncertainties in the data and discrepancies between the model and the measured quantities. We tested their method using two elementary models defined by algebraic expressions, a linear function and an exponential function, and found that the calculated variances did not adequately reflect the effects of modeling errors. There was no clear relationship between the calculated parameter variances and the extent to which the models deviated from "reality" (i.e., the "data" generated using the other model). In another study in which this method was applied (Yetter et al., 1989), modeling errors were attributed to uncertainties in fixed parameters only, rate constants specifically, and did not arise from an unknown functional relationship between the parameters and the observable quantities, which is our concern here.

In the absence of a suitable theory for assessing the effects of modeling uncertainties (or other systematic errors), we opted for an empirical approach, which necessarily limits the generality of our conclusions. Nevertheless, the results provide certain guidelines as to what is needed to be able to accurately estimate $\overline{\Delta P}$ from sieving curves. Our main findings can be summarized as follows. When random experimental errors were the only source of uncertainty and when the experimental errors were small enough (i.e., $\sigma_i \leq 5\%$ of Θ_i), then the estimate of $\overline{\Delta P}$was almost always accurate to within 5% and the confidence intervals obtained from equation (3-14) was always reliable. When there were also modeling uncertainties arising from the type of pore-size distribution chosen, the p statistic defined by equation (3.15), which is based in the number of runs in the residuals, was a useful predictor of success. Specifically, there was a high probability that the estimate of $\overline{\Delta P}$ was within 10% of the true value, provided that $p > 0.2$. For $\sigma_i \leq$ 5% of Θ_i and $p > 0.2$, the probability that the pressure estimate would be at least that accurate was 88.3%. Larger random errors in the sieving coefficients materially reduced the probability of accurately estimating $\overline{\Delta P}$. Modeling errors of a more major type, as exemplified by omission of the mass balance equations, tended to negate the predictive ability of p.

Insight into the inherent limitations in attempting to estimate $\overline{\Delta P}$ from real sieving data is provided by a retrospective analysis of several studies in rats which reported micropuncture measurements of $\overline{\Delta P}$ together with sieving data for dextran or Ficoll. As an extension of the study done by Oliver (1992), we analyzed the results of eight such studies, comparing the micropuncture values of $\overline{\Delta P}$ to estimates we obtained using three different sieving models. For this purpose we chose pore-size distributions that are in current use and are presently viewed as being the most realistic available. We used the isoporous-with-shunt model and the lognormal model as described above and a "lognormal-with-shunt" model as described by Oliver et al (1992). The results are shown in Table 3-3. The fitted $\overline{\Delta P}$ was within 3 mmHg of the measured value in only 14 of 54 cases. Given that σ_i tended to be large (averaging from 13-87 % of Θ_i in the various experimental conditions) and that p was generally very small, this is not surprising. Indeed, $p \geq 0.2$ in only seven cases, in all of which the average σ_i was ≥ 17% of Θ_i, and in all of which the estimated pressure was not very accurate. As already emphasized, random experimental errors in Θ_i must be small for p to be an accurate predictor of success in estimating $\overline{\Delta P}$. It is noteworthy that the most complex of the three models, the lognormal-with-shunt model, did not necessarily give a better estimate of $\overline{\Delta P}$ than the other two. In addition, although Ficoll is a more ideal tracer than dextran, its use in the studies by Oliver et al. (1992) did not lead to better pressure estimates.

Differences in $\overline{\Delta P}$ between superficial and deep nephrons, to the extent that they exist, might contribute to the discrepancies between the measured and estimated values in Table 3-3. The micropuncture results are for superficial nephrons, whereas the whole-kidney sieving data reflect the average function of all nephrons. If, for example, values of $\overline{\Delta P}$ in deep glomeruli are larger than in superficial ones, then the values of $\overline{\Delta P}$ derived

Table 3-3

Comparison of directly measured pressures in rat with estimates from fits to sieving data

Condition	σ_i/Θ_i, %	$\overline{\Delta P}$, mmHg		$\overline{\Delta P}$*, mmHg		Reference
			Isoporous with shunt	Lognormal	Lognormal with shunt	
Normal hydropenia	14	34.0	32.0	34.5	34.5	Chang et al., 1975
Normal + PVE	16	38.0	27.4	27.4*	27.7	Chang et al., 1975
NSN hydropenia	13	39.9	29.4*	24.3	24.3	Chang et al., 1976
NSN + PVE	19	40.0	29.8	23.9	21.5	Chang et al., 1976
Normal euvolemia	19	33.9	34.5	34.5	34.5	Ichikawa and Brenner, 1979
Normal + histamin	17	39.5	30.4*	30.5 †	30.4 †	Ichikawa and Brenner, 1979
Normal euvolemia	14	33.0	34.3	31.4	31.5	Yoshioka et al., 1986
Normal + RVC	26	42.0	38.7	36.7	36.8	Yoshioka et al., 1986
PHN baseline	29	40.0	42.2	30.9	31.1†	Yoshioka et al., 1987
PHN + ANG II	39	52.0	45.4	38.7	38.6†	Yoshioka et al., 1987
PHN baseline	25	42.0	48.0	32.9	33.1†	Yoshioka et al., 1987
PHN + ACh	30	35.0	50.8	30.0	30.2	Yoshioka et al., 1987
NPX baseline	26	52.0	39.9	33.1†	33.3†	Yoshioka et al., 1988
NPX + Ver	24	34.0	35.0	26.9	25.9	Yoshioka et al., 1988
Normal euvolemia	47	33.8	87.8	31.6	35.0*	Oliver et al., 1992
Normal euvolemia¶	67	33.8	122.4	39.4	36.1	Oliver et al., 1992
FH UNX baseline¶	87	55.9	45.1	29.9	28.5	Oliver et al., 1994
FH UNX + ENA¶	61	43.6	36.9	31.5	31.5	Oliver et al., 1994

$\overline{\Delta P}$, measured hydraulic pressure difference; $\overline{\Delta P}$*, estimated values of $\overline{\Delta P}$. PVE, plasma volume expansion; NSN, nephrotoxic serum nephritis; RVC, renal vein constriction; PHN, passive Heymann's nephritis; ANG II, angiotensin II; ACh, acetylcholine; NPX, subtotal (~5/6) nephrectomy; Ver, verapamil; FH, Fawn-hooded rats; UNX, uniphrectomy; and ENA, enalapril. Except where noted, all studies used dextran in Munich-Wistar rats, and $p < 0.1$ from Eq. (3-15). *$0.1 \leq p \leq 0.02$. † $p \geq 0.2$. ¶ Ficoll sieving data.

from sieving data might tend to be larger than those obtained by micropuncture. However, judging from the random nature of the discrepancies between the measured and calculated values of $\overline{\Delta P}$ in Table 3-3, it seems unlikely that differences in nephron populations were an important factor.

In conclusion, the experimental precision typically achieved in sieving studies in vivo, together with the limitations of current mathematical models, make it unlikely that an accurate group-mean value of $\overline{\Delta P}$ will be estimated from any given set of sieving data. The fact that good pressure estimates are sometimes obtained is probably fortuitous. The refinement of laboratory techniques may help to some extent, but actual subject-to-subject variability will always introduce some random error in the mean values of sieving coefficients. Most studies have been hampered also by systematic errors, one of which comes from interpreting dextran data using theories derived for rigid, spherical molecules. That problem can be mitigated in future studies by the use of more ideal tracers such as Ficoll, but it is less clear how to overcome other systematic errors, including those inherent in the current generation of equivalent-pore models. The predicted effects of pressure on sieving curves are relatively subtle, making the estimation of $\overline{\Delta P}$ a much more demanding task than other uses of these mathematical models. Accomplishing that task may require a much more sophisticated and structurally accurate representation of the glomerular barrier.

Chapter Four

Previous Work on Ultrastructural Models for Glomerular Ultrafiltration

4.1 Introduction

Many glomerular diseases are characterized by changes in the morphology of the capillary wall, such as a thickening of the basement membrane or broadening of the foot processes. These subtle variations cannot be captured by the pore models, which treat the membrane as a homogenous barrier perforated by uniform cylindrical pores. In addition, we have shown that pore models are not accurate enough to allow us to determine the mean hydraulic pressure difference $\overline{\Delta P}$ from sieving data. A more faithful representation of the glomerular capillary wall is thus needed. For this purpose, a new model based on the fine ultrastucture of the barrier has recently been proposed by Drumond and Deen (1994a, 1994b, 1995), describing water flow across the capillary wall and solute transport across the epithelium. Our goal is to extend this so-called ultrastructural model to predict overall sieving coefficient of macromolecules.

This chapter summarizes the previous work based on this approach. The model for water flow and that for the filtration of solutes across the epithelial slits are described in sections 4.2 and 4.3, respectively.

4.2 Mathematical Model for Hydraulic Permeability

4.2.1 Idealized Structural Unit

Electron micrographs indicate that the glomerular capillary wall can be accurately represented by an alignment of approximate repeating units, termed unit cells, each composed of a single filtration slit in between two foot processes, a layer of basement membrane lying underneath, and fenestrated endothelial cells at the interface between the membrane and the capillary lumen. The model assumes that a periodic idealized unit cell, shown in Figure 4-1, repeats itself along the entire length of the capillary. Flux occurs in the z-direction, from the lumen to Bowman's space; W corresponds to the width of the structural unit, and δ_{gbm} to the thickness of the glomerular basement membrane.

The fenestrae are assumed to be channels of circular cross-section with varying radii, as indicated by Lea et al (1989). As described in Chapter 2, the glomerular basement membrane is a network of fibers whose exact size, shape and orientation have not been fully characterized. The GBM is therefore treated as a homogenous random fiber array. As also indicated in Chapter 2, two configurations have been proposed for the slit diaphragm, referred to as the "ladder" and the "zipper", respectively. Both are illustrated on Figure 4-2.

The three layers are first treated separately in this approach, water flow across each one of them being determined independently. The overall permeability of the barrier k is then calculated based upon the individual hydraulic permeabilities of the three layers:

$$k_i = \frac{J_v}{\Delta P_i} \qquad (i = en, gbm, ep) \qquad (4.1)$$

where the subscripts *en, gbm* and *ep* refer to the endothelium, glomerular basement membrane and epithelium, respectively. J_v is the volume flux, and ΔP_i the net pressure difference across the layer i, both averaged over the cross-sectional area of a unit cell. The hydraulic permeability of the glomerular capillary wall is then calculated by:

$$\frac{1}{k} = \sum_i \frac{1}{k_i} \qquad (4.2)$$

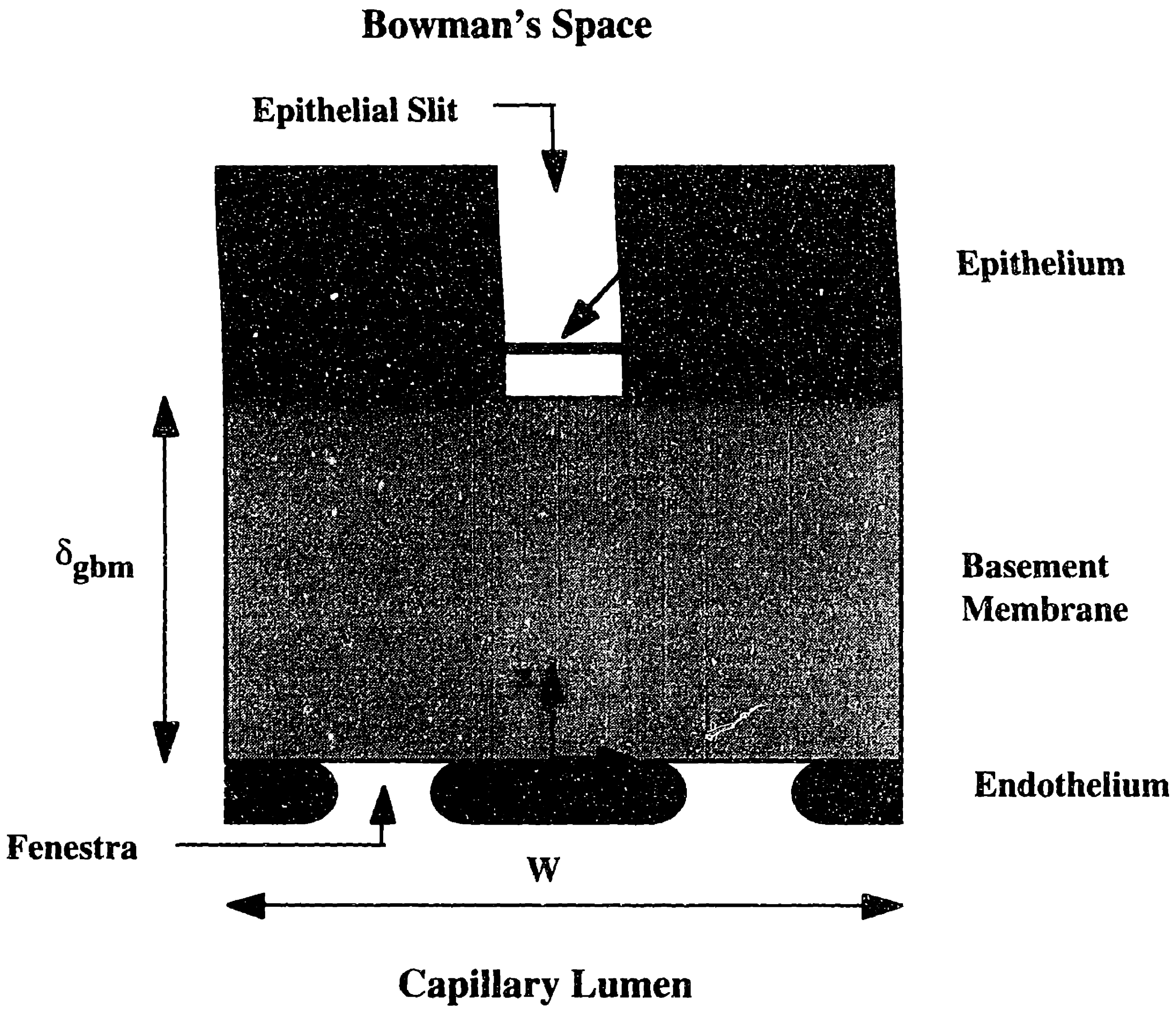
Bowman's Space
Epithelial Slit
Epithelium
δ_{gbm}
Basement Membrane
Endothelium
Fenestra
W
Capillary Lumen

Figure 4-1

Idealized structural unit of the glomerular capillary wall. The unit cell corresponds to one filtration slit and is repeated periodically along the length of the capillary.

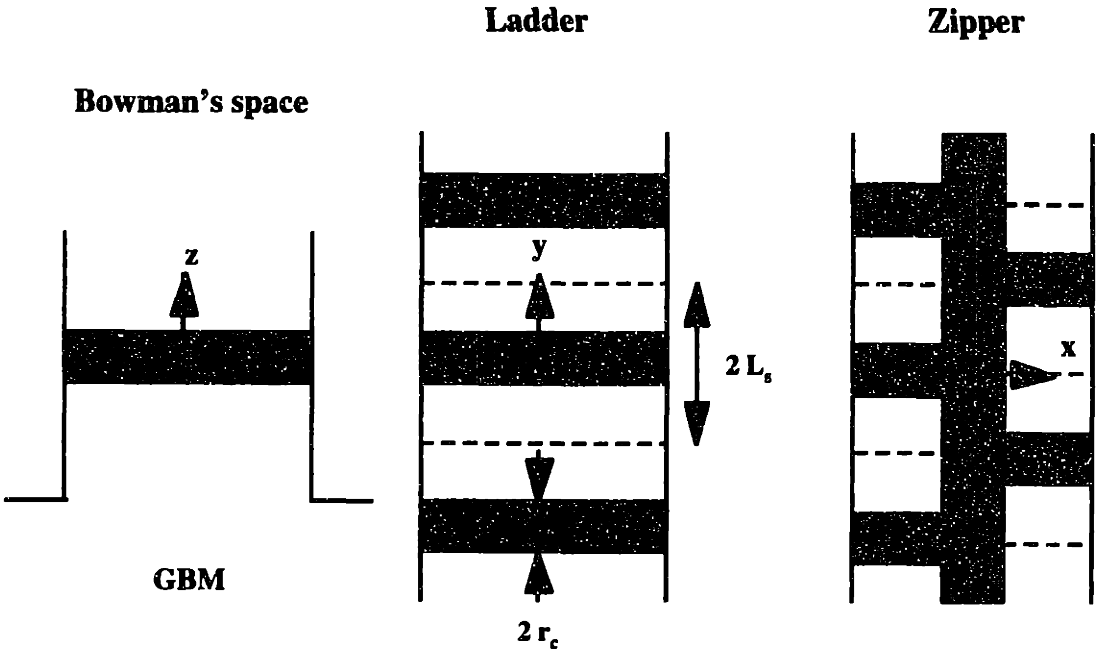
Ladder
Zipper
Bowman's space
z
GBM
y
2 L_s
2 r_c
x

Figure 4-2
Structure of the epithelial slit diaphragm. The direction of the flow is along the z-axis, as indicated by the arrow. The center and right panels are top views, corresponding to the ladder and zipper configuration of the diaphragm, respectively.

The fluid mechanics equations in the endothelial and epithelial layers are solved using the software package FIDAP (Fluid Dynamics International, Evanston, Illinois) which is based upon a Galerkin finite element method.

4.2.2 Endothelium

The fenestrae are assumed to be filled with fluid. Since the Reynolds number is very small under the conditions examined ($Re \sim 10^{-6}$), the Stokes and continuity equations can be used to determine the local pressure P and the velocity vector **V**:

$$\nabla P = \mu \nabla^2 \mathbf{V} \tag{4.3}$$

$$\nabla \bullet \mathbf{V} = 0 \tag{4.4}$$

where μ is the viscosity, and ∇ and ∇^2 are the gradient and Laplacian differential operators, respectively. The boundary conditions are described in detail by Drumond and Deen (1994a), and can be summarized as follows: fluid velocity is zero on all surfaces; at the entrance of the fenestrae, the radial and angular components of the fluid velocity are also equal to zero and the net pressure ($P_{GC} - \Pi_{GC}$), i.e., the difference between the hydraulic and the osmotic pressure in the capillary lumen, is imposed; at the interface between the fenestrae and the basement membrane, pressure and viscous stresses are matched.

The hydraulic permeability of the endothelium k_{en} is then given by:

$$k_{en} = \frac{J_v}{(P_{GC} - \Pi_{GC}) - P_0} = \frac{\varepsilon_f V_z}{(P_{GC} - \Pi_{GC}) - P_0} \tag{4.5}$$

where P_0 is the average pressure at the exit of the fenestra, V_z is the average fluid velocity in the z-direction (based on the cross-sectional area at $z = 0$) and ε_f is the fraction of the capillary surface covered by the fenestrae. Assuming that $r_f = 30$ nm (Kubosawa and Kondo, 1985) and that $\varepsilon_f = 0.2$ (Lea et al., 1989), Drumond and Deen (1994a) obtained $k_{en} = 2.0 \times 10^{-7}$ m/s/Pa.

As described below, the contribution of the endothelial layer to the overall resistance of the barrier to water flow is negligible. The case of fenestrae filled with a glycocalyx was also considered and led to similar conclusions.

4.2.3 Glomerular Basement Membrane

The glomerular basement membrane is considered as a porous medium, for which Darcy's law can be used to determine the flow:

$$\mathbf{V} = -\frac{K_{Darcy}}{\mu} \nabla P \qquad (4.6)$$

K_{Darcy} is the Darcy permeability of the GBM fibers. As described in Chapter 7, its value was determined from a series of filtration experiments with isolated fragments of glomerular basement membrane. The boundary conditions are:

$$\frac{\partial P}{\partial z} = 0 \qquad \text{at all the areas covered by the endothelium and epithelium} \qquad (4.7a)$$

$$\frac{\partial P}{\partial x} = 0 \qquad \text{at } x = 0 \text{ and } x = W/2 \text{ (symmetry in the x-direction)} \qquad (4.7b)$$

$$\frac{\partial P}{\partial y} = 0 \qquad \text{at } y = 0 \text{ and } y = L/2 \text{ (symmetry in the y-direction)} \qquad (4.7c)$$

In addition, at the endothelial and slit openings, one can specify either constant pressures, or constant velocities. These two assumptions are almost equivalent as shown by Drumond and

Deen (1994a). The authors also demonstrated that, with no significant effect on the results, the original three-dimensional domain can be transformed into a two-dimensional domain (Figure 4-3) by substituting for the circular openings of the fenestrae stripes of equivalent area. Using constant velocity boundary conditions, analytical expressions can then be obtained for P, **V** and the hydraulic permeability k_{gbm} of the GBM. k_{gbm} is given by:

$$k_{gbm} = \frac{J_v}{P_0 - P_l} \tag{4.8}$$

where P_l is the average pressure at the slit opening. The two-dimensional pressure field with constant velocity boundary conditions can be written as:

$$P = A - \frac{J_v \mu}{K_{Darcy}} \sum_{n=1}^{\infty} \left(\frac{\xi_n \cosh(\lambda_n z/W) - \gamma_n \sinh(\lambda_n z/W)}{\lambda_n \sinh(\lambda_n \delta_{gbm}/W)} \right) \cos(\lambda_n x/W) \tag{4.9}$$

where

$$\lambda_n = 2\pi \text{[illegible]} \tag{4.10a}$$

$$\xi_n = \frac{2 \sin(n\pi\varepsilon_s)}{n\pi\varepsilon_s} \tag{4.10b}$$

$$\gamma_n = \frac{1}{n\pi\varepsilon_f} \sum_{i=1}^{N_f} \left[\sin(\lambda_n x_{2i}/W) - \sin(\lambda_n x_{2i-1}/W) \right] \tag{4.10c}$$

A is a constant depending on P_0, and x_{2i-1} and x_i ($i = 1, .., N_f$) are the x-coordinates defining the positions of the fenestrae in a unit cell. The analytical expressions for the two components of the velocity vector **V** are then obtained by multiplying the gradient of P by ($-K_{Darcy}/\mu$), as shown by equation (4.6). The hydraulic permeability of the glomerular basement membrane is then given by:

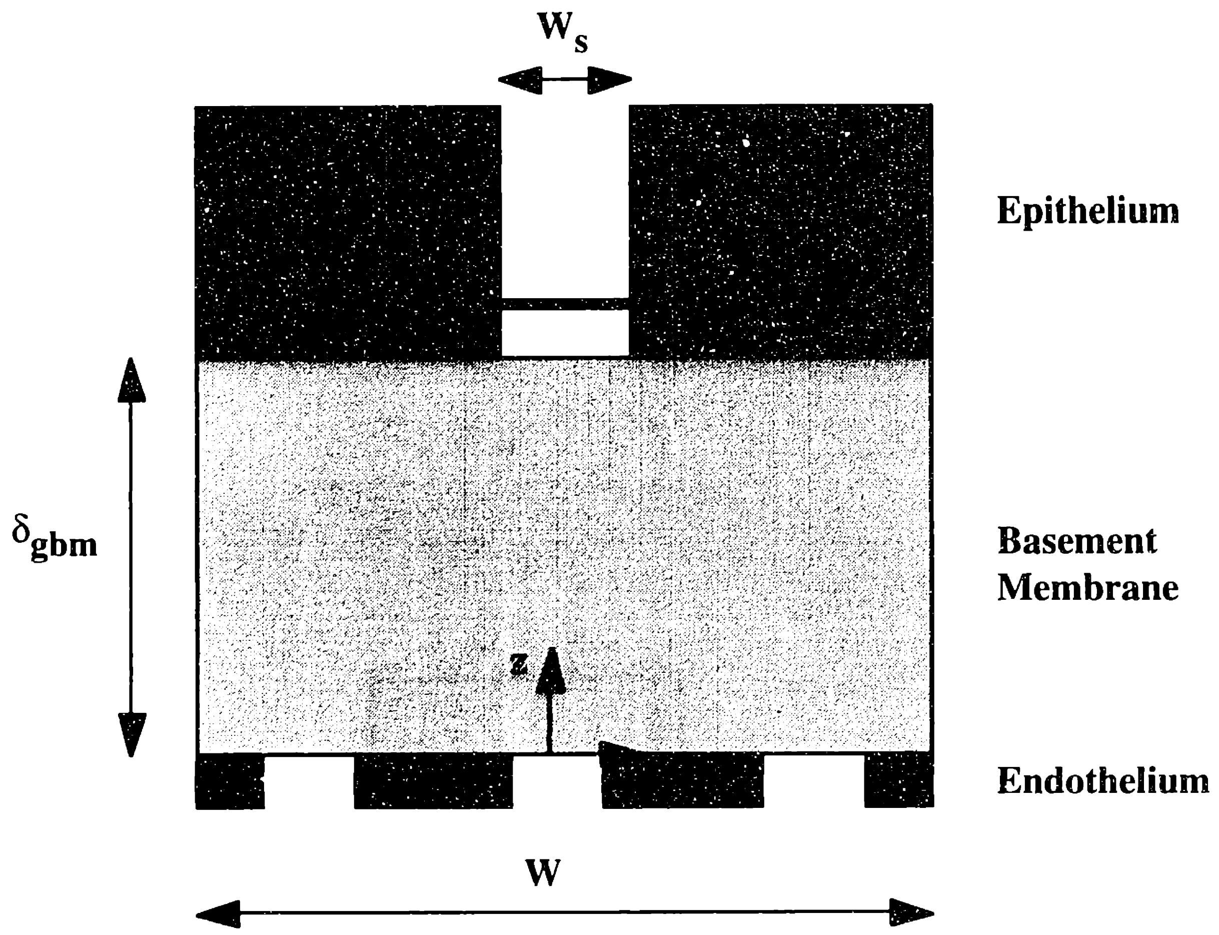
W_s
Epithelium
δ_{gbm}
Basement Membrane
z
Endothelium
W

Figure 4-3

Structural unit substituting stripes for the endothelial fenestrae

$$k_{gbm} = \frac{K_{Darcy}}{\mu W}\left[\frac{\delta_{gbm}}{W} + \sum_{n=1}^{\infty}\frac{\gamma_n^{\,2} + \xi_n^{\,2}}{2\,\lambda_n \tanh(\lambda_n \delta_{gbm}/W)}\right]^{-1} \tag{4.11}$$

Representative values for the ultrastructural parameters of the GBM are $W = 360$ nm, $L = 120$ nm, $\delta_{gbm} = 200$ nm, and $N_f = 3$ (Drumond and Deen, 1994a). Based upon the study of Daniels et al. (1992), the value of the Darcy permeability was estimated as 2.7 nm^2, yielding $k_{gbm} = 8.3\times10^{-9}$ m/s/Pa.

4.2.4 Epithelium

For the water flow model, both the ladder and the zipper configurations of the slit diaphragm were considered, and yielded very similar results. As in the endothelium, the local pressure P and fluid velocity **V** in the filtration slit can be obtained by solving Stokes and continuity equations:

$$\nabla P = \mu \nabla^2 \mathbf{V} \tag{4.12}$$

$$\nabla \bullet \mathbf{V} = 0 \tag{4.13}$$

The velocity should vanish on all solid surfaces; due to symmetry, we have:

$$V_y = 0 \text{ at } y = 0 \text{ and } y = L_s \tag{4.14a}$$

$$V_x = V_y = 0 \text{ at } z = 0 \tag{4.14b}$$

and for the ladder configuration, $V_x = 0$ at $x = 0$ (4.14c)

The boundary conditions upstream and downstream are based upon the assumption of unperturbed plane Poiseuille flow at a distance δ far enough from the cylinders:

$$V_z = \frac{3}{2} V_s \left[1 - \left(\frac{x}{W_s}\right)^2 \right], \; V_x = V_y = 0 \qquad \text{at } z = \pm\delta \qquad (4.14d)$$

where V_s is the average fluid velocity in the z-direction in the slit channel.

The hydraulic permeability of the epithelium k_{ep} is given by:

$$k_{ep} = \frac{J_v}{P_l - P_T} = \frac{\varepsilon_s V_s}{P_l - P_T} \qquad (4.15)$$

where P_T is the pressure in Bowman's space, and ε_s is the fraction of the capillary surface covered by the filtration slit. Rodewald and Karnovsky (1974) reported the following average measurements for the ultrastructural parameters: $r_b = 3.5$ nm, $r_c = 5.45$ nm, $L_s = 5.6$ nm, and $W_s = 19.7$ nm. Using these values, the hydraulic permeability k_{ep} is found to be equal to 8.6×10^{-9} m/s/Pa (Drumond and Deen, 1994b).

4.2.5 Comparison with Experimental Data

Combining all these results, the overall hydraulic permeability of the barrier is calculated to be 4.1×10^{-9} m/s/Pa. This predicted value is in excellent agreement with experimental measurements in normal adult Munich-Wistar rats, the observed range of k being $3\text{-}5 \times 10^{-9}$ m/s/Pa (Maddox et al, 1992; Pinnick and Savin, 1986). It appears thus that the contribution of the endothelium to the overall resistance to water flow across the glomerular capillary wall is negligible (~ 2%), and that those of the glomerular basement membrane and the epithelium are nearly similar (50 % and 48 %, respectively).

The ultrastructural model for water flow has also been very successfully applied to cases of glomerular diseases, both in humans and rats. Data for nephrotic rats reported in a study by Miller et al (1990) agreed very well with theoretical predictions based on the model (Drumond and Deen, 1994a). In another study of patients with miminal change or membranous nephropathies, the mean values of the experimental and theoretical hydraulic permeabilities were very similar (Drumond et al., 1994), thereby indicating that morphological changes such as a thickening of the basement membrane and/or a decrease in slit frequency are properly accounted for by the ultrastructural model.

4.3. Transport of Macromolecules Across the Epithelial Slit Diaphragm

4.3.1 Mathematical Model

Filtration of macromolecules across the epithelial layer can be modeled assuming that the slit diaphragm is formed by a row of infinitely long cylinders, that is, assuming the ladder configuration without taking into consideration the wall effects due to the podocytes. For this purpose, Drumond and Deen (1995) developed an approximate hydrodynamic model for rigid, non-interacting spherical particles of radius r_s moving with velocity **U** through a row of infinitely long cylinders of radius r_c; their approach is summarized here. As shown on Figure 4-4, L_s is the half distance between the centers of two adjacent cylinders. If **V** is the local velocity of the solvent, a force balance on a single particle yields:

$$-kT\nabla \ln C - 6\pi\mu r_s(\mathbf{f}\bullet\mathbf{U} - \mathbf{g}\bullet\mathbf{V}) = 0 \qquad (4.16)$$

where k is Boltmann's constant, T is the absolute temperature and C is the solute concentration. The first term in equation (4.16) represents the effective body force acting on the sphere, due to a gradient in chemical potential. This force is equal and opposite to the

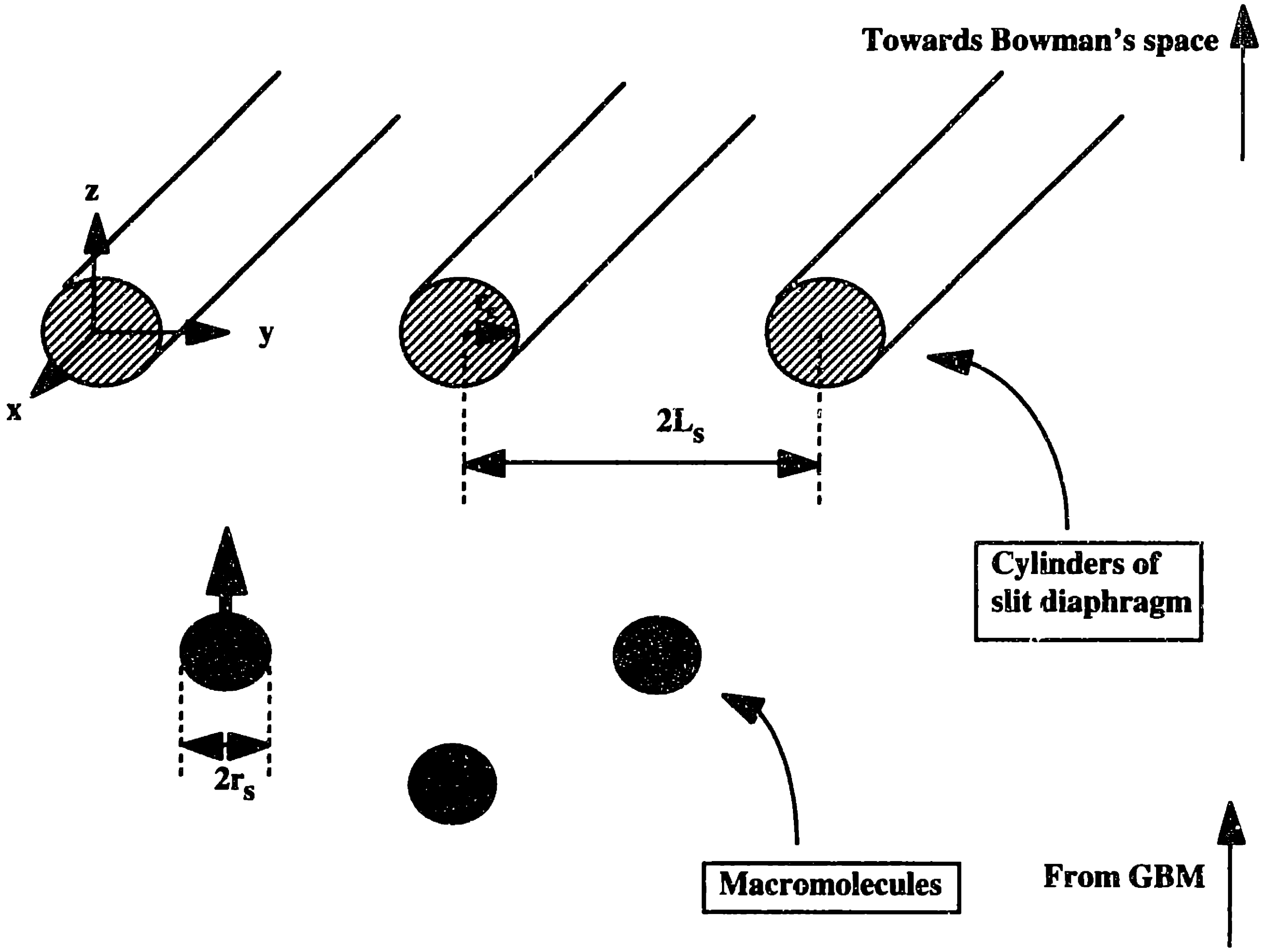
Towards Bowman's space
z
y
x
$2L_s$
Cylinders of slit diaphragm
$2r_s$
Macromolecules
From GBM

Figure 4-4
Idealized representation of the epithelial slit diaphragm for solute transport.
The direction of the flow is indicated by the thick arrow.

hydrodynamic force exerted on the particle, expressed by the second term. The tensors **f** and **g** account for translation of the sphere and flow past the sphere, respectively. The solute flux **N** can then be expressed by:

$$\mathbf{N} = \mathbf{U} C = - D_\infty \mathbf{d} \bullet \nabla C + \mathbf{h} \bullet \mathbf{V} C \qquad (4.17)$$

where D_∞ is the diffusivity of the solute in dilute bulk solution, and the tensors **d** and **h** are given by :

$$\mathbf{d} = \mathbf{f}^{-1} \qquad (4.18a)$$

$$\mathbf{h} = \mathbf{f}^{-1} \bullet \mathbf{g} \qquad (4.18b)$$

In addition, the solute conservation equation can be written as:

$$\nabla \bullet \mathbf{N} = 0 \qquad (4.19)$$

Combining equations (4-17) and (4-19), the steady-state concentration field in the slit is obtained by solving:

$$\nabla^* \bullet (- \mathbf{d} \bullet \nabla^* C + Pe_S \, \mathbf{h} \bullet \mathbf{V}^* C) = 0 \qquad (4.20)$$

where $\nabla^* = r_C \nabla$, $\mathbf{V}^* = \mathbf{V} / V_S$, V_S is the undisturbed fluid velocity far from the cylinders and Pe_S is a Peclet number based on the cylinder radius:

$$Pe_S = \frac{V_S \, r_C}{D_\infty} \qquad (4.21)$$

The boundary conditions are the following:

$$N_z = N_0 \qquad \text{at } z = -\delta \qquad (4.22a)$$

$$C = C_B = \frac{N_0}{V_s} \qquad \text{as } z \to \infty \qquad (4.22b)$$

$$N_y = 0 \qquad \text{at } y = 0 \text{ and } y = L_s \qquad (4.22c)$$

$$N_r = 0 \qquad \text{at } r = r_c + r_s \qquad (4.22d)$$

where δ is the distance from the basement membrane to the center of the cylinders, C_B the solute concentration in Bowman's space (i.e., downstream) and N_0 a specified constant flux. The fluid velocity field **V** is determined using Stokes and continuity equations, as shown above (equations 4.12, 4.13). Since the cylinders are assumed to be infinitely long in this configuration, the boundary conditions after adjustment become:

$$V_y = 0 \qquad \text{at } y = 0 \text{ and } y = L_s \qquad (4.23a)$$

$$V_y = 0 \qquad \text{at } z = -\delta \text{ and } z \to \infty \qquad (4.23b)$$

$$\mathbf{V} = \mathbf{0} \qquad \text{at } r = r_c \qquad (4.23c)$$

In the absence of theoretical results for the tensors **f** and **g** in that configuration, Drumond and Deen (1995) opted for an approximate approach, dividing the fluid domain into hydrodynamic regions of simple shape, for each of which existing results could be used to estimate **f** and **g**. Their method is outlined elsewhere (Drumond and Deen, 1995). The downstream boundary condition for both **V** and C was applied at a finite value of z, $z = \delta_1$, chosen large enough so that further increases would not affect the sieving coefficient (see equation 4.24 below). It was verified that $\delta_1 = 5L_s$ was sufficient for all cases.

Having thus determined solute concentration profiles, sieving coefficients for the slit diaphragm were computed as:

$$\Theta_{sd}^{loc} = \frac{C_B}{C_0} \tag{4.24}$$

where C_0 is the average concentration at $z = -\delta$, adjacent to the basement membrane. The subscript *loc* indicates that Θ_{sd} is a local quantity here, calculated on the basis of one unit cell. An approximate analytical relationship between Θ_{sd}^{loc} and its determinants was found to fit the data well and was used in all subsequent calculations:

$$\Theta_{sd}^{loc} = \frac{1 - \lambda}{1 - \lambda\left[1 - e^{-Pe_s\delta/r_c}\left(1 - e^{-APe_s}\right)\right]} \tag{4.25}$$

where

$$\lambda = \frac{r_s}{L_s - r_c} \tag{4.26a}$$

$$A = \frac{3.65}{r_c/L_s} + \frac{0.573}{1 - r_c/L_s} \tag{4.26b}$$

4.3.2 Distribution of Cylinder Spacings

The model presented above predicts a sharp cutoff in sieving curves for the filtration slit, as macromolecules larger than the gap between adjacent cylinders are expected not to be able to go through the slit diaphragm. However, whereas the average distance between cylinders reported by Rodewald and Karnovski (1974) is 40 Å, macromolecules of radius greater than 60 Å have been shown to cross the barrier (Oliver et al., 1992; Remuzzi et al., 1993). This result could be explained by the existence of inhomogeneities in the structure of the slit diaphragm, which recent electron microscopy data also indicate (Hora et al., 1990).

To account for such heterogeneities, Drumond and Deen (1995) assumed that the spacings between cylinders follow a continuous probability distribution. Defining u as the half-width of the gap between two neighbouring cylinders, that is, $u = L_s - r_c$, the average sieving coefficient for the slit diaphragm $\langle\Theta_{sd}\rangle^{loc}$ is then given by:

$$< \Theta_{sd} >^{loc} = \int_0^{\infty} \Theta_{sd}^{loc}(u)\, G(u)\, du \tag{4.27}$$

where G(u)du is the fraction of filtrate volume passing through gaps of half-width between u and u+du. The function G(u) is equal to the product of the probability function for the gap half-width, g(u), and the volume flow rate of filtrate q(u) passing through gaps of half-width u. Introducing the dimensionless hydraulic resistance f_T defined by Deen and Drumond (1994b) as:

$$f_T = \frac{L_s\, (\Delta P)_s}{\mu\, V_s} = \frac{(r_c + u)\, (\Delta P)_s}{\mu\, V_s} \tag{4.28}$$

where $(\Delta P)_s$ is the net pressure difference across the slit channel, the volume flow rate q(u), proportional to $L_s\, V_s$, can be written as:

$$q(u) = \frac{K_0}{\mu}\, (r_c + u)^2\, f_T^{-1}(u)\, (\Delta P)_s \tag{4.29}$$

where K_0 is a constant. Noting that $\int_0^{\infty} G(u)\, du = 1$, the function G(u) is therefore given by:

$$G(u) = \frac{g(u)\, (r_c + u)^2\, f_T^{-1}(u)}{\int_0^{\infty} g(u)\, (r_c + u)^2 f_T^{-1}(u)} \tag{4.30}$$

Approximate analytical expressions for the dimensionless hydraulic resistance $f_T = f_T\, (\delta/L_s,\ r_c/L_s,\ L_s/W_s)$were derived for the ladder configuration (Drumond and Deen, 1994b), and later extrapolated in order to be valid for the entire range of spacings and slit widths considered here (Drumond and Deen, 1995). The wall effects due to the podocytes, neglected in computing Θ_{sd}^{loc}, are nevertheless accounted for in the calculation of f_T. f_T can be expressed as the sum of the dimensionless Poiseuille flow resistance f_p ($f_p = 3\,\delta_T\,L_s/W_s^2$, where δ_T is the total length of the slit channel), and a dimensionless additional flow resistance f. Since the value of δ_T doesn't significantly affect the results, $\delta_T = \delta$ is used in the calculations. The results are repeated here for convenience. For $L_s/W_s >> 1$ and $r_c/L_s << 1$, it was shown that:

$$f = 3\left(\frac{L_s}{W_s}\right)^2 \left\{ \frac{1}{\sqrt{1 - (r_c/L_s)^2}}\left[\pi + 2\tan^{-1}\left(\frac{r_c/L_s}{\sqrt{1 - (r_c/L_s)^2}}\right)\right] - \pi \right\} - \frac{6\,L_s\,r_c}{W_s^2} \tag{4.31}$$

For $L_s/W_s \leq 4$ and $0.7 \leq r_c/L_s \leq 0.9$, we have:

$$f = A\,(1 - r_c/L_s)^B \tag{4.32a}$$

$$\log A = \log\left(\frac{9\pi}{4\sqrt{2}}\right) + 0.144\left(\frac{L_s}{W_s}\right) + 0.0111\left(\frac{L_s}{W_s}\right)^2 \tag{4.32b}$$

$$B = -2.5 + 0.110\left(\frac{L_s}{W_s}\right) + 0.00957\left(\frac{L_s}{W_s}\right)^2 \tag{4.32c}$$

For $L_s/W_s \leq 4$ and $0.1 \leq r_c/L_s \leq 0.7$, we have:

$$f = C + D\left(\frac{L_s}{W_s}\right) \tag{4.33a}$$

$$C = 0.336 + 2.74\left(\frac{r_c}{L_s}\right) - 2.74\left(\frac{r_c}{L_s}\right)^2 + 3.16\left(\frac{r_c}{L_s}\right)^3 \qquad (4.33b)$$

$$D = 0.0639 + 0.454\left(\frac{r_c}{L_s}\right) - 0.652\left(\frac{r_c}{L_s}\right)^2 + 0.512\left(\frac{r_c}{L_s}\right)^3 \qquad (4.33c)$$

For $L_s/W_s > 4$ or $r_c/L_s < 0.1$, f was given by a linear interpolation between the equations (4.32) and (4.33). The average hydraulic permeability $<k_s>$ is then given by:

$$< k_s > \; = \frac{< V_s >}{(\Delta P)_s} = \frac{\int_0^\infty (r_c + u)\, g(u)\, V_s\, du}{(\Delta P)_s \int_0^\infty (r_c + u)\, g(u)\, du} \qquad (4.34)$$

where $<V_s>$ is the mean filtrate velocity in the slit channel, averaged over all cylinder spacings. Combining equations (4.28) and (4.34), we obtain:

$$< k_s > \; = \frac{1}{\mu} \frac{\int_0^\infty (r_c + u)^2\, g(u)\, f_T^{-1}(u)\, du}{\int_0^\infty (r_c + u)^2\, g(u)\, du} \qquad (4.35)$$

Since the hydraulic permeability of the slit was determined previously (see paragraph 4.2.4), the value of $<k_s>$ is known in equation (4.35), and a constraint thereby imposed on the probability distribution function g(u). In the absence of quantitative data regarding structural heterogeneities in slit diaphragms, several choices can be made for g(u); the gamma and lognormal distributions appear to be reasonable options. In both cases g(u) is cen around a single value and vanishes as the gap half-width u goes to zero or to infinity. Both probability functions are defined by two parameters, one of which needs to be specified, the other one being implicity given by the relationship presented above.

The gamma distribution is given as:

$$g(u) = \frac{\exp\left[\gamma_1 \ln(\gamma_2) + (\gamma_1 - 1)\ln(u) - u\gamma_2\right]}{\Gamma(\gamma_1)} \tag{4.36}$$

where Γ is the gamma function. The mean and variance of g(u) are γ_1/γ_2 and γ_1/γ_2^2, respectively. With this choice for g(u), the denominator in equation (4.35) is equal to $r_c + \gamma_1/\gamma_2$. A possible choice for the parameter to be specified is $\gamma_1^{-1/2}$, i.e., the standard deviation divided by the mean. As described in Chapter 2, the lognormal distribution is defined by:

$$g(u) = \frac{1}{\sqrt{2\pi}\, u \ln(s)} \exp\left[-\frac{1}{2} \left(\frac{\ln(u) - \ln(\bar{u})}{\ln(s)} \right)^2 \right] \tag{4.37}$$

where $\bar{u}$ is the mean of the distribution, and ln(s) the standard deviation. In this case, the denominator of equation (4.35) is equal to $r_c + \bar{u} \exp(\ln^2(s)/2)$. As will be shown later in Chapter 8, the lognormal distribution yielded more consistent results than the gamma one. We chose s as the independent parameter, and $\bar{u}$ was calculated using equation (4.35), with $\langle k_s \rangle = k_{ep}/\varepsilon_s = 7.9\times10^{-8}$ m/s/Pa.

4.4 Conclusions

To complete this new approach to glomerular filtration, the model must be extended to account for the filtration of macromolecules across the two remaining layers, the glomerular basement membrane and the endothelium. Since the resistance of the latter is believed to be negligible, our main effort was to characterize the transport properties of the

GBM. In the absence of well established theories for hindered transport in random fibrous media, experiments were performed to obtain direct measurements of the permeability of isolated rat GBM to macromolecules. These studies are described in the following three chapters. In the first set of experiments, the diffusion of narrow fractions of Ficoll across isolated glomerular capillary wall and isolated GBM was assessed by confocal microscopy, and diffusive hindrance coefficients were thereby obtained. In the second set of measurements, isolated fragments of rat GBM were packed to form a uniform membrane in an ultrafiltration cell, and sieving coefficients of Ficoll were then determined. To interpret these results, the effects of concentration polarization have to be taken in consideration, which is the purpose of the preliminary study described in Chapter 5.

Chapter Five

Concentration Polarization in Ultrafiltration Studies

The permselective properties of the GBM were determined by performing two sets of experiments which are described in the following chapters. In particular, we studied the convection and diffusion of Ficoll across a membrane formed of packed isolated GBM fragments. Filtration studies require that the effects of concentration polarization next to the permeating membrane be taken into account. Because of significant uncertainties in literature data, our aim in the present chapter was to determine experimentally the value of the mass transfer coefficient in the filtration studies with Ficoll. For this purpose, we performed a parallel set of experiments, using a similar ultrafiltration cell, and maintaining identical flow rates and concentration levels. Based on our results, we then interpreted anew GBM permeability data published in the literature.

5.1 Background

Transport of a solute across a membrane is partially controlled by the concentration boundary layers adjacent to the membrane, which offer additional resistance to mass transfer. This effect can be minimized by increasing stirring next to the membrane, yet never entirely eliminated. In ultrafiltration, the solute concentration in the boundary layer rises exponentially from the bulk retentate towards the membrane, as shown in Figure 5-1. In this stagnant film model, the mass transfer coefficient k_S is equal to the ratio of D_∞, the solute diffusivity, over δ, the boundary layer thickness. The determinants of k_S in various systems have been widely investigated. Many early studies (Johnson and Huang, 1956; Marangozis and Johnson, 1961; Holmes et al.,1963; Scattergood and Lightfoot, 1968) were limited in scope and largely experimental in nature. The first extensive analysis was

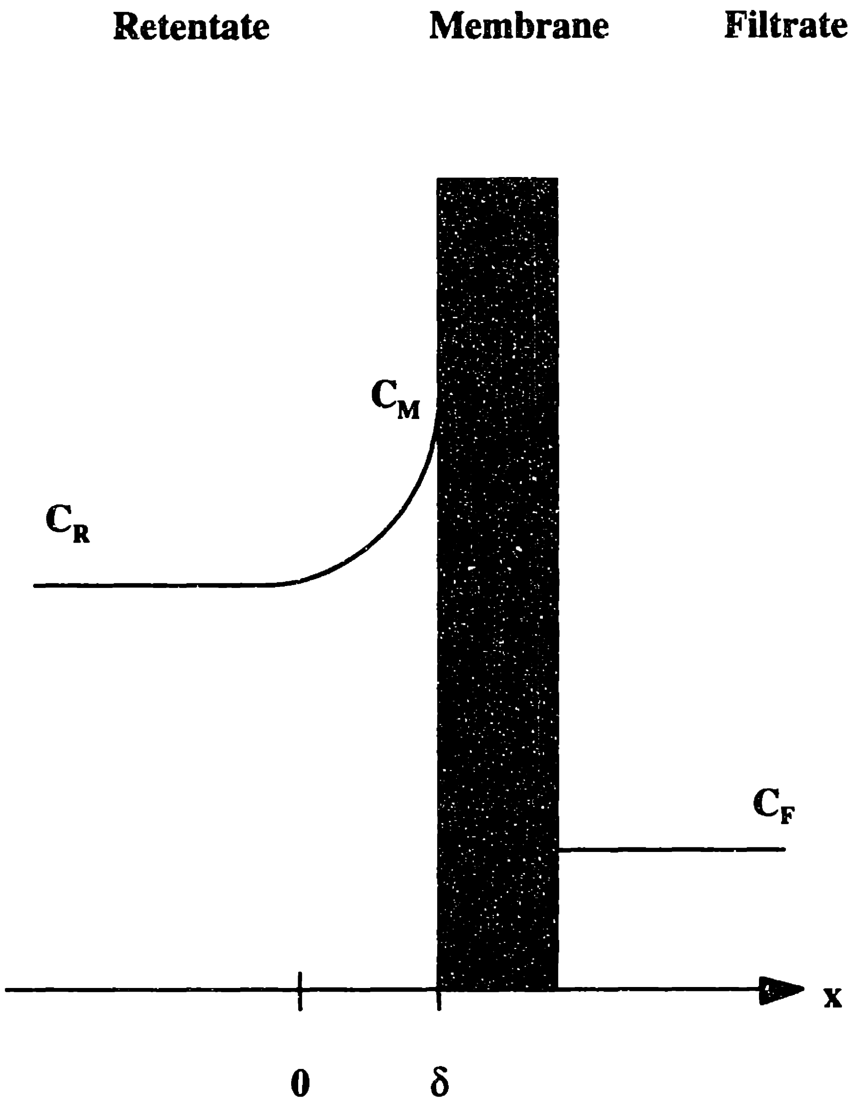
Retentate
Membrane
Filtrate
C_M
C_R
C_F
x
0
δ

Figure 5-1
Concentration polarization in an ultrafiltration cell. δ is the thickness of the boundary layer.

performed by Smith et al. (1968), who studied convective transport in an agitated batch dialyzer and proposed a correlation to estimate liquid-phase mass transfer coefficients. Colton and Smith (1972a,b) then studied both theoretically and experimentally mass transfer to the base of a cylindrical tank agitated by an axially-mounted impeller. In a first paper, they developed solutions for mass transfer between a fluid undergoing solid body rotation and a coaxial disk located on a stationary infinite surface. These results were then used in a second paper in conjunction with measurements of local mass transfer coefficients for benzoic acid in a diaphragm cell, and expressions for k_s in both laminar and turbulent regimes were derived. Defining γ as the dimensionless ratio of the angular velocity in the core above the stationary base to the impeller angular velocity, the authors derived the following asymptotic expression for the Sherwood number as the Schmidt number increases towards infinity:

$$Sh = \frac{k_s\, b}{D_\infty} = 0.768\, \gamma^{1/2}\, Sc^{1/3} Re^{1/2} \tag{5.1}$$

where $Re = \omega b^2/\nu$ and $Sc = \nu/D_\infty$, b being the tank radius, ω the stirring rate, and ν the kinematic viscosity. For laminar flow, a best fit of their experimental results to the theory yielded $\gamma = 0.49$. The data showed a dependence of Sh on $Re^{0.567}$, a result also obtained by Smith et al. (1968).

Malone and Anderson (1977) determined overall mass transfer coefficients for potassium chloride diffusion across track-etch membranes of uniform, low porosity. While their results showed a Sherwood number dependence on Re which agreed very well with the correlation of Colton and Smith (1972), the mass transfer coefficients that the authors measured were three times lower than those predicted by that correlation. It was not concluded whether these discrepancies were due to a slightly different cell design or to the heterogeneous nature of the membrane. Deen et al. (1981), in their study of the effects of molecular size and configuration on diffusion on microporous membrane, found mass transfer coefficients for sucrose and glucose about twice those predicted by that same correlation. Bohrer (1983) measured diffusional fluxes across well-characterized track-etch membranes, and observed a strong dependence of the diffusional boundary layer resistance on membrane porosity, the mass transfer coefficient varying by as much as a factor of 2. as the porosity changed. More recently, in a study of diffusive and convective protein transport through asymetric membranes using a 25-mm-diameter Amicon UF cell, Opong and Zydney (1991) obtained experimental values of the mass transfer coefficient and fitted to their data the expression first presented by Smith et al. (1968). The values they report are about 17% less than those predicted by the correlation. Finally, Juhasz and Deen (1991) showed in their analysis that the stagnant film model should be used with caution when using heterogeneous membranes with active areas, i.e., pores or active sites. When the Peclet number (based on the film thickness and maximum velocity) exceeds $10 \sim 10^2$, the convective interactions between these sites cannot be neglected.

All these studies underline the danger in extrapolating results of previous studies in order to calculate mass transfer coefficients for a specific system. For this reason, we opted for an experimental approach to determine the value of k_s in our filtration studies. The design of the experiments described below was analogous to that described later in Chapter 7; bovine serum albumin was filtered across a cellulose membrane, and we determined the solute concentration in the bulk retentate, the retentate adjacent to the membrane, and the filtrate in order to calculate the mass transfer coefficient.

5.2 Methods

All experiments were done using a 25-mm-diameter Amicon UF cell (Amicon Corporation, Danvers, MA). An applied pressure ranging from 25 to 75 mmHg was generated with compressed nitrogen, measured by a pressure transducer (Model DP15, Validyne Engineering, Northridge. CA), and modified by a pressure regulator. The stirrer, previously calibrated using a strobe light, was set at a rotational speed of 220 RPM. A 10,000 MW cut-off cellulose membrane (Millipore, Bedford, MA) was mounted in the stirred cell, allowing less than 3 % of albumin to be filtered. After a 10-min equilibration time, the filtration rate was evaluated by collecting filtrate for 10 minutes, the mass of which (on the order of 0.05 g) was then determined using a digital balance. A 3 ml volume of NaCl solution (0.15 M, ph = 7.40) were first added to the cell, and the hydraulic permeability of the membrane determined. The cell was then rinsed, and filled anew with 3 ml of bovine serum albumin (BSA, Sigma Chemical Company, St-Louis, Missouri) suspended in NaCl buffer at a concentration of 4 g/dl. After a 10 minute equilibration period, the filtrate was collected for 10 minutes. The retentate was sampled at the start and completion of the collection period. BSA concentration in the bulk retentate and in the filtrate was measured by spectrophotometry (Shimadzu, Columbia, Maryland), at a wavelength of 280 nm. This procedure was followed by another measurement of the membrane hydraulic permeability with NaCl solution only. Only if it differed by less than 5% from the value determined at the start of the experimental run were the results taken into account. All experiments were conducted at room temperature (21°C).

Statistics

Results are given as mean ± SE. For group comparisons, t tests were performed to determine significance. $P < 0.05$ was considered to be significant.

5.3 Calculations

5.3.1 Sieving Coefficients

The measured sieving coefficient (Θ') of a macromolecule is given by :

$$\Theta' = \frac{C_F}{C_R} \tag{5.2}$$

where C_F and C_R are the solute concentration in the filtrate and in the bulk retentate respectively, as shown in Figure 5-1. The true membrane sieving coefficient (Θ) is defined as :

$$\Theta = \frac{C_F}{C_M} \tag{5.3}$$

where C_M is the solute concentration on the retentate side immediately adjacent to the membrane surface. Because of concentration polarization at the membrane surface, $C_M \geq C_R$, or $\Theta \leq \Theta'$. At steady-state, the solute flux J_s in the solution is given by :

$$J_s = -D \frac{\partial C}{\partial x} + J_v C \tag{5.4}$$

where J_v is the filtration rate, and D the solute diffusivity, assumed here to be equal to its value in dilute bulk solution, D_∞. Under steady state conditions, solvent and solute fluxes are constant across the membrane, and equation (5.4) can be integrated to determine the concentration profile of the solute, using the ultrafiltration boundary condition :

$$J_s = C_F J_v \tag{5.5}$$

As $C(x = 0) = C_M$, we find that :

$$\frac{C_M}{C_R} = (1 - \Theta')\,B + \Theta' \tag{5.6}$$

where

$$B = \exp(J_v/k_s) \tag{5.7}$$

As defined above, the mass transfer coefficient k_s is equal to D/δ, where δ is the boundary layer thickness. The relationship between Θ and Θ' can then be obtained by rearranging equation (5.6) :

$$\Theta = \frac{\Theta'}{(1-\Theta')\,B + \Theta'} \tag{5.8}$$

5.3.2 Mass Transfer Coefficient

When albumin is the only osmotically active solute, the hydraulic permeability L_p of the membrane is related to the filtration rate J_v by Starling's equation :

$$J_v = L_p\,(\,\Delta P - \sigma_{alb}\Delta\Pi_{alb}\,) \tag{5.9}$$

where ΔP is the transmembrane hydraulic pressure difference, and σ_{alb} and $\Delta\Pi_{alb}$ the reflection coefficient and oncotic pressure difference, respectively, for albumin. We assumed that $\sigma_{alb} \approx 1 - \Theta_{alb}$. To obtain ΔP, the hydrostatic pressure was substracted from the value given by the pressure transducer. The contribution of capillary pressure was calculated to be negligible. We first determined the hydraulic permeability of the membrane, in the absence of albumin, when L_p is simply the ratio of J_v over ΔP.

In the presence of albumin, equation (5.9) yields the product $(1-\Theta_{alb})\Delta\Pi_{alb}$, all other quantities being measured or known. To determine the albumin concentration C_M at the membrane on the retentate side, we used the semi-empirical correlation developped by Vilker et al. (1981), relating albumin osmotic pressure to albumin concentration :

$$\Pi_{alb} = RT\,\{\,2\,[\,(\frac{ZC_{alb}}{2M_{alb}})^2 + m_s^2\,]^{1/2} - 2m_s\,\} + \frac{RT}{M_{alb}}\,(\,C_{alb} + A_2C_{alb}^2 + A_3C_{alb}^3\,) \tag{5.10}$$

where M_{alb} is the molecular weight of albumin, C_{alb} its concentration in g/l, and m_s the molar salt concentration. At pH = 7.40, under the conditions described above, we have $A_2 = -1.089\text{x}10^{-2}$ and $A_3 = 1.243\text{x}10^{-4}$. $\Delta\Pi_{alb}$ and Θ_{alb} (or equivalently, $C_M = C_F/\Theta_{alb}$) were calculated by an iterative procedure, solving simultaneously equations (5.9) and (5.10), taking $\Theta'_{alb} = C_F/C_R$ as a first approximation for Θ_{alb}. Rearranging equation (5.8), the polarization factor B is given by

$$B = \frac{C_M - C_F}{C_R - C_F} \tag{5.11}$$

and the mass transfer coefficient k_s for albumin under these experimental conditions thus determined.

5.4 Results

In order to interpret in vitro Ficoll sieving data, the mass transfer coefficient of each Ficoll fraction has to be determined. The experiments with BSA in NaCl solution were done using a filtration cell identical to that used in the Ficoll studies, at the same stirring rate of 220 RPM, with the same initial BSA concentration of 4 g/dl, and adjusting the pressure to obtain similar volume fluxes. Under these conditions, the mass transfer coefficient of BSA was found to be equal to $2.00\text{x}10^{-4} \pm 0.05$ cm/s (n = 16), at 21°C, for an averaged volume flux of $1.20\text{x}10^{-4}$ cm/s. The results are illustrated on Figure 5-2.

The value of the mass tranfer coefficient at 27°C, the temperature at which the Ficoll studies were performed, for albumin or any Ficoll fraction of a given Stokes-Einstein radius, can be obtained by using the theoretical expression of Colton and Smith (1972), which yields :

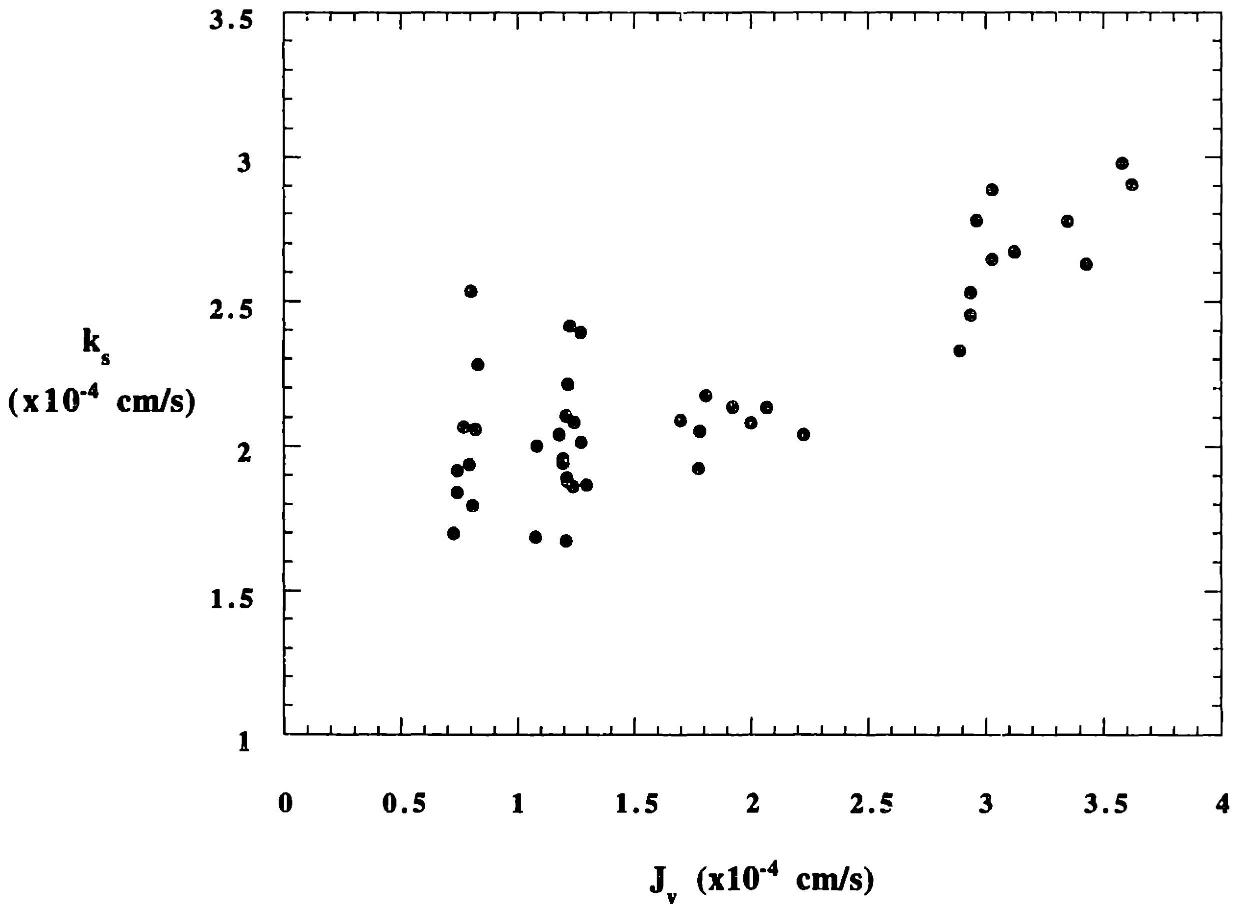

Figure 5-2
Mass transfer coefficient of albumin at 21°C versus volume flux

$$k_s \ \alpha \ \omega^{1/2} \, \nu^{1/6} \, D_\infty^{2/3} \tag{5.12}$$

It was thus calculated that $k_s^{alb} = 2.28 \times 10^{-4}$ cm/s at 27°C.

We also performed similar measurements of k_S on a wider range of filtration rates, to gain additional insight into the determinants of k_S. The value of the mass transfer coefficient should be independent of the filtration rate, as shown by equation (5.12). Shown on Figure 5-2 and Table 5-1 are results obtained for J_V ranging from 0.72×10^{-4} cm/s to 3.7×10^{-4} cm/s. Four groups were distinguished: J_V was comprised between 7.2×10^{-5} and 8.3×10^{-5} cm/s, 1.0×10^{-4} and 1.3×10^{-4} cm/s, 1.7×10^{-4} and 2.3×10^{-4} cm/s, and 2.8×10^{-4} and 3.7×10^{-4} cm/s, in groups 1, 2, 3 and 4, respectively. As expected, we found no significant difference in the value of the mass transfer coefficient between groups 1, 2 and 3. There is however a significant difference between the values of k_S reported for each of these three groups and that of the fourth one, but the reason for this phenomenon is not well understood.

Table 5-1

Mass transfer coefficient of albumin at 21°C

n	flow rate Q (ml/h)	J_V (10^{-4} cm/s)	k_S (10^{-4} cm/s)
9	0.318 ± .005	0.78 ± 0.01	2.01 ± 0.09*
16	0.492 ± .006	1.21 ± 0.01	2.00 ± 0.05
8	0.718 ± .026	1.76 ± 0.06	2.08 ±0.03*
11	1.291 ± .033	3.17 ± 0.08	2.69 ± 0.06†

Values are mean ± SE. The baseline case of corresponds to an average flow rate of 0.492 ml/h.* $P > 0.05$ vs. baseline. † $P < 0.05$ vs.baseline.

5.5 Discussion

Daniels et al. (1992) performed in vitro studies of water and protein permeability of the glomerular basement membrane by consolidating isolated cell-free glomeruli in an ultrafiltration cell identical to the one we used, and measuring fluxes across the membrane following a protocol similar to that described above. In their study, the value of the mass transfer coefficient was estimated from the correlation of Colton and Smith (1972b) as 4.34×10^{-4} cm/s at 25°C, i.e., twice the value that we determined here (2.18×10^{-4} cm/s at 25°C). We therefore interpreted their data anew based on our results for k_s.

We first calculated again the hydraulic permeability of the GBM membrane as a function of the transmembrane pressure ΔP, in the presence of 4 g/dl of albumin in the buffer. The results are summarized in Table 5-2, and do not differ significantly from those reported by Daniels et al. (1992, Table 1). As illustrated, the effects of ΔP on the membrane hydraulic permeability are very important: L_p decreases by a factor 2.5 when ΔP is increased from 50 to 150 mmHg.

Table 5-2

Effect of transmembrane pressure on the permeability of GBM filters at 4 g/dl albumin

ΔP (mmHg)	L_p (10^{-6} cm.s^{-1}.mmHg^{-1})	
	$k_s = 2.18 \times 10^{-4}$ cm/s (present results)	$k_s = 4.34 \times 10^{-4}$ cm/s (Daniels et al., 1992)
50	4.16 ± 0.52	4.61 ± 0.49
150	1.69 ± 0.08†	1.45 ± 0.03†

Values are mean ± SE. † $P < 0.05$ vs. 50 mmHg.

We then determined the effect of albumin concentration on L_p at $\Delta P = 50$ mmHg. As shown in Table 5-3, there was no significant difference in the permeability of the membrane when the albumin concentration was increased from 0 to 4 g/dl ($4.24\text{x}10^{-6}$ vs. $4.59\text{x}10^{-6}$ $\text{cm.s}^{-1}.\text{mmHg}^{-1}$). The data obtained at a concentration of 8 g/dl were not all consistent, sometimes yielding negative values of L_p, and are not reported here.

Combining the results of Tables 5-2 and 5-3, the averaged hydraulic permeability of the GBM filters at $\Delta P = 50$ mmHg and $C_{alb} = 4$ g/dl was estimated as $L_p^{25^\circ} = 4.38\text{x}10^{-6}$ $\text{cm.s}^{-1}.\text{mmHg}^{-1}$. The Darcy permeability of the glomerular basement membrane at 37°C, $\Delta P = 50$ mmHg, and $C_{alb} = 4$ g/dl was then calculated as:

$$K_{Darcy} = L_p^{37^\circ} \mu^{37^\circ} L = L_p^{25^\circ} \mu^{25^\circ} L \tag{5.13}$$

where L is the thickness of the membrane, which was estimated as 8.8 μm. We thus obtained the following estimate: $K_{Darcy} = 2.57\text{x}10^{-18}\ \text{m}^2 = 2.6\ \text{nm}^2$. This value differs very little from the estimate of 2.7 nm^2 used by Drumond and Deen (1994a), and does not change significantly the relative hydraulic resistances of the three layers of the glomerular capillary wall, as shown in Table 5-4.

These Darcy permeability values differ however significantly from those which we obtained in experiments analogous to those of Daniels et al. (1992), as will be described later in Chapter 7. Based on our measurements, we estimated K_{Darcy} as 1.48 and 0.82 nm^2 at $\Delta P = 35$ and 60 mmHg, respectively, yielding a value of 1.08 nm^2 at $\Delta P = 50$ mmHg by linear intrapolation. The reason for this discrepancy is not clear. It is possible that the estimate of $L = 8.8$ μm in the study of Daniels et al. (1992) is too high, since the membrane thickness was not measured systematically, nor was it corrected to account for deformation under pressure. However the values of L_p in the study of Daniels et al. (1992) were also significantly higher than those we measured in our experiments, and uncertainties in L cannot account entirely for the discrepancy.

The in vivo conditions are best approximated by ΔP = 35 mmHg, and we recommend for the Darcy permeability under typical conditions a baseline value of 1.48 nm^2, based on the data presented in Chapter 7. This value seems preferable over the one obtained from the study of Daniels et al. (1992) because more attention was paid to determining the thickness of each membrane. From this estimate, we calculated again the relative hydraulic resistances of the three layers. The results are shown in Table 5-4. Since the hydraulic permeability of the GBM is lowered by a factor 1.7, the relative resistance of the GBM is now almost twice that of the epithelial layer, while the calculated permeability of the capillary wall is at the lower end of the experimental range (~ 3-5 $x10^{-9}$ $m.s^{-1}.Pa^{-1}$, as reviewed in Chapter 4).

5.6 Conclusions

Our conclusions are different than those reached previously in two respects. Firstly, our results indicate that there is no significant difference between the hydraulic permeability of the GBM in the presence of 0 and 4 g/dl albumin, respectively, whereas Daniels et al. (1992, Table 3) had observed a biphasic relationship, with L_p significantly lower at 4 g/dl than at either 0 or 8 g/dl albumin. The conclusion attained here justifies one aspect of the experimental protocols described in the following two chapters. In diffusion experiments across isolated glomerular capillary wall and GBM (Chapter 6), no albumin was present in the solution in order to preserve cell viability, while the buffer in filtration experiments across isolated GBM (Chapter 7) contained 4 g/dl to simulate normal physiological conditions.

In addition, we estimated the hydraulic resistance of the GBM to be twice that of the epithelial layer, as opposed to equivalent to it (Drumond and Deen, 1994a). These results should be accounted for in determining the in vivo ultrafiltration coefficient of the barrier.

Table 5-3

Effects of albumin concentration on L_p at $\Delta P = 50$ mmHg

C_{alb} (g/dl)	L_p (10^{-6} cm.s^{-1}.mmHg^{-1})
0	4.24 ± 0.46
4	4.59 + 0.74*

Values are mean ± SE. * $P > 0.05$ vs. 0 g/dl.

Table 5.4

Hydraulic resistance of the capillary wall

	Drumond and Deen (1994a)	$K_{Darcy} = 2.56$ nm^2 (Daniels et al., 1992)	$K_{Darcy} = 1.48$ nm^2 (Chapter 7)
k (m.s^{-1}.Pa^{-1})	$4.1\text{x}10^{-9}$	$4.1\text{x}10^{-9}$	$2.9\text{x}10^{-9}$
% resistance endothelium	2.1	2.0	1.5
% resistance GBM	49.8	50.8	64.4
% resistance epithelium	48.1	47.2	34.1

Chapter Six

Hindered Diffusion of Macromolecules across Isolated Glomerular Basement Membrane and Glomerular Capillary Wall

6.1 Introduction

We first determined the diffusional resistance of the GBM in a series of experiments whereby the diffusion of Ficoll across isolated rat GBM was assessed by confocal microscopy. In an effort to better characterize the epithelial slit diaphragm, we also measured Ficoll diffusion rates across isolated intact capillary wall and developed a model to interpret the results. These measurements enabled us in addition to estimate the relative contribution of each layer to the overall permeability properties of the glomerular capillary wall.

The relative resistance of the GBM and the cell layers has been an open question for many years. While some authors have emphasized the importance of the glomerular basement membrane (GBM) in restricting solute transport (Farquhar et al., 1961; Rennke et al., 1975; Kanwar, 1984), others have remained more skeptical (Bray and Robinson, 1984; Daniels et al., 1992). Since all these studies were based either on the localization of electron dense tracers within the GBM in fixed tissues or on permeability measurements of GBM, they did not allow for a quantitative assessment of the role of each layer.

Daniels et al. (1993) developed a new technique to isolate rat glomeruli and glomerular basement membrane, and measured the diffusion rate of dextran from the capillary lumen with confocal microscopy. While their study showed an important effect of the cells in the overall resistance to solute transport, the results were difficult to interpret quantitatively, due to the non-ideal behavior of the tracer and the fact that a polydisperse sample was used. In the present study, we used their method to determine the diffusion rates of narrow fractions of Ficoll across intact or denuded glomeruli. Four narrow fractions of Ficoll were labeled with fluorescein, the diffusion of the macromolecules across isolated rat glomerular capillary wall and glomerular basement membrane (GBM) was assessed by confocal microscopy, and mass transfer coefficients were obtained from the experimental data. The results were then interpreted using a theoretical model for diffusion across each layer of the filtration barrier.

6.2 Methods

Preparation of Glomeruli

Adult male Sprague-Dawley rats weighing ~ 350 g were anesthetized with Inactin (100 mg/Kg body weight) and kidneys were perfused in situ at 110 mmHg with modified Eagle's medium (pH 7.4) to remove blood. The perfusion was completed within 10 s. The cortex was diced into 1 mm^3 bits and passed sequentially through 250, 150 and 75-mm pore size nylon filters to isolate glomeruli. The isolation procedure was performed on ice in the presence of buffer with 5 mM pyruvate, 5 mM butyrate, and 1 mM alanine. As revealed by light microscopy, the resulting glomerular preparation contained >95% glomeruli and <5% tubular fragments. Over 95 % of the glomeruli were devoid of Bowman's capsule and arterioles.

Diffusion studies were performed using both intact glomeruli and glomeruli from which the cells had been removed. Acellular glomeruli were prepared by incubating glomeruli with N-lauryl sarcosine to remove cells and DNAse to remove nucleoprotein, as described previously (Ligler and Robinson, 1977; Daniels et al., 1992). The resulting glomerular skeletons maintained the general shape of the glomerulus, and were composed predominantly of GBM, with a few areas of residual mesangial matrix. Immunofluorescence microscopy of GBM obtained in that manner shows the presence of laminin, type IV collagen and heparan sulfate proteoglycan (Daniels et al., 1992).

Confocal Microscopy Apparatus

Diffusional permeabilities of intact or cell-free capillary loops to fluorescein-labeled macromolecules were measured using the confocal microscopy apparatus described by Daniels et al. (1993). Briefly, a fluorescent cell analysis system (model ACAS 570; Meridian Instruments Inc., Okemos, MI) modified by the cell manufacturer for confocal microscopy was used. A 5-W Argon laser (Coherent Inova 90-5) was the source for fluorescence excitation. An Olympus epifluorescence inverted microscope was equipped with a precision gear to provide measured alteration in the vertical axis. Either phase contrast or fluorescent images could be obtained. A pinhole limited the entrance of light to the photodetector to that originating from within the plane of focus and was adjustable to facilitate variations of optical section thickness. For these studies, a pinhole of 225 μm was used to produce a section thickness of about 1 μm. A 28-μm line was scanned at a step size of 0.4 μm, a peak velocity of 0.4 mm/s, using a laser power of approximately 3 mW. Each point was sampled 8 times, the first time for 8 μs and subsequent samplings for 4 μs so that the total laser exposure time was 36 μs. Approximately 30 % of the laser power is present in the 488-nm line (the excitation length used) so that about 0.9 mW of laser power was transmitted to the sample. All laser parameters were set to limit photobleaching to less than 5% loss of the initial fluorescence per 100 scans. Images were stored digitally on Bernoulli disks and subsequently analyzed with image analysis software integral to the ACAS system.

Macromolecules

Four narrow fractions of Ficoll, with Stokes Einstein radii (r_S) of 3.0, 3.8, 4.8 and 6.2 nm were obtained by special order from Pharmacia LKB (Piscataway, NJ). These samples were labeled with fluorescein and characterized as described previously (Johnson et al., 1996). The values of the polydispersity index (ratio of weight-average to number-average molecular weight) ranged from 1.13 to 1.22, as determined by the manufacturer. The number of fluorescein molecules per Ficoll molecule was estimated to be less than 3, so that the net molecular charge resulting from the fluorescein label was assumed to be negligible.

Permeability Measurements

Diffusional permeabilities were measured using the procedure described by Daniels et al (1993). Intact or acellular glomeruli were incubated at 27°C for 20 min in a buffer solution containing 2 g/ml of one of the fluorescent-Ficoll fractions. The buffer consisted of DME (25 mM Hepes) buffer with 5 mM butyrate, 5 mM alanine and 5 mM pyruvate substituted for equimolar NaCl. This resulted in diffusional equilibration of Ficoll between the bath and the capillary lumen. Glomeruli were then placed in a coverglass chamber (Nunc Inc., Naperville, IL) and immobilized with weighted nylon mesh to minimize movement during the scans. A longitudinal section of glomerular capillary without an overlying epithelial cell body was located by phase contrast microscopy and a plane of focus through the maximal diameter of the capillary was selected for ease in repeated identification of the original place of focus. An initial fluorescent scan was then obtained to quantitate intracapillary fluorescence. The background fluorescence was rapidly decreased by diluting the bathing fluid with Ficoll-free buffer; this resulted in a 75% decrease in bath fluorescence over 2 s. Although the change in bath concentration required only a few seconds, the first scan was delayed by up to 120 s to confirm the original plane of focus. Since the diffusion of Ficoll was very rapid across acellular glomeruli, only glomeruli that did not move were used. The decline in fluorescence within the capillary was assessed by obtaining confocal images every 20-40 s. The bath fluorescence usually remained constant because of its large volume relative to intraglomerular or intracapillary volume. The lumen and the bath were characterized by the mean pixel fluorescence for a 5 and 17 μm line, respectively, typically separated by a distance of 7 μm. The number of experiments performed for each of the 8 combinations of molecular size and barrier type ranged from 7 to 11.

The capillary lumen and the bath (corresponding to Bowman's space in vivo) were assumed to be well-mixed compartments separated by a membrane of surface area A. Because the bath concentration (C_B) remained constant during the period of observation, the mass-balance equation governing the concentration in the lumen (C_L) is:

$$\frac{dC_L}{dt} = - k_s \frac{A}{V_L} (C_L - C_B) \tag{6.1}$$

where V_L is the volume of the luminal compartment, and k_s is the diffusional permeability of the intact or acellular capillary wall for the test solute ($k_s=k_s^{wall}$ and $k=k_s^{bare}$, respectively). For a capillary segment of radius R and length L, the surface-to-volume ratio $A/V_L = 2/R$. Integration of equation (6.1) gives:

$$\ln \left(\frac{C_L(t) - C_B}{C_L(0) - C_B} \right) = - \frac{2 k_s t}{R} \tag{6.2}$$

The value of k_s/R was obtained from the slope of a semilogarithmic plot of the bracketed concentration ratio versus time. The capillary radius R was determined using the image software analysis integral to the ACAS system, allowing calculation of k_s. The change in fluorescence in the lumen and in the bath as the macromolecules diffuse across the barrier is shown in Figure 6-1 for a representative glomerulus.

The measurements were done in the laboratory of Dr. Barbara S. Daniels at the University of Minnesota with the technical assistance of Michael Ahlquist. We prepared and provided the narrow fractions of fluorescein-labeled Ficoll.

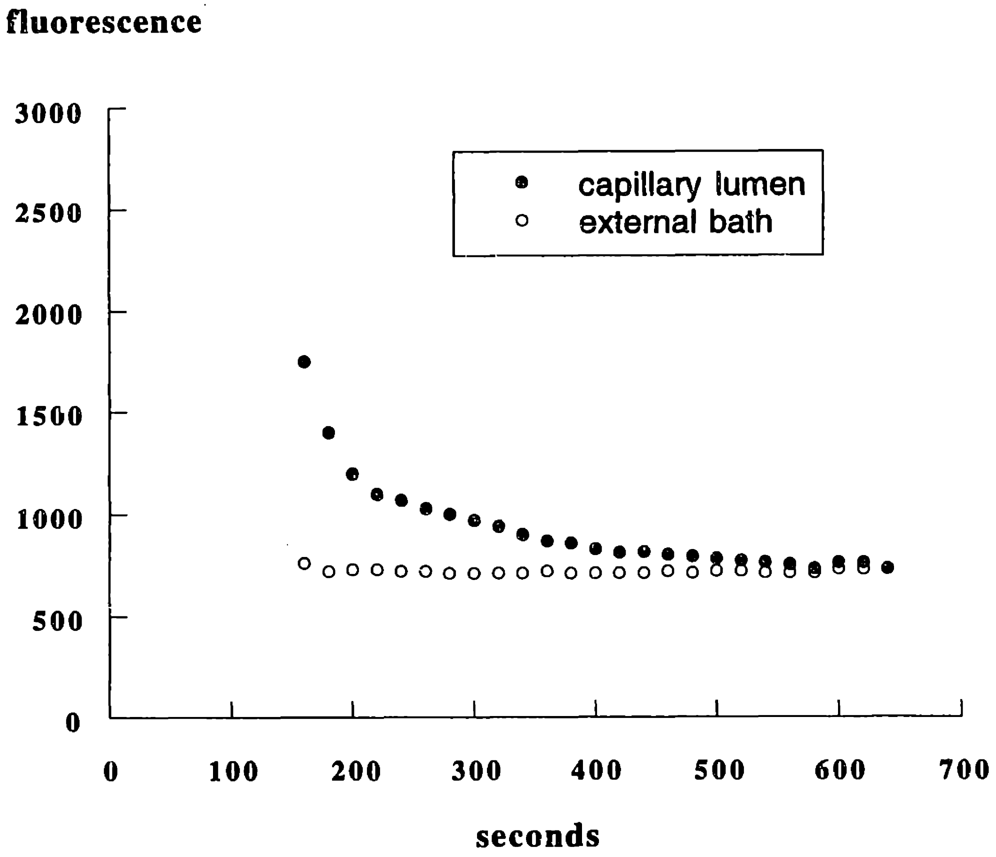

Figure 6-1

Fluorescence in the capillary lumen and in the bath as a function of time. The exponential decline of concentration in the lumen as fluorescein-labeled Ficoll diffuses out is apparent.

In order to justify the assumption that the concentration in the bath is uniform, we computed the corresponding Biot number, i.e., the bath-to-wall resistance to mass transfer ratio, given as $\mathrm{Bi} = k_s^{\mathrm{wall}} L_B / D_\infty$, where L_B is a characteristic dimension for the bath. Since the mean pixel fluorescence in the bath is calculated over a distance $L_B = 17$ μm, the upper limit on Bi was estimated as 0.043, thereby confirming the validity of our assumption.

6.3 Results

The Ficoll permeabilities measured for the intact capillary wall (k_s^{wall}) and the acellular capillary (k_s^{bare}) are shown in Figure 6-2 and Table 6-1. As expected, both k_s^{wall} and k_s^{bare} were found to decrease with increases in solute size. Moreover, for any given solute size, k_s^{bare} greatly exceeded k_s^{wall}.

An assessment of the relative contribution of the cells and the GBM to the overall diffusional resistance of the capillary wall requires that account be taken of the fact that, in the intact capillary wall, most of the surface of the GBM is covered by cells. The exposed areas on the luminal and the Bowman's space sides correspond to the endothelial fenestrae and epithelial filtration slits, respectively. The blockage of most of the GBM surface by cells results in tortuous rather than straight diffusion paths across the GBM, which tends to increase the concentration drop across this layer. Thus, an indirect effect of the cell layers is to make the apparent diffusional resistance of GBM in the intact capillary wall greater than that for bare GBM. To determine the apparent permeability of the GBM within the intact capillary (k_s^{gbm}), we used the following approach.

The GBM was modeled as a homogeneous, isotropic material. Accordingly, for the pseudo-steady state conditions of our experiments, the concentration C of any solute was assumed to be governed by Laplace's equation:

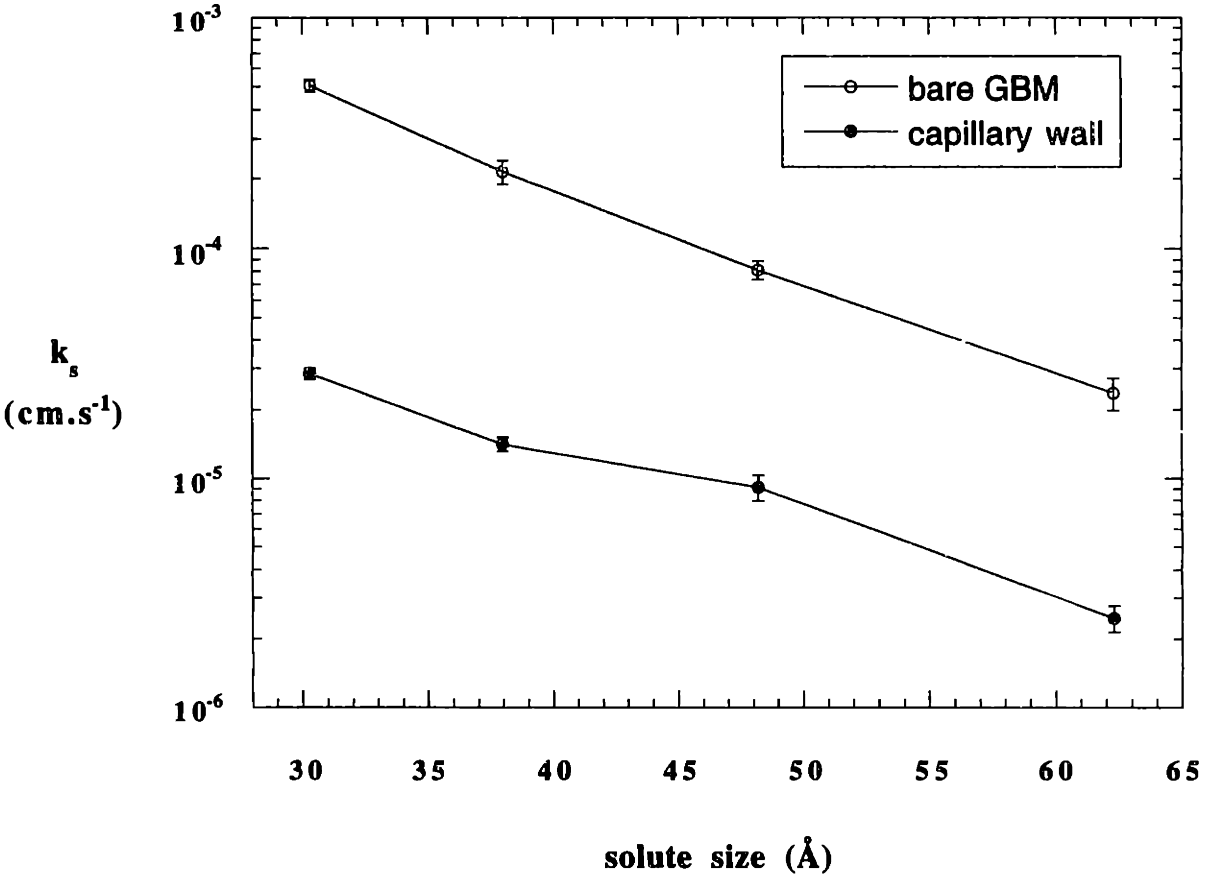

Figure 6-2
Mass transfer coefficient for the isolated capillary wall (k_S^{gcw}) and bare GBM (k_S^{bare}), as a function of Ficoll Stokes-Einstein radius. Results are shown ± SE.

Table 6-1

Ficoll permeabilities for the glomerular capillary wall

r_s (nm)	k_s^{wall} ($\times 10^{-6}$ cm/s)	k_s^{bare} ($\times 10^{-6}$ cm/s)	k_s^{gbm} ($\times 10^{-6}$ cm/s)	k_s^{cells} ($\times 10^{-6}$ cm/s)
3.0	28.51 ± 1.49	508 ± 31.0	219 ± 13.4	32.8 ± 2.3
3.8	14.15 ± 0.97	214 ± 25.0	92.2 ± 10.8	16.7 ± 1.7
4.8	9.15 ± 1.19	81 ± 7.5	34.9 ± 3.3	12.4 ± 2.6
6.2	2.47 ± 0.32	23.51 ± 3.7	10.1 ± 1.6	3.25 ± 0.73

Results are given as mean ± SE. The number n of experiments in each case varied from 7 to 11.

$$\nabla^2 C = 0 \tag{6.3}$$

Refering to the idealized structural unit shown in Figure 4-3, the boundary conditions used were $\mathbf{n} \bullet \nabla C = 0$ at the cell surfaces and planes of symmetry, and $\mathbf{n} \bullet \nabla C$ equal to specified constants on the areas occupied by endothelial fenestrae and epithelial filtration slit, where $\mathbf{n}$ is a unit vector normal to the boundary. The mathematical problem just described is identical to that for water flow governed by Darcy's law; in that case, the pressure replaces C. Accordingly, an analytical solution derived previously for the water-flow problem (equation 21 of Drumond and Deen, 1994a) was used to compute k_s^{gbm} from k_s^{bare}. The following expression was obtained:

$$k_s^{gbm} = k_s^{bare} \left[1 + \frac{W}{\delta_{gbm}} \sum_{n=1}^{\infty} \frac{\xi_n^2 + \gamma_n^2}{2\,\lambda_n \tanh(\lambda_n\,\delta_{gbm}/W)} \right]^{-1} \tag{6.4}$$

where the parameters λ_n, ξ_n and γ_n were defined in Chapter 4 (equation 4.10). Values representative of glomerular capillaries in normal rats are W = 360 nm, δ_{gbm} = 200 nm, and N_f = 3 fenestrae per unit cell (Drumond and Deen, 1994a). For these inputs, it was found that $k_s^{gbm} = k_s^{bare}/2.33$.

We also compared results for k_s^{gbm} given by four different sets of boundary conditions, using a Galerkin finite elements method in each case, with a total of 1600 elements. At each interface (i.e., with the endothelial fenestrae or the epithelial filtration slit), either the concentration or the flux was kept constant, and calculations were done for solute radii ranging from 20 to 70 Å. We found that the dependence of k_s^{gbm} on the type of boundary conditions was not significant. The maximum difference between the estimates of k_s^{gbm} was 9%, and it was always less than 6.2% when results for constant flux and constant concentration boundary conditions were compared.

Using the concept of resistances in series, the individual permeabilities for the intact capillary wall are related by:

$$\frac{1}{k_s^{wall}} = \frac{1}{k_s^{gbm}} + \frac{1}{k_s^{cells}} \qquad (6.5)$$

where k_s^{cells} represents the combined contribution of the two cells layers. As will be discussed, we assume that k_s^{cells} is determined almost entirely by the epithelial slit diaphragm. The calculated values of k_s^{gbm} and k_s^{cells} are shown in Table 6-1. Even with the correction factor 2.33 embedded in k_s^{gbm}, the cells still offered the greater resistance to diffusion. Nonetheless, the diffusional resistance of the GBM was not negligible. As shown in Figure 6-3, the relative contribution of the GBM to the overall diffusional resistance increased with molecular size, from 13% at r_s = 3.0 nm to 26% at r_s = 6.2 nm.

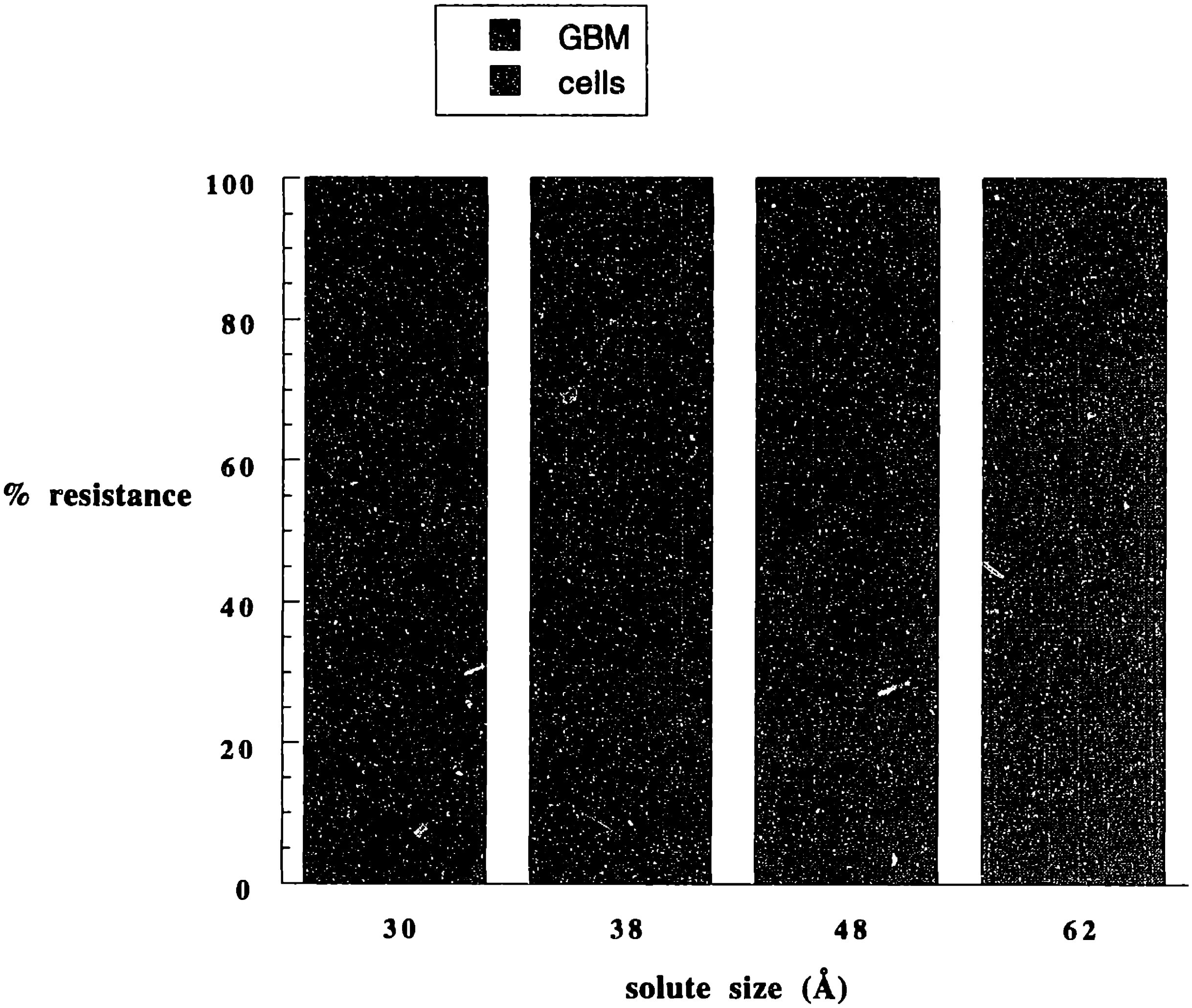

Figure 6-3

Relative resistance of the GBM and the epithelial layer to macromolecular diffusion across the glomerular capillary wall.

For diffusion through a simple aqueous layer, the permeability will vary in proportion to the solute diffusivity in dilute bulk solution (D_∞), so that k_s/D_∞ will be constant for all molecular sizes. As shown in Table 6-2, k_s^{bare}/D_∞ was found to decrease with increasing molecular size, confirming that the GBM offers size-dependent hindrances to diffusion. The cellular contribution to the permeability depended somewhat less strongly on molecular size than did that for GBM. That is, k_s^{cells}/D_∞ declined by a factor ~ 5 over the range of molecular sizes studied, whereas k_s^{bare}/D_∞ (or k_s^{gbm}/D_∞) decreased by a factor ~ 10. Consequently, the GBM resistance became a greater fraction of the total for larger molecular sizes, as already noted.

A more detailed examination of the factors which determine the permeability of the GBM reveals that:

$$k_s^{bare} = \frac{\Phi D}{\delta_{gbm}} = \frac{\Phi K_d D_\infty}{\delta_{gbm}} \tag{6.6}$$

where Φ and D are the partition coefficient and diffusivity of the solute, respectively, in the GBM and δ_{gbm} is the GBM thickness. The partition coefficient is defined here as the volume-average solute concentration in the GBM divided by that in external solution, at equilibrium. The apparent diffusivity of a solute in the GBM, relative to that of an equivalent layer of water, is given by the factor ΦK_d, where $K_d = D/D_\infty$. Values of ΦK_d were calculated from k_s^{bare} and D_∞ by assuming a typical GBM thickness in the rat of $\delta_{gbm} = 200$ nm (Daniels et al, 1993). The results are shown in Table 6-2. Whereas $\Phi K_d = 1$ corresponds to no steric or diffusional hindrances, the actual values in the GBM are roughly 10^{-2} to 10^{-3}. These low values indicate that the GBM does indeed represent a substantial barrier to diffusion. The results for ΦK_d are represented well by the empirical formula,

$$\Phi K_d = 0.1045 \exp(-0.7302\, r_s) \tag{6.7}$$

where r_s is in nm. This expression should be used only within or near the range of molecular radii studied, $3.0 \le r_s \le 6.2$ nm.

This study provides the first direct measurements of the diffusional permeabilities of isolated glomerular capillaries to well-characterized macromolecules of varying size. In the previous application of our confocal microscopy technique, the diffusion data were limited to a single dextran fraction (Daniels et al., 1993). In addition to covering a wide range of molecular sizes, the Ficoll fractions used here as test macromolecules offered two advantages: they were relatively monodisperse, and it has been shown that Ficoll (unlike dextran) diffuses through small pores at the rates expected for ideal, neutral spheres (Davidson and Deen, 1998). Thus, a more definitive characterization of size-dependent restriction was possible. For any given size of Ficoll, a comparison of the permeabilities of

Table 6-2

Size-dependent hindrances to diffusion in the GBM and the cell layers

r_s (nm)	D_∞ (cm^2/s)	$k_s^{bare\ gbm} / D_\infty$ (cm^{-1})	k_s^{cells} / D_∞ (cm^{-1})	ΦK_d
3.0	8.52×10^{-7}	596 ± 36	38 ± 3	1.19×10^{-2}
3.8	6.79×10^{-7}	315 ± 37	25 ± 3	6.30×10^{-3}
4.8	5.36×10^{-7}	151 ± 14	23 ± 5	3.03×10^{-3}
6.2	4.14×10^{-7}	57 ± 9	8 ± 2	1.13×10^{-3}

Results are given as mean ± SE. The values of ΦK_d are based on data for bare GBM.

intact and acellular glomerular capillary loops showed that the cell layers offered the dominant resistance to diffusion. This is in keeping with the conclusion reached in the previous study with dextran (Daniels et al., 1993). Although the GBM was calculated to offer an average of only about 20% of the diffusional resistance of the intact capillary wall, it is by no means a negligible part of the barrier. Indeed, bare GBM was found to have a diffusional permeability ranging from 10^{-2} to 10^{-3} times that of a layer of water of the same thickness, depending on molecular size.

It has been shown that for a given Stokes-Einstein radius (r_s), dextran diffuses more readily than Ficoll through synthetic membranes (Davidson and Deen, 1988), suggesting that such a difference may occur also in GBM and other biological structures. Consistent with this supposition is that the glomerular sieving coefficient (filtrate-to-plasma concentration ratio) for dextran in vivo has been found to exceed that for Ficoll of the same r_s (Oliver et al., 1992). Steric, hydrodynamic, and other factors which may cause ΦK_d to depend on molecular configuration as well as molecular size are discussed by Davidson and Deen (1988). The dextran fraction employed previously had a weight-average molecular weight of 70,000, corresponding to an average r_s of 6.4 nm, and its permeability in acellular glomeruli (k_s^{bare}) was found to be 1.6×10^{-5} cm.s^{-1} (Daniels et al., 1993). A modest extrapolation of the present data for Ficoll, using equation (6.7), gives $k_s^{bare} = 2.0 \times 10^{-5}$ cm.s^{-1} for $r_s = 6.4$ nm, or ~ 25 % higher than the value for dextran. However, these numbers may not reflect the actual difference between dextran and Ficoll, since the dextran sample is likely to have been much more polydisperse than the Ficoll fractions used here, which would have led to an underestimate of the true value of k_s^{bare} for a 6.4 nm dextran. Because the smaller molecules in a mixture reach diffusional equilibrium first, any delay in data acquisition (e.g., the ~ 120 s delay in acquiring fluorescence data by confocal microscopy) will cause the measured permeability to be more representative of the larger molecules in the mixture; a more quantitative discussion of this effect in given by Davidson and Deen (1988). It is therefore not possible to conclude from these results whether dextran diffuses faster than Ficoll in GBM.

The permeability properties of GBM are discussed in more detail in Chapter 7, where additional data are presented concerning the hydraulic permeability and the size-dependence hindrances to convective movement of macromolecules through this structure. In the remainder of the present chapter, we focus on the cellular contribution to the diffusional resistance of the glomerular capillary wall, in an effort to elucidate the specific structures which might be responsible for that part of the resistance.

6.4 Diffusional Permeability of the Epithelial Slit

The slit diaphragm, which spans the filtration slits formed by the spaces between the epithelial foot processes, has been shown to have a fibrous structure which makes it a likely candidate to present the major part of the cellular resistance. As described in Chapter 2, two possible structures have been suggested, a "zipper" and a "ladder" configuration. Although the two structures differ in detail, they share the important feature that permeating molecules must pass through a single row of cylindrical fibers, in which the smallest dimension of the opening is the distance between adjacent cylinders. We wished to explore the hypothesis that the slit diaphragm accounts for essentially all of the cellular part of the diffusional resistance, just as it has been shown to account for virtually all the of the cellular resistance of the glomerular filtration of water (Drumond and Deen, 1994a). This hypothesis assumes that the diffusional resistance of the endothelial fenestrae is equivalent, at most, to that of a slight increase in the thickness of the GBM.

To describe the diffusion of macromolecules through the filtration slit and slit diaphragm, we adapted the hydrodynamic model used by Drumond and Deen (1995) to describe convective movement of macromolecules through these structures. The model used here for diffusion estimated the increased hydrodynamic drag, and the consequent reduction in the local mobility or diffusivity, which is experienced by a spherical macromolecule moving through a single row of closely spaced cylinders. To simplify the computations, only the ladder geometry was considered. The primary geometric parameters were the solute radius (r_s), the radius of the cylinders which constitute the slit diaphragm (r_c) and the center-to-center spacing of the cylinders ($2L_s$). As described in Chapter 4, a more useful measure of cylinder spacing is the opening half-width, $u = L_s - r_c$. As also discussed earlier, the spacing of the slit diaphragm is not uniform. Ficoll macromolecules of approximately 12 nm in diameter (i.e., 6.2 nm Stokes-Einstein radius) were found here to diffuse across the intact glomerular capillary wall, and even larger Ficolls appear in the urine of normal rats (Oliver et al., 1992). As already mentioned, previous structural, hydrodynamic, and diffusion data suggest that Ficoll closely resembles a rigid sphere (Davidson and Deen, 1988). Thus, the transmural passage of these large Ficoll molecules is plainly inconsistent with uniform openings in the slit diaphragm of 4x14 nm, as in the zipper structure. In particular, suppose that the hydraulic permeability of the slit diaphragm is equal to that predicted for the zipper structure (i.e., 7.9×10^{-8} $m.s^{-1}.Pa^{-1}$, Drumond and Deen, 1994b). To achieve that same hydraulic permeability with the ladder structure, assuming uniformly spaced cylinders with $r_c = 2$ nm, the required opening between the cylinders (corresponding to the quantity 2u) is only 2.4 nm. Such small openings would preclude the passage of rigid spheres of even 2 nm in radius, again in clear contradiction with experimental findings. For the reasons just described, we assumed that in the slit diaphragm there is a distribution of gap haf-widths, u. A lognormal distribution was used, characterized by a mean spacing $\bar{u}$ and a parameter which describes the variance of the spacing (s). As described in Chapter 4, the hydraulic permeability of the slit was fixed at the value given above, so that only one of these parameters could be varied independently. The independent parameter in the lognormal distribution was chosen as s, and the slit diaphragm structure was characterized by r_c, s and the hydraulic permeability.

6.4.1 Epithelial Slit Diaphragm

The slit diaphragm was treated separately from the channel, as justified below. The key aspect of the diffusional problem for the slit diaphragm is that hydrodynamic interactions with the cylinders cause the diffusivity of a spherical macromolecule to depend on both its position and its direction of movement. Accordingly, the scalar diffusivity D_∞ must be replaced by a position-dependent tensor. Using the dimensionless tensor $\mathbf{d}$ computed by Drumond and Deen (1995), which is defined such that the diffusivity is given by $\mathbf{d}\, D_\infty$, the steady concentration field is governed by:

$$\nabla \bullet (\mathbf{d} \bullet \nabla C) = 0 \qquad (6.8)$$

Equation (6.8), subject to the boundary conditions stated below, was solved using a Galerkin finite element method with quadrilateral elements and bilinear basis functions. With references to the coordinates shown in Figure 6-4, the boundary conditions used were:

$$\mathbf{e_z} \bullet (\mathbf{d} \bullet \nabla C) = -J_0/D_\infty \qquad \text{at } z \rightarrow -\infty \qquad (6.9a)$$

$$C = C_0 \qquad \text{at } z \rightarrow +\infty \qquad (6.9b)$$

$$\mathbf{e}_r \bullet (\mathrm{d} \bullet \nabla C) = 0 \qquad \text{at } y = 0 \text{ and } y = L_S \qquad (6.9c)$$

$$\mathbf{e}_y \bullet (\mathrm{d} \bullet \nabla C) = 0 \qquad \text{at } r = r_C + r_S \qquad (6.9d)$$

where $\mathbf{e_j}$ is a unit vector directed along coordinate j. Equation (6.9a) specifies a constant flux J_0 far upstream from the cylinders and equation (6.9b) sets a constant concentration C_0 far downstream. It was found that $z = \pm 15\, L_S$ was large enough to approximate $\pm\, \infty$ in all cases. That is, applying the upstream and downstream conditions farther away had a negligible effect on the results. Equations (6.9c) and (6.9d) state that the solute flux normal

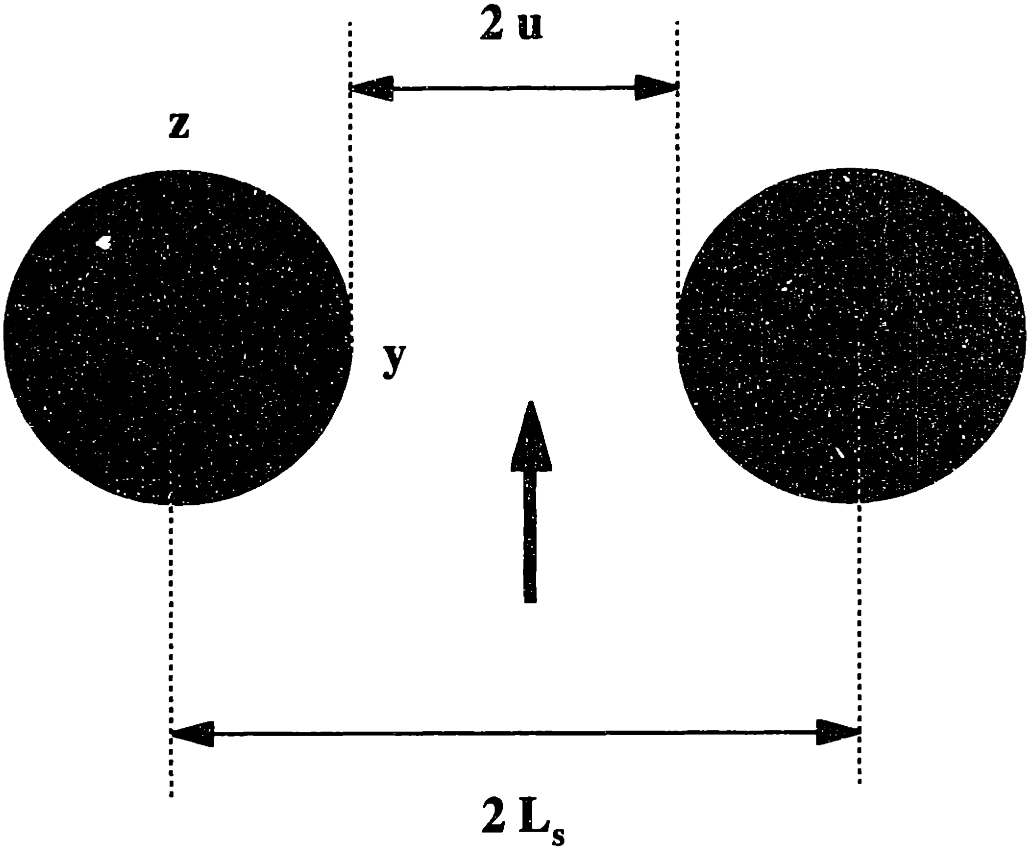

Figure 6-4
Schematic representation of the slit diaphragm. The arrow indicates the direction of diffusion.

to the boundary of the domain is zero at the symmetry planes and where a sphere contacts a cylinder.

The permeability for a row of uniformly spaced cylinders, k_S^{cyl}, was defined as:

$$k_s^{cyl} = \frac{J_0}{(\Delta C)_{cyl}} \tag{6.10}$$

where $(\Delta C)_{cyl}$ is the concentration drop in the z-direction above that corresponding to a uniform flux J_0 and a constant diffusivity D_∞. The results for various combinations of the geometric parameters were correlated in terms of the dimensionless mass transfer coefficient, or Sherwood number, defined by:

$$Sh = \frac{k_s^{cyl} r_s}{D_\infty} \tag{6.11}$$

The Sherwood number could be expressed as a function of only two dimensionless quantities, r_c/L_s and r_c/u, where $u = L_S - r_C$. For convenience in other calculations, the results were fitted by an empirical formula:

$$Sh = \frac{A[1-(r_s/u)]^B[1-(r_s/L_s)]^C(r_c/L_s)^D}{1+(r_s/u)^E(r_c/L_s)^F} \tag{6.12}$$

which was chosen to give the correct limit of $Sh \rightarrow 0$ for $r_c/u \rightarrow 1$ or $r_c/L_S \rightarrow 1$. Results were obtained for $0.1 \leq r_c/u \leq 0.95$, and $0.1 \leq r_c/L_s \leq 0.9$, for a total of 306 values of Sh. Powell's method (Press et al., 1989) was used to find the constants in equation (6.12), giving $A = 0.111$, $B = 0.795$, $C = 1.138$, $D = 0.080$, $E = -0.883$, and $F = 3.731$. Equation (6.12) represented the numerical results very accurately, the root-mean-square error being only 3.9 %.

As mentioned above, non-uniformities in the structure of the slit diaphragm were modeled by assumed a lognormal distribution of cylinder spacings. To determine the average permeability for the slit diaphragm, k_s^{sd}, the results were integrated over the distribution. The average permeability for a given solute size was calculated as:

$$\frac{k_s^{sd}\, r_s}{D_\infty} = \frac{\int_0^\infty Sh(u)\,(r_c + u)\, g(u)\, du}{\int_0^\infty (r_c + u)\, g(u)\, du} \qquad (6.13)$$

The weighting factor $L_S = r_C + u$, comes from the fact that the solute flux must be integrated over the total cross-sectional area of the slit diaphragm; the area of a single unit (pair of adjacent cylinders) is proportional to L_S. The integrals in equation (6.13) were evaluated numerically using Romberg's method (Press et al., 1989).

To justify the assumption that the slit diaphragm and the slit channel can be treated separately, that is, as resistances in series, we first verified that the concentration in the slit becomes almost constant in the direction normal to diffusion at a short distance after the diaphragm. In the coordinate system shown in Figure 6-4, the maximum variation of the solute concentration in the y-direction was determined to be less than 1% at a distance greater or equal to $2(r_C+r_S)$ from the cylinders. In addition, we found that the gradient of solute concentration in the z-direction becomes uniform relatively soon after the cylinders. The distance after which it varies by less than 1% is approximately $10(r_C+r_S)$ for the entire parameter range; however, that distance is much shorter when the cylinder and the solute radii are of comparable size. In the worst case, with a cylinder radius of 4 nm and a solute radius of 6 nm, the gradient varies by less than 5 % at a distance of $5(r_C+r_S)$ from the cylinders, or 50 nm, i.e., less than half the slit channel length (see below). Assuming that the diaphragm in the slit can be treated separately from the rest of the channel therefore appears reasonable.

6.4.2 Epithelial Slit Channel

The filtration slit between two adjacent podocytes was modeled as a channel bounded by flat, parallel walls, with a half-width h and length H. Electron micrographs indicate that, in reality, the slit generally tapers outward as one moves away from the basement membrane, as shown in Figure 6-5. That is, the half-width is smaller at the upstream end (h_{min}) than at the downstream end (h_{max}). To simplify the model for the slit, we replaced the tapered channel by a parallel-wall channel which had an equivalent diffusional permeability. This was done by setting $h = h_{min}$, and computing the value of H which gave equivalent results to those for a channel where the half-width varies linearly from h_{min} to h_{max} over an actual length H_0. A consequence of choosing $h = h_{min}$ is that $H < H_0$.

The diffusional permeability of a tapered channel was computed by solving equation (6.3) with a constant flux at the upstream end, a constant concentration at the downstream end, and no flux normal to the walls. The Galerkin finite element method was used, with quadrilateral elements and bilinear basis functions. Results were obtained for $h_{min} = 20$ nm, $60 \leq h_{max} \leq 110$ nm, and $200 \leq H_0 \leq 400$ nm, corresponding to approximate ranges of values determined form electron micrographs. To confirm the validity of our calculations, the results were compared to the analytical solution in the limit of slow tapering, i.e., when $(h_{max} - h_{min})/h_{min} << 1$. In that limit, a regular perturbation method can be used to find the concentration profile in the channel, given the boundary conditions stated above. Let $\varepsilon = (h_{max} - h_{min})/h_{min}$. It can be shown that:

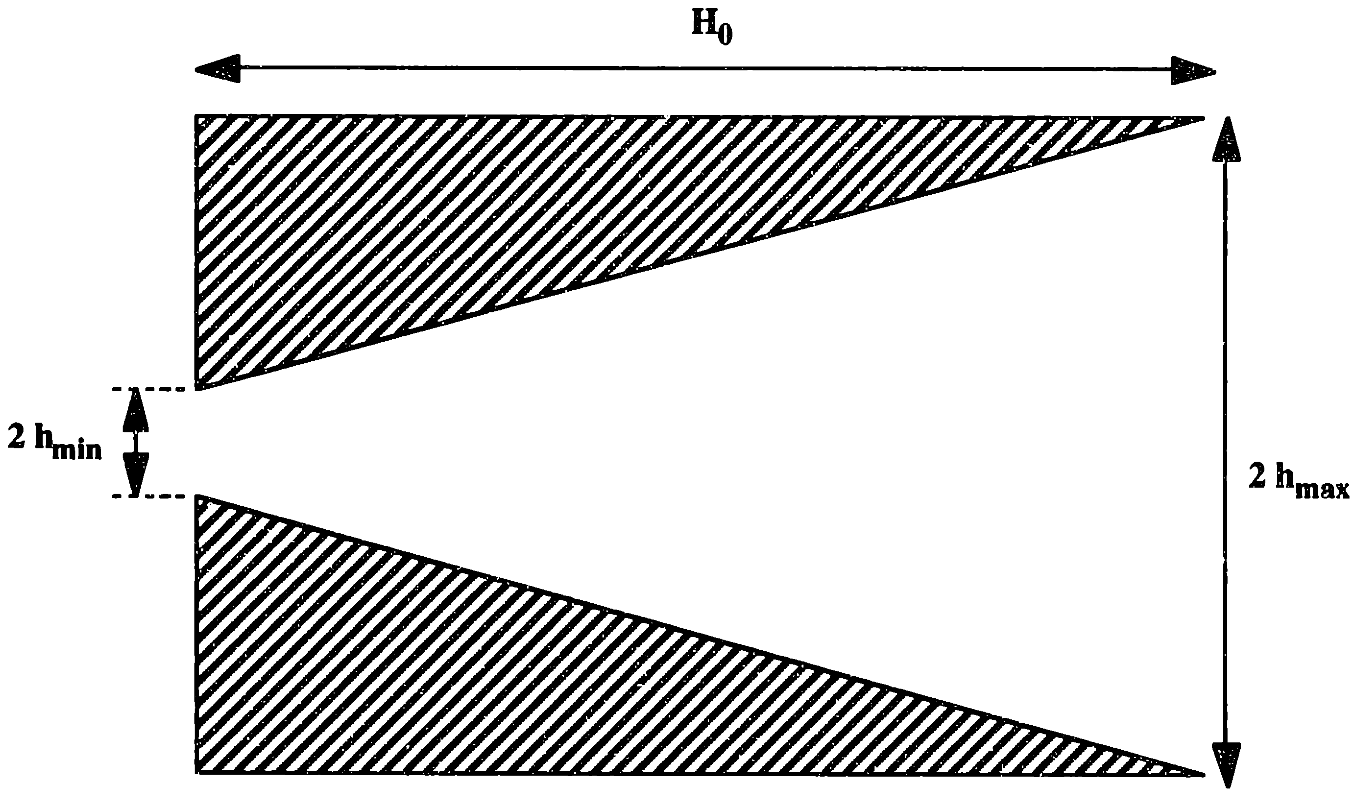
H_0
2 h_{min}
2 h_{max}

Figure 6-5
Schematic representation of the slit channel

$$\frac{H}{H_0} = 1 - \varepsilon \sum_{n=0}^{\infty} \frac{2(-1)^n}{(\pi/2)^3(2n+1)^3} + O(\varepsilon^2) \tag{6.14}$$

We found an excellent agreement between the analytical results and the FEM solution for $\varepsilon \leq 0.1$. The two methods yielded values of H_0 which were equal up to 3 digits. The results for all cases were then fitted to the expression:

$$\frac{H}{H_0} = \left(\frac{h_{max}}{h_{min}}\right)^c \exp\left[a\left(\frac{h_{max}}{h_{min}} - 1\right)^b\right] \tag{6.15}$$

which ensures that $H/H_0 \rightarrow 1$ as $h_{max}/h_{min} \rightarrow 1$. Using Powell's method (Press et al, 1989), the best-fit values for the constants were found to be a = - 0.7010, b = 0.6511 and c = - 0.4426. The root-mean-square error for 121 cases was 0.8%. Choosing h_{max} = 90 nm and H_0 = 300 nm as most representative of the actual shape, equations (6.15) gives H = 132 nm.

Hindered diffusion of a macromolecule through a parallel-plate channel has been analyzed by Pawar and Anderson (1993). Their result for the diffusivity, denoted here as D_{sc}, is:

$$\frac{D_{sc}}{D_\infty} = 1 + \frac{9}{16}\lambda \ln\lambda - 1.19358\lambda + 0.159317\lambda^3 + O(\lambda^4) \tag{6.16}$$

with $\lambda = r_s/h$. This is the apparent diffusivity based on concentration difference between bulk solutions at the ends of the channel; that is, it includes the effects of steric partitioning between the channel and external solutions. For h = 20 nm and the range of Ficoll sizes used here, $0.15 \leq \lambda \leq 0.31$, so that $0.43 \leq D_{sc}/D_\infty \leq 0.66$.

Using equation (6.16), the permeability of the slit channel is given by:

$$k_s^{sc} = \frac{D_{sc}}{H} \tag{6.17}$$

6.5 Discussion

We first examined the theoretical effects on k_S^{cells} of varying r_C and s, with the hydraulic permeability of the slit diaphragm fixed. Results are given in Figure 6-6 for r_C = 2 or 4 nm, and s ranging from 1.5 to 2.0. All of the curves in this semilogarithmic plot are roughly linear. In response to selective increases in either r_C or s, the slopes decrease and the absolute values of k_S^{cells} increase. Also shown in Figure 6-6 are the measured values of k_S^{cells}. Although the data are within the overall range of the theoretival curves, it is seen that for parameters combinations which give the correct order of magnitude for k_S^{cells}, the slopes predicted by the hindered diffusion model are much too large. In other words, the data show much less size-selectiviy than is expected for a structure with the hydraulic permeability that has been inferred for the slit diaphragm.

A possible explanation for the discrepancy between the predicted and the measured values of k_S^{cells} is that, in addition to a continuous distribution of cylinder spacings, there were defects in the slit diaphragm consisting of areas of missing cylinders. That is, the ladders might have had missing rungs. To test this hypothesis, it was assumed that the fractional area of the slit occupied by the defects was f, so that the fractional area containing a distribution of cylinders was 1-f. Thus the cellular permeability was given by:

$$k_s^{cells} \equiv k_s^{ep} = \varepsilon_s \left[(1-f)\left(1/k_s^{sd} + 1/k_s^{sc} \right)^{-1} + f\, k_s^{sc} \right] \tag{6.18}$$

where k_S^{sd} and k_S^{sc} are the permeabilities of the slit diaphragm and slit channel, respectively, based on the cross-sectional area of a single filtration slit. The factor ε_S, the

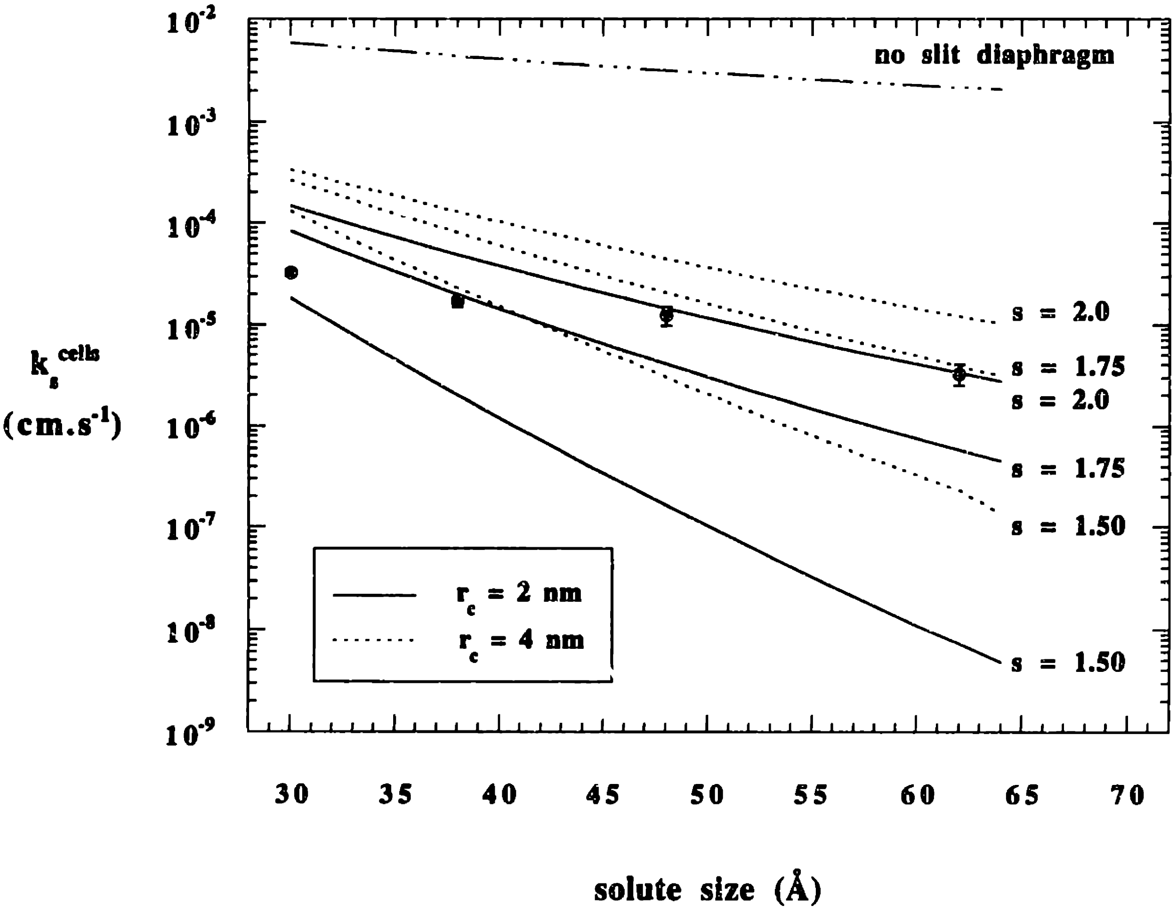

Figure 6-6

Measured values and theoretical predictions of the mass transfer coefficient for the cells, assuming that all filtration slit diaphragms are either intact or entirely absent. The measured values of k_s^{cells} are shown as mean ± SE. Results are shown for two values of the slit diaphragm cylinder radius, r_c = 2 and 4 nm, with the parameter s of the cylinder spacing distribution varying between 1.5 and 2.0.

fraction of the basement membrane area in contact with filtration slits, is needed because k_s^{cells} and the epithelial permeability k_s^{ep} are based on total surface area tather than slit area. It is seen that if the slit diaphragm is assumed to be absent (i.e., f = 1), the diffusional permeability of the slit will equal that of the open channel. As shown by the curve in Figure 6-6 labeled "no slit diaphragm", k_s^{cells} in this case would have a smaller slope, and much larger absolute values, than the experimental data. Thus, it appears that a very small value of f shoud be sufficient to account for the experimental results.

To determine the values of r_c, s and f which provided the best fits to the data for k_s^{cells}, we minimized the error given by:

$$\chi^2 = \sum_{i=1}^{4}\left(\frac{\ln(y_i/z_i)}{\ln\sigma_i}\right)^2 \tag{6.19}$$

where y_i and z_i are the measured and calculated values of k_s^{cells}, respectively, for Ficoll fraction i, and σ_i is the standard deviation of y_i. Logarithms were employed in the sum of squares because of the wide range of k_s^{cells}. Powell's method (Press et al., 1989) was used for the nonlinear parameter estimation. Preliminary calculations revealed that small values of r_c (<< 1 nm) tended to give the best fits to the permeability data. However, as discussed by Drumond and Deen (1995), values of r_c < ~ 2 nm are inconsistent with the range of slit diaphragm thicknesses estimated from electron micrographs in several published studies. For example, the bridge fibers reported by Rodewald and Karnovsly (1974) have a radius of 3.5 nm. Accordingly, we chose to fix r_c at either 1.0, 2.0 or 4.0 nm. Fits were performed by allowing s to vary with f = 0, or by allowing both s and f to vary.

The parameters values calculated for the slit diaphragm are shown in Table 6-3. As expected, allowing f to be non-zero provided much better fits to the data. This was true for either choice of r_c, as shown by the values of χ^2 in Table 6-3 and by the plots of k_s^{cells} in

Figure 6-7. Based on a F-test (Motulsky and Ransnas, 1987), the improvements in the fits to the data with $f \neq 0$ were greater than what could have been expected by increasing the number of adjustable parameters from 1 to 2. With or without the postulated defect in the slit diaphragm, the model predictions for r_c values of 1.0, 2.0 and 4.0 nm were quite similar. For all cases, the best fit value of f was ~ 0.002. That is, the area occupied by the postulated defects is inferred to be very small, only ~ 0.2% of the slit area.

An important feature of the present experiments is that the fluorescent measurements were so localized that any one permeability determination was affected by a very small number of slits. A critical examination of the slit diaphragm model requires some consideration of the anatomical implications of the best-fit parameter values. The filtration slits extend around the circumference of the capillaries, the slit diaphragm being located typically at a diameter of ~ 8 μm. Accordingly, the total length of a single, idealized slit diaphragm is ~ 25 μm. The average center-to-center distance between the cylindrical fibers is $2(\bar{u}+r_c)$, so that taking $r_c = 2$ nm, and $\bar{u} = 1$ nm as an example (Table 6-3), the length occupied by the average unit is 6 nm. Thus, the number of openings in one slit diaphragm is calculated to be extremely large, $(25\mu m)/(6nm) = 4x10^3$. This justifies the use of a continuous (e.g., lognormal) probability distribution for the cylinder spacings in the model. With $f = 0.002$, the length of the perimeter occupied by defects is only $0.002x25\mu m = 50$ nm, a space equivalent to that needed by ~ 8 average units. This emphasizes how tiny a defect is needed to significantly reduce the slope of a plot of k_s^{cells} versus r_s. Similar conclusions are reached with $r_c = 1$ or 4 nm. Given the consistency of the permeability results from one experiment to another, it appears that the same structural features were present, to only a slightly varying degree, in the slit diaphragms of all the regions examined. The value of $f = 0.002$ cannot be explained, for example, by postulating that two of every thousand slit diaphragms were completely absent.

Molecular charge has been shown to be an important determinant of the selectivity of the glomerular barrier to macromolecules, the passage of negatively charged molecules being normally more restricted that that of neutral molecules of similar size and chemical structure (Farquhar et al., 1961; Rennke et al., 1975; Bray and Robinson, 1984; Kanwar, 1984). Although the GBM was found to offer less resistance than the cells to diffusion of neutral macromolecules, it remain possible that the GBM is a more prominent part of the barrier to anionic macromolecules. Future studies are needed to characterize the charge-selectivity of the GBM in diffusion.

In summary, we measured the diffusional permeability of intact and acellular glomerular capillaries to Ficoll of varying molecular size. The cellular part of the resistance to diffusion, which we attribute largely to the epithelial slit diaphragm, was found to greatly exceed that of the GBM. A novel hydrodynamical model was developed to relate the cellular part of the diffusional resistance to proposed structures for the slit diaphragm. The data were most consistent with a ladder-like structure having a broad distribution of rung spacings, together with occasional regions devoid of rungs.

Table 6-3

Parameters values calculated for the slit diaphragm

r_C (nm)	1.0	1.0	2.0	2.0	4.0	4.0
s	2.20	1.82	1.89	1.53	1.63	1.30
f	0	0.0020	0	0.0026	0	0.0028
$\bar{u}$ (nm)	0.40	0.55	0.75	0.98	1.33	1.62
$\chi^2 x 10^2$	0.56	0.16	1.09	0.19	2.15	0.22

r_C corresponds to the cylinder radius in the slit diaphragm, s and $\bar{u}$ are the parameters characterizing the lognormal distribution of cylinder spacings, and f is the fraction of the epithelial surface which is denuded of diaphragms.

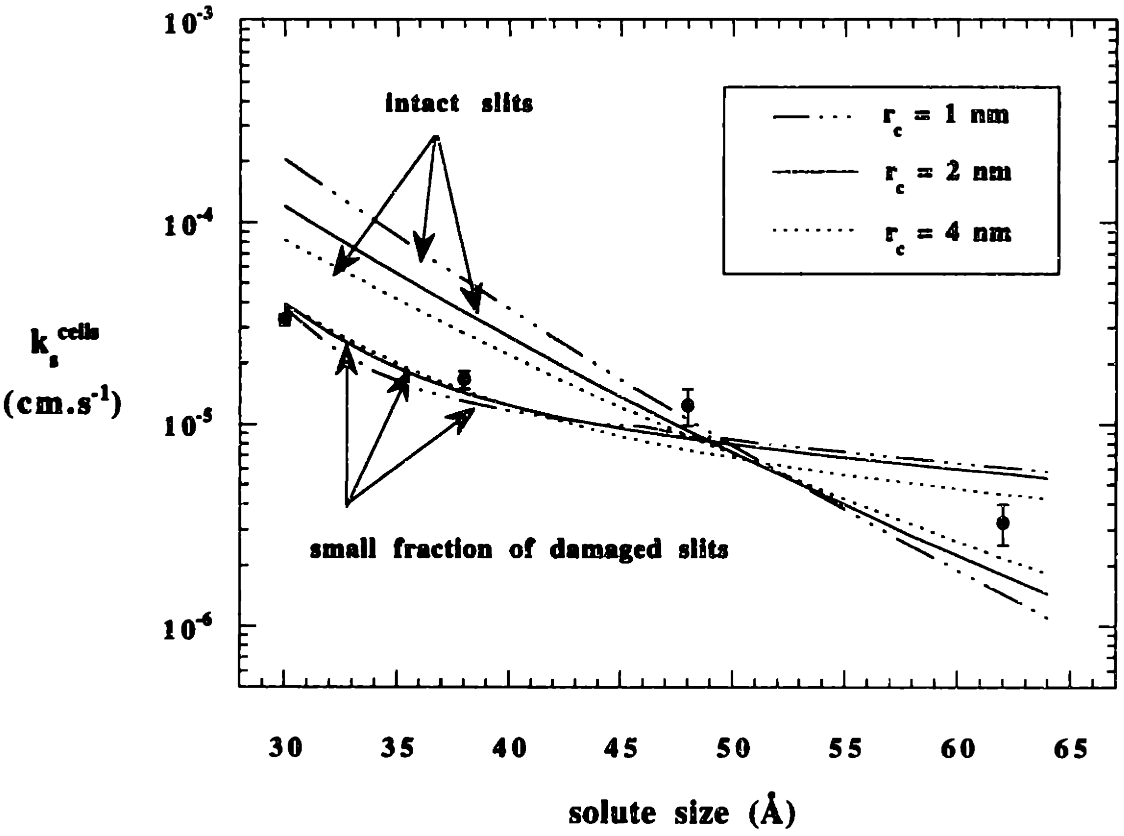

Figure 6-7

Measured values and theoretical predictions of the mass transfer coefficient for the cells, assuming that a small fraction of the filtration slit diaphragms were removed. The measured values of k_s^{cells} are shown as mean ± SE. The calculated values were obtained by assuming a cylinder radius of 1, 2 or 4 nm, and determining the parameters s and f that best fitted the data.

Chapter Seven

Filtration of Macromolecules across Isolated Glomerular Basement Membrane

7.1 Introduction

In this chapter, we further investigated the permselective properties of the glomerular basement membrane. The filtration of Ficoll across isolated GBM was studied using a technique developed by Daniels et al. (1992, 1993). Fragments of acellular glomeruli were packed in a filtration cell to form a homogeneous membrane across which test macromolecules were then filtered under applied pressure. Measurements of sieving were obtained with dextran in earlier experiments (Daniels et al., 1993), but the non-ideal behavior of that tracer has made it difficult to interpret the results quantitatively. The objective of our study was to apply that technique to Ficoll, which more nearly resemble ideal solid spheres (Davidson and Deen, 1988; Oliver et al., 1992), and to interpret the data using results of Chapter 6.

In the absence of a complete description of its ultrastructure, the GBM is treated as a random fiber network. In this isotropic medium, the flux J_S of a macromolecule is the sum of two terms, a diffusive and a convective component, respectively:

$$J_s = - K_d D_\infty \nabla C + K_c J_v C \tag{7.1}$$

J_V is the local solvent flux, C is the solute concentration, D_∞ is the diffusivity of the solute in dilute bulk solution, and ∇ the gradient differential operator. K_d and K_c are the hindrance coefficients for diffusion and convection, respectively, which account for the fact that the presence of fibers restricts solute diffusion and convection by means of steric obstruction and hydrodynamical interactions. Assumed to be independent of position in an isotropic medium, these factors depend upon pressure, molecular size and membrane structure. Because of the boundary conditions, the relevant quantities are in actuality the products ΦK_d and ΦK_c, where Φ is the partition coefficient of the macromolecule in the GBM. We determined empirically ΦK_d in isolated GBM as described in Chapter 6, and the present experiments were designed to obtain ΦK_c as a function of the hydraulic pressure difference across the membrane (ΔP) and solute radius (r_s).

In the filtration cell, solvent and solute fluxes across the GBM membrane are assumed to be one-dimensional. At steady-state J_v and J_s are constant, and equation (7.1) can be integrated to determine the concentration profile of the solute, using the ultrafiltration boundary condition $J_s = C_F J_v$, where C_F is the solute concentration in the filtrate. The solute concentration is dependent on the Peclet number, Pe, which expresses the relative importance of convective to diffusive forces acting on the macromolecule:

$$\mathrm{Pe} = \frac{\Phi K_c J_v L}{\Phi K_d D_\infty} \tag{7.2}$$

where L is the membrane thickness.

The true membrane sieving coefficient (Θ) of a macromolecule is defined as:

$$\Theta = \frac{C_F}{C_M} \tag{7.3}$$

where C_M is the solute concentration on the retentate side immediately adjacent to the membrane surface. It can be shown that:

$$\Theta = \frac{\Phi K_c}{1 - (1 - \Phi K_c) \exp(-\mathrm{Pe})} \tag{7.4}$$

To illustrate the dependence of sieving coefficients on the Peclet number, changes in Θ with the flow rate J_v for an ideal case are plotted on Figure 7-1. Although these curves were obtained assuming that the membrane is perforated by a homogeneous population of pores, in which case ΦK_d and ΦK_c can be readily computed using available theories for porous media, similar qualitative trends are expected in the GBM. As shown in Figure 7-1, the sieving coefficient of a macromolecule of given radius decreases when J_v increases, since the solute flux rises less than the solvent flux due to its diffusive component. Moreover, the decrease in Θ is more pronounced for smaller macromolecules, diffusion playing a lesser part as the size of the solute becomes large. Figure 7-1 thus illustrates the theoretical effect of pressure (or flow rate) on the permselective properties of the membrane, which we studied experimentally by measuring sieving coefficients across isolated GBM at two different values of ΔP, 35 and 60 mmHg, respectively.

7.2 Methods

Preparation of Acellular Glomeruli

The experimental procedures were as described in Chapter 6.

Filtration Cell

The GBM fragments were consolidated in a modified mini-ultrafiltration cell (model 3; Amicon, Beverly, MA) as described previously (Daniels et al., 1993). Briefly, 150 μm GBM suspended in Krebs HCO_3 buffer (pH 7.4) were added to the cell. Stirring was initiated, and 1,500 mmHg of pressure, generated with compressed air, was applied for 1 h to pack the GBM into a homogeneous layer. The GBM then formed at the base of the cell a filter which was uniform, as assessed by light microscopy, and impermeant to 1,000,000 MW blue dextran. After consolidation, the buffer was removed and replaced with identical buffer containing 4 g/dl bovine serum albumin (BSA). Filtration studies were performed at

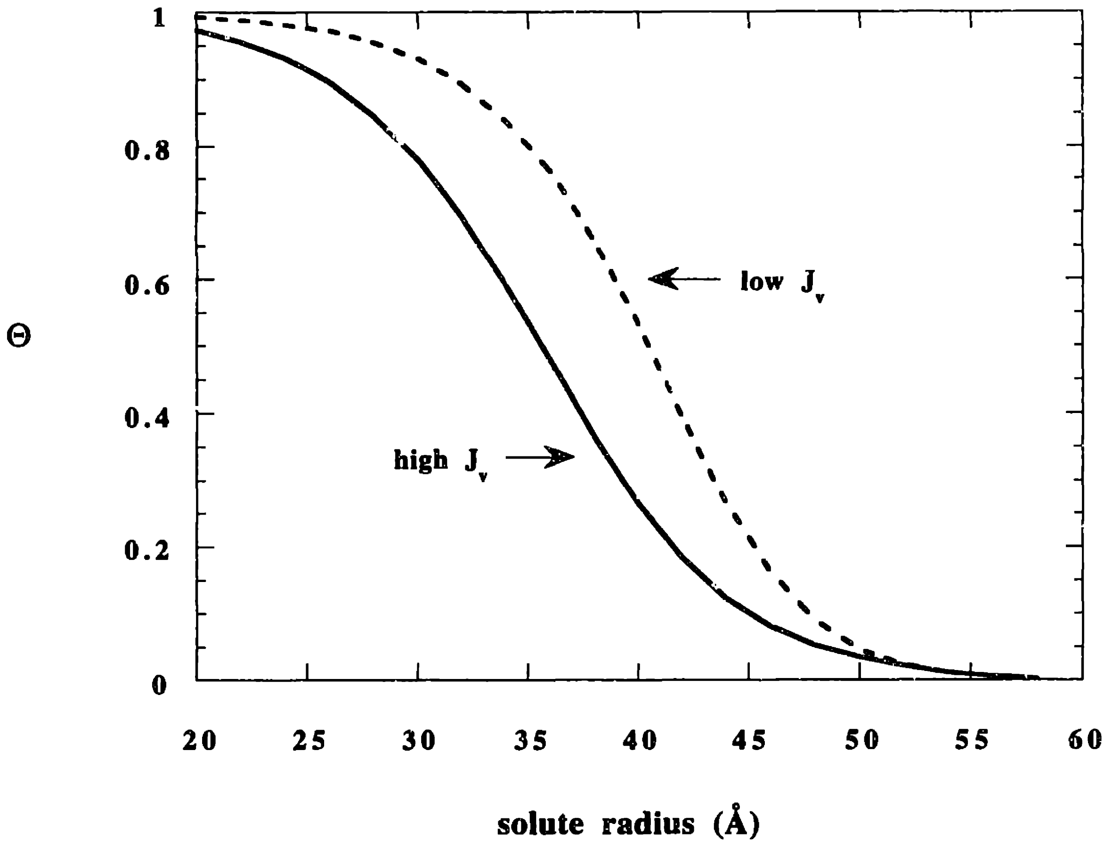

Figure 7-1

Predicted efffects of changes in the flow rate (J_V) on sieving coefficients (Θ) across a membrane perforated by uniform pores (60 Å in radius). The flow rate was increased from $0.75x10^{-7}$ m/s to $3x10^{-7}$ m/s.

27°C, with an applied pressure of either 35 or 60 mmHg. The stirring rate was 220 RPM. After a 10-min equilibration period, the filtrate was collected for an hour, and the water flux and fractional clearance of albumin were calculated. The retentate was sampled at the start and completion of the collection period.

Ficoll Sieving

Four narrow fractions and a polydisperse sample of Ficoll were obtained from Pharmacia LKB (Piscataway, NJ), and labelled with DTAF (dichlorotryazinyl amino fluorescein, Sigma Chemical Co., St. Louis, MO) using a procedure described by De Belder and Granath (1973). Samples were purified from unreacted label using desalting columns (Bio-Rad, Hercules, CA) and freeze-dried until used. The number of fluorescein molecules per Ficoll molecule was estimated to be less than 3, and the added charged components were assumed to have a negligible effect.

Polydisperse fluorescein-labelled Ficoll (0.05 g/dl) was added to the filtration cell, and after a 10-min equilibration period, the filtrate was collected throughout a 1 h clearance period.

Ficoll Separation

Filtrate and retentate were subjected to gel permeation chromatography. GPC columns of 2.6 cm diameter (Model C 26/100, Pharmacia Fine Chemicals, Piscataway, NJ) were packed with Sephacryl S-300 HR (Pharmacia). The eluent buffer was 0.05 M ammonium acetate at pH 7.0. Continuous Ficoll elution curves were determined by fluorescent light spectrophotometry (spectrofluorometric detector model RF-551, Shimadzu, Columbia, MD). The void volume of the column was determined by the elution of fluorescent isothiocyanate dextran (FITC-dextran, 2,000,000 MW, Sigma); the elution volume of four narrow fractions of fluorescein-labelled Ficoll of known Stokes-Einstein radius (r_s = 30.3, 38.0, 48.2 and 62.3 Å, respectively) was also measured, and the GPC columns were thus calibrated.

Morphometry

The thickness of the GBM layer was determined after completion of the filtration study by use of standard morphometric techniques, as described previously (Daniels et al., 1992).

Statistics

Results are means ± SE except where noted.

Calculations

Due to concentration polarization, the solute concentration in the bulk retentate, C_R, is smaller than C_M, and the measured sieving coefficient (Θ') is larger than the true membrane sieving coefficient, as described in Chapter 5. The relationship between Θ and Θ' was derived earlier and is repeated here:

$$\Theta = \frac{\Theta'}{(1-\Theta')\,B + \Theta'} \qquad (7.5)$$

where B, the polarization factor, is related to the mass transfer coefficient k_s by :

$$B = \exp(J_v/k_s) \qquad (7.6)$$

The mass transfer coefficient k_s was determined experimentally as described in Chapter 5.

The tissue isolation and the sampling of Ficoll were performed in the laboratory of Dr. Barbara S. Daniels at the University of Minnesota, while the chromatography studies were done by us at MIT.

7.3 Results

7.3.1 Darcy Permeability of the GBM

Membrane thickness (L) was measured in our study after completion of the experiment, when the membrane was no longer under applied pressure. To account for the change in thickness due to compression, we used experimental results obtained by Walton et al. (1992). Reported in their study were measurements of L under a wide range of pressure conditions, from which we derived a relationship between the deformation of the GBM membrane and the applied pressure. It was thus estimated that L/L_0, where L_0 is the membrane thickness under no compression, is equal to 0.939 at 35 mmHg and 0.896 at 60 mmHg.

The hydraulic permeability L_p of the membrane was determined for each run, based on equation (5.9). Both ΔP and J_v were measured; the reflection coefficient σ_{alb} and the oncotic pressure difference $\Delta\Pi_{alb}$ were calculated knowing the measured sieving coefficient of albumin and its concentration in the bulk retentate (4 g/dl). The Darcy permeability of the membrane is then given by:

$$K_{Darcy} = \mu L L_p \tag{7.7}$$

where μ is the viscosity of the solvent at 27°C, taken to be that of water. The average Darcy permeability was found to be equal to 1.48 ± 0.10 nm^2 (n = 6) at 35 mmHg, and 0.82 ± 0.07 nm^2 (n = 6) at 60 mmHg. The results are summarized in Table 7-1.

Table 7-1

Experimental values of flow rates and permeabilities

	ΔP = 35 mmHg	ΔP = 60 mmHg
J_v ($\times 10^{-7}$ m/s)	6.26 ± 0.44	9.34 ± 0.38
L_0 (µm)	7.77 ± 0.69	6.02 ± 0.49
L (µm)	7.29 ± 0.65	5.42 ± 0.44
L_p ($\times 10^{-8}$ m/s/mmHg)	3.29 ± 0.29	2.37 ± 0.13
K_{Darcy} (nm^2)	1.48 ± 0.10	0.82 ± 0.07

Results are given as mean ± SE. The number of experiments was 6 for each value of ΔP.

7.3.2 Sieving Curves

Filtration experiments were performed at two different pressures in random order, 35 and 60 mmHg; the averaged measured sieving coefficients are given in Table 7-2, and the calculated ones are shown in Table 7-3 and plotted in Figure 7-2. The curves correspond to theoretical predictions and are described below. The sieving coefficient of Ficoll decreases with increasing solute radius, due to the size-selectivity of the glomerular basement membrane. In addition, as expected, the sieving curve is shifted upwards when the pressure difference applied across the membrane is decreased from 60 to 35 mmHg. However, this shift is not due to a significant change in Pe, as opposed to Figure 7-1. Indeed the average product J_vL is equal to 5.05 ± 0. 41 ($\times 10^{-6}$ m^2.s^{-1}) for ΔP = 60 mmHg, and 4.46 ± 0.26 for ΔP = 35 mmHg. As the Darcy permeability results suggest, the differences between the two curves arise from the fact that the permeability properties of the membrane depend upon the hydraulic pressure difference. It should also be noted that sieving coefficients do not decrease drastically as r_s goes from 20 to 70 Å: there is less than

Table 7-2

Ficoll measured sieving coefficients for isolated glomerular basement membrane

r_s (Å)	Θ' ($\Delta P = 35$ mmHg)	Θ' ($\Delta P = 60$ mmHg)
20	$9.46x10^{-1}\pm2.56x10^{-2}$	$6.85x10^{-1}\pm2.46x10^{-2}$
22	$9.12x10^{-1}\pm2.59x10^{-2}$	$6.29x10^{-1}\pm1.81x10^{-2}$
24	$8.43x10^{-1}\pm2.45x10^{-2}$	$5.72x10^{-1}\pm1.72x10^{-2}$
26	$7.52x10^{-1}\pm2.22x10^{-2}$	$5.17x10^{-1}\pm1.95x10^{-2}$
28	$6.56x10^{-1}\pm2.18x10^{-2}$	$4.59x10^{-1}\pm2.21x10^{-2}$
30	$5.62x10^{-1}\pm2.18x10^{-2}$	$4.04x10^{-1}\pm2.35x10^{-2}$
32	$4.76x10^{-1}\pm2.09x10^{-2}$	$3.53x10^{-1}\pm2.31x10^{-2}$
34	$4.00x10^{-1}\pm2.02x10^{-2}$	$3.05x10^{-1}\pm2.20x10^{-2}$
36	$3.35x10^{-1}\pm1.93x10^{-2}$	$2.66x10^{-1}\pm2.09x10^{-2}$
38	$2.61x10^{-1}\pm1.81x10^{-2}$	$2.12x10^{-1}\pm1.89x10^{-2}$
40	$2.23x10^{-1}\pm1.71x10^{-2}$	$1.82x10^{-1}\pm1.78x10^{-2}$
42	$1.89x10^{-1}\pm1.54x10^{-2}$	$1.56x10^{-1}\pm1.65x10^{-2}$
44	$1.63x10^{-1}\pm1.42x10^{-2}$	$1.35x10^{-1}\pm1.56x10^{-2}$
46	$1.39x10^{-1}\pm1.30x10^{-2}$	$1.16x10^{-1}\pm1.41x10^{-2}$
48	$1.22x10^{-1}\pm1.23x10^{-2}$	$1.02x10^{-1}\pm1.37x10^{-2}$
50	$1.01x10^{-1}\pm1.13x10^{-2}$	$8.55x10^{-2}\pm1.27x10^{-2}$
52	$9.07x10^{-2}\pm1.06x10^{-2}$	$7.71x10^{-2}\pm1.22x10^{-2}$
54	$8.23x10^{-2}\pm1.04x10^{-2}$	$6.99x10^{-2}\pm1.17x10^{-2}$
56	$7.76x10^{-2}\pm1.04x10^{-2}$	$6.47x10^{-2}\pm1.14x10^{-2}$
58	$6.81x10^{-2}\pm9.51x10^{-3}$	$5.97x10^{-2}\pm1.12x10^{-2}$
60	$6.58x10^{-2}\pm9.47x10^{-3}$	$5.63x10^{-2}\pm1.14x10^{-2}$
62	$6.06x10^{-2}\pm9.58x10^{-3}$	$5.13x10^{-2}\pm1.11x10^{-2}$
64	$5.80x10^{-2}\pm9.59x10^{-3}$	$4.83x10^{-2}\pm1.12x10^{-2}$
66	$5.67x10^{-2}\pm9.85x10^{-3}$	$4.70x10^{-2}\pm1.12x10^{-2}$
68	$5.46x10^{-2}\pm9.45x10^{-3}$	$4.52x10^{-2}\pm1.09x10^{-2}$
70	$5.29x10^{-2}\pm9.61x10^{-3}$	$4.26x10^{-2}\pm1.03x10^{-2}$

Results are given as mean ± SE. The number of experiments was 6 for each value of ΔP.

Table 7-3

Ficoll calculated sieving coefficients for isolated glomerular basement membrane

r_s (Å)	Θ (ΔP = 35 mmHg)	Θ (ΔP = 60 mmHg)
20	$9.37x10^{-1}\pm2.89x10^{-2}$	$6.25x10^{-1}\pm2.46x10^{-2}$
22	$8.96x10^{-1}\pm2.97x10^{-2}$	$5.59x10^{-1}\pm1.73x10^{-2}$
24	$8.14x10^{-1}\pm2.77x10^{-2}$	$4.96x10^{-1}\pm1.64x10^{-2}$
26	$7.10x10^{-1}\pm2.41x10^{-2}$	$4.36x10^{-1}\pm1.85x10^{-2}$
28	$6.03x10^{-1}\pm2.29x10^{-2}$	$3.76x10^{-1}\pm2.03x10^{-2}$
30	$5.03x10^{-1}\pm2.20x10^{-2}$	$3.22x10^{-1}\pm2.07x10^{-2}$
32	$4.15x10^{-1}\pm2.02x10^{-2}$	$2.74x10^{-1}\pm1.96x10^{-2}$
34	$3.39x10^{-1}\pm1.86x10^{-2}$	$2.30x10^{-1}\pm1.79x10^{-2}$
36	$2.78x10^{-1}\pm1.70x10^{-2}$	$1.95x10^{-1}\pm1.64x10^{-2}$
38	$2.11x10^{-1}\pm1.53x10^{-2}$	$1.51x10^{-1}\pm1.40x10^{-2}$
40	$1.77x10^{-1}\pm1.40x10^{-2}$	$1.26x10^{-1}\pm1.27x10^{-2}$
42	$1.48x10^{-1}\pm1.23x10^{-2}$	$1.06x10^{-1}\pm1.14x10^{-2}$
44	$1.25x10^{-1}\pm1.13x10^{-2}$	$8.94x10^{-2}\pm1.05x10^{-2}$
46	$1.05x10^{-1}\pm1.02x10^{-2}$	$7.52x10^{-2}\pm9.29x10^{-3}$
48	$9.11x10^{-2}\pm9.56x10^{-3}$	$6.53x10^{-2}\pm8.82x10^{-3}$
50	$7.44x10^{-2}\pm8.72x10^{-3}$	$5.35x10^{-2}\pm8.04x10^{-3}$
52	$6.61x10^{-2}\pm8.09x10^{-3}$	$4.74x10^{-2}\pm7.58x10^{-3}$
54	$5.93x10^{-2}\pm7.83x10^{-3}$	$4.23x10^{-2}\pm7.14x10^{-3}$
56	$5.56x10^{-2}\pm8.09x10^{-3}$	$3.86x10^{-2}\pm6.91x10^{-3}$
58	$4.82x10^{-2}\pm7.19x10^{-3}$	$3.51x10^{-2}\pm6.71x10^{-3}$
60	$4.62x10^{-2}\pm7.06x10^{-3}$	$3.26x10^{-2}\pm6.79x10^{-3}$
62	$4.22x10^{-2}\pm7.07x10^{-3}$	$2.93x10^{-2}\pm6.47x10^{-3}$
64	$4.01x10^{-2}\pm6.99x10^{-3}$	$2.75x10^{-2}\pm6.47x10^{-3}$
66	$3.88x10^{-2}\pm7.12x10^{-3}$	$2.62x10^{-2}\pm6.41x10^{-3}$
68	$3.71x10^{-2}\pm6.80x10^{-3}$	$2.48x10^{-2}\pm6.21x10^{-3}$
70	$3.56x10^{-2}\pm6.82x10^{-3}$	$2.31x10^{-2}\pm5.73x10^{-3}$

Results are given as mean ± SE. The number of experiments was 6 for each value of ΔP.

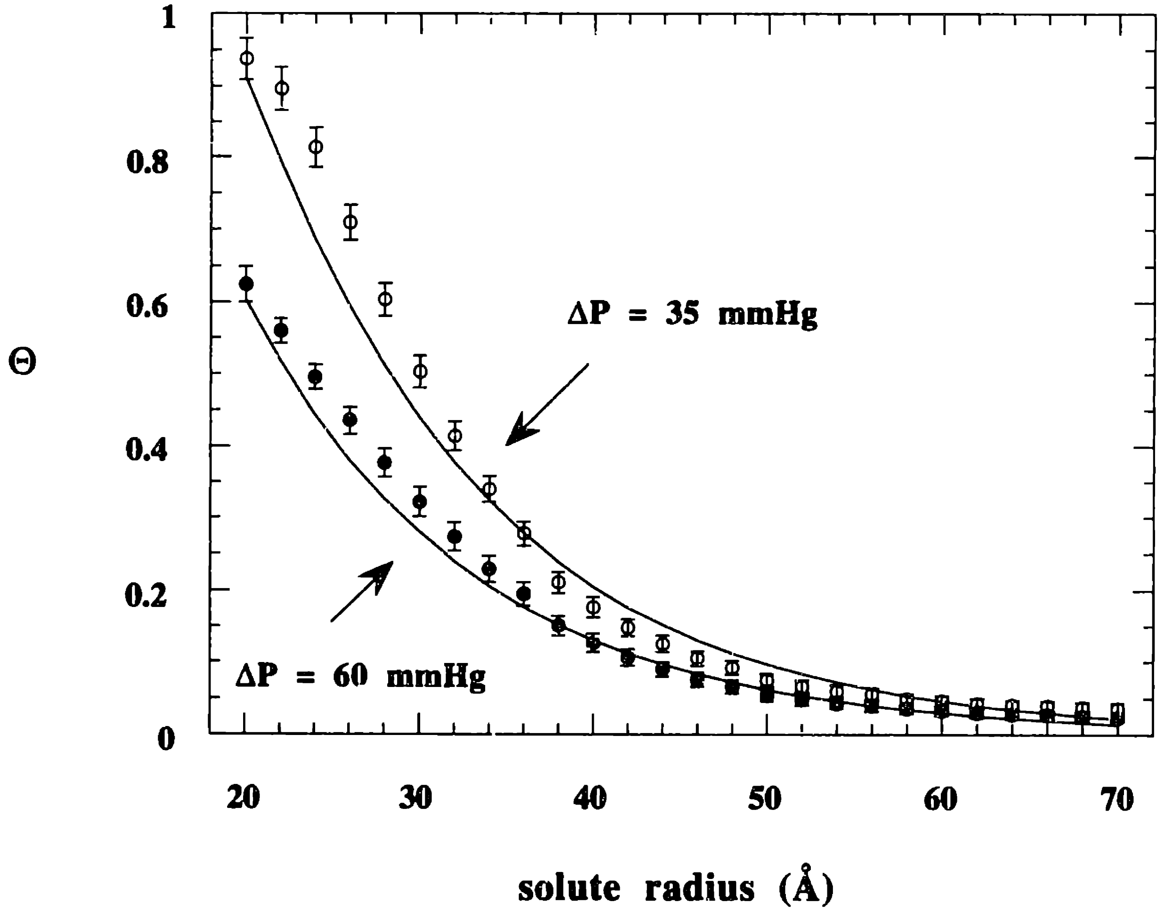

Figure 7-2

Ficoll sieving coefficients for isolated GBM, for ΔP = 35 mmHg (filled circles) and 60 mmHg (open circles), respectively (n = 6 in both cases). Results are given as mean ± SE. The curves correspond to the theoretical predictions of the model, assuming a linear dependence of the hindrance coefficients on ΔP.

a two order of magnitude difference between the value of Θ at the extremes of molecular radius.

In order to gain more insight into the specific role of the GBM in glomerular filtration, we compared Ficoll sieving curves obtained for acellular glomeruli in vitro with those obtained for intact glomeruli in vivo. In vivo rat sieving data analyzed in our laboratory in a similar manner were provided by Oliver et al. (1992). To be fair, the comparison has to be made on the basis of a constant product J_vL, as appears in the Peclet number (equation 7.2). We therefore adjusted our experimental curve for GBM at 35 mmHg by estimating the thickness of one layer of GBM as 200 nm (Daniels et al., 1992); the value of the SNGFR in the study of Oliver et al (1992) was 49.8 nl/min, and a typical value for the glomerular filtration surface area is 0.002cm^2 (Maddox et al., 1992), yielding a flux J_v of 4.17 x10^{-6}m/s. The results are shown in Figure 7-3. It should be noted that in general, the overall sieving coefficient for the capillary wall is equal to the product of the sieving coefficient for the GBM and that for the cell layers; it is not strictly the case here since the flux across bare GBM is one-dimensional, as opposed to two-dimensional when the GBM is lined by the endothelium and the epithelium. Nevertheless, for the purpose of comparison, the sieving coefficient for the cell layers, Θ_{cells}, can be roughly estimated as the ratio of the overall Θ_{wall} by Θ_{GBM}. At 25 Å, Θ is equal to 0.944 for GBM (adjusted curve) and 0.074 for intact glomeruli, therefore $\Theta_{cells} \sim 0.08$. At 65 Å, Θ is about 60 times larger in the GBM than in intact glomeruli ($\Theta = 5.8\text{x}10^{-2}$ and $7.1\text{x}10^{-4}$, respectively), yielding $\Theta_{cells} \sim 1.2\text{x}10^{-2}$. Although the in vivo experiments were performed on a different strain of animals (i.e., Munich-Wistar rats) and flux across the GBM was modified in the absence of cells, these results seem to confirm the fact that the contribution of the cell layers to the overall size-selectivity of the intact glomerular capillary wall is dominant throughout the range of solute radii considered here, but that the role of the GBM is not negligible.

7.3.3 Hindrance Coefficients

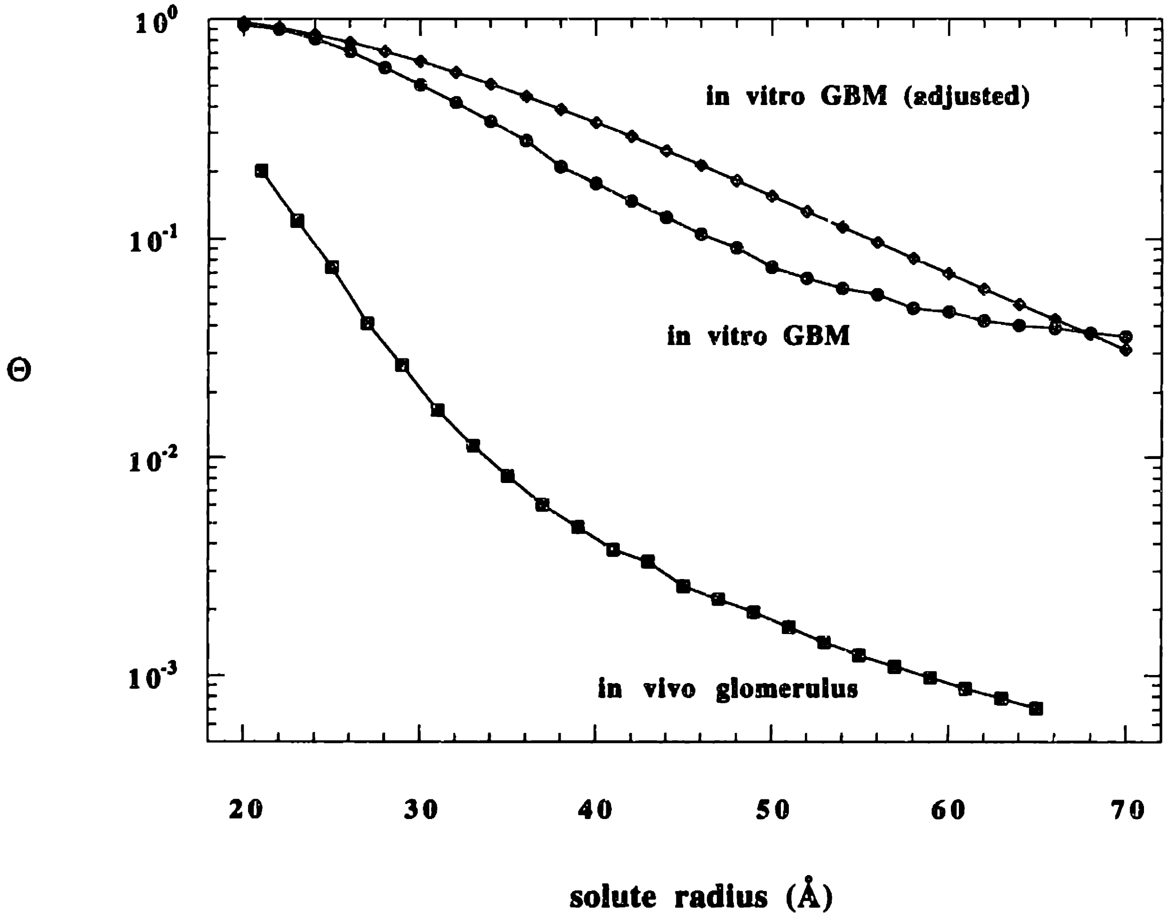

Figure 7-3
Ficoll sieving coefficients for in vitro GBM (n = 6) and in vivo glomerulus (n=9). For the purpose of comparison with the in vivo glomerulus data, the in vitro GBM curve was adjusted based on the values of solvent flux and membrane thickness characteristic of the in vivo data.

The product of the partition and the diffusional hindrance coefficients, ΦK_d, was determined for a zero transmembrane pressure in Chapter 6. The following empirical relationship was obtained:

$$(\Phi\, K_d)_0 = 0.1045 \exp(-0.07302\, r_s) \tag{7.8}$$

where the subcript "0" corresponds to $\Delta P = 0$. To extrapolate the results to the present conditions (ΔP = 35 and 60 mmHg), we assumed a linear dependence of ΦK_d on the hydraulic pressure difference, i.e.:

$$\frac{(\Phi K_d)_{\Delta P}}{(\Phi K_d)_0} = 1 - \beta\, \Delta P \tag{7.9}$$

This assumption was justified as described below. We assumed in addition that the product ΦK_c depends on ΔP in the same manner:

$$\frac{(\Phi K_c)_{\Delta P}}{(\Phi K_c)_0} = \frac{(\Phi Kd)_{\Delta P}}{(\Phi K_d)_0} = 1 - \beta\, \Delta P \tag{7.10}$$

For each solute size, the two unknowns β and $(\Phi K_c)_0$ were then determined from the two sieving curves, using the relationship between Θ, ΦK_c and ΦK_d (equation 7.4). Since the dependence of the slope β on solute radius appeared to be very weak, we then considered the assumption that β remains constant for all r_s. The most consistent results were obtained assuming that $\beta = 0.0096$ mmHg^{-1}.

Plotted in Figure 7-4 are the products $(\Phi K_d)_0$ and $(\Phi K_c)_0$ as a function of solute radius, with $\beta = 0.0096$ mmHg^{-1}. The partition coefficient Φ is expected to decrease significantly between 20 and 70 Å, as size-exclusion effects become more important. Nevertheless, as described below, ultrastructural studies of the GBM indicate that the

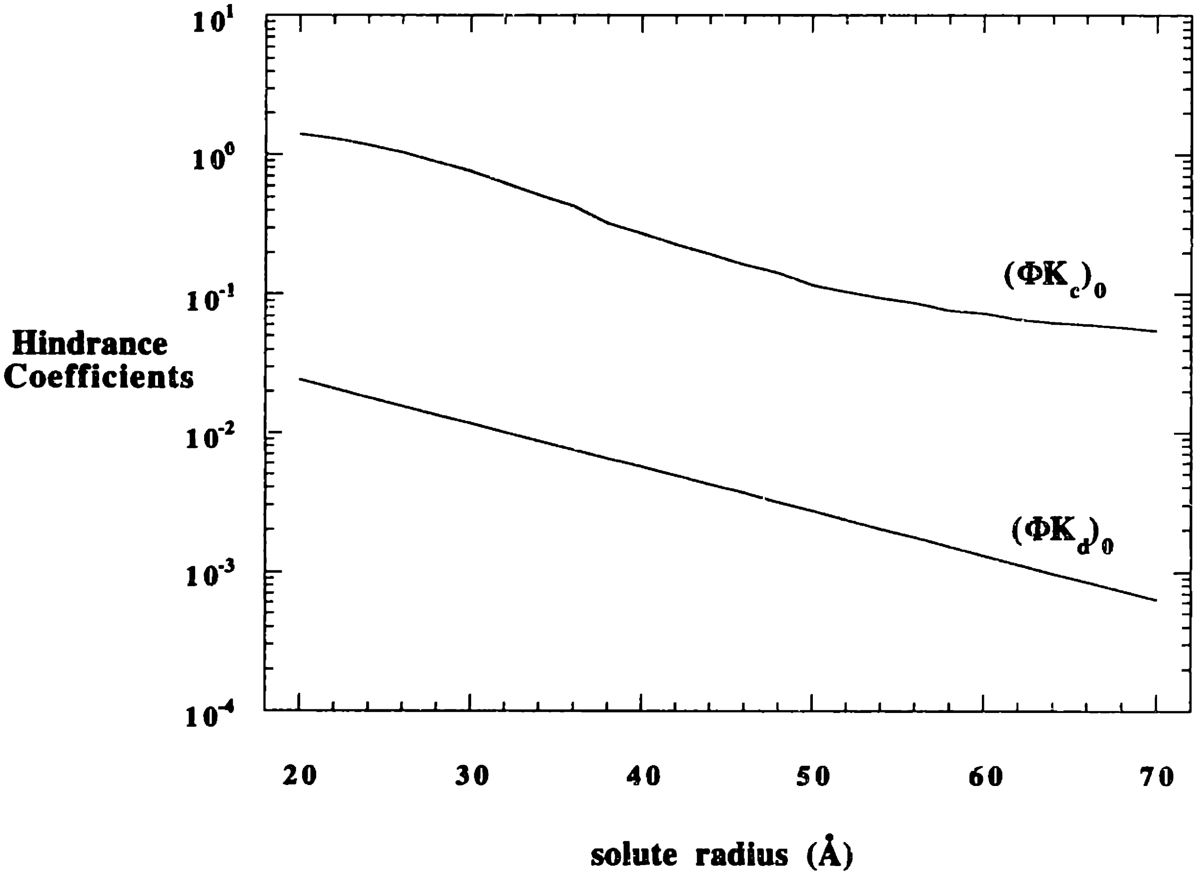

Figure 7-4

Hindrance coefficients in the GBM as a function of macromolecular size. Φ corresponds to the partition coefficient, K_c and K_d to the convective and diffusional hindrance coefficients, respectively. The subscript "0" denotes zero pressure.

spacings between the GBM fibers are quite large, and the partition coefficient should not become infinitely small for that size-range. For the convective hindrance coefficient K_c, which corresponds to the solute-to-solvent velocity ratio, the following behavior is expected: because of their finite size, macromolecules can not sample flow regions near solid boundaries where velocities are smaller, and small solutes are thus expected to move slightly faster than the solvent (i.e., $K_c \geq 1$). As the size of the particle increases however, the hydrodynamic interactions with the fibers become predominant and K_c should start to decrease, reaching zero when the particle is too large to pass through the medium. As illustrated in Figure 7-4, these trends were confirmed by our results: $(\Phi K_c)_0$ decreases in a monotonic manner with increasing molecular size, from values slightly above 1 for the smallest solutes to values on the order of 5×10^{-2} for the largest ones. The values of $(\Phi K_c)_0$ for small solute radii are slightly above what we would expect. Φ is always smaller than unity, and the convective hindrance coefficient K_c should not be greater than $1/(1-\phi)$, where ϕ is the solid volume fraction in the GBM; assuming a value of ϕ as large as 0.2, $(\Phi K_c)_0$ shouldn't exceed 1.25, whereas we obtained a value of 1.41 for $r_s = 20$ Å. The reason for which we are slightly overpredicting $(\Phi K_c)_0$ is probably that our assumptions based on linearity are oversimplified. We also examined the effect of assuming that the slope of ΦK_d versus ΔP was different than that of ΦK_c versus ΔP, and found very similar results; the difference between the two slopes was small, and the predicted values of $(\Phi K_c)_0$ close to those obtained above.

There is no available model predicting the convective hindrance coefficient in random fibrous media. Phillips et al. (1990) applied generalized Taylor dispersion theory to determine K_c in square and checkered lattices of bead-and-string fibers, but their study is limited to spatially periodic media, making any comparison with our results difficult. Nevertheless, the trends appear to be qualitatively similar.

For convenience, an analytical relationship between $(\Phi K_c)_0$ and r_s was found to predict the data well:

$$(\Phi K_c)_0 = 6.0240 \exp(-0.07469\, r_s) \tag{7.11}$$

where r_s is expressed in Å. Shown in Figure 7-2 is a comparison between the experimental sieving data and the theoretical curves obtained using the correlations we determined for $(\Phi K_d)_0$ and $(\Phi K_c)_0$, and assuming a linear dependence of these coefficients on ΔP as given by equation (7.10) with $\beta = 0.0096$ mmHg^{-1}. The total number of data points was 102, and that of adjustable parameters only 3. The agreement between the measured and calculated sieving coefficients is very good, and our assumption that ΦK_c and ΦK_d depend linearly on ΔP with an identical slope appears to yield accurate results. Equation (7.4) combined with the expressions (7.8-7.11) can therefore be used to predict Θ for GBM at any pressure, given the flow rate J_v and the membrane thickness L.

The Ficoll sieving data were then compared to dextran sieving data obtained in a similar manner in a previous study (Daniels et al., 1993). Because the experiments with dextran were performed at $\Delta P = 50$ mmHg, we determined the Ficoll sieving coefficients for that ΔP value as described above, i.e., based upon equations (7.4, 7.8-7.11) and the values of J_v and L given in the dextran study. The corresponding curves are shown in Figure 7-5. As illustrated, the sieving coefficients were lower with Ficoll than with dextran throughout the entire size range ($r_s < 60$ Å), confirming the results of previous studies (Oliver et al, 1992). However, one should be cautious in making that comparison since the value of the Darcy permeability in the dextran study was not measured, and there could have been differences in the GBM filters from one study to the other.

7.4 Discussion

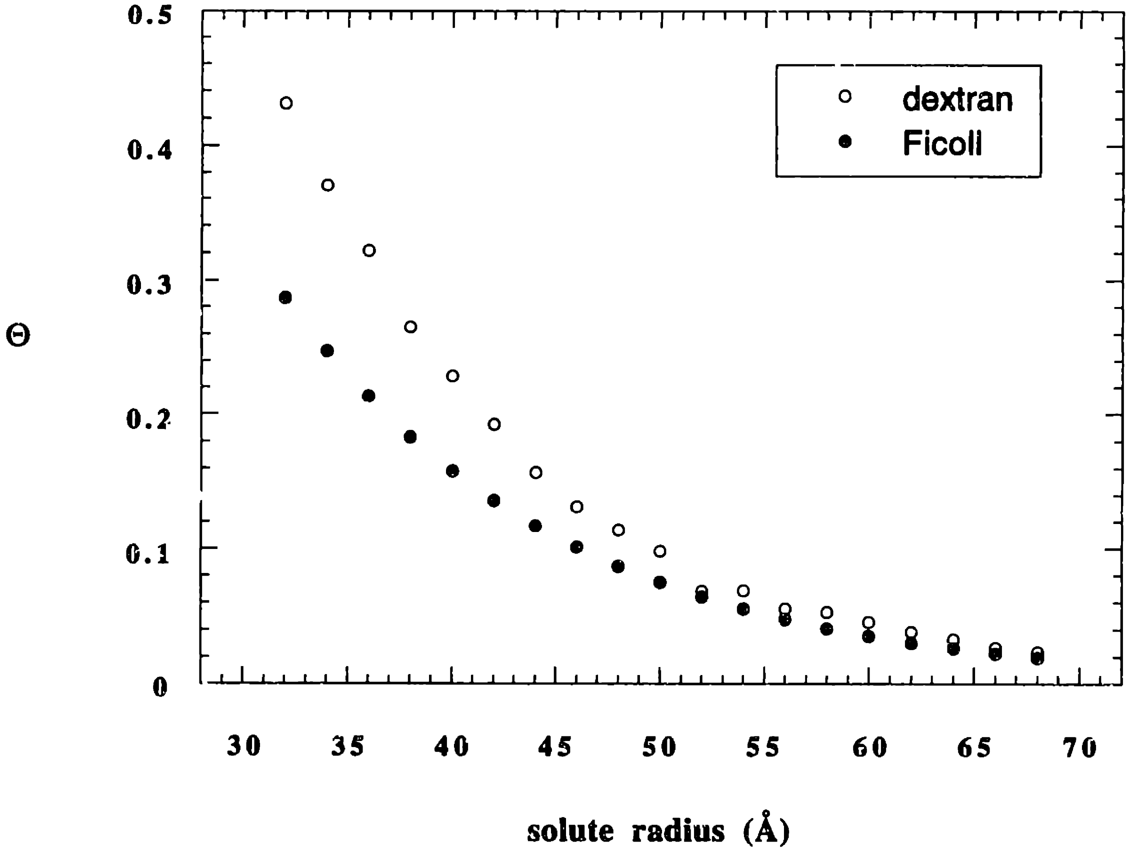

Figure 7-5
Dextran and Ficoll sieving coefficients for isolated GBM. For the purpose of comparison, the Ficoll curve was extrapolated to ΔP = 50 mmHg assuming a linear dependence of ΦK_c and ΦK_d on ΔP, and using the values of solvent flux and membrane thickness obtained in the dextran study.

The goals of this study were to provide a biophysical interpretation of GBM permeability data and to develop a model to predict sieving coefficients in the GBM. In this section, several fiber matrix models are discussed. We first compared the hindrance coefficients predicted by these models with our results, and then interpreted the water permeability data using two different approaches.

7.4.1 Comparison with Fiber Matrix Models

We compared our experimental results for ΦK_d with theoretical predictions using a recently developed theory for hindered diffusion in random fibrous media. As recently suggested (Brady, 1994; Johnson et al., 1996), K_d can be expressed as the product of two terms, one of which accounts for hydrodynamical interactions due to the presence of fibers, the other for steric effects. The first term, referred to as K_{dh}, can be derived from Brinkman's effective medium calculation of the viscous force exerted by a flowing fluid on a spherical particle embedded in porous media (1947):

$$K_{dh} = \frac{1}{1 + \dfrac{r_s}{\sqrt{K_{Darcy}}} + \dfrac{r_s^2}{3K_{Darcy}}} \tag{7.12}$$

where K_{Darcy} is the Darcy permeability of the medium. The second term, K_{ds}, takes exclusively into consideration the geometry of the system, and was derived from calculations made by Johansson and Löfroth (1993), who performed Brownian dynamics simulations of hard sphere diffusion in polymer networks of wormlike chains, neglecting all hydrodynamical interactions. The following semi-empirical expression for K_{ds} was obtained:

$$K_{ds} = \exp\{ - 0.84 [\phi (1 + \frac{r_s}{r_f})^2]^{1.09} \} \qquad (7.13)$$

where r_f is the fiber radius. Assuming that $K_d = K_{dh} K_{ds}$ as given by equations (7.12,7.13), Johnson et al. (1996) were able to predict well protein and Ficoll diffusion data in agarose gels without any adjustable parameters.

The partition coefficient Φ was computed using the expresssion derived by Ogston (1958), based upon the distribution of spaces in a random network of fibers:

$$\Phi = \exp[- \phi^* (1 + \frac{r_s}{r_f})^2] \qquad (7.14)$$

where ϕ^* is the solid volume fraction occupied by the fibers, corrected to account for overlap. Indeed, the calculations of Ogston (1958) are based upon a total length of fiber per unit volume; in calculating the solid volume fraction, the space occupied by two overlapping fibers should be counted only once.The relationship between the "corrected" (ϕ^*) and the "uncorrected" (ϕ) solid volume fraction is given by:

$$\phi = 1 - \exp(\phi^*) \qquad (7.15)$$

The validity of equation (7.14) was recently confirmed by Booth and Lumsden (1993), who calculated the void volume accessible to hard spheres in computer-generated three-dimensional random fiber matrices.

Our assumptions regarding the fiber thickness were founded upon morphological observations from previous studies, reviewed in Chapter 2. Based on transmission electron micrographs, Laurie et al (1984) observed in the GBM 4-nm-thick cords, straight 7-10-nm-thick rods, as well as 3.5 nm paired rods. Kubosawa and Kondo (1985) found in the lamina rarae externa and interna a three-dimensional, polygonal network, constituted by interconnected 6-8-nm-thick fibrils. The size of the mesh was quite variable, ranging mostly between 20 and 25 nm in width. The three-dimensional mesh-like structure of the lamina densa was also visualized in situ by Takami et al. (1991); the authors observed in the middle layer of the GBM 6-10 nm fibrils arranged as a polygonal network. The average long dimension of the space between the fibers was estimated as 16.8±6.2 nm, the short one as 12.0±6.2 nm. Thus, in the following analysis, we assumed a fiber radius comprised between 2 to 5 nm, corresponding to 4-10 nm thick fibers.

Since no measurements of ϕ in GBM have been reported, it was assumed to vary between 0.10 and 0.50. To our knowledge, the only estimates of fiber volume fraction in basement membranes are 0.11-0.12 in mice EHS tumors (Haskin et al., 1993), and 0.17-0.21 in Descemet's membrane (Krause, 1934; Dohlman and Bazals, 1955). It is not clear whether these values are representative of the GBM. For the Darcy permeability, we used as an estimate the value of 2.40 nm^2 when there is no pressure difference across the membrane, as derived below. Varying the parameters ϕ and r_f, we found a poor agreement between the values of $(\Phi K_d)_0$ calculated using equations (7.12-7.15) and those derived from our measurements. The slope of $(\Phi K_d)_0$ versus solute radius predicted by the model tended to be too elevated. The best results were obtained with a fiber radius of 4 nm and a solid volume fraction of 0.39, which is very likely too high an estimate as discussed below; even in this "optimal" case, $(\Phi K_d)_0$ was overpredicted by a factor ~ 2 for r_s = 20 Å and underpredicted by a factor ~ 3 for r_s = 70 Å, as shown in Table 7-4. In the study of Johnson et al. (1996), the solid volume fraction was much smaller ($\leq$ 0.08), and one possibility is that the theory presented above is not as accurate in denser fibrous networks.

In the absence of any accurate model, we used this theoretical approach to justify our assumption that the product ΦK_d varies linearly with the hydraulic pressure difference ΔP. To do so, we examined whether the model proposed by Brady (1994) predicts a linear dependence for a certain combination of parameters. The fiber radius r_f was varied between

2 and 5 nm. For $\Delta P = 35$ and 60 mmHg, the values of K_{Darcy} were those obtained in the experiments, and the solid volume fraction ϕ was computed using the correlation of Jackson and James (1986, equation 7.18 below). These results were extrapolated to obtain the solid volume fraction at zero pressure difference, knowing that the product ϕL remains constant. We then calculated the product ΦK_d for $\Delta P = 0$, 35 and 60 mmHg using equations (7.12-7.15). With a fiber radius of 4 or 5 nm, we found that the dependence of ΦK_d on ΔP was almost linear for all solute radii. Shown on the two panels of Figure 7-6 are results corresponding to $r_f = 5$ nm. The theoretical values of ΦK_d are plotted as a function of ΔP for several molecular sizes. As illustrated, the assumption of linearity appears very reasonable for all solute sizes.

Table 7-4

Measured and predicted values of $(\Phi K_d)_0$

r_s (Å)	$(\Phi K_d)_0^{meas.}$	$(\Phi K_d)_0^{calc.}$ Brady (1994)	$(\Phi K_d)_0^{calc.}$ Ogston et al.(1958,1973)
20	$2.43\text{x}10^{-2}$	$5.58\text{x}10^{-2}$	$5.92\text{x}10^{-2}$
30	$1.17\text{x}10^{-2}$	$1.90\text{x}10^{-2}$	$1.26\text{x}10^{-2}$
40	$5.63\text{x}10^{-3}$	$6.10\text{x}10^{-3}$	$2.03\text{x}10^{-3}$
50	$2.71\text{x}10^{-3}$	$1.83\text{x}10^{-3}$	$2.50\text{x}10^{-4}$
60	$1.31\text{x}10^{-3}$	$5.02\text{x}10^{-4}$	$2.35\text{x}10^{-5}$
70	$6.30\text{x}10^{-4}$	$1.26\text{x}10^{-4}$	$1.68\text{x}10^{-6}$

$(\Phi K_d)_0$ denotes the product of the partition and the diffusional hindrance coefficient for a transmembrane pressure equal to zero.

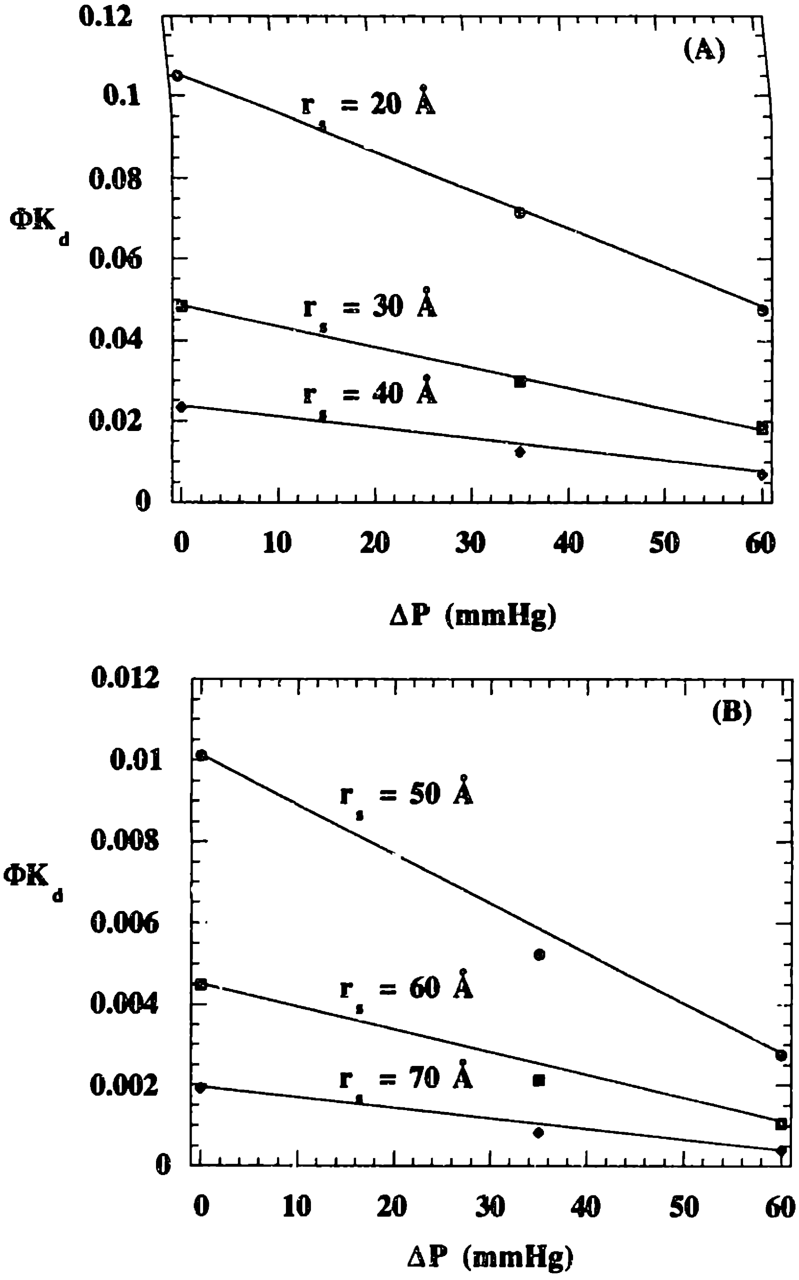

Figure 7-6

Theoretical dependence of the diffusional hindrance coefficient on the transmembrane pressure. Results are given for solute radii varying from 20 to 40 Å (panel A), and from 50 to 70 Å (panel B).

A fiber matrix theory for random fibrous networks was also developed by Michel and Curry (1980). In their model, the transport of macromolecules is assumed to be restricted only by steric obstruction. Both the partition coefficient and the diffusive hindrance coefficient are based on calculations made by Ogston et al. (1958, 1973), who neglected the hydrodynamical interactions between the fibers and the permeating molecules in determining K_d. In the absence of a theory for solute convection in random fiber media, reflection coefficients are taken to be equal to $(1-\Phi)^2$, an approximation only valid when convection is dominant. The hydraulic permeability is calculated based upon the Kozeny-Carman equation (Carman, 1956), which relates L_p to the fiber radius and the length of fiber per unit volume (l_f):

$$L_p = \frac{r_f^2\,(1-\pi r_f^2 l_f)^3}{4\,\mu\,K\,L\,(\pi r_f^2 l_f)^2} \tag{7.16}$$

where K is the Kozeny constant.

We first compared our results for $(\Phi K_d)_0$ with theoretical predictions based upon the calculations of Ogston et al. (1958, 1973). In their model, K_d is given by:

$$K_d = \exp(-\, r_s\sqrt{\pi\, l_f}) \tag{7.17}$$

where l_f is related to the solid volume fraction by $l_f = \phi/\pi r_f^2$. Throughout the parameter range, we observed differences of several orders of magnitude between the data and the model predictions. The smallest differences were obtained assuming with a fiber radius of 2 nm and a solid volume fraction as high as 0.42, but even with these values, the discrepancies remained very large, as illustrated in Table 7-4. The product $(\Phi K_d)_0$ was overestimated by a factor ~ 2 at 20 Å, and underestimated by a factor 400 at 70 Å. This theory also predicted too sharp a decline of $(\Phi K_d)_0$ with solute size.

We then attempted to interpret our data using the model of Curry and Michel (1980), according to the method outlined by Robinson and Walton (1989). For a given solute and at a given pressure difference, we determined the unique set of parameters (r_f,l_f) which predicted both the sieving coefficient (taken as 1- $(1-\Phi)^2$) and the hydraulic permeability as given by equation (7.16). We then examined whether the value of r_f which was obtained could be used to predict sieving coefficients for other solute sizes and pressure values. It should first be emphasized that the assumption that the Kozeny constant has a fixed value of 5 - the value used by that Robinson, Walton and their coworkers (1987, 1989, 1992) - is only valid for solid volume fractions greater than 0.40 (Happel and Brenner, 1983); we nevertheless also used that value for the entire range of ϕ for lack of better knowledge. Since the approach of Curry and Michel (1980) can only be used when convection is dominant (i.e., $Pe \geq 3$), we restricted our analysis to solute radii greater than 30 Å, given the value of Pe in our studies (reported in Table 7-5).

Table 7-5

Values of the Peclet number in the filtration experiments

r_s (Å)	Pe @ $\Delta P = 35$ mmHg	Pe @ $\Delta P = 60$ mmHg
20	1.81	2.03
30	2.96	3.31
40	4.28	4.79
50	5.82	6.51
60	7.59	8.49
70	9.62	10.8

For each solute size, we determined the value of the fiber radius which gave the best agreement between Θ and L_p at $\Delta P = 60$ mmHg. From this value of r_f and that of Θ at $\Delta P = 35$ mmHg, we then calculated L_p at the latter pressure difference and compared it to the data. Results are shown in Figure 7-7. There was a fair agreement between the calculated and the measured value of L_p at 35 mmHg in the intermediate range of solute radii; however, L_p was overpredicted by 50 % at 30 Å and underpredicted by 20 % at 70 Å. Moreover, the value of the fiber radius which best fitted the data varied significantly with solute radius, ranging from 1.7 nm for r_s = 30 Å to 2.5 nm for r_s = 70 Å (by comparison, estimates of the GBM fiber radius obtained by Robinson and Walton (1989) varied between of 0.8 to 1.15 nm, values which are not in the range of those reported in morphological studies). Since the hydraulic permeability in the Kozeny-Carman equation is proportional to r_f^2, changes by a factor 1.5 are significant. To illustrate that point, we fixed the values of r_f and l_f (chosen so as to fit the water permeability and the sieving data at midrange, i.e., for r_s = 50 Å) and calculated the sieving coefficients from 30 to 70 Å, at 35 and 60 mmHg, respectively. As shown in Table 7-6, the discrepancy between the predicted and the measured values of Θ could be as high as 80 %. These results indicate that the model fails to predict sieving data accurately with a fiber radius independent of solute size. For all these reasons, the fiber matrix model of Michel and Curry appears to be incomplete.

7.4.2 Models for the Darcy Permeability

One Fiber Approach

In order to understand the ultrastructural basis for the permselective properties of the GBM, we then compared two possible representations of the GBM as a random fibrous network. In the first approach, we made the traditional assumption that all the GBM fibers were identical, of radius r_f. The solid volume fraction ϕ of the matrix, for which no

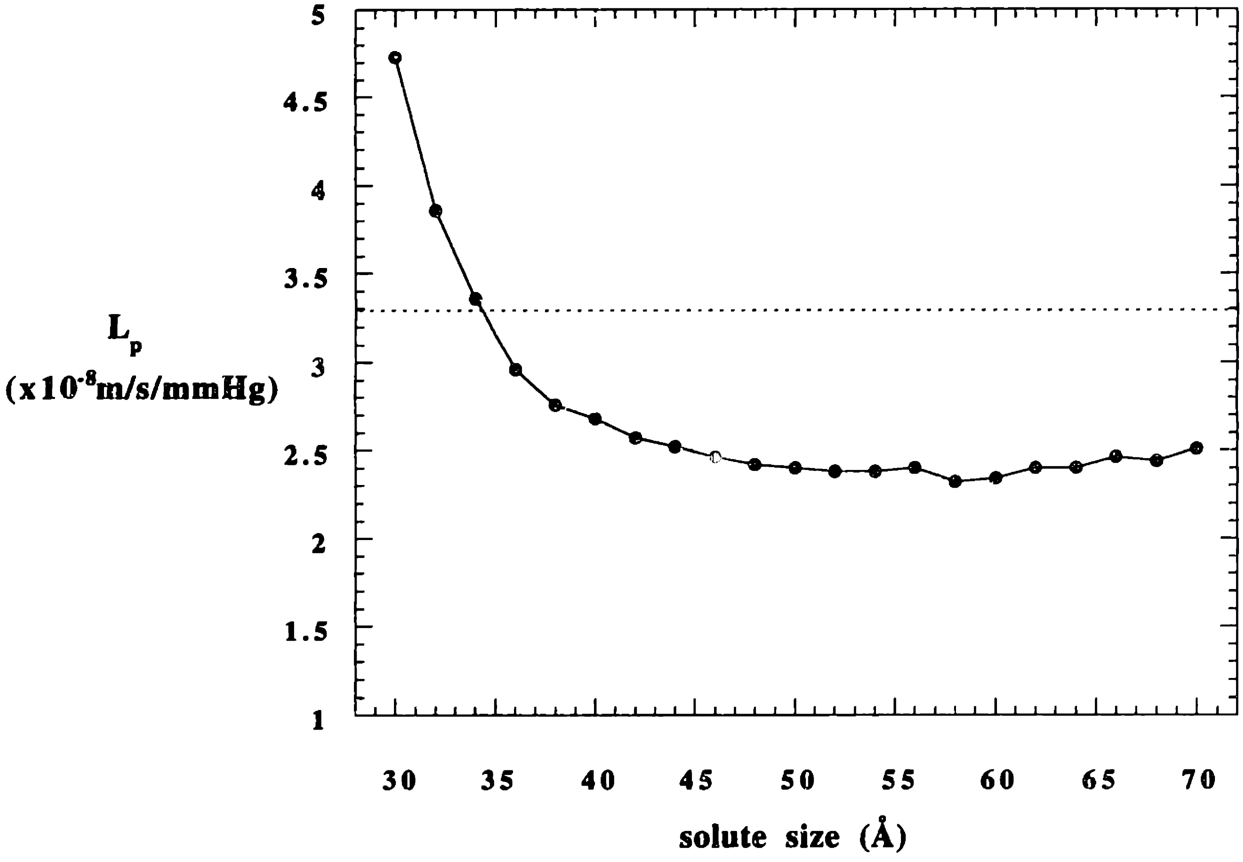

Figure 7-7

Theoretical predictions of the membrane hydraulic permeability at $\Delta P = 35$ mmHg using the fiber matrix model of Curry and Michel (1980). The dashed line indicates the measured value of L_p in our experiments.

Table 7-6

Measured and predicted sieving coefficients using the fiber matrix model of Curry and Michel (1980)

	$\Delta P = 35$ mmHg		$\Delta P = 60$ mmHg	
r_s (Å)	$\Theta^{\text{meas.}}$	$\Theta^{\text{calc.}}$ (% error)	$\Theta^{\text{meas.}}$	$\Theta^{\text{calc.}}$ (% error)
30	0.497	0.396 (-20.2)	0.319	0.347 (+8.9)
40	0.181	0.0190 (+5.4)	0.129	0.153 (+18.5)
50	0.0764	0.0764 (0)	0.0549	0.0549 (0)
60	0.0456	0.00256 (-46.9)	0.0321	0.00166 (-48.3)
70	0.0355	0.00736 (-79.3)	0.0231	0.00420 (-81.9)

The values of the fiber radius (r_f) and the length of fiber per unit volume (l_f) at 35 and 60 mmHg were chosen so as to best fit the data at 50 Å.

---

measurement is available, was calculated using the correlation of Jackson and James (1986) for three-dimensional arrays, which relates ϕ to the fiber radius and the Darcy permeability:

$$K_{Darcy} = \frac{3\, r_f^2}{20\, \phi} \left[- \ln \phi - 0.931 + O(\ln \phi)^{-1} \right] \tag{7.18}$$

To determine the Darcy permeability of the GBM in the absence of a hydraulic pressure difference, we assumed a linear dependence of K_{Darcy} upon ΔP. Extrapolating the measured values obtained at 35 and 60 mmHg, we obtained the following relationship:

$$K_{Darcy} = 2.404 - 0.0264\,\Delta P_{gbm} \qquad (7.19)$$

where ΔP is expressed in mmHg. As shown, the estimate of the Darcy permeability of GBM at $\Delta P = 0$ mmHg is 2.404 nm^2.

There seems however to be a discrepancy between the calculated volume fractions using this model and those inferred from structural observations. With a fiber radius of 20 Å, the correlation of Jackson and James yields a solid volume fraction ϕ equal to 0.19 at 0 mmHg, 0.23 at 35 mmHg, and 0.27 at 60 mmHg (with $r_f = 50$ Å, $\phi = 0.32$, 0.34 and 0.36, respectively). Assuming that the coarse fibers form a square or hexagonal array, we estimated that the average spacing between fibers should then be on the order of 3-7 nm, a value which is lower than that reported in the literature. A spacing of 16 nm as reported by Takami et al. (1991) corresponds to a volume fraction of 0.04 with $r_f = 20$ Å, and 0.13 with $r_f = 50$ Å, assuming a hexagonal fiber array. Thus the values of ϕ yielded by this one fiber model appear to be too high.

One possible source for this discrepancy could be the expression we use to obtain ϕ from r_f and K_{Darcy} (equation 7.18). As illustrated in the paper of Jackson and James (1986), actual permeabilities can differ by a factor of 4 from the value given by their correlation. Overestimating or underestimating K_{Darcy} by a factor of that magnitude would translate into an error in the volume fraction ϕ of only 10 to 40 % in our case. Such deviations are hence not likely to explain the discrepancy apparent in the results.

Two Fiber Approach

Another possibility is that our representation of the GBM as a network of identical fibers with a uniform radius is overly simplified. Indeed, the main components of the GBM (type IV collagen, laminin, heparan sulfate proteoglycans, entactin and fibronectin) vary in size and structure, and a more accurate picture of the membrane seems to be that of a basic fiber meshwork to which a variety of particles are linked, as described in Chapter 2. The real structure of the matrix might be more closely approximated if the GBM were treated as a composite fibrous medium, with at least two different types of fibers. Shown in Figure 7-8 is a possible schematic picture, in which we considered two populations of fibers in the GBM, one consisting of thick strands, the other of finer fibrils. In this second approach, the two-component matrix was idealized as a random array of coarse fibers (radius a_c, volume fraction ϕ_c) embedded in a matrix of fine fibers (radius a_f, volume fraction ϕ_f).

Ethier (1991) developed a model for flow through a mixed fibrous material composed of two types of fibers with significantly different radii. In this analysis, the disparity in sizes has to be such that the fine matrix appears homogeneous on the length scale of the coarse fibers. The Debye-Brinkman equation was used to model the flow. For a fibrous random array, a cylindrical unit cell was constructed around each coarse fiber; and the effect of surrounding fibers was accounted for via the boundary conditions at the cell boundary ($r = b_c$). Two sets of conditions were examined: at $r = b_c$, the shear was set to zero or the velocity was matched to an idealized external flow field. The net Darcy permeability of the matrix was then calculated as a function of the solid volume fraction of the coarse fibers, the fine fiber radius and the permeability of the fine matrix.

We used these results to show how the concept of a two fiber model might apply to the GBM. Assuming a fine fiber radius of 0.40 nm, the value obtained by Ogston (1973) for hyaluronic acid based on partitioning experiments, and a coarse fiber radius comprised between 2 and 5 nm as suggested above, we computed the net Darcy permeability of the matrix as a function of the coarse fiber solid volume ϕ_c, applying the zero shear model of Ethier (1991; equations 22, 40 and 46) which yields an analytical solution for K_{Darcy}. ϕ_c

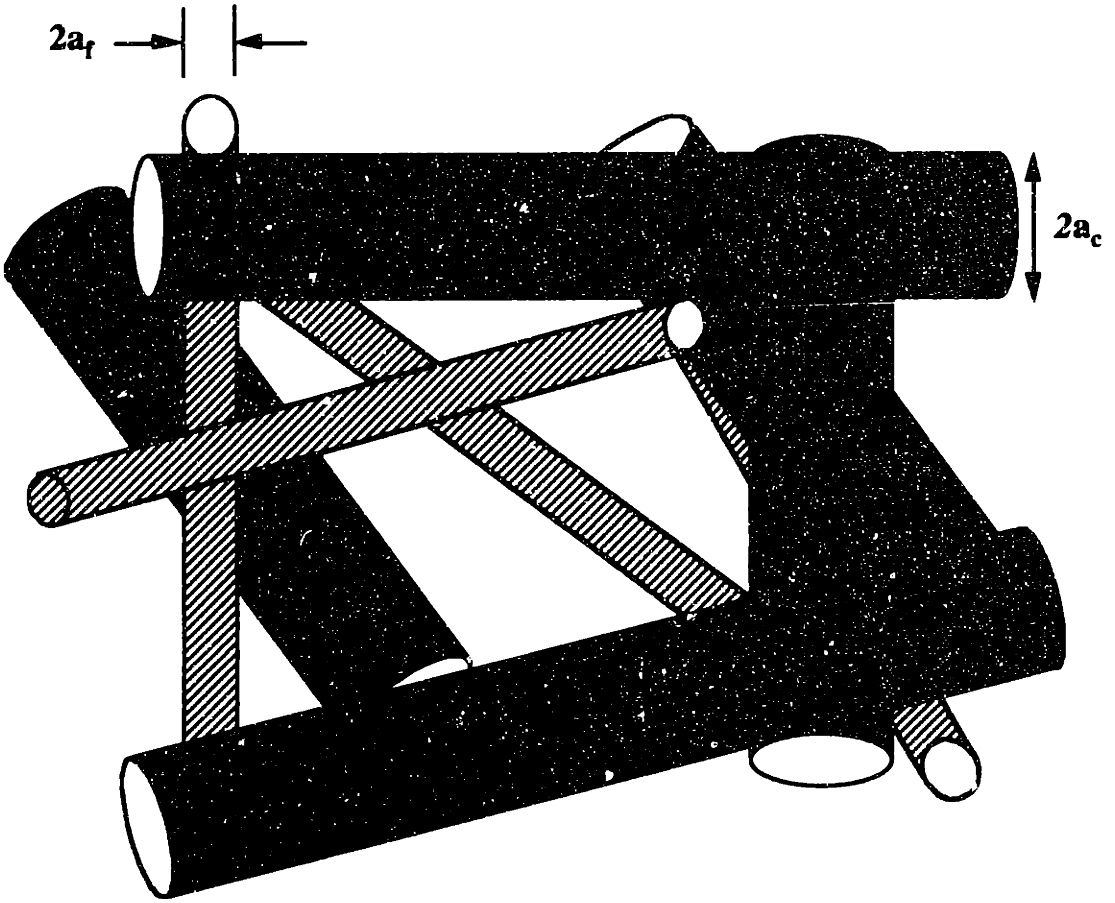

Figure 7-8
Representation of the GBM as a composite fibrous medium with two populations of fibers. a_c and a_f are the radius of the coarse and fine fibers, respectively.

was then related to the spacing between the coarse fibers assuming that the latter formed a hexagonal array. Three different values of the total solid volume fraction, $\phi_t = \phi_c + \phi_f$, were considered, and the permeability of the fine matrix was calculated using the correlation of Jackson and James (equation 7.18). The results are qualitatively similar for a_c ranging from 2 to 5 nm, and are shown in Figure 7-9 for 3 different cases: $\phi_t = 0.10$, 0.15 and 0.20, with $a_c = 4$ nm. As expected, for a fixed coarse fiber spacing (i.e., a fixed ϕ_c), the smaller the total solid volume fraction, the larger the net permeability of the matrix. Given ϕ_t, K_{Darcy} increases with ϕ_c, i.e., it decreases as ϕ_f increases, showing that the permeability is predominantly determined by the population of small fibers. Also indicated in Figure 7-9 are the values of the Darcy permeability which we measured in this study at $\Delta P = 35$ and 60 mmHg, and that extrapolated at $\Delta P = 0$. If we assume a certain value for the total solid volume fraction of the GBM, the coarse fiber spacing can be determined from the curve. If we postulate that $\phi_t = 0.15$, the coarse fiber volume fraction for $\Delta P = 0$ is equal to 0.13 and the corresponding fiber spacing to 13 nm (10 nm with $a_c = 3$ nm). With $\phi_t = 0.10$, $\phi_c = 0.08$ and the computed spacings are on the order of 19 nm (15 nm with $a_c = 3$ nm). These values are close to experimental measurements, thereby showing that a mixed fibrous medium model for the GBM can accomodate the water permeability data quite well. Unfortunately, no such model is available presently for solute transport, and additional theoretical and experimental studies are needed to further extend this model to account for macromolecular sieving.

7.5 Conclusion

In summary, we found that the contribution of the GBM to the overall size-selectivity of the capillary wall is smaller than that of the cell layers, yet not negligible. We obtained consistent results for permeability coefficients assuming a linear dependence on ΔP. The semi-empirical expressions for the hindrance coefficients presented here allow for predictions of sieving data across the GBM given any ΔP. Water permeability data for isolated GBM are consistent with a representation of the GBM as a random fibrous network with two homogeneous populations of fibers.

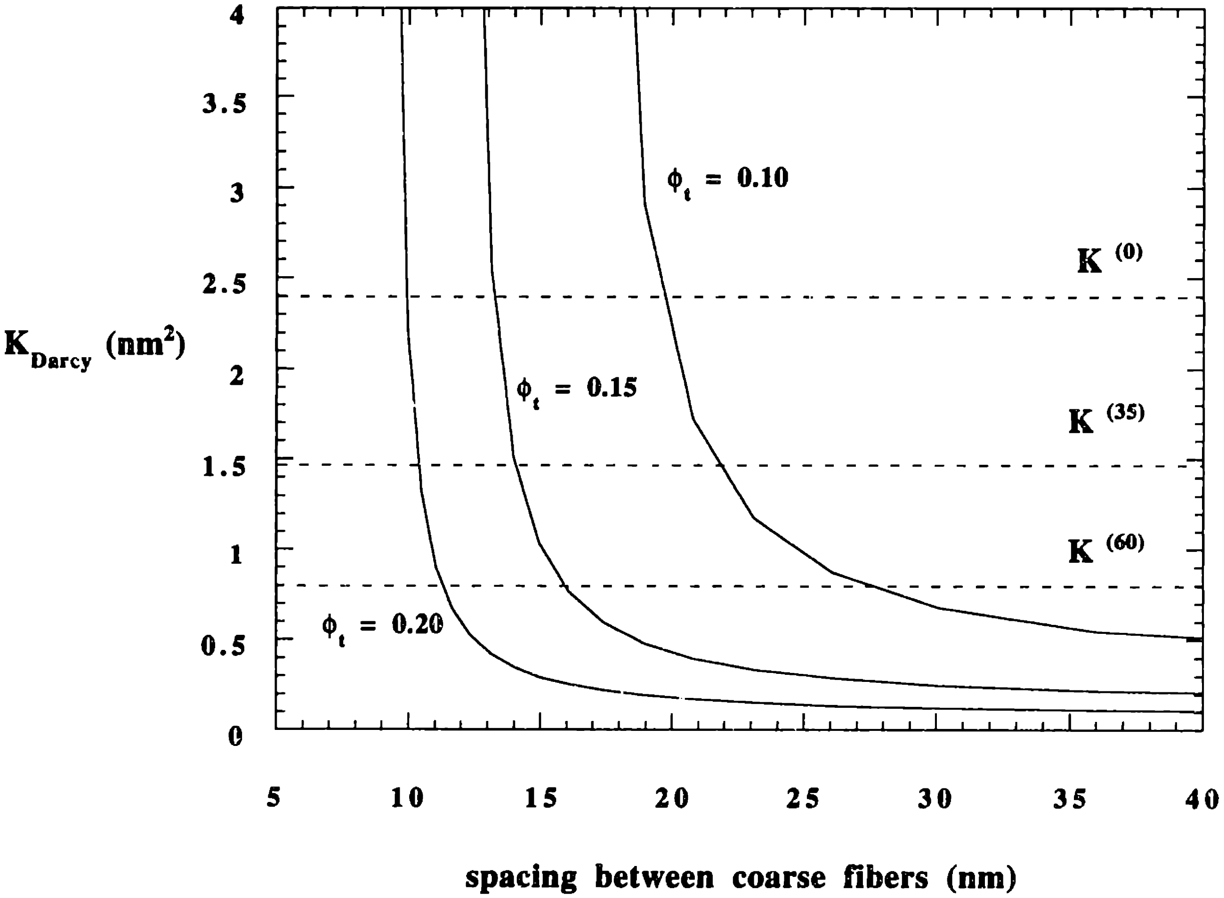

Figure 7-9

Theoretical predictions of the Darcy permeability of the matrix as a function of the spacing between the coarse fibers, using a two-component fibrous medium approach. The results are plotted for three different values of the total solid volume fractions, $\phi_t = 0.10$, 0.15 and 0.20, assuming a fine and coarse fiber radius of 0.4 and 4 nm, respectively. Also shown are the experimental values of the Darcy permeability for $\Delta P = 0$, 35 and 60 mmHg (dashed lines).

Chapter Eight

Macromolecular Sieving Coefficients across the Glomerular Capillary Wall

8.1 Introduction

Glomerular permselectivity is usually assessed by measuring the urinary clearance of exogenous test solutes and inferring from these measurements, by means of a mathematical model, geometrical parameters related to the structure of the wall; the effects of diseases can thereby be associated with changes in these parameters. We therefore wished to extend the ultrastructural model to predict macromolecular sieving coefficients. The development of the model for that purpose is presented in this chapter.

The transport of macromolecules across the glomerular basement membrane is first described in part 8.2, and an estimate of the contribution of the endothelium is calculated in part 8.3. The assembly of overall model is then presented in part 8.4. Shown in section 8.5 are theoretical sieving curves for various ultrastructural parameter values, as well as results of fits to experimental data. Finally, the strengths and weaknesses of this approach are discussed in the last part.

8.2 Transport of Macromolecules across the Glomerular Basement Membrane

As described in Chapter 7, the flux N of a macromolecule in the GBM is given by:

$$\mathbf{N} = -K_d D_\infty \nabla C + K_c \mathbf{V} C \qquad (8.1)$$

where C and **V** are the solute concentration and the filtrate velocity, respectively, both averaged over a length scale that is large compared to that of the microstructure of the GBM fibers. The hindrance coefficients for diffusion and convection, K_d and K_c, respectively, were determined in the last two chapters. The velocity vector **V** was obtained by solving Darcy's equation, as described in Chapter 4. At steady-state, the (local) concentration profile based upon the unit cell (Figure 4-3) is obtained by solving the solute conservation equation:

$$\nabla \bullet \mathbf{N} = 0 \tag{8.2}$$

with the following boundary conditions:

$$N_z = \frac{\varepsilon_s N_0}{\varepsilon_f} \qquad \text{at the interface between the GBM and the fenestrae} \tag{8.3a}$$

$$C = \Phi C_0 \qquad \text{at the interface between the GBM and the slit} \tag{8.3b}$$

$$\nabla C \bullet \mathbf{n} = 0 \qquad \text{at the areas covered by cells} \tag{8.3c}$$

where C_0 is the average concentration in the fluid adjacent to the slit opening, **n** is a unit vector orthogonal to the surface, and Φ the partition coefficient of the solute between the GBM and the adjacent fluid. If the sieving coefficient for the slit diaphragm (written as $<\Theta_{sd}>^{loc}$, as described in Chapter 4) is known, the second boundary condition at the interface between the GBM and the filtration slit can be replaced by:

$$C = \frac{\Phi C_B}{< \Theta_{sd} >^{loc}} = \frac{\Phi N_0}{< V > \ < \Theta_{sd} >^{loc}} \tag{8.3d}$$

The set of equations (8.1-8.3) was solved using a Galerkin finite element method.We used a finite element mesh with 1600 elements, and the CPU time needed to solve this problem was about 20 seconds on a DECstation 5000/133. The sieving coefficient for the GBM is then given by:

$$\Theta_{gbm}{}^{loc} = \frac{C_0}{C_l} \tag{8.4}$$

where C_l is the average concentration at the endothelial opening adjacent to the GBM, and the subscript "loc" indicates that Θ_{gbm} is a local quantity here, calculated on the basis of one unit cell. A non-dimensional analysis shows that $\Theta_{gbm}{}^{loc}$ is a function of ΦK_c, Pe, ε_f, ε_s, δ_{gbm}/W, and $<\Theta_{sd}>^{loc}$, where:

$$Pe = \frac{\Phi\, K_c < V > \ \delta_{gbm}}{\Phi\, K_d\, D_\infty} \tag{8.5}$$

Since the computational time needed to determine the concentration profile is not negligible, we determined an approximate analytical relationship to relate all the variables. The following expression was fitted to numerical values of $\Theta_{gbm}{}^{loc}$:

$$\Theta_{gbm}{}^{loc} = \frac{\Phi\, K_c}{< \Theta_{sd} >^{loc} - (< \Theta_{sd} >^{loc} - \Phi K_c) \exp\left[-Pe(1+f)\right]} \tag{8.6a}$$

where

$$f = a\,(1 - \varepsilon_s \varepsilon_f)^b\, (\delta_{gbm}/W)^{-c} \tag{8.6b}$$

and a, b and c are three positive constants. This expression has the expected limiting behavior, namely: (i) if ε_f and ε_s approach 1, then $\Theta_{gbm}{}^{loc}$ approaches the solution of the one dimensional problem ; (ii) if $\delta_{gbm}/W >> 1$, $\Theta_{gbm}{}^{loc}$ approaches the solution of the one dimensional problem as well ; (iii) if Pe = 0, then $\Theta_{gbm}{}^{loc}$ is equal to 1. It was assumed that the fractional area covered by the fenestrae remains constant ($\varepsilon_f = 0.20$). The range of parameters used to fit the numerical data was $10^{-5} \leq Pe \leq 10$, $10^{-4} \leq \Phi K_c \leq 1$, $0.01 \leq \varepsilon_s \leq 1$, $0.05 \leq \delta_{gbm}/W \leq 1$, and $10^{-4} \leq \langle\Theta_{sd}\rangle \leq 1$. Using Powell's method (Press et al., 1989) and 10,600 data points, we obtained the following values, with a root-mean square of 5 %:

$$a = 0.7366 \; ; \; b = 11.9864 \; ; \; c = 1.2697. \qquad (8.7)$$

8.3 Contribution of the Endothelium to the Permselectivity of the Barrier

As described in Chapter 4, the resistance of the endothelium to water flow is negligible when compared to that of the slit diaphragm and the glomerular basement membrane, due to the large size of the fenestrae. The exact composition of the fenestrae has not been entirely elucidated. It has been suggested that they are filled with a sparse glycocalyx (Abrahamson, 1987; Avasthi and Koshy, 1988). To determine whether the role of the endothelial layer in solute transport could be neglected, we calculated an upper bound on its contribution by assuming a worst-case scenario, namely, that the fenestrae are filled with the same dense matrix as the glomerular basement membrane. Making that assumption, we computed solute sieving coefficients across the two layers, i.e., endothelium plus GBM, and compared the results with those obtained neglecting the contribution of the endothelium. The fenestrae were represented by two-dimensional rectangular channels, as shown in Figure 4-3.

The concentration profile in the domain composed of the fenestrae and GBM is given by solving equations (8.1-8.2), applying the boundary condition (8.3a) at the interface between the fenestrae and the capillary lumen in this case. The analytical results for the pressure and the velocity in the GBM presented in Chapter 4 are no longer valid here. To obtain the velocity vector **V**, we used Darcy's law (equation 4.7) in the entire domain defined by the GBM and the fenestrae. The continuity equation implies that P verify Laplace's equation, $\nabla^2 P = 0$. Constant volume flux boundary conditions were used at the interface with the capillary lumen on one side and with the slit opening on the other. (As demonstrated in chapter 6, differences due to different types of boundary conditions when solving Laplace's equation are not significant). Once the concentration profile is known, the solute sieving coefficient for that domain can be computed as:

$$\Theta_{gbm+fen}{}^{loc} = \frac{C_0}{C_l} \tag{8.8}$$

where C_l is here the mean concentration at the interface between the fenestrae and the lumen, averaged in the x-direction.

We assumed that the fenestrae are straight channels 60 nm in length, and of such width that ε_f equals 0.2 and the frequency of fenestrae is 1/120 nm^{-1} (Drumond and Deen, 1994a). A Galerkin finite elements method was used to solve the problem numerically, and results are shown for solute radii ranging from 20 to 70 Å. As indicated in Table 8-1, we found that the difference between sieving coefficients with and without the endothelial fenestrae never exceeded 20 %. Since this figure represents an upper bound, it seems reasonable to neglect the contribution of the endothelial fenestrae to the overall resistance to macromolecular transport. With that assumption, the sieving coefficient for the unit cell is given by:

$$\Theta^{loc} = \Theta_{gbm}{}^{loc} <\Theta_{sd}>^{loc} \tag{8.9}$$

8.4 Glomerular Capillary Wall Sieving Coefficients

Table 8-1

Upper bound on the effect of endothelial fenestrae upon solute sieving

r_S (Å)	$\Theta_{gbm+fen}^{loc}$	Θ_{gbm}^{loc}	percent difference (%)
20	0.733	0.789	7.1
25	0.559	0.629	11.1
30	0.387	0.453	14.6
35	0.254	0.303	16.2
40	0.167	0.198	15.7
45	0.114	0.133	14.3
50	0.0812	0.0946	14.2
55	0.0591	0.0701	15.7
60	0.0428	0.0524	18.3
65	0.0311	0.0387	19.6
70	0.0228	0.0282	19.1

The superscrit "loc" indicates that the sieving coefficients are calculated locally, on the basis of one unit cell. Θ_{gbm}^{loc} corresponds to the sieving coefficient across the GBM only, and $\Theta_{gbm+fen}^{loc}$ to that across the endothelial fenestrae and the GBM, assuming that both are filled with the same fibrous matrix.

The coefficients Θ_{gbm}^{loc} and $<\Theta_{sd}>^{loc}$ determined above are local sieving coefficients, corresponding to a given volume flux $J_v = <V>$ based on the area of a unit cell. However, J_v varies along the length of the capillary; since proteins do not cross the barrier as plasma is being filtered, their concentration and thus the osmotic pressure rise in the lumen, thereby decreasing the solvent flux across the capillary wall. As described in Chapter 2, the local volume flux at position y along the capillary is given by Starling's equation:

$$J_v(y) = k\,(\,\overline{\Delta P} - \Delta\Pi(y)\,) \tag{8.10}$$

where the hydraulic permeability k of the capillary wall is calculated based upon the hydraulic permeability of each of the three layers as shown in Chapter 4. The values of k_{ep} and k_{en} were derived previously (Drumond and Deen, 1994a, 1994b) and are assumed to be fixed, while the hydraulic permeability of the GBM depends on the average hydraulic pressure difference across the GBM, $\overline{\Delta P_{gbm}}$. Combining earlier results (equations 4.12 and 7.19), k_{gbm} can be written as:

$$k_{gbm} = K_1\, K_{Darcy} = K_1\, K_{Darcy}^0 (\,1 - \beta\, \overline{\Delta P_{gbm}}\,) \tag{8.11}$$

where K_1 is a proportionality constant and K_{Darcy}^0 is the Darcy permeability of the GBM at zero pressure difference. In order to determine k_{gbm} and thus k, $\overline{\Delta P_{gbm}}$ has to be obtained first. It can be shown to satisfy the following relationship:

$$K_2\, \beta\, \overline{\Delta P_{gbm}}^2 - (\,1 + K_2\,)\, \overline{\Delta P_{gbm}} + \overline{\Delta P} = 0 \tag{8.12a}$$

where

$$K_2 = K_1\, K_{Darcy}^0 \left(\frac{1}{k_{en}} + \frac{1}{k_{ep}} \right) \tag{8.12b}$$

The solute concentration profiles can then be determined by solving the mass balance equations (2.3-2.5), where the solute flux is given by the ultrafiltration boundary condition:

$$J_i(y) = \Theta_{gbm}{}^{loc} < \Theta_{sd} >^{loc} C_i(y)\ J_v(y) \tag{8.13}$$

The overall sieving coefficient of solute i is then computed as:

$$\Theta_i = \frac{\int_0^1 J_i(y)\, dy}{C_{iA} \int_0^1 J_v(y)\, dy} \tag{8.14}$$

where C_{iA} is the afferent concentration of solute i.

All integrals were evaluated using Romberg's method, and differential equations were solved using a Runga-Kutta scheme of order 4 (Press et al., 1989). The CPU time required to compute the sieving coefficients of solutes ranging from 20 to 70 Å in radius on an IBM RS 6000 (model 370) station was approximately 10 s.

8.5 Results

8.5.1 Effect of Ultrastructural Parameters on Sieving Curves

The effect of various ultrastructural parameters on the sieving curves was then assessed as follows. The permeabilities k_{en} and k_{ep} of the endothelium and epithelium, respectively, were assumed to retain the values given earlier (Chapter 4), as well as the number density of fenestrae, the fractional area of fenestrae, and the width of the filtration slit. Values of GBM thickness and filtration slit density were obtained from the study of Drumond et al. (1994), together with hemodynamic inputs. All the parameters used for the simulations are listed in Table 8-2.

As described in Chapter 4, the epithelial slit diaphragms in this model are represented as parallel cylinders (radius r_c), and the spacings between these cylinders are assumed to follow a continuous probability distribution. Calculations were done assuming either a gamma or a lognormal distribution. As shown below, the latter probability function yielded more accurate predictions of in vivo sieving data than the former one. Using a gamma distribution, the model systematically predicted exceedingly small sieving coefficients for large solute radii. For all these reasons, a lognormal distribution of cylinder spacings was preferred and subsequently retained for all calculations. As seen in Chapter 4, this distribution is characterized by two parameters, $\bar{u}$ and s, which can not be chosen independently if we assume that the hydraulic permeability of the slit diaphragm is fixed. The latter hypothesis was made in all subsequent calculations; the parameter s was specified, and the value of $\bar{u}$ was then inferred according to equation (4.35).

Estimates of the ultrastructural parameters related to the slit diaphragm were obtained based on measurements of the diffusional permeability of isolated glomeruli, as described in Chapter 6. Due to the small number of data points (four narrow fractions were used in this study), the uncertainty regarding these parameters is quite high. Using equation (3.14), we computed the 90 % confidence intervals for s based on the results presented in Table 6-4, and obtained the following bounds:

$$\text{for } r_c = 1.0 \text{ nm},\ 1.64 \leq s \leq 1.96 \qquad (8.15a)$$

$$\text{for } r_c = 2.0 \text{ nm},\ 1.40 \leq s \leq 1.64 \qquad (8.15b)$$

$$\text{for } r_c = 4.0 \text{ nm},\ 1.22 \leq s \leq 1.38 \qquad (8.15c)$$

In the absence of more precision, we first examined the effect of varying these two parameters on the sieving curves. The qualitative effects on Θ of changes in the cylinder radius for a given spread of the distribution, which translate into changes in $\bar{u}$ for a fixed s, are illustrated in Figure 8-1. The general shape of the sieving curve appears to be dictated

Table 8-2

Ultrastructural parameters and hemodynamic quantities used to predict sieving data

Ultrastructural parameters :

Permeability of endothelium k_{en} (m/s/Pa)	$2.0\text{x}10^{-7}$†
Permeability of epithelium k_{ep} (m/s/Pa)	$8.6\text{x}10^{-9}$†
Fractional area of fenestrae ε_f	0.2†
Number density of fenestrae N_f/W (m^{-1})	$8.33\text{x}10^{6}$†
Width of epithelial slits W_s (nm)	39†
Darcy permeability of GBM for $\overline{\Delta P_{gbm}} = 0$ (nm^2)	2.40¶
GBM thickness δ_{gbm} (nm)	518*
Width of structural unit cell W (nm)	465*

Hemodynamic parameters :

GFR (ml/min)	113*
Afferent plasma flow rate Q_A (ml/min)	618*
Afferent oncotic pressure $\Pi_{GC,A}$ (mmHg)	23.2*
$\overline{\Delta P}$ (mmHg)	40*

---

† Drumond and Deen (1994a); ¶ Chapter 7; * Drumond et al. (1994).

by s; if s remains constant, the curve is nearly uniformly shifted downwards as the cylinder radius decreases, as confirmed by similar plots for other fixed values of s (data not shown).

For a fixed value of the cylinder radius, s was then varied from 1.0 to 2.0. Representative results are plotted in Figure 8-2, for the case $r_c = 2$ nm. Assuming that the cylinder spacing remains constant (i.e., s = 1.0), the gap half-width is equal to 12 Å, so that solutes with a radius larger than 20 Å can not be filtered ($\Theta = 0$). As expected, for a fixed r_c, the larger the spread of distribution, the larger $\Theta(r_s)$. As shown in Figures 8-1 and 8-2, the sieving curves are strongly dependent upon the values of r_c and s.

We then investigated the effects of an increase in the thickness δ_{gbm} of the glomerular basement membrane, and/or a decrease in the filtration slit frequency (i.e., an increase in the width W of the unit cell, which is based upon one epithelial slit). The parameters of the cylinder spacing distribution were kept identical in all cases, and changes in the sieving curves following a two-fold increase in δ_{gbm} and/or a threefold increase in W were examined. Such structural changes are representative of what has been observed in patients with membranous nephropathy and minimal change nephropathy (Drumond et al., 1994). The baseline inputs were those given in Table 8-2. Results are shown in Figure 8-3 for $r_c = 2$ nm and s = 1.50. Changes in W and/or δ_{gbm} appear to have very little effect on overall sieving coefficients. The biggest differences in Θ are seen for the largest solute radii and never exceed one order of magnitude. The largest deviations from the baseline case occur when δ_{gbm} is multiplied by two and W kept constant. The sieving coefficients are then increased, as the direction of the flow in the GBM is then more unidirectional. Conversely, when W is multiplied by three and δ_{gbm} kept constant, Θ slightly decreases, since the unit cell becomes larger and the flow in the GBM more tortuous. When both W and δ_{gbm} are multiplied, the opposite effects do not compensate each other, and the sieving coefficients remain lower than in the baseline case. Overall, changes in the filtration slit frequency and δ_{gbm} only are unlikely to explain large difference in the permselective properties of the glomerular capillary wall.

Macromolecular hindrance coefficients for the GBM were determined based on the results presented in Chapters 6 and 7. The effects of uncertainties in ΦK_c and ΦK_d on sieving curves were assessed here by assuming an error by a factor 2 or 0.5 in either of these coefficients. As indicated by equation (8.6), the local sieving coefficient for the GBM depends significantly on ΦK_c and ΦK_d, and $\Theta^{loc} = \Theta_{gbm}{}^{loc} <\Theta_{sd}>^{loc}$ is thus expected to vary accordingly. Results are shown in Figure 8-4. As predicted by the theory, sieving coefficients vary significantly with ΦK_c and ΦK_d, and the magnitude of the changes decreases with increasing solute size. The sieving curve is shifted upward as either ΦK_c is increased, or ΦK_d is decreased; in the latter case, the increase in Pe which is the only effect results in an increase in Θ because of concentration polarization. Conversely, the sieving curve is lowered when ΦK_d increases or ΦK_c decreases; the effect of multiplying ΦK_d by 2 is almost indistinguishable from that of dividing ΦK_c by 2. When the two coefficients are either both multiplied or both divided by the same factor, the Peclet number remains unaffected and the changes in Θ are minimal, as shown by the curves labeled "$2\Phi K_c$ -$2\Phi K_d$" and "$0.5\Phi K_c$ -$0.5\Phi K_d$". Overall, uncertainties or changes in the hindrance coefficients can affect the sieving curve significantly. The physiological factors that would cause isolated changes in ΦK_c and ΦK_d remain to be investigated, possibly using the methods that we are pioneering.

8.5.2 Predicting In Vivo Ficoll Sieving Data

The ultrastructural model was then used to predict in vivo sieving data. Ficoll sieving measurements in rats were obtained from Oliver et al (1992, 1994) and Remuzzi et al. (1993). The hydrodynamical inputs were those given in each of these studies, and the ultrastructural parameters were those listed in Table 8.2, except for the unit cell width and

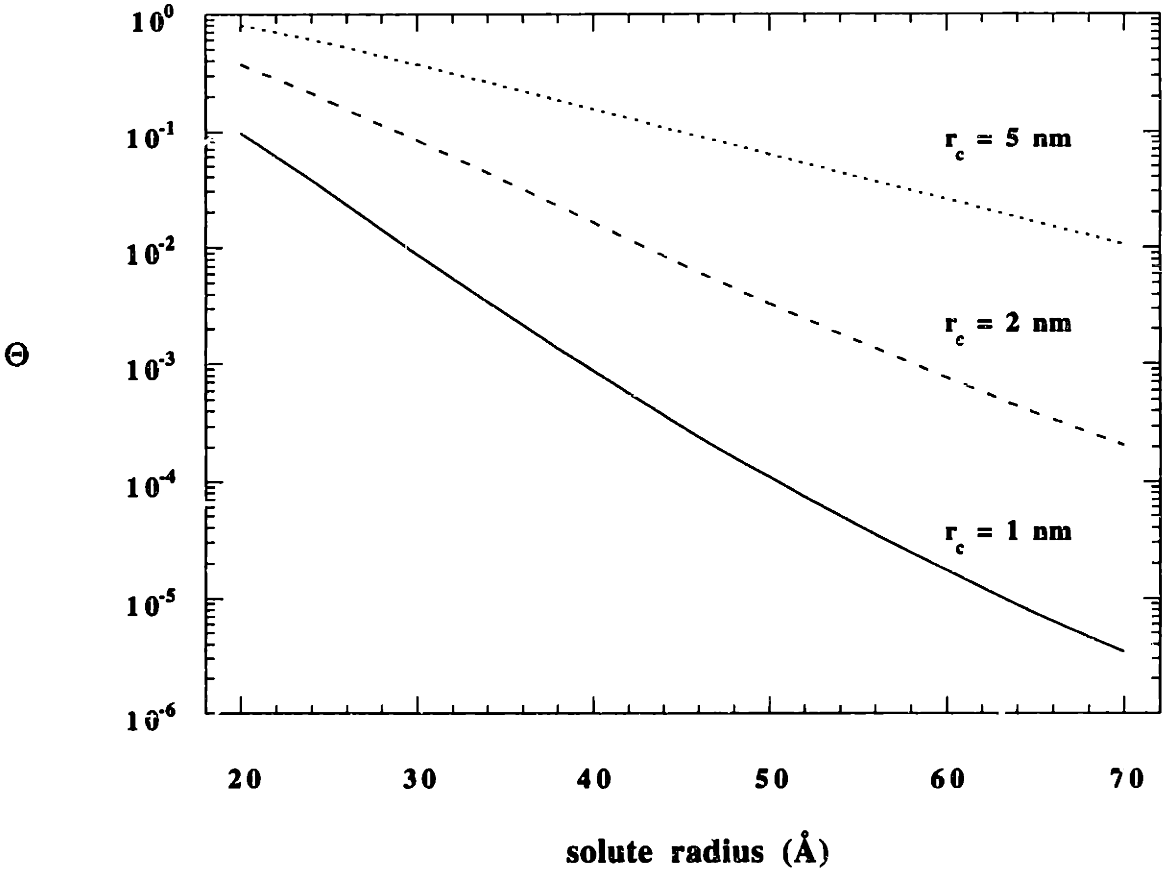

Figure 8-1

Theoretical effects of changes in the slit diaphragm cylinder radius on the sieving coefficients (Θ). Results are plotted for a spread s of the cylinder spacing distribution equal to 1.50, and three different values of the cylinder radius (r_c = 1, 2 and 5 nm).

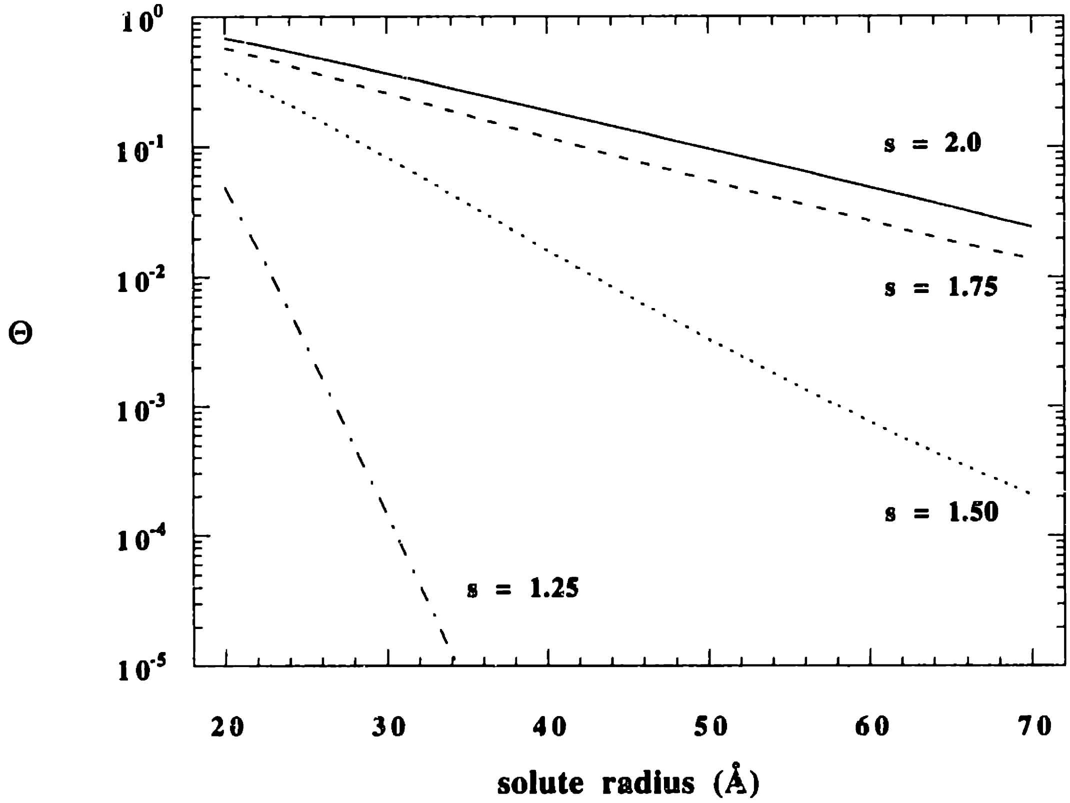

Figure 8-2
Theoretical effects of changes in the spread s of the cylinder spacing distribution on the sieving coefficients (Θ). Results are given for a fixed r_c of 2 nm.

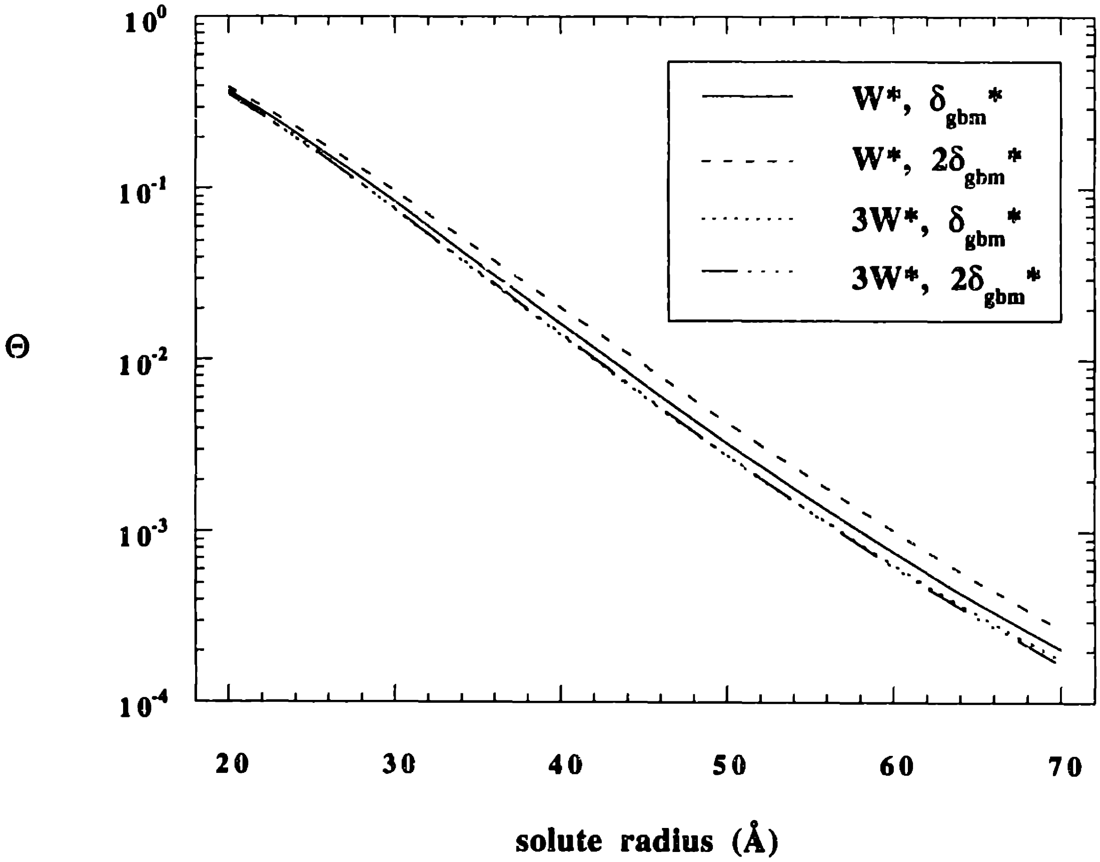

Figure 8-3
Theoretical effects of changes in GBM thickness and unit cell width (i.e., filtration slit frequency) on the sieving coefficients (Θ). Results are plotted for $r_c = 2$ nm and $s = 1.50$. The curve labeled (W*, δ_{gbm}*) corresponds to the baseline case.

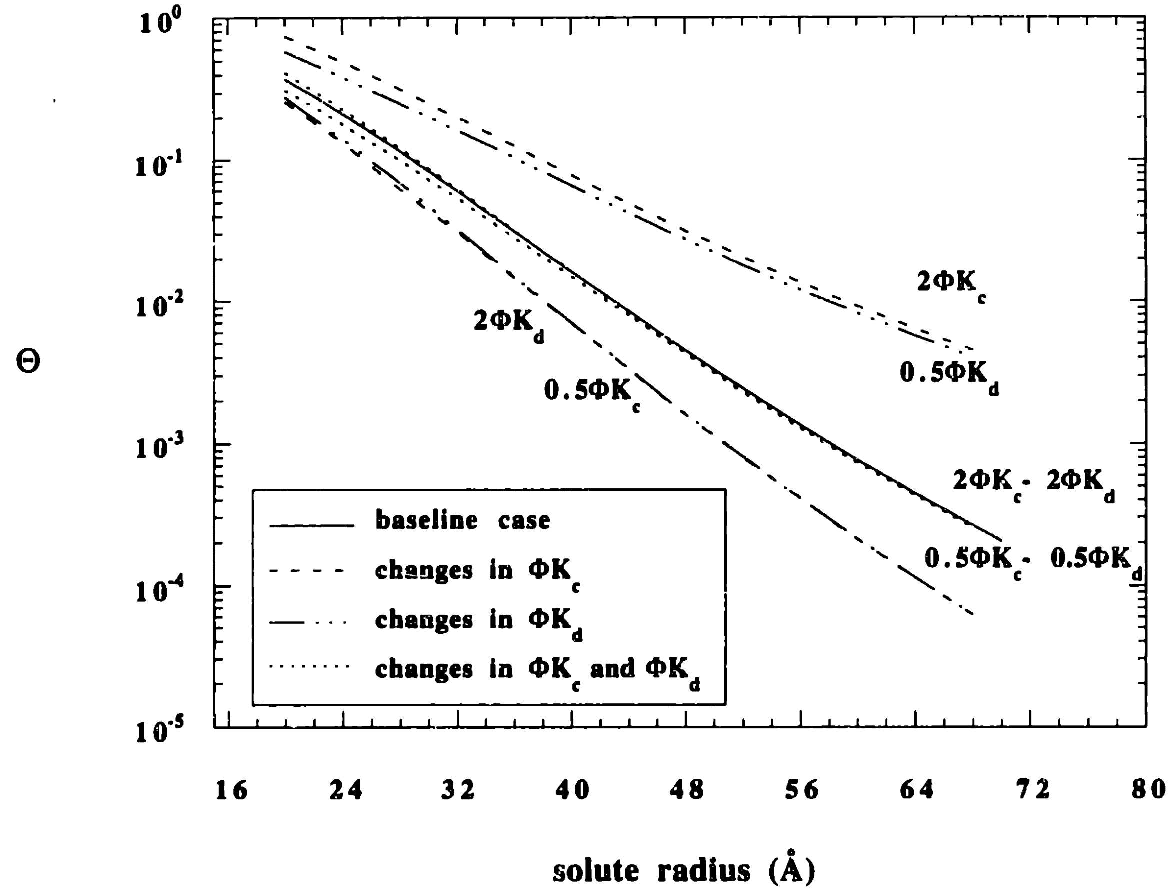

Figure 8-4

Theoretical effects of changes in the GBM hindrance coefficients (ΦK_c, ΦK_d) on the sieving coefficients (Θ). Results are plotted for $r_c = 2$ nm and $s = 1.50$. The plain line corresponds to the baseline case. The hindrance coefficients were varied by a factor 0.5 and 2.0.

the GBM thickness; values of 360 nm for W and 200 nm for δ_{gbm} were chosen as more representative of rat data. The transmembrane pressure difference $\overline{\Delta P}$ was not measured by Remuzzi et al. (1993), and we assumed a value of 40 mmHg. The parameters r_c and s were those obtained in Chapter 6, as listed in Table 6-3. We assumed that the correct parameters were those calculated if small defects in the epithelial slit diaphragm were postulated in the Ficoll diffusion experiments ($f \neq 0$), defects which we assumed were not present in vivo. Results are shown in Figures 8-5, 8-6 and 8-7, corresponding to the data of Oliver et al. (1992), Remuzzi et al (1993) and Oliver et al. (1994), respectively. In general, there was a poor agreement between the data and the theoretical predictions of our model with these sets of parameter values for r_c and s. In Figure 8-5, the slope of the experimental cuve was close to that predicted with $r_c = 1.0$ nm, but the absolute values of Θ were significantly lower. The data of Remuzzi et al. (1993, Figure 8-6) were best predicted assuming $r_c = 2.0$ nm, but in that case the sieving coefficients were overpredicted by a factor 2-5 in the middle range of solute sizes. The best agreement between the theory and the measurements was obtained with the data of Oliver et al. (1994); as illustrated in Figure 8-7, the experimental sieving curve was close to that calculated assuming $r_c = 4.0$ nm, except for large solutes ($r_s > 50$ Å). In light of the significant uncertainties in the values of r_c and s, as well as the important effects that small changes in these parameters have on sieving coefficients, these results are hardly surprising. We then considered the opposite approach: the parameters r_c and s were inferred from the sieving data, and used to predict the diffusion data presented in Chapter 6.

8.5.3 Fitting In Vivo Ficoll Sieving Data

The Ficoll sieving data were fitted by finding the values of r_c and the parameters of the distribution which minimized the least-square difference χ^2 given by:

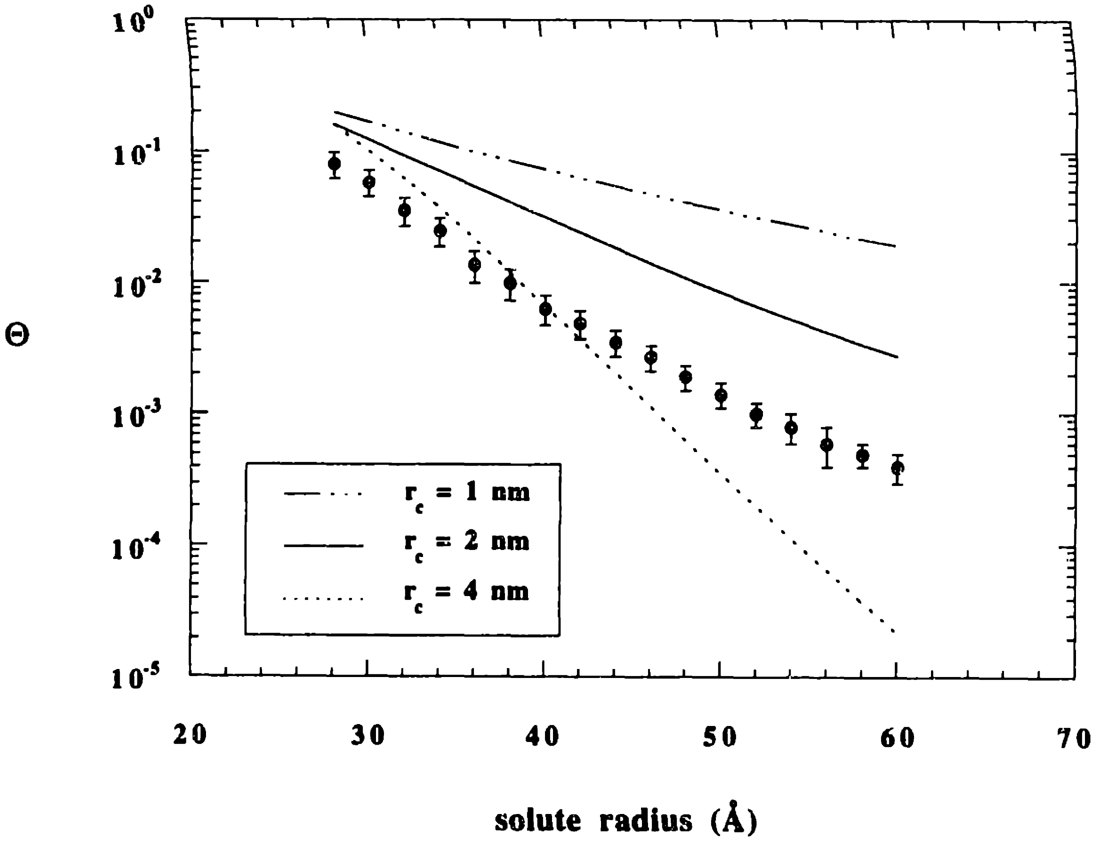

Figure 8-5

Experimental values and theoretical predictions of in vivo Ficoll sieving coefficients (Θ) from the study of Oliver et al. (1992). The experimental results are given as mean ± SE. Theoretical predictions were obtained assuming a lognormal distribution of cylinder spacings, the values of the ultrastructural parameters (r_c,s) being those given in Table 6-3 (corresponding to $f \neq 0$).

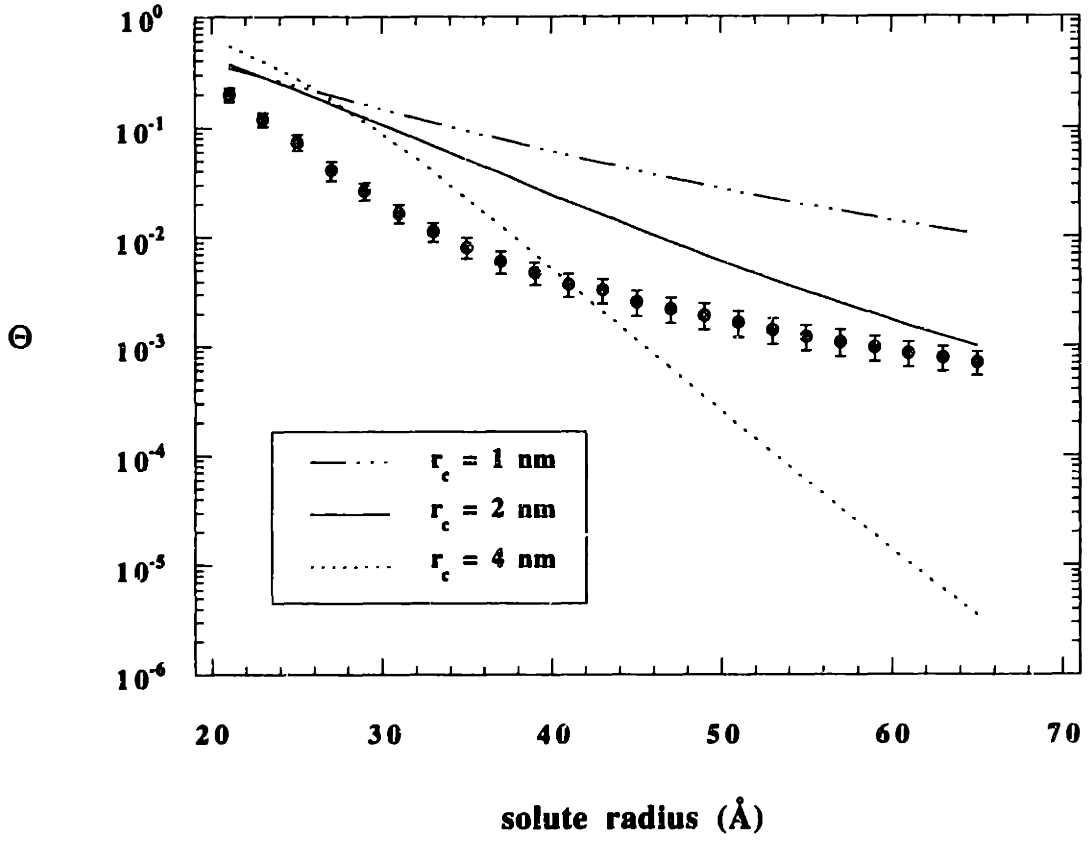

Figure 8-6

Experimental values and theoretical predictions of in vivo Ficoll sieving coefficients (Θ) from the study of Remuzzi et al. (1993). The experimental results are given as mean ± SE. Theoretical predictions were obtained assuming a lognormal distribution of cylinder spacings, the values of the ultrastructural parameters (r_c,s) being those given in Table 6-3 (corresponding to $f \neq 0$).

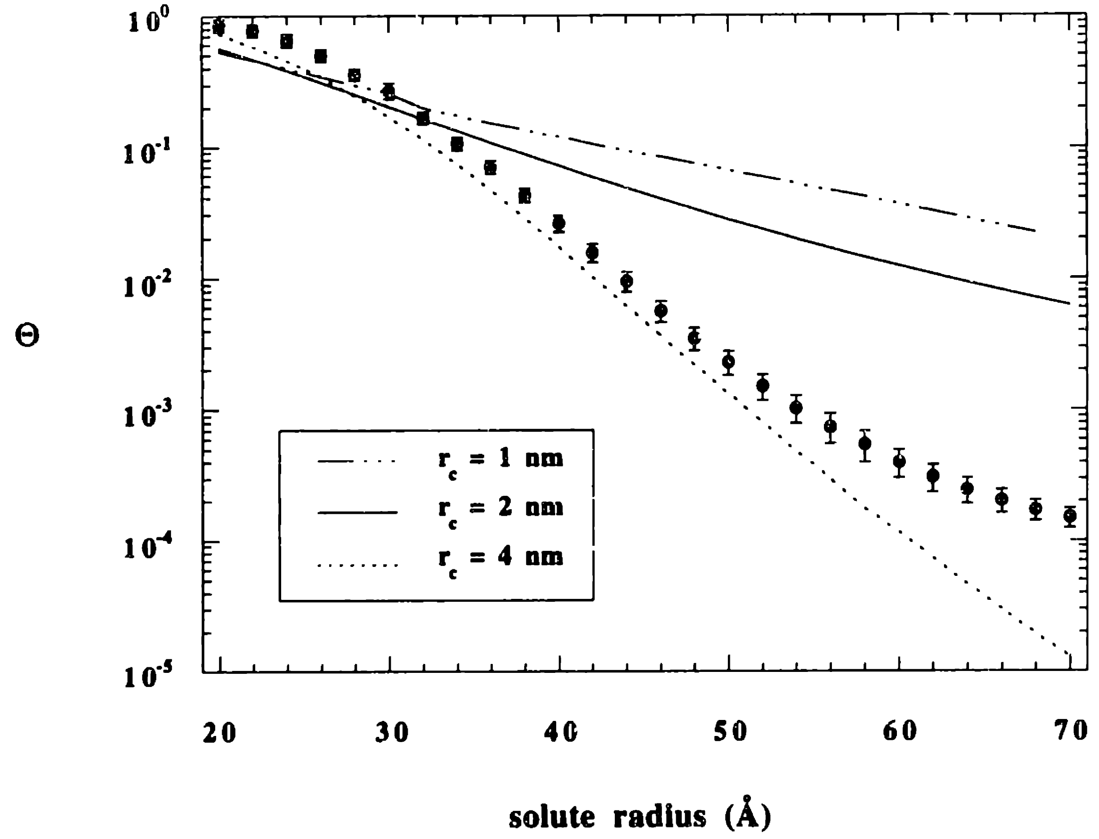

Figure 8-7

Experimental values and theoretical predictions of in vivo Ficoll sieving coefficients (Θ) from the study of Oliver et al. (1994). The experimental results are given as mean ± SE. Theoretical predictions were obtained assuming a lognormal distribution of cylinder spacings, the values of the ultrastructural parameters (r_c,s) being those given in Table 6-3 (corresponding to f≠0).

$$\chi^2 = \sum_{i=1}^{n}\left(\frac{\Theta_i^{exp} - \Theta_i^{calc}}{\sigma_i}\right)^2 \tag{8.16}$$

where n is the number of data points in the sieving curve, Θ_i^{exp} and Θ_i^{calc} are the measured and calculated sieving coefficient of solute i, respectively, and σ_i is the standard deviation of Θ_i^{exp}. Because the data from three experimental studies were obtained from different rat species and/or different physiological conditions, the parameters were fitted to each set separately.

Powell's method (Press et al., 1989) was employed to minimize χ^2, and no boundaries were set on the parameters. The results of the fit are shown in Table 8-3. We considered here two possible distributions for the cylinder spacings, a gamma and a lognormal distribution. The gamma distribution can be characterized by the parameter $\gamma_l^{-1/2}$ (Drumond and Deen, 1995), i.e., the standard deviation divided by the mean, which would correspond to $\ln(s)/\bar{u}$ for the lognormal distribution. As illustrated, the model yielded in the former case a smaller cylinder radius and a wider distribution than in the latter one. Better fits were consistently obtained with a lognormal distribution: the minimum value of χ^2 was about twice higher using a gamma distribution. In light of these results, the lognormal distribution appears to be preferable.

Plotted in Figure 8-8 are the measured and calculated sieving curves, assuming a lognormal distribution. The sieving coefficients predicted by the model are in excellent agreement with all three sets of data. The values of r_c obtained from the data of Remuzzi et al. (1993) and Oliver et al. (1994) are consistent with physiological estimates. In the latter case, the parameters which yielded the best fit (r_c = 4.02 nm and s = 1.32) were close to one of the sets of parameters inferred from the diffusion experiments (r_c = 4.0 nm and s = 1.30), as expected from Figure 8-7. The value of the cylinder radius corrresponding to the study of Oliver et al. (1992), r_c = 0.5 nm, appears to be relatively small compared with estimates reported in the literature, but the reason for that remains unclear. It is possible that there was an artefact in the measurements; this set of data is peculiar in that there is only a 50-fold reduction in Θ between 20 and 65 Å, as opposed to a 300 or 400-fold reduction over a comparable range in the other sets.

We then examined whether the parameters r_c and s obtained by fitting in vivo sieving data are consistent with the in vitro diffusion data obtained in Chapter 6. Three sets of parameters were considered, corresponding to the best-fitted values calculated for the studies of Oliver et al. (1992), Remuzzi et al. (1993) and Oliver et al. (1994), respectively (see Table 8-3). Plotted in Figure 8-9 are the theoretical predictions of the mass transfer coefficient for the cell layers versus the experimental data. The agreement between the calculated and the measured values is poor if we assume that the epithelial layer remained intact during the diffusion experiments. However if a small fraction (~ 0.20-0.30 %) of the surface area was damaged, thereby creating a shunt pathway, the agreement is almost as good as the best fit to the data. These results illustrate once more the fact that since different sets of parameters can predict the diffusion data quite well, r_c and s can not be inferred from them without large uncertainties.

In conclusion, the parameters inferred from in vivo sieving data appear to be consistent with in vitro measurements of diffusion rates across the capillary wall, confirming the validity of our theoretical approach.

8.5.4 Comparison with Pore Models for Glomerular Filtration

Reported in Table 8-4 are the values of χ^2 obtained by the authors of the three studies when fitting to their sieving data the most sophisticated of pore models, the lognormal plus shunt pore models, which has 3 fitted parameters, i.e., one more than the ultrastructural model. Based on this comparison, the ultrastructural model assuming a

Table 8-3

Ultrastructural parameters for the slit diaphragm

Data	Lognormal distribution				Gamma distribution		
	r_c (nm)	s	$\ln(s)/\bar{u}$ (%)	χ^2	r_c (nm)	$\gamma_1^{-1/2}$ (%)	χ^2
Oliver et al. (1992)	0.51±0.08	1.73±0.03	128.8±25.2	44.68	0.03±0.04	747±1018	103.75
Oliver et al. (1994)	4.02±0.21	1.32±0.01	16.94±1.29	75.33	2.67±0.37	43.4±3.4	138.20
Remuzzi et al. (1993)	1.53±0.08	1.50±0.01	46.62±2.99	3.07	0.14±0.10	212±105	7.48

Values for fitted parameters are best-fit values ± SE. The cylinder radius of the slit diaphragm is denoted as r_c; s and $\bar{u}$ are the parameters characteristic of the lognormal distribution of the cylinder spacings, and $\gamma_1^{-1/2}$ that of the gamma distribution.

lognormal distribution of cylinder spacings appears to fit the data almost as well as the lognormal plus shunt pore model. Morevoer, it always yields a better agreement with the data than all the other pore models (data not shown).

Due to the complexity of the ultrastructural model, non-negligible CPU times are required to fit experimental sieving data. To estimate the difference relative to pore models, we compared the length of time needed to find the parameter values minimizing χ^2 using the ultrastructural model with that using the lognormal plus shunt model. The same parameter vector was used as a starting point in all three studies, and computations were carried on a IBM RS 6000 (model 370) workstation. The results, shown in Table 8-4, indicate that the fit can be ~ 3 to 20 times slower with the ultrastructural model. We do not feel however that this is a strong limitation, since significant improvements in CPU time could be obtained by performing the calculations on faster computers.

8.6 Discussion

The ultrastructural model for glomerular filtration presented above is based upon a representation of the glomerular capillary wall which is closer to the real structure than any previous model. It is therefore able to account for changes that previous pore models could not capture, by predicting the effect of specific alterations in any of the three layers of the barrier. Theoretical predictions show that changes in the structural parameters of the slit diaphragm affect the sieving curve very significantly, as well as changes in the hindrance properties of the GBM; variations in GBM thickness or filtration slit frequency have little effect. The GBM may play besides an important role in determining the charge-selective properties of the barrier, which remains to be elucidated.

Table 8-4

Comparison between the ultrastructural and pore models

Source of data	Ultrastructural model lognormal distribution of spacings		Pore model lognormal+shunt	
	χ^2	time (min)	χ^2	time (min)
Oliver et al. (1992)	44.68	23.0	12.5	1.0
Oliver et al. (1994)	75.33	26.0	44.6	1.5
Remuzzi et al. (1993)	3.07	5.0	1.6	1.5

The quantity χ^2 was minimized to fit the model to experimental data. Reported here also is the time required to compute the fitted parameters on an IBM RS 6000 workstation.

The most severe limitation of the model today stems from the fact that the exact structure of the epithelial slit has not been precisely determined. The zipper configuration observed by Rodewald and Karnovsky (1994) was confirmed by Kubosawa and Kondo (1985), but questioned by other groups (Hora et al. 1990; Furukawa et al., 1991). In the absence of a precise description, the slit diaphragm was modeled as a row of parallel cylinders in order to estimate the diffusional and convective hindrances based on available hydrodynamic theories (Drumond and Deen, 1995). As experimental techniques improve, we hope to direct the model to more accurate observations.

Yet, despite the large number of parameters involved, the ultrastructural model appears to give very accurate theoretical predictions for sieving coefficients of neutral macromolecules. Although several of the parameters that are needed, such as the frequency of filtration slits and the thickness of the glomerular basement membrane, were not measured in routine experiments and had to be estimated, fits to available Ficoll sieving data were very satisfactory.

In comparing the ultrastructural model with the widely used pore models of glomerular filtration, we found that it is able to predict published Ficoll sieving data as well as the most performing pore model, the lognormal plus shunt model, which has nevertheless an additional degree of freedom; that, despite the large number of ultrastructural parameters which have to be estimated. Although the calculations for our model are lengthier, we do not feel that this constitutes a major obstacle. It should be noted that our results do not invalidate the use of pore models for comparative purposes.

The model for glomerular filtration therefore appears very promising, and its usefulness will increase as morphological studies provide more accurate data on the exact structure of the capillary wall. It should also be extended to account for the charge selectivity of the glomerular capillary wall, in order to predict the transport of anionic or cationic solutes.

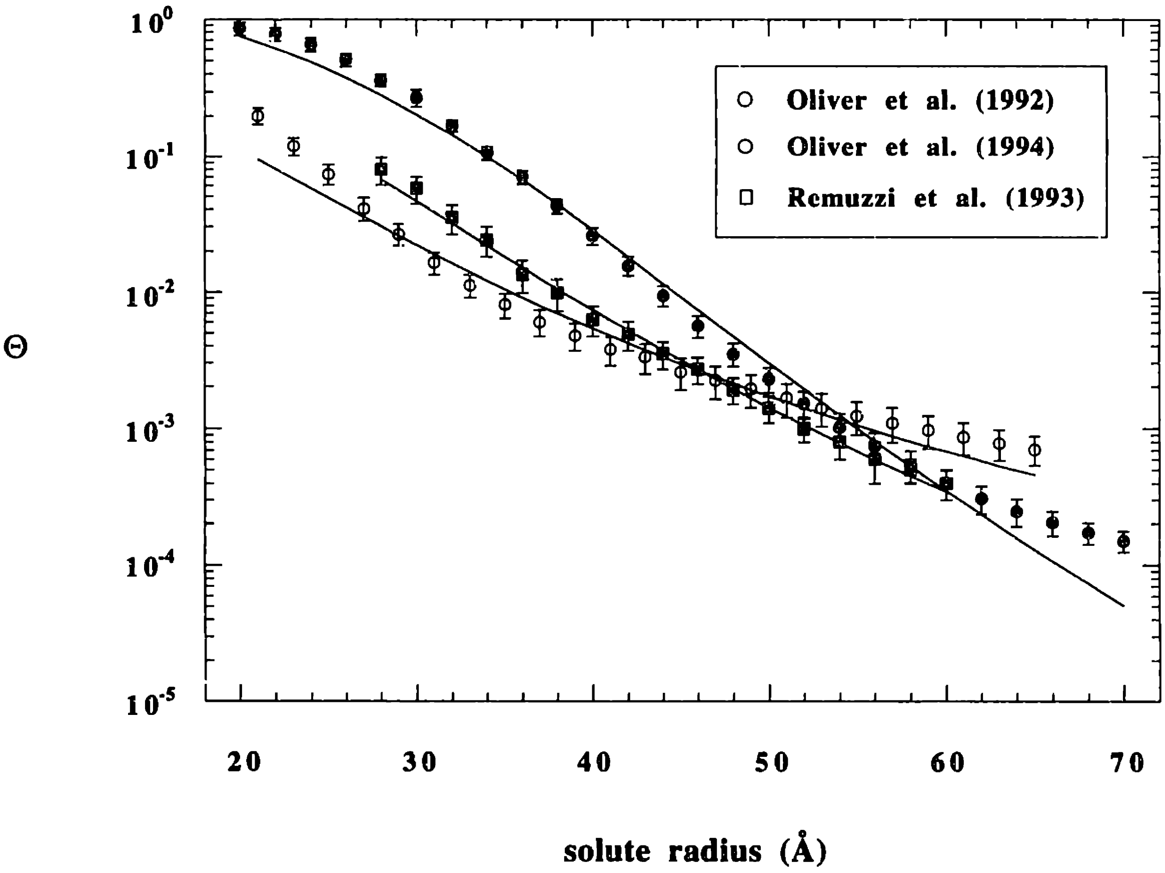

Figure 8-8

Best-fit to in vivo Ficoll sieving data. The experimental results are given as mean ± SE. Theoretical predictions were obtained assuming a lognormal distribution of cylinder spacings, and finding the parameters r_c and s for the slit diaphragm which best fitted the data.

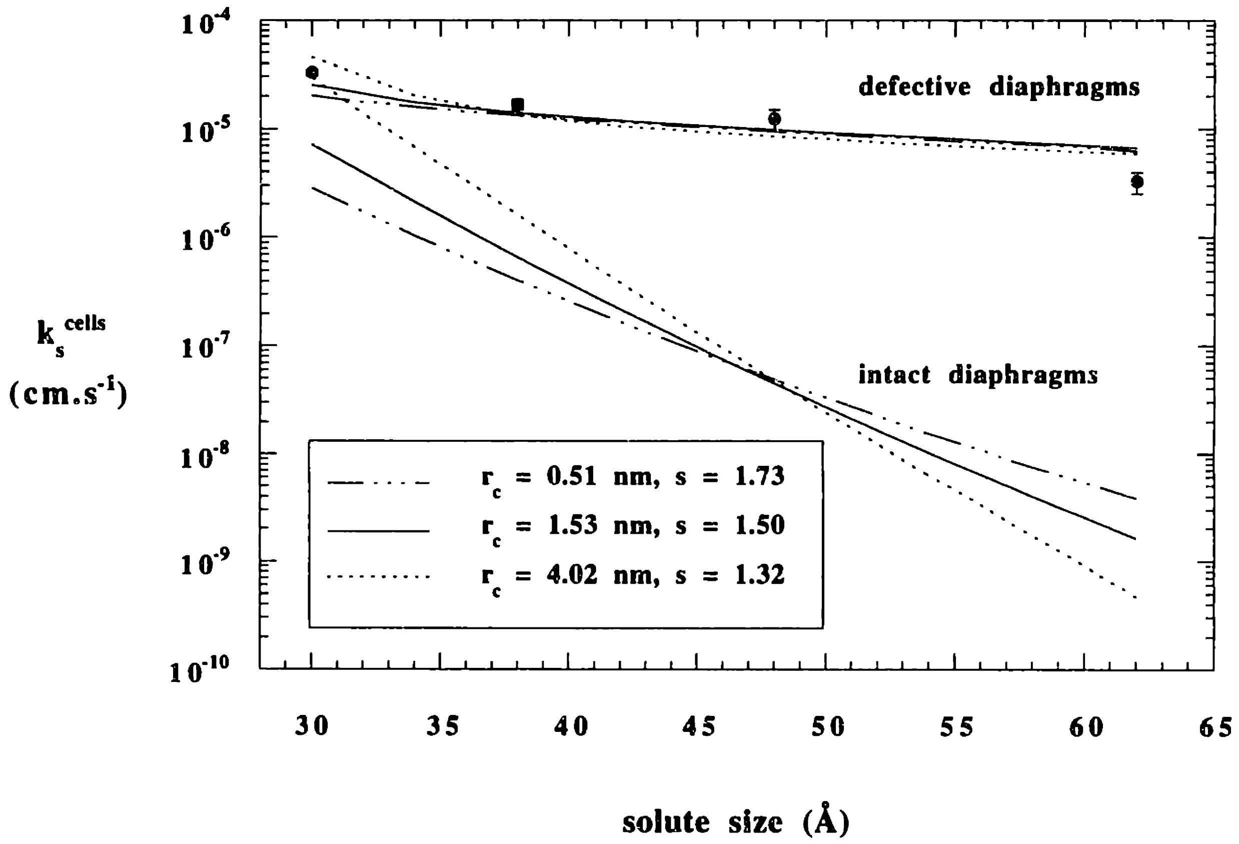

Figure 8-9

Experimental values and theoretical predictions of in vitro mass transfer coefficients for the epithelium (k_S^{cells}). The experimental results are given as mean ± SE. The three sets of the ultrastructural parameters r_C and s were those obtained in fitting in vivo Ficoll sieving coefficients. Two hypotheses were considered: in the first case, all the slit diaphragms were assumed to remain intact; in the second one, a fraction of ~ 0.20 % of the epithelial slit surface had no "ladder rungs".

Chapter Nine

Conclusions and Recommendations

The main contribution of this thesis was to provide a better understanding of the ultrastructural basis for the filtration of macromolecules by glomerular capillaries. Traditional pore models do not account for the complex structure of the filtration barrier, which consists of an endothelial layer, a glomerular basement membrane and an epithelial layer. In this work, we developed a new approach to glomerular filtration by a combination of experimental and theoretical studies.

In Chapter 3, we first demonstrated that pore models of glomerular filtration can not be used to infer the mean transmembrane hydraulic pressure difference ($\overline{\Delta P}$) from macromolecular sieving data. Although these models have been repeatedly employed for that purpose, they appear to be unable to capture the subtle effects of pressure on the sieving curves, and we strongly recommend that they not be used to estimate $\overline{\Delta P}$.

The pore models of glomerular filtration were abandoned in the later chapters in favor of an approach based on the ultrastructure of the capillary wall, presented in Chapter 4. The permselective properties of the glomerular basement membrane (GBM) and the epithelial slit were determined by performing two sets of experiments. We first measured the diffusional permeability of Ficoll across isolated glomerular capillary wall and GBM (Chapter 6), and thereby determined the diffusional resistance of each layer. We then studied the convection and diffusion of these same test solutes across isolated GBM packed in an ultrafiltration cell (Chapter 7). The effects of pressure on water and solute permeability were assessed, and hindrance coefficients in were obtained. We also showed that a two-fiber model, which assumes that two populations of fibers are present in the GBM, was consistent both with the Darcy permeability data and electrom-micrographs observations.

This analysis was then combined with previous results to assemble the ultrastructural model for glomerular filtration, described in Chapter 8. We showed that this model is able to fit in vivo sieving data as well as pore models. Its main advantage is that it can account for specific changes in any of the layers of the capillary wall, and it is our hope that it will eventually provide a much better understanding of the relationship between structural changes and alterations in glomerular function observed in specific diseases.

These conclusions do not invalidate the use of traditional pore models for comparative purposes. However, interpretation of their results is necessarily limited.

The next step in improving upon the ultrastructural approach to glomerular filtration will be to incorporate the effects of macromolecular charge. The charge-selective properties of the glomerular capillary wall are very significant and need to be taken into consideration. In addition, when a more accurate physical description of the epithelial slit diaphragm is available, further improvements in the model will be possible.

We also suggest that a more systematic investigation of the effects of pressure on the permeability of the glomerular basement membrane be performed. Finally, we recommend additional theoretical and experimental studies in order to extend the two-fiber approach to account for solute transport in such a medium.

Bibliography

Abrahamson, D.R. Structure and development of the glomerular capillary wall and basement membrane. *Am. J. Physiol.* 253 (*Renal Fluid Electrolyte Physiol.* 22): F783-F794, 1987.

Anderson, J.L., and J.A. Quinn. Restricted transport in small pores. A model for steric exclusion and hindered particle motion. *Biophys. J.*, 14: 130-150, 1974.

Anderson, S., H.G. Rennke, and B.M. Brenner. Therapeutic advantag eof converting enzyme inhibitors in tarresting progressive renal disease associated with systemic hypertension in the rat. *J. Clin. Invest.*, 77: 1993-2000, 1986.

Andrews, P.M., and A.K. Coffey. Cytoplasmic contractile elements in glomerular cells. *Federation Proc.*, 42: 3046-3052, 1983.

Aumailey, D., and M. Paulson. Cross-linking of laminin-nidogen complexes by tissue transglutaminase: a novel mechanism for basement membrane stabilization. *J. Biol. Chem.*, 266: 308-315, 1989.

Aumailley, M., H. Wiedemann, K. Mann, and R. Timpl. Binding of nidogen and the laminin-nidogen complex to basement membrane collagen type IV. *Eur. J. Biochem.*, 184: 241-248, 1989.

Avasthi, P.S., and V. Koshy. The anionic matrix at the rat glomerular endothelial surface. *Anat. Rec.*, 220: 258-266, 1988.

Bard. Y. *Nonlinear Parameter Estimation.* Academic Press, New York, 1974.

Bates, D.M., and D.G. Watts. *Nonlinear Regression Analysis and its Applications.* Wiley, New York, 1988.

Baylis, C., I. Ichikawa, W.T. Willis, C.B. Wilson, and B.M. Brenner. Dynamics of glomerular ultrafiltration. IX. Effects of plasma protein concentration. *Am. J. Physiol.* 232 (*Renal Fluid Electrolyte Physiol.* 1): F58-F71, 1977.

Ballermann, B.J., D.J. Levenson, and B.M. Brenner. Renin, angiotensin, kinins, prostaglandins, and leukotrienes. In: *The Kidney.* Vol. I, chapt. 9, pp 281-340. B.M. Brenner and F.C. Rector, Jr., editors. W.B. Saunders Co., Philadelphia, 1986.

Blantz, R.C. Effect of mannitol on glomerular ultrafiltration in the hydropenic rat. *J. Clin. Invest.*, 54: 1135-1143, 1974.

Blantz, R.C., K.S. Konnen, and B.J. Tucker. Angiotensin II effects upon the glomerular microcirculation and ultrafiltration coefficient in the rat. *J. Clin. Invest.*, 57: 419-434, 1976.

Blantz, R.C., F.C. Rector, Jr., and D.W. Seldin. Effect of hyperoncotic albumin expansion upon glomerular ultrafiltration in the rat. *Kidney Int.*, 6: 209-221, 1974.

Bohrer, M.P., W.M. Deen, C.R. Robertson, J.L. Troy, and B.M. Brenner. Influence of molecular configuration on the passage of macromolecules across the glomerular capillary wall. *J. Gen. Physiol.*, 74: 584-593, 1979.

Booth, J.M., and C.J. Lumsden. Explaining glomerular pores with fiber matrices. A visualization based on computer modeling. *Biophys. J.*, 64: 1727-1734, 1993.

Brady, J. Hindered diffusion. AIChE Annual Meeting, November 13-18, San Francisco, CA, American Institute of Chemical Engineers, 1994.

Bray, J., and G.B. Robinson. Influence of charge on filtration across renal basement membrane films in vitro. *Kidney Int.*, 25: 527-533, 1984.

Brenner, B.M., N. Schor, and I. Ichikawa. Role of angiotensin II in the physiologic regulation of glomerular filtration. *Am. J. Cardiol.*, 49: 1430-1433, 1982.

Brenner, H., and L.J. Gaydos. The constrained Brownian movement of spherical particles in cylindrical pores of comparable radius. Models of the diffusive and convective transport of solute molecules in membranes and porous media. *J. Colloid Interface Sci.*, 58: 312-356, 1977.

Brinkman, H.C. A calculation of the viscous force exerted by a flowing fluid on a dense swarm of particles. *Appl. Sci. Res.*, A1 : 27-34, 1947.

Bungay, P.M., and H. Brenner. The motion of a closely fitting-sphere in a fluid-filled tube. *Int. J. Multiphase Flow*, 1: 25-56, 1973.

Carman, P.C. *Flow of Gases through Porous Media.* Academic Press, New York, 1956.

Chang, R.L.S. A model to study the dynamics of glomerular ultrafiltration and glomerular capillary permselectivity characteristics. *Microvasc. Res.*, 16: 141-150, 1978.

Chang, R.L.S., W.M. Deen, C.R. Robertson, C.M. Bennett, R.J. Glassock, and B.M. Brenner. Permselectivity of the glomerular capillary wall. Studies of experimental glomerulonephritis in the rat using neutral dextran. *J. Clin. Invest.*, 57: 1272-1286, 1976.

Chang, R.L.S., W.M. Deen, C.R. Robertson, and B.M. Brenner. Permselectivity of the glomerular capillary wall to macromolecules. I. Theoretical considerations. *Biophys. J.*, 15: 861-886, 1975.

Chang, R.L.S., I.F. Ueki, J.L. Troy, W.M. Deen, C.R. Robertson, and B.M. Brenner. Permselectivity of the glomerular capillary wall to macromolecules. II. Experimental studies in rats using neutral dextran. *Biophys. J.*, 15: 887-906, 1975.

Clementi F., and G.E. Palade. Intestinal capillaries. II. Structural effects of EDTA and histamine. *J. Cell Biol.*, 42: 706-714, 1969.

Colton, C.K., and K.A. Smith. Mass transfer to a rotating fluid. I Transport from a stationary disk to a fluid in Bodewadt flow. *Am. Inst. Chemical Eng. J.*, 18: 949-958, 1972.

Colton, C.K., and K.A. Smith. Mass transfer to a rotating fluid. II. Transport from the base of an agitated cylindrical tank. *Am. Inst. Chemical Eng. J.*, 18: 958-967, 1972.

Courtoy, P.J., Y.S. Kanwar, R.D. Hynes, and M.G. Farquhar. Fibronectin localization in the rat glomerulus. *J. Cell Biol.*, 87: 691-696, 1980.

Curry, F.E., and C.C. Michel. A fiber matrix model of capillary permeability. *Microvasc. Res.*, 20: 96-99, 1980.

Daniels, B.S., E.H. Hauser, W.M. Deen, and T.H. Hostetter. Glomerular basement membrane: in vitro studies of water and protein permeability. *Am. J. Physiol.* 262 (Renal Fluid Electrolyte Physiol. 31): F919-F926, 1992.

Daniels, B.S., W.M. Deen, G. Mayer, T. Meyer, and T.H. Hostetter. Glomerular permeability barrier in the rat: functional assessment by in vitro methods. *J. Clin. Invest.*, 92: 929-936, 1993.

Davidson, M. G, and W.M. Deen. Hindered diffusion of water-soluble macromolecules in membranes. *Macromolecules*, 21: 3474-3481, 1988.

De Belder, A.N., and K. Granath. Preparation and properties of fluorescein-labelled dextran. *Carbohydrate Res.*, 30: 375-378, 1973.

Deen, W.M. Hindered transport of large molecules in liquid-filled pores. *Am. Inst. Chem. Eng. J.*, 33: 1409-1425, 1987.

Deen, W.M., M.P. Bohrer, and N.B. Epstein. Effects of molecular size and configuration on diffusion in microporous membranes. *Am. Inst. Chem. Eng. J.*, 27: 952-959, 1981.

Deen, W.M., C.R. Bridges, B.M. Brenner, and B.D. Myers. Heteroporous models of glomerular size selectivity: application to normal and nephrotic humans. *Am. J. Physiol.* 249 (*Renal Fluid Electrolyte Physiol.* 18) : F374-F389, 1985.

Deen, W.M., C.R. Robertson, and B.M. Brenner. A model of glomerular filtration in the rat. *Am. J. Physiol.*, 223: 1178-1183, 1972.

Deen, W.M., C.R. Robertson, and B.M. Brenner. Concentration polarization in an ultrafiltering capillary. *Biophys. J.*, 14: 412-431, 1974.

Dohlman, C.H. and E.A. Bazals. Descemet's membrane of the bovine cornea. *Arch. of Biochem. and Biophys.*, 57:445, 1955.

Drumond, M.C., B. Kristal, B.D. Myers, and W.M. Deen. Structural basis for reduced glomerular filtration capacity in nephrotic humans. *J. Clin. Invest.*, 94: 1187-1195, 1994.

Drumond, M.C., and W.M. Deen. Structural determinants of glomerular hydraulic permeability. *Am. J. Physiol.* 266 (*Renal Fluid Electrolyte Physiol.* 35): F1-F12, 1994a.

Drumond, M.C., and W.M. Deen. Stokes flow through a row of cylinders between parallel walls: model for the glomerular slit diaphragm. *J. Biochem. Eng.*, 116: 184-189, 1994b.

Drumond, M.C., and W.M. Deen. Hindered transport of macromolecules through a single row of cylinders: application to glomerular filtration. *J. Biomech. Eng.*, 117: 414-422, 1995.

Du Bois, R., P. Decoodt, J.P. Gassee, A. Verniory, and P.P. Lambert. Determination of glomerular intracapillary and transcapillary pressure gradients from sieving data. I. A mathematical model. *Pfluegers Arch.*, 356: 299-316, 1975.

Du Bois, R., and E. Stoupel. Permeability of artificial membranes to a pluridisperse solution of ^{125}I-polyvinylpyrrolidone. *Biophys. J.*, 16: 1427-1445, 1076.

Dworkin, L.D., I. Ichikawa, and B.M. Brenner. Hormonal modulation of glomerular function. *Am. J. Physiol.* 244 (*Renal Fluid Electrolyte Physiol.* 13): F95-F104, 1983.

Edwards, R.M. Segmental effects of norepinephrine and angiotensin II on isolated renal microvessels. *Am. J. Physiol.*, 244: F526-F534, 1983.

Edwards, A., and W.M. Deen. Error propagation in the estimation of glomerular pressure from macromolecular sieving data. *Am. J. Physiol.* 268 (*Renal Fluid Electrolyte Physiol.* 37): F736-F745, 1995.

Eno, L., J.G. Beume, and H. Rabitz. Sensitivity analysis of experimental data. *Appl. Math. Comp.*, 16: 153-163, 1985.

Ethier, C.R. Flow through mixed fibrous porous materials. *AIChE J.*, 37: 1227-1236, 1991.

Farquhar, M.G. The glomerular basement membrane: a selective macromolecular filter. In: *Cell Biology of Extracellular Matrix*, pp 335-378. E.D. Hay, Plenum, New York, 1981.

Farquhar, M.G., S.L. Wissig, and G.E. Palade. Glomerular permeability. I. Ferritin transfer across the normal glomerular capillary wall. *J. Exp. Med.*, 113: 47-56, 1961.

Forster, R.P., and J.P. Maes. Effect of experimental neurogenic hypertension on renal blood flow and glomerular filtration rates in intact denervated kidneys of unanesthetized rabbits with adrenal glands demedullated. *Am. J. Physiol.*, 150: 534-540, 1947.

Furukawa, T., S. Ohno, H. Oguchi, K. Hora, S. Tokunaga, and S. Furuta. Morphometric study of glomerular slit diaphragms fixed by rapid-freezing and freeze-substitution. *Kidney Int.*, 40: 621-624, 1991.

Happel, J., and H. Brenner. *Low Reynolds Number Hydrodynamics*. Martinus Nijhoff Publishers, The Hague, 1983.

Haskin, C.L., I.L. Cameron, and D. H. Rohrbach. Role of water hydration on the filtration function of proteoglycans. In: *Molecular and Cellular Aspects of Basement Membranes*, pp 89-106. D. Rohrbach and R. Timpl. editors. Academic Press, Inc., New York, 1993.

Gassee, J.P., P. Decoodt, A. Verniory, and P.P. Lambert. Autoregulation of effective glomerular pressure. *Am. J. Physiol.*, 226: 616-623, 1974.

Gassee, J.P., R. Du Bois, M. Stakourine, and P.P. Lambert. Determination of glomerular intracapillary and transcapillary pressure gradients from sieving data. III. The effect of Angiotensin II. *Pfluegers Arch.*, 367: 15-24, 1976.

Glassock, R.J., S.D. Adler, H.J. Ward, and A.H. Cohen. Primary glomerular diseases. In: *The Kidney*. Vol. I, chapt. 22, pp 929-1013. B.M. Brenner and F.C. Rector, Jr., editors. W.B. Saunders Co., Philadelphia, 1986.

Goldberg, M., and F. Escaig-Haye. Is the lamina lucida of the basement membrane a fixation artifact ? *Eur. J. Cell. Biol.*, 42: 365-368, 1986.

Golbetz, H., V. Black, O. Shemesh, and B.D. Myers. Mechanism of antiproteinuric effect of indomethacin in nephrotic humans. *Am. J. Physiol.*, 256 (*Renal Fluid Electrolyte Physiol.* 25) : F44-F51, 1989.

Grodzinsky, A.J. Electromechanical and physicochemical properties of connective tissue. *Critical Rev. Biomed. Eng.*, 9: 133-199, 1983.

Gunther, S., R.W. Alexander, W.J. Atkinson and M.A. Gimbrone, Jr. Functional angiotensin II receptors in cultured vascular smooth muscle cells. *J. Cell Biol.*, 92: 289-298, 1982.

Hall, B.V. A slit pore theory of capillary filtration based on electron microscopic data on the filtration pathway through the cellular layers of mammalian glomerular capillary walls. *Trans. Am. Micros. Soc.*, 96: 413-437, 1977.

Haley, D.P., M. Sarrafian, R.E. Bulger, D.C. Dobyan, and G. Eknoyan. Structural and functional correlates of effects of angiotensin-induced changes in rat glomerulus. *Am. J. Physiol.* 253 (*Renal Fluid Electrolyte Physiol.* 22): F111-F119, 1987.

Holmes, J.T., C.R. Wilke, and D.R. Olander. Convective mass transfer in a diaphragm diffusion cell. *J. Phys. Chem.*, 67: 1949-1472, 1963.

Hora, K., S. Ohno, H. Oguchi, T. Furukawa, and S. Furuta. Three-dimensional study of the glomerular slit diaphragm by the quick-freezing and deep-etching replica method. *European J..Cell Biol.*, 53: 402-406, 1990.

Huss, R.E., D.J. Marsh, and R.E. Kalaba. Two models of glomerular filtration rate and renal blood flow in the rat. *Ann. Biomed. Eng.*, 3: 72-99, 1975.

Ichikawa, I., and B.M. Brenner. Mechanisms of action of histamine and histamine antagonists on the glomerular microcirculation in the rat. *Circ. Res.*, 45: 737-745, 1979.

Jackson, G.W., and D.F. James. The permeability of fibrous porous media. *Can. J. Chem. Eng.*, 64: 364-374, 1986.

Johansson, L., and J-E. Löfroth. Diffusion and interaction in gels and solutions. IV. Hard sphere dynamics simulations. *J. Chem. Phys.*, 98: 7471-7479, 1993.

Johnson, A.I., and C.J. Huang. Mass transfer studies in an agitated vessel. *Am. Inst. Chem. Eng. J.*, 2: 412 ,1956.

Johnson, E.M., D.A. Berk, R.K. Jain, and W.M. Deen. Hindered diffusion in agarose gels: test of effective medium model. To appear in *Biophys. J.*, 1996.

Juhasz, N.M., and W.M. Deen. Effects of local Peclet number on mass transfer to a heterogeneous surface. *Ind. Eng. Chem. Res.* , 29: 556-562, 1991.

Kanwar, Y.S. Biology of disease. Biophysiology of glomerular filtration and proteinuria. *Lab. Invest.*, 51: 7-21, 1984.

Kanwar, Y.S., and M.A. Venkatachalam. Ultrastructure of glomerulus and juxtaglomerulus apparatus. In: *Handbook of Physiology. Renal Physiology*, sect. 8, vol. I, chapt. 1, p3-40. Am. Physiol. Soc., Bethesda MD, 1992.

Kasinath, B.S., and Y.S. Kanwar. Glomerular basement membrane: biology and physiology. In: *Molecular and Cellular Aspects of Basement Membranes*, pp 89-106. D. Rohrbach and R. Timpl. editors. Academic Press, Inc., New York, 1993.

Kondo, H. Rat glomerular basement membrane visualized in situ by embedment-free sectioning and subsequent platinum-carbon replication. *J. Electron Microscopy Tech.*, 14: 63-69, 1990.

Krause, A.C. *The Biochemistry of the Eye*. Monograph 2. The John Hopkins Press, Baltimore, 1934.

Krishnaiah, P.R. *Handbook of Statistics. Analysis of Variance*. New York: North-Holland, 1980, vol.1, p.294-298.

Kubosawa, H., and Y. Kondo. Ultrastructural organization of the glomerular basement membrane as revealed by a deep-etch replica method. *Cell Tissue Res.*, 242: 33-39, 1985.

Lambert, P.P., B. Aeikens, A. Bohle, F. Hanus, S. Pegoff, and M. Van Damme. A network model of glomerular function. *Microvasc. Res.*, 23: 99-128, 1982.

Lambert, P.P., R. Du Bois, P. Decoodt, J.P. Gassee, and A. Verniory. Determination of glomerular intracapillary and transcapillary pressure gradients from sieving data. II. A phyiological study in the normal dog. *Pfluegers Arch.*, 359: 1-22, 1975.

Lambert, P.P., J.P. Gassee, A. Verniory, and P. Ficheroulle. Measurement of the glomerular filtration pressure from sieving data for macromolecules. *Pfluegers Arch.*, 329: 34-58, 1971.

Lambert, P.P., A. Verniory, J.P. Gassee, and P. Ficheroulle. Sieving equations and effective glomerular pressure. *Kidney Int.*, 2: 131-146, 1972.

Laurie, G.W., C.P. Leblond, S. Inoue, G.R. Martin, and A. Chung. Fine structure of the glomerular basement membrane and immunolocalization of five basement membrane components to the lamina densa (basal lamina) and its extensions in both glomeruli and tubules of the rat kidney. *Am. J. Anat.*, 169: 463-481, 1984.

Lea, P.J., M. Silverman, R. Hegele, and M.J. Hollenberg. Tridimensional ultrastructure of glomerular capillary endothelium revealed by high-resolution scanning electron microscopy. *Microvasc. Res.*, 38: 296-308, 1989.

Ligler, F.S., and G.B. Robinson. A new method for the isolation of renal basement membrane. *Biochim. Biophys. Acta*, 468: 327-340, 1977

Maddox, D.A., W.M. Deen, and B.M. Brenner. Glomerular filtration. In: *Handbook of Physiology. Renal Physiology*, sect. 8, vol. I, chapt. 13, p 545-638. Am. Physiol. Soc., Bethesda MD, 1992.

Malone, D.M, and J.L. Anderson. Diffusional boundary-layer resistance for membranes with low porosity. *Am. Inst. Chemical Eng. J.*, 23: 177-184, 1977.

Marangozis, J., and A.I. Johnson. Mass transfer with and without chemical reaction. *Can. J. Chem. Eng.*, 39: 152, 1961.

Miller, P.L., J.W. Scholey, H.G. Rennke, and T.M. Meyer. Glomerular hypertrophy aggravates epithelial cell injury in nephrotic rats. J. Clin. Invest., 85: 1119-1126, 1990.

Motulsky, H.J., and L.A. Ransnas. Fitting curves to data using nonlinear regression: a practical and nonmathematical review. *FASEB J.*, 1: 365-374, 1987.

Myers, B.D., W.M. Deen, and B.M. Brenner. Effects of norepinephrine and angiotensin II on the determinants of glomerular ultrafiltration and proximal tubule fluid reabsorption in the rat. *Circ. Res.*, 37: 101-110, 1975.

Myers, B.D., C. Peterson, C. Molina, S.J. Tomlanovich, L.D. Newton, R. Nitkin, H. Sandler, and F. Murad. Role of cardiac atria in the human renal response to changing plasma volume. *Am. J Physiol.*, 254 (Renal Fluid Electrolyte Physiol., 23): F562-F573, 1988.

Ogston, A.G. The spaces in a uniform random suspension of fibers. *Trans. Faraday Soc.*, 54: 1754-1757, 1958.

Ogston, A.G., B.N. Preston, and J. D. Wells. On the transport of compact particles through solutions of chain-polymers. *Proc. R. Soc. Lond.*, A 333: 297-316, 1973.

Oliver, J.D. *Analysis of Glomerular Permselectivity in the Rat Using Theoretical Models of Hindered Transport* (PhD thesis). Cambridge, MA: Massachusetts Institute of Technology, 1992.

Oliver, J.D., S. Anderson, J.L. Troy, B.M. Brenner, and W.M. Deen. Determination of glomerular size selectivity in the normal rat with Ficoll. *J. Am. Soc. Nephrol.*,3: 214-228, 1992.

Oliver, J.D., J.L. Simmons, J.L. Troy, A.P. Provoost, B.M. Brenner, and W.M. Deen. Proteinuria and impaired glomerular permeselectivity in uninephrectomized fawn-hooded rats. *Am. J.Physiol.*, 267 (*Renal Fluid Electrolyte Physiol.*, 36), F917-F925, 1994.

Opong, W.S, and A.L. Zydney. Diffusive and convective protein transport through asymmetric membranes. *Am. Inst. Chemical Eng. J.*, 37: 1497-1510, 1991.

Pappenheimer, J.R. Passage of macromolecules through the capillary walls. *Physiol. Rev.*, 33: 384-423, 1953.

Peterson, C., B. Madsen, A. Perlman, A.Y.M. Chan, and B.D. Myers. Atrial natriuretic peptide and the renal response to hypervolemia in nephrotic humans. *Kidney Int.*, 34: 825-831, 1988.

Phillips, R.J., W.M. Deen, and J.F. Brady. Hindered transport in fibrous membranes and gels: effect of solute size and fiber configuration. *J. Colloid Interf. Sci.*, 139: 363-373, 1990.

Pinnick, R.V., and V.J. Savin. Filtration by superficial and deep glomeruli of norvolemic and volume depleted rats. *Am. J. Physiol.* 250 (*Renal Fluid Electrolyte Physiol.* 19): F86-F91, 1986.

Press, W.H., B.P. Flannery, S.A. Teukolsky, and W.T. Wetterling. *Numerical Recipes.* New York, NY: Cambridge Univ. Press, 1989.

Remuzzi, A., N. Perico, C.S. Amuchastegui, B. Malanchini, M. Mazerska, C. Battaglia, T. Bertani, and G. Remuzzi. Short- and long-term effect of Angiotensin II receptor blockade in rats with experimental diabetes. *J. Am. Soc. Nephrol.*, 4: 40-49, 1993.

Remuzzi, A., and W.M. Deen. Theoretical effects of a distribution of capillary dimensions on glomerular ultrafiltration. *Microvasc. Res.*, 32: 131-144, 1986.

Remuzzi, A. and W.M. Deen. Theoretical effect of network structure on glomerular filtration of macromolecules. *Am. J. Physiol* 257 (*Renal Fluid Electrolyte Physiol.* 26): F152-F158, 1989.

Renkin, E.M. Filtration, diffusion, and molecular sieving through porous cellulose membranes. *J. Gen. Physiol.*, 38: 225-243, 1954.

Renkin, E.M., and J.P. Gilmore. Glomerular filtration. In: *Handbook of Physiology. Renal Physiology,* sect. 8, chapt. 9, pp 185-248. J. Orloff and R.W. Berliner, editors. Am. Physiol. Soc., Washington DC, 1973.

Rennke, H.G., R.S. Cotran, and M.A. Ventkatachalam. Role of molecular charge in glomerular permeability. *J. Cell Biol.*, 67: 638-646, 1975.

Rhodin, J.A.G. The diaphragm of capillary endothelial fenestrations. *J. Ultrastructure Res.*, 6: 171-185, 1962.

Robertson, C.R., W.M. Deen, J.L. Troy, and B.M. Brenner. Dynamics of glomerular filtration in the rat. III. Hemodynamics and autoregulation. *Am. J. Physiol.*, 223: 1191-1200, 1972.

Robinson, G.B., and H.A. Walton. Ultrafiltration through basement membrane. In: *Renal basement membranes in health and disease*, pp 147-161. Price, R.G., and B.G. Hudson, editors. Academic Press, London, 1987.

Robinson, G.B., and H.A. Walton. Glomerular basement membrane as a compressible ultrafilter. *Microvasc. Res.*, 38: 36-48, 1989.

Rodewald, R., and M.J. Karnovsky. Porous substructure of the glomerular slit diaphragm in the rat and mouse. *J. Cell Biol.*, 60: 423-433, 1974.

Rose, B.D. *Clinical Physiology of Acid-Base and Electrolyte Disorders,* pp 547-64. McGraw-Hill Book Co., New York, 1977.

Ryan, G.B. The glomerular filtration barrier. In: *Advances in Renal Physiology,* pp 1-32. C.J. Lote, editor. Alan R. Liss, Inc., New York, 1986.

Scattergood, E.M., and E.N. Lightfoot. Diffusional interaction in an ion-exchange membrane. *Trans. Faraday Soc.*, 64: 1135-1146, 1968.

Shirato, I., Y. Tomino, H. Koide, and T. Sakai. Fine structure of the glomerular basement membrane of the rat visualized by high-resolution scanning electron microscopy. *Cell Tissue Res.*, 266: 1-10, 1991.

Shorecki, K.L., B.J. Ballermann, G.H. Rennke, and B.M. Brenner. Angiotensin II receptor regulation in isolated renal glomeruli. *Federation Proc.* 42: 3064-3070, 1983.

Smith, K.A., C.K. Colton, E.W. Merrill, and L.B. Evans. Convective transport in a batch dialyzer: determination of true membrane permeability from a single measurement. *Chem. Eng. Prog. Symp. Ser.*, 64: 45-58, 1968.

Swed, F.S., and C. Eisenhart. Tables for testing the randomness of grouping in a sequence of alternatives. *Ann. Math. Statis.*, 14: 66-87, 1943.

Takami, H, A. Naramoto, H. Shigematsu, and S. Ohno. Ultrastructure of glomerular basement membrane by quick-freeze and deep-etch methods. *Kiney Int.*, 39: 659-664, 1991.

Tisher, C., and K.M. Madsen. Anatomy of the kidney. In: *The Kidney*, pp 3-60. B.M. Brenner and F.C. Rector, Jr., editors. W.B. Saunders Co., Philadelphia, 3rd edition, 1986.

Tucker, B.J., and R.C. Blantz. Effects of glomerular filtration dynamics on the glomerular permeability coefficient. *Am. J. Physiol.* 240 (*Renal Fluid Electrolyte Physiol.* 9): F245-F254, 1981.

Vernoiy, A., R. Du Bois, P. Decoodt, J.P. Gassee, and P.P. Lambert. Measurement of the permeability of biological membranes. Application to the glomerular wall. *J. Gen. Physiol.*, 62: 489-507, 1973.

Vilker, V.L., C.K. Colton, and K.A. Smith. The osmotic pressure of concentrated protein solutions : effect of concentration and pH in saline solutions of bovine serum albumin. *J. Colloid. Interf. Sci.*, 79: 548-566, 1981.

Walton, H.A., J. Byrne, and G.B. Robinson. Studies of the permeation properties of glomerular basement membrane: cross-linking renders glomerular basement membrane permeable to protein. *Biochim. et Biophys. Acta*, 1138: 173-183, 1992.

Yetter, R.A., H. Rabitz, F.L. Dryer, R.G. Maki, and R. B. Klemm. Evaluation of the rate constant for the reaction OH + H_2CO. *J. Chem. Phys.*, 91: 4088-4097, 1989.

Yoshioka, T., T. Mitarai, V. Kon, W. M. Deen, H.G. Rennke, and I. Ichikawa. Role for Angiotensin II in an overt functional proteinuria. *Kidney Int.*, 30: 538-545, 1986.

Yoshioka, T., H.G. Rennke, D.J. Salant, W.M. Deen, and I. Ichikawa. Role of abnormally high transmural pressure in the permselectivity defect of glomerular capillary waall: a study in early passive Heymann nephritis. *Circ. Res.*, 61: 531-538, 1987.

Yoshioka, T,., H. Shiraga,Y. Yoshida, A. Fogo, A.D. Glick, W.M. Deen, J.R. Royer, and I. Ichikawa. "Intact nephrons" as the primary origin of proteinuria in chronic renal disease. Study in the rat model of subtotal nephrectomy. *J. Clin. Invest.*, 82: 1614-1623, 1988.

Yurchenko, P.D., and J. O'Rear. Supramolecular organization of basement membranes. In: *Molecular and Cellular Aspects of Basement Membranes*, pp 19-47. D. Rohrbach and R. Timpl., editors. Academic Press, Inc., New York, 1993.

Wolgast, M., and G. Öjteg. Electrophysiology of renal capillary membranes: gel concept applied and Starling model challenged. *Am. J. Physiol.* 254 (*Renal Fluid Electrolyte Physiol.* 23) : F364-F373, 1988.

Zimmerhackl, B., N. Parekh, H. Kücherer, and M. Steinhausen. Influence of systemically applied angiotensin II on the microcirculation of glomerular capillaries in the rat. *Kidney Int.*, 27: 17-24, 1985.

Appendix A

List of Principal Symbols

B	polarization factor
C	solute concentration
C_{alb}	concentration of albumin
C_{iA}	afferent concentration of solute i
C_{pA}	afferent protein concentration
C_F	solute concentration in the filtrate
C_M	solute concentration on the retentate side adjacent to the membrane surface
C_R	solute concentration in the bulk retentate
D_∞	diffusivity of the solute in dilute bulk solution
f	fraction of the epithelial surface denuded of slit diaphragms
GFR	glomerular filtration rate
h	half-width of slit channel upstream
H	length of slit channel
J_s	solute flux
J_v	solvent (water) flux
k_s	mass transfer coefficient
K_c	convective hindrance coefficient
K_d	diffusional hindrance coefficient
K_{Darcy}	Darcy permeability of the GBM
K_f	ultrafiltration coefficient
L_p	hydraulic permeability of the membrane
L_s	half-distance between the centers of two adjacent cylinders in the slit
M	molecular weight
N_f	number of endothelial fenestrae per unit cell
p	probability that residuals are randomly distributed
P_{GC}	glomerular hydraulic pressure
ΔP	hydraulic pressure difference
$\overline{\Delta P}$	average capillary transmural hydraulic pressure difference
Pe	Peclet number
Q_A	single nephron afferent capillary plasma flow rate
r_c	cylinder radius in slit diaphragm

r_f	fiber radius
r_0	isoporous pore radius
r_s	Stokes-Einstein radius
R	capillary radius
RPF	renal plasma flow
s	lognormal distribution parameter
SNGFR	single nephron glomerular filtration rate
T	absolute temperature
$\bar{u}$	lognormal distribution parameter
u	half-width of gap between the cylinders
W	width of the unit cell

Greek symbols

δ_{gbm}	thickness of GBM
ε_f	fractional area covered by the endothelial fenestrae
ε_s	fractional area covered by the slit
Θ	true membrane sieving coefficient
Θ'	measured sieving coefficient
μ	solvent viscosity
ν	kinematic viscosity
π_A	afferent arteriole oncotic pressure
$\Delta\Pi_{alb}$	oncotic pressure difference for albumin
σ	standard error of the mean
σ_{alb}	reflection coefficient of albumin
ϕ	solid volume fraction
Φ	partition coefficient
χ^2	sum of squared residuals
ω_o	shunt parameter for heteroporous models
∇	gradient operator

Appendix B

Program for Computing Sieving Coefficients
with the Ultrastructural Model

```
******************************************************************
*       this program yields overall sieving coefficients for the glomerular
*       capillary wall based on a lognormal distribution of the cylinder
*       spacings in the slits and the GBM hindrance coefficients obtained in vitro.
******************************************************************

        program thetawall

        implicit double precision(a-h,o-z), integer(i-n)
        external funcdg,funcjv,funcjs,funkg,midpnt,midinf
        parameter(nterms=200)
        common/hemo/hqa,hcpa,hdp,hfkf,hgfr
        common/values/surf,delg,xchar,es,nrs,nsol,yl
        common/solute/rs(40),phikc(40),phikd(40)
        common/sieving/thetabm(100,40),thetasl(100,40)
        common/data/sc(40),sig(40),theta(40)
        common/path/xx(5002),qcs(40,5002),fjv(5002),nstepar
        common/bl1/permslit,visc,rc,uav,denom
        common/bl2/a1fit,a2fit,s,per,ped,rso,dif,delta,delpslit
        common/bl3/deltat,ws
        common/array/params(10),lista(10)
        dimension xf(20),nf(20),temp(20),p(10),xi(10,10)
        dimension valbegin(40)

******************************
*       description of parameters
******************************

c       hqa: RPF or QA (in ml/min)
c       hcpa: afferent plasma protein concentration (in g/dl)
c       hfkf: ultrafiltration coefficient of capillary wall (ml/min/mmHg)
c       hgfr: GFR or SNGFR (in ml/min)
c       hpd: deltaP, hydraulic pressure difference across the wall (mmHg)
c       darcyk: Darcy permeability of GBM (in m2)
c       rc: cylinder radius in slit diaphragm (in m)
c       s,uav: parameters of lognormal distribution (uav non-dimensionalized by rc)
c       nrs: number of observations (number of solutes)
c       sc: measured sieving coefficient
c       sig: standard deviation of measured sieving coefficient
c       theta: predicted sieving coefficient
c       thetabm: local GBM sieving coefficient
c       thetasl: local slit diaphragm sieving coefficient
```

```
c       surf: surface area available for filtration (m2)
c       xchar: characteristic length, length of the unit cell (m)
c       delg: non-dimensional thickness of GBM
c       es: fractional area covered by the slit
c       ef: fractional area covered by the fenestrae
c       permslit: hydraulic permeability of slit diaphragm (m/s/Pa)
c       permfen: hydraulic permeability of fenestrae (m/s/Pa)
c       visc: viscosity of solvent
c       delta: distance between GBM interface and center of slit cylinders
c       ws: width of filtration slit (m)
c       delpslit: pressure drop across the filtration slit
c       delpgbm: pressure drop across GBM

*******************************
*       Read input parameterts
*******************************


        open(1,file='lognormalin',status='old')
        open(2,file='lognormalout',status='old')
        read(1,*) hqa,hcpa,hdp,hfkf
        read(1,*) xchar,delg,es,ef
        read(1,*) visc,permslit,permfen
        read(1,*) nrs
        read(1,*) (rs(i),i=1,nrs)
        read(1,*) (sc(i),i=1,nrs)
        read(1,*) (sig(i),i=1,nrs)
        read(1,*) rc,delta,deltat,ws
        read(1,*) alfa,beta,a1fit,a2fit,s
        close(unit=1,status='keep')

        write(2,*)'hemodynamic parameters : RPF,Cpa,DP'
        write(2,16)hqa,hcpa,hdp
        write(2,*)'ultrastructural parameters : w,delbm,es,ef'
        write(2,16)xchar,delg*xchar,es,ef
        write(2,*)'permeabilities : slit and fenestrae'
        write(2,16)permslit,permfen
        write(2,*)'radius of cylinders :'
        write(2,16)rc

******************************************************
*       Calculate coordinates of slit (xs) and fenestrae (xf(i))
******************************************************


        pi = 4.d0*datan(1.d0)
        nfen = int(xchar/120.e-9)
        xs = es/2.d0
* wfnd,wsnd = dimensionless width of fenestra and slit
        wsnd = 2.d0*xs
        wfnd = ef/real(nfen)
        xf(1) = (1.d0-ef)/real(nfen)/2.d0
        xf(2) = xf(1)+wfnd
        nxf = 2
        do 20 l=3,nfen,2
                xf(l) = xf(l-1)+(1.d0-ef)/dble(nfen)
                xf(l+1) = xf(l)+wfnd
                nxf = l+1
20      continue
        if (nxf.eq.nfen+1) xf(nxf) = 0.5d0
* Change coordinates of fenestrae (still symmetric unit cell)
        do 33 ifen=1,nxf
                temp(ifen) = 0.5d0-xf(ifen)
33              continue
        do 34 ifen=1,nxf
                xf(ifen) = temp(nxf-ifen+1)
34      continue

*************************************************
*       Calculate hydraulic permeability of GBM and GCW
*************************************************
        darcyk0=2.404
        denom = delg
        do 40 n=1,nterms
                ev = 2.d0*dble(n)*pi
                aux = 0.
                do 42 l=1,nxf
                        sign = (-1.)**l
                        aux = aux+sign*sin(ev*xf(l))
42              continue
                gama = aux/dble(n)/ef/pi
                zeta = sin(ev*xs)/dble(n)/es/pi
                denom = denom+2.d0*(zeta**2+gama**2)/ev/tanh(ev*delg)
                denom = denom-4.d0*gama*zeta/ev/sinh(ev*delg)
40      continue
        permgbm0 = darcyk0/visc/xchar/denom
        enres=1./permfen/ef
        epres=1./permslit/es
        rescells=enres+epres
* Determine the pressure drop across the GBM in order to compute KDarcy
        a = rescells*permgbm0*(0.0264/2.404)
        b = (1+rescells*permgbm0)
        c = hdp
        discrim=(b**2-4*a*c)
        delpgbm=(b-sqrt(discrim))/(2*a)
        darcyk=darcyk0*(1-0.0264/2.404*delpgbm)
        permgbm=permgbm0*(1-0.0264/2.404*delpgbm)
        gbmres=1./permgbm
        totalres=enres+gbmres+epres
        permgcw = 1./totalres
        write(2,*)'Darcy permeability of GBM :'
        write(2,16)darcyk
        write(2,*)
        write(2,*) 'kgbm (m/s/Pa) =',permgbm
        write(2,*) 'kgcw (m/s/Pa) =',permgcw
* 1 mmHg = 133.322 Pa => 1 m3/s/Pa = 8.0e9 ml/min/mmHg
* hfkf in ml/min/mmHg
        surf = hfkf/(permgcw*8.0d9)

**********************************************
```

```
*       Compute the GBM hindrance coefficients
********************************************

        do 100 i = 1,nrs
                rsa=rs(i)*1.d10
                phikd(i)=0.1045*exp(-0.07302*rsa)*(1-0.0096*delpgbm)
                phikc(i)=6.0240*exp(-0.07469*rsa)*(1-0.0096*delpgbm)
100     continue

*****************************************
*       Find parameter uav of spacings distribution
*****************************************

        pi = 4.*datan(1.d0)
        uavinit = 0.50
        ftol = 1.d-4
        nparamsmax = 2
        nparamsfit = 1
        params(1) = uavinit
        do 150 i=1,nparamsfit
                lista(i) = i
150     continue
        do 180 i=1,nparamsmax
                p(i) = params(i)
                do 190 j=1,nparamsfit
                        xi(i,j) = 0.0
                        if (i.eq.j) xi(i,j) = p(i)*0.10
190             continue
180     continue
        call powellbis(p,xi,nparamsfit,nparamsmax,ftol,iter,fret)
        do 200 i=1,nparamsfit
                params(i) = p(i)
200     continue
        uav = params(1)
        write(2,*)
        write(2,*)'parameters v and s of the distribution :'
        write(2,16)uav*rc,s
        print*,'final u and s :',uav*rc,s

********************************************
*       Determine the local thetas (GBM and slit)
********************************************

        nstepar = 2**5
        ya = 0.0d0
        yb = 1.0d0
        h = (yb-ya)/nstepar
        do 300 k=1,nstepar+1
                y = ya + h*(k-1)
                do 320 irs=1,nrs
                        thetasl(k,irs) = tetasloc(y,irs)
                        thetabm(k,irs) = tetabmloc(y,irs)
320             continue
300     continue
```

```
*******************************************
*       Determine Q, Jv and Q*soluteconcentration
*******************************************

* the array qcs(1,i) is the flow rate Q
* the array qcs(j+1,i) is Q*C for solute j at position i
        do 400 irs=1,nrs+1
                valbegin(irs) = hqa
400     continue
        call rkdumb(valbegin,ya,yb,nstepar)
        hgfr = qcs(1,1)-qcs(1,nstepar+1)
        write(2,*)
        write(2,*)'glomerular filtration rate (ml/min) :',hgfr
        do 420 i=1,nstepar+1
                fint = 1.629*hqa*hcpa/qcs(1,i)+ 0.2935*(hqa*hcpa/qcs(1,i))**2
                fjv(i)= hfkf/surf/6d+07*(hdp-fint)
420     continue
* hfkf in ml/min/mmHg => *1.d-6/60 in m3/s/mmHg

*********************************************************
*       Determine sieving coefficients by integrating from y = 0 to 1
*********************************************************

        call qrombflux(ya,yb,totflux,funcjv)
        do 700 irs=1,nrs
                nsol=irs
                call qrombflux(ya,yb,sum,funcjs)
                theta(irs)=sum/totflux
700     continue
        write(2,*)
        do 750 i=1,nrs
                write(2,16)rs(i),theta(i)
750     continue
16      format(5(1x,d12.6,1x))
        END

*******************************************************
*       To find the parameter uav of cylinder spacing distribution
*******************************************************

        function chisqbis(pms)
        implicit double precision (a-h,o-z), integer(i-n)
        external midpnt,midinf,funkg
        common/bl1/permslit,visc,rc,uav,denom
        common/bl2/a1fit,a2fit,s,per,ped,rso,dif,delta,delpslit
        common/bl3/deltat,ws
        dimension pms(10)
        uav = pms(1)
        if ((uav.le.0.05).or.(uav.gt.10)) then
                chisqbis = 1.d23
                return
        endif
        call qromo(funkg,0.d0,1.d0,s1,midpnt)
```

```
      call qromo(funkg,1.d0,1.d32,s2,midinf)
      denom = s1+s2
      chisqbis = (permslit*visc/rc - denom)**2
      return
      end

*************************************************
*     To calculate local sieving coefficient for GBM
*************************************************

      function tetabmloc(y,i)
      implicit double precision(a-h,o-z), integer(i-n)
      common/hemo/hqa,hcpa,hdp,hfkf,hgfr
      common/solute/rs(40),phikc(40),phikd(40)
      common/sieving/thetabm(100,40),thetasl(100,40)
      common/path/xx(5002),qcs(40,5002),fjv(5002),nstepar
      common/values/surf,delg,xchar,es,nrs,nsol,yl
      common/bl1/permslit,visc,rc,uav,denom
      dinf = 2.270647658d-22/rs(i)/visc
      call cpandjv(y,cprot,wflux)
      pe=wflux*phikc(i)*delg*xchar/(dinf*phikd(i))
      k = y*nstepar+1
      tetsl = thetasl(k,i)
      tetabmloc=phikc(i)/(tetsl - (tetsl-phikc(i))*
     $     dexp(-pe*(1+0.7366*((1-0.2*es)**11.9864)/(delg**1.2697))))
      return
      end

***********************************************
*     To calculate local sieving coefficients for slit
***********************************************

      function tetasloc(y,i)
      implicit double precision(a-h,o-z), integer(i-n)
      double precision permslit,delpslit,unifinite,rso,visc
      double precision dinf,rc,snum,s1,s2
      external funcdg,funkg,funkg1,ft3d,funk,midinf,midpnt
      common/hemo/hqa,hcpa,hdp,hfkf,hgfr
      common/solute/rs(40),phikc(40),phikd(40
      common/values/surf,delg,xchar,es,nrs,nsol,yl
      common/bl1/permslit,visc,rc,uav,denom
      common/bl2/a1fit,a2fit,s,per,ped,rso,dif,delta,delpslit
      common/bl3/deltat,ws
      call cpandjv(y,cprot,wflux)
      delpslit = wflux/es/permslit
      uinfinite = 1.d32
      rso = rs(i)
      dif = 2.270647658e-22/rs(i)/visc
      call qromo(funk,rso/rc,uinfinite,snum,midinf)
      tetasloc = snum/denom
      end

*************************************************
*     To find protein concentrations along the capillary
```

```
*************************************************

      subroutine cpandjv(y,cprot,wflux)
      implicit double precision(a-h,o-z), integer (i-n)
      external funcdp
      common/hemo/hqa,hcpa,hdp,hfkf,hgfr
      common/array/params(10),lista(10)
      common/values/surf,delg,xchar,es,nrs,nsol,yl
      yl = y
      cpacc = 1.d-10
      cpinf = 0.d0
      discrim = 1.629d0**2 + 4.d0*0.2935d0*hdp
      cpsup = -(1.629d0 - dsqrt(discrim))/(2*0.2935d0)/hcpa
      cp = rtnewt(funcdp,cpinf,cpsup,cpacc)
      cprot=cp*hcpa
      wflux = hfkf*(hdp-1.629e0*cprot-0.2935e0*cprot**2)/(surf*6.0e7)
      if (wflux .le. 0.e0) then
      cprot = cprotmax
      wflux = 0.e0
      endif
      return
      end

      subroutine funcdp(var,f,df)
      implicit double precision(a-h,o-z), integer(i-n)
      common/hemo/hqa,hcpa,hdp,hfkf,hgfr
      common/values/surf,delg,xchar,es,nrs,nsol,yl
      aa1=1.629d0
      aa2=0.2935d0
      a1=aa1*hcpa/hdp
      a2=aa2*hcpa*hcpa/hdp
      delta = a1**2.d0+ 4.d0*a2
      sdel=dsqrt(delta)
      func1=-1.0d0 - a1/2*dlog(abs(1-a1-a2))+(a1**2+2*a2)/(2*sdel)*
     $  dlog(abs((2*a2+a1+sdel)/(2*a2+a1-sdel)))
      rhs= func1+hfkf*hdp*yl/hqa
      cp = var
      func=-1/cp + a1/2*dlog(abs(cp**2/(1-a1*cp-a2*cp**2)))
     $    +(a1**2+2*a2)/(2*sdel)*dlog(abs((2*a2*cp+a1+sdel)/
     $    (2*a2*cp+a1-sdel)))
      f= func - rhs
      df = 1/(cp**2)/(1-a1*cp-a2*cp**2)
      return
      end

*******************************************************************
*     Subroutines for slit diaphragm, adapted from Drumond and Deen (1995)
*******************************************************************

      function funkg(u)
* Integrand in calculation of average hydraulic permeability
      implicit double precision(a-h,o-z)
      external ft3d
      common/bl1/permslit,visc,rc,uav,denom
      common/bl2/a1fit,a2fit,s,per,ped,rso,dif,delta,delpslit
      common/bl3/deltat,ws
      pi = 4*datan(1.d0)
      z = dlog(s)
      exterm=dexp(-0.5d0*((dlog(u)-dlog(uav))/z)**2)
      sum = dexp(dlog(uav) + z**2/2)
      funkg = 1/dsqrt(2*pi)/z/u*exterm*(1.+u)**2/(1.+sum)/ft3d(u)
      end

      function ft3d(u)
      implicit double precision(a-h,o-z)
* ft3d = total dimensionless resistance
* u corresponds to u/rc
      common/bl1/permslit,visc,rc,uav,denom
      common/bl2/a1fit,a2fit,s,per,ped,rso,dif,delta,delpslit
      common/bl3/deltat,ws
      pi = 4.*datan(1.d0)
      rw = rc/ws
      plw = (u+1.)*rw
      rl = 1./(u+1.)
      fp = 3.d0*deltat/ws*plw
      if ((plw.le.4.).and.(rl.ge.0.1)) then
              f3d = fladder(rl,plw)
      else
              f0 = 3.*plw**2*((pi+2.*datan(rl/sqrt(1.-rl**2)))/
     $                sqrt(1.-rl**2)-pi)-6.*rw*plw
              plw1 = 4.
              rl1 = rw/plw1
              if (rl1.ge.0.1) then
                      f1 = fladder(rl1,plw1)
                      f3d = f0+(f1-f0)/0.25/plw
              else
                      rl2 = 0.1
                      plw2 = rw/rl2
                      f2 = fladder(rl2,plw2)
                      f3d = f0+(f2-f0)/0.1*rl
              endif
      endif
      ft3d = f3d+fp
      end

      function fladder(rl,plw)
      implicit double precision(a-h,o-z)
      pi = 4.*datan(1.d0)
      if (rl.lt.0.7) then
              c = 0.336+2.74*rl-2.74*rl**2+3.16*rl**3
              d = 0.0639/rl+0.454-0.652*rl+0.152*rl**2
              fladder = 10.d0**(c+d*rl*plw)
      else
              a = 9.d0*pi/4.d0/dsqrt(2.d0)*
     $                10.d0**(0.144*plw+0.0111*plw**2)
              b = -2.5d0+0.11*plw+0.00957*plw**2
              fladder = a*(1.d0-rl)**b
      endif
      end

      function funk(u)
* Integrand in calculation of average sieving coefficient
* u corresponds to u/rc
      implicit double precision(a-h,o-z)
      external funkg
      common/bl1/permslit,visc,rc,uav,denom
      common/bl2/a1fit,a2fit,s,per,ped,rso,dif,delta,delpslit
      common/bl3/deltat,ws
      velslit=delpslit*rc*(u+1.)/visc/ft3d(u)
      per = velslit*rc/dif
      ped = per*delta/rc
      a = a2fit*(u+1.)/u+a1fit*(u+1.)
      d = 1.-dexp(-ped)*(1.-dexp(-a*per))
      theta = (u-rso/rc)/(u-d*rso/rc)
      funk = theta*funkg(u)
      end

************************************************************
*     Subroutines to determine integrals of solute and solvent fluxes
************************************************************

      SUBROUTINE qrombflux(a,b,ss,choose)
      implicit double precision(a-h,o-z),integer(i-n)
      external choose
      common/values/surf,delg,xchar,es,nrs,nsol,yl
      parameter (eps = 1.d-6, jmax = 14, jmaxp = jmax+1, k=5, km=k-1)
      dimension h(JMAXP),s(JMAXP)
      h(1)=1.
      do 11 j=1,JMAX
         call trapzd(a,b,s(j),j,choose)
         if (j.ge.K) then
            call polint(h(j-KM),s(j-KM),K,0.,ss,dss)
            if (abs(dss).le.EPS*abs(ss)) return
         endif
         s(j+1)=s(j)
         h(j+1)=0.25*h(j)
11    continue
      pause 'too many steps in qrombflux'
      END

      SUBROUTINE trapzd(a,b,s,n,choose)
      implicit double precision(a-h,o-z),integer(i-n)
      external choose
      common/hemo/hqa,hcpa,hdp,hfkf,hgfr
      common/solute/rs(40),phikc(40),phikd(40)
      common/path/xx(5002),qcs(40,5002),fjv(5002),nstepar
      common/values/surf,delg,xchar,es,nrs,nsol,yl

      if (n.eq.1) then
         funca = choose(1)
         funcb = choose(nstepar+1)
         s=0.5*(b-a)*(funca+funcb)
```

```
        else
                it=2**(n-2)
                tnm=it
                del=(b-a)/tnm
                x=a+0.5*del
                sum=0.
                do 11 j=1,it
                        k = nstepar*(j-0.5)/tnm + 1
                        funcx = choose(k)
                        sum=sum+funcx
                        x=x+del
11              continue
                s=0.5*(s+(b-a)*sum/tnm)
        endif
        return
        END

        function funcjv(k)
        implicit double precision(a-h,o-z),integer(i-n)
        common/path/xx(5002),qcs(40,5002),fjv(5002),nstepar
        funcjv=fjv(k)
        return
        end

        function funcjs(k)
        implicit double precision(a-h,o-z),integer(i-n)
        common/path/xx(5002),qcs(40,5002),fjv(5002),nstepar
        common/values/surf,delg,xchar,es,nrs,nsol,yl
        common/sieving/thetabm(100,40),thetasl(100,40)
        irs=nsol
        tetbm=thetabm(k,irs)
        tetsl=thetasl(k,irs)
        funcjs = qcs(irs+1,k)*tetbm*tetsl*fjv(k)/qcs(1,k)
        return
        end

*****************************************************
*       To calculate derivative of the product Q(y) and Q*Cs(y)
*****************************************************

        subroutine derivs(pos,qci,derivee)
* qci(1) is actually the flow rate Q itself
        implicit double precision(a-h,o-z),integer(i-n)
        common/hemo/hqa,hcpa,hdp,hfkf,hgfr
        common/values/surf,delg,xchar,es,nrs,nsol,yl
        common/solute/rs(40),phikc(40),phikd(40)
        common/sieving/thetabm(100,40),thetasl(100,40)
        common/path/xx(5002),qcs(40,5002),fjv(5002),nstepar
        dimension derivee(40),qci(40)
        derivee(1) = -hfkf*(hdp-1.629*(hqa*hcpa)/qci(1) - 0.2935*
     $          (hqa*hcpa/qci(1))**2)
        do 20 irs=1,nrs
                        k = pos*nstepar + 1
                        tetsl = thetasl(k,irs)
                tetbm = thetabm(k,irs)
                derivee(irs+1) = derivee(1)*tetbm*tetsl*qci(irs+1)/qci(1)
20      continue
        return
        end

***********************************
*       Subroutines for integration
***********************************

        subroutine qromo(func,a,b,ss,choose)
        implicit double precision(a-h,o-z)
        external func,choose
        parameter (eps=1.d-6, jmax=14, jmaxp=jmax+1, k=5, km=k-1)
        dimension h(jmaxp),s(jmaxp)
        h(1)=1.
        do 11 j=1,jmax
            call choose(func,a,b,s(j),j)
            if (j.ge.k) then
                call polint(h(j-km),s(j-km),k,0.,ss,dss)
                if (dabs(dss).le.eps*dabs(ss)) return
            endif
            s(j+1)=s(j)
            h(j+1)=h(j)/9.
11      continue
        pause 'too many steps in qromo'
        end

        subroutine polint(xa,ya,n,x,y,dy)
        implicit double precision(a-h,o-z)
        parameter (nmax=10)
        dimension c(nmax),d(nmax),xa(n),ya(n)
        ns=1
        dif=dabs(x-xa(1))
        do 11 i=1,n
            dift=dabs(x-xa(i))
            if (dift.lt.dif) then
                ns=i
                dif=dift
            endif
            c(i)=ya(i)
            d(i)=ya(i)
11      continue
        y=ya(ns)
        ns=ns-1
        do 13 m=1,n-1
            do 12 i=1,n-m
                ho=xa(i)-x
                hp=xa(i+m)-x
                w=c(i+1)-d(i)
                den=ho-hp
                if(den.eq.0.)pause 'failure in polint'
                den=w/den
                d(i)=hp*den
```

```
                        c(i)=ho*den
12              continue
                if (2*ns.lt.n-m)then
                        dy=c(ns+1)
                else
                        dy=d(ns)
                        ns=ns-1
                endif
                y=y+dy
13      continue
        return
        end

        subroutine midpnt(func,a,b,s,n)
        implicit double precision(a-h,o-z)
        external func
        if (n.eq.1) then
                s=(b-a)*func(0.5*(a+b))
        else
                it=3**(n-2)
                tnm=it
                del=(b-a)/(3.*tnm)
                ddel=del+del
                x=a+0.5*del
                sum=0.
                do 11 j=1,it
                        sum=sum+func(x)
                        x=x+ddel
                        sum=sum+func(x)
                        x=x+del
11              continue
                s=(s+(b-a)*sum/tnm)/3.
        endif
        return
        end

        subroutine midinf(funk,aa,bb,s,n)
        implicit double precision(a-h,o-z)
        external funk
        func(x)=funk(1.d0/x)/x**2
        b=1./aa
        a=1./bb
        if (n.eq.1) then
                s=(b-a)*func(0.5*(a+b))
        else
                it=3**(n-2)
                tnm=it
                del=(b-a)/(3.*tnm)
                ddel=del+del
                x=a+0.5*del
                sum=0.
                do 11 j=1,it
                        sum=sum+func(x)
                        x=x+ddel
```

```
                    sum=sum+func(x)
                    x=x+del
11              continue
                s=(s+(b-a)*sum/tnm)/3.
        endif
        return
        end

        function rtnewt(funcd,x1,x2,xacc)
* Modified from original subroutine in Numerical Recipes
        implicit double precision(a-h,o-z)
        external funcd
        parameter (jmax=100)
        x2in=x2
        icycle=0
10      continue
        icycle=icycle+1
        if (icycle.eq.2) x2=0.5*x2in
        if (icycle.eq.3) x2=2.*x2in
        if (icycle.gt.3) pause
   $            'rtnewt did not converge for given initial guesses'

        rtnewt=.5*(x1+x2)
        do 11 j=1,jmax
                call funcd(rtnewt,f,df)
                dx=f/df
                rtnewt=rtnewt-dx
                if((x1-rtnewt)*(rtnewt-x2).lt.0.) goto 10
                if(dabs(dx).lt.xacc) return
11      continue
        pause 'rtnewt exceeded maximum iterations'
        end

********************************************************
*       Subroutines for differential equations (Runge-Kutta scheme)
********************************************************

        subroutine rkdumb(vstart,x1,x2,nstep)
        implicit double precision(a-h,o-z),integer(i-n)
        parameter(nstpmx=10000)
        common/path/xx(5002),qcs(40,5002),fjv(5002),nstepar
        common/hemo/hqa,hcpa,hdp,hfkf,hgfr
        common/values/surf,delg,xchar,es,nrs,nsol,yl
        dimension vstart(40),v(40),dv(40)
        do 10 irs=1,nrs+1
                v(irs) = vstart(irs)
                qcs(irs,1) = v(irs)
10      continue
        xx(1) = x1
        x = x1
        h = (x2-x1)/nstep
        do 20 k=1,nstep
                call derivs(x,v,dv)
                call rk4(v,dv,x,h,v)
                if ((x+h) .eq. x) PAUSE 'Stepsize not significant in RKDUMB'
                x = x + h
                xx(k+1) = x
                do 30 irs=1,nrs+1
                        qcs(irs,k+1) = v(irs)
30              continue
20      continue
        do 40 irs=1,nrs+1
                qcs(irs,nstep+2)=qcs(irs,nstep+1)
40      continue
        return
        end

        subroutine rk4(y,dydx,x,h,yout)
        implicit double precision(a-h,o-z),integer(i-n)
        common/hemo/hqa,hcpa,hdp,hfkf,hgfr
        common/values/surf,delg,xchar,es,nrs,nsol,yl
        dimension y(40),yout(40),dydx(40),yt(40),dyt(40),dym(40)
        hh = h*0.5
        h6 = h/6.0
        xh = x + hh
        do 10 irs=1,nrs+1
                yt(irs) = y(irs) + hh*dydx(irs)
10      continue
        call derivs(xh,yt,dyt)
        do 20 irs=1,nrs+1
                yt(irs) = y(irs) + hh*dyt(irs)
20      continue
        call derivs(xh,yt,dym)
        do 30 irs=1,nrs+1
                yt(irs) = y(irs) + h*dym(irs)
                dym(irs) = dyt(irs)+dym(irs)
30      continue
        xhh = x + h
        call derivs(xhh,yt,dyt)
        do 40 irs=1,nrs+1
                yout(irs) = y(irs) + h6*(dydx(irs)+dyt(irs)+2.0*dym(irs))
40      continue
        return
        end

************************************************************************
*       Subroutines for Powell's method, from Numerical Recipes (Press et al, 1989)
************************************************************************

C     POWELL'S ROUTINE
      SUBROUTINE POWELLbis(P,XI,N,NP,FTOL,ITER,FRET)
       implicit double precision (a-h,o-z), integer (i-n)
      PARAMETER (NMAX=20,ITMAX=200)
      DIMENSION P(10),XI(10,10),PT(nmax),PTT(nmax),XIT(nmax)

      FRET = chisqbis(P)
      DO 11 J=1,N
        PT(J)=P(J)
```

```
11   CONTINUE
     ITER=0
1    ITER=ITER+1
     FP=FRET
     IBIG=0
     DEL=0.
     DO 13 I=1,N
       DO 12 J=1,N
         XIT(J)=XI(J,I)
12       CONTINUE
       FPTT=FRET
       CALL LINMINbis(P,XIT,N,FRET)
       IF(ABS(FPTT-FRET).GT.DEL)THEN
         DEL=ABS(FPTT-FRET)
         IBIG=I
       ENDIF
13     CONTINUE
     IF(2.*ABS(FP-FRET).LE.FTOL*(ABS(FP)+ABS(FRET)))RETURN
     IF(ITER.EQ.ITMAX) then
       print*, 'Powell exceeding maximum iterations.'
       return
     endif
     DO 14 J=1,N
       PTT(J)=2.*P(J)-PT(J)
       XIT(J)=P(J)-PT(J)
       PT(J)=P(J)
14     CONTINUE
     FPTT =chisqbis(PTT)
     IF(FPTT.GE.FP)GO TO 1
     T=2.*(FP-2.*FRET+FPTT)*(FP-FRET-DEL)**2-DEL*(FP-FPTT)**2
     IF(T.GE.0.)GO TO 1
     CALL LINMINbis(P,XIT,N,FRET)
     DO 15 J=1,N
       XI(J,IBIG)=XIT(J)
15     CONTINUE
     GO TO 1
     END

      SUBROUTINE LINMINbis(P,XI,N,FRET)
       implicit double precision (a-h,o-z), integer (i-n)
     PARAMETER (NMAX=50,TOL=1.d-4)
     EXTERNAL F1DIMbis
     DIMENSION P(n),XI(n)
     COMMON /F1COM/ PCOM(NMAX),XICOM(NMAX),ncom
     NCOM=N
     DO 11 J=1,N
       PCOM(J)=P(J)
       XICOM(J)=XI(J)
11     CONTINUE
     AX=0.
     XX=1.
      CALL MNBRAKbis(AX,XX,BX,FA,FX,FB)
      FRET=BRENTbis(AX,XX,BX,TOL,XMIN)
     DO 12 J=1,N
```

```
        XI(J)=XMIN*XI(J)
         P(J)=P(J)+XI(J)
12      CONTINUE
      RETURN
      END

        SUBROUTINE MNBRAKbis(AX,BX,CX,FA,FB,FC)
         implicit double precision (a-h,o-z), integer (i-n)
       PARAMETER (GOLD=1.618034, GLIMIT=100., TINY=1.d-20)

       FA=f1dimbis(AX)
       FB=f1dimbis(BX)
        IF(FB.GT.FA)THEN
         DUM=AX
         AX=BX
         BX=DUM
         DUM=FB
         FB=FA
         FA=DUM
       ENDIF
       CX=BX+GOLD*(BX-AX)
       FC=f1dimbis(CX)
1        IF(FB.GE.FC)THEN
          R=(BX-AX)*(FB-FC)
          Q=(BX-CX)*(FB-FA)
          U=BX-((BX-CX)*Q-(BX-AX)*R)/(2.*SIGN(MAX(ABS(Q-R),TINY),Q-R))
          ULIM=BX+GLIMIT*(CX-BX)
           IF((BX-U)*(U-CX).GT.0.)THEN
            FU=f1dimbis(U)
             IF(FU.LT.FC)THEN
              AX=BX
              FA=FB
              BX=U
              FB=FU
              RETURN
             ELSE IF(FU.GT.FB)THEN
              CX=U
              FC=FU
              RETURN
            ENDIF
            U=CX+GOLD*(CX-BX)
            FU=f1dimbis(U)
          ELSE IF((CX-U)*(U-ULIM).GT.0.)THEN
            FU=f1dimbis(U)
             IF(FU.LT.FC)THEN
              BX=CX
              CX=U
              U=CX+GOLD*(CX-BX)
              FB=FC
              FC=FU
              FU=f1dimbis(U)
            ENDIF
          ELSE IF((U-ULIM)*(ULIM-CX).GE.0.)THEN
            U=ULIM
         FU=f1dimbis(U)
        ELSE
         U=CX+GOLD*(CX-BX)
         FU=f1dimbis(U)
        ENDIF
        AX=BX
        BX=CX
        CX=U
        FA=FB
        FB=FC
        FC=FU
        GO TO 1
      ENDIF
      RETURN
      END

       FUNCTION BRENTbis(AX,BX,CX,TOL,XMIN)
        implicit double precision (a-h,o-z), integer (i-n)
      PARAMETER (ITMAX=100,CGOLD=.3819660,ZEPS=1.d-10)

      A=MIN(AX,CX)
      B=MAX(AX,CX)
      V=BX
      W=V
      X=V
      E=0.
      FX=f1dimbis(X)
      FV=FX
      FW=FX
      DO 11 ITER=1,ITMAX
        XM=0.5*(A+B)
        TOL1=TOL*ABS(X)+ZEPS
        TOL2=2.*TOL1
        IF(ABS(X-XM).LE.(TOL2-.5*(B-A))) GOTO 3
        IF(ABS(E).GT.TOL1) THEN
         R=(X-W)*(FX-FV)
         Q=(X-V)*(FX-FW)
         P=(X-V)*Q-(X-W)*R
         Q=2.*(Q-R)
          IF(Q.GT.0.) P=-P
         Q=ABS(Q)
         ETEMP=E
         E=D
          IF(ABS(P).GE.ABS(.5*Q*ETEMP).OR.P.LE.Q*(A-X).OR.
     *        P.GE.Q*(B-X)) GOTO 1
         D=P/Q
          U=X+D
          IF(U-A.LT.TOL2 .OR. B-U.LT.TOL2) D=SIGN(TOL1,XM-X)
         GOTO 2
        ENDIF
1        IF(X.GE.XM) THEN
         E=A-X
        ELSE
         E=B-X
      ENDIF
      D=CGOLD*E
2      IF(ABS(D).GE.TOL1) THEN
        U=X+D
      ELSE
        U=X+SIGN(TOL1,D)
      ENDIF
      FU= f1dimbis(U)
       IF(FU.LE.FX) THEN
        IF(U.GE.X) THEN
          A=X
        ELSE
          B=X
        ENDIF
        V=W
        FV=FW
        W=X
        FW=FX
        X=U
        FX=FU
      ELSE
        IF(U.LT.X) THEN
          A=U
        ELSE
          B=U
        ENDIF
        IF(FU.LE.FW .OR. W.EQ.X) THEN
          V=W
          FV=FW
          W=U
          FW=FU
        ELSE IF(FU.LE.FV .OR. V.EQ.X .OR. V.EQ.W) THEN
          V=U
          FV=FU
        ENDIF
      ENDIF
11    CONTINUE
c     PAUSE 'Brent exceed maximum iterations.'
3     XMIN=X
     BRENTbis=FX
     RETURN
     END

     FUNCTION F1DIMbis(X)
      implicit double precision (a-h,o-z), integer (i-n)
     PARAMETER (NMAX=50)
     COMMON /F1COM/ PCOM(NMAX),XICOM(NMAX),ncom
     DIMENSION XT(nmax)
     DO 11 J=1,NCOM
      XT(J)=PCOM(J)+X*XICOM(J)
11    CONTINUE
     F1DIMbis = chisqbis(XT)
     RETURN
     END
```